Het 3D elektromagnetische kwantitatieve
inverse verstrooiingsprobleem: algoritmes en regularisatie

On the 3D Electromagnetic Quantitative
Inverse Scattering Problem: Algorithms and Regularization

Jürgen De Zaeytijd

Promotor: prof. dr. ir. A. Franchois
Proefschrift ingediend tot het behalen van de graad van
Doctor in de Ingenieurswetenschappen: Toegepaste Natuurkunde

Vakgroep Informatietechnologie
Voorzitter: prof. dr. ir. D. De Zutter
Faculteit Ingenieurswetenschappen
Academiejaar 2008 - 2009

UNIVERSITEIT
GENT

ISBN 978-90-8578-248-3
NUR 928, 959
Wettelijk depot: D/2009/10.500/6

Dankwoord

Voila, het ligt voor u, beste lezer. Mijn doctoraatsproefschrift. Vermoedelijk is uw interesse in de rest van dit boek omgekeerd evenredig met de mate waarin u mij persoonlijk kent. Als u mij goed kent, is de kans groot dat u ofwel al min of meer weet wat erin staat, ofwel dat u eigenlijk vooral wil zien of u in het dankwoord vermeld wordt. Lees dan maar snel verder (spannend!). Als u aan de andere kant werkelijk van plan bent dit doctoraat tot op de letter door te nemen, dan doet u dat waarschijnlijk beroepsmatig en wens ik u veel doorzettingsvermogen.

Mijn onderzoek zou er niet zijn zonder de onderzoeksgroep elektromagnetisme, die deel is van de vakgroep Informatietechnologie en die zou er op zijn beurt niet zijn zonder Paul Lagasse. Ik wil dus Paul bedanken voor de kans die mij werd gegeven (en voor de INTEC avondfeesten natuurlijk!). Maar ik wil toch vooral de mensen die dichter bij mij stonden bedanken.

Laat mij beginnen met de persoon die na mij het nauwst betrokken was bij dit doctoraat: Ann Franchois, mijn promotor. Bedankt voor de aangename samenwerking de voorbije vier jaar. Bedankt vooral voor de vrijheid die ik genoot, voor de energie die je stak in al onze schrijfsels, inclusief dit proefschrift, en voor de zachte, doch ondersteunende hand die mij in de buurt van het juiste pad hield. Verder wil ik ook speciaal Femke Olyslager bedanken, want zij heeft mij bij de onderzoeksgroep elektromagnetisme binnengeleid. Van haar onthou ik vooral het vermogen om mensen te motiveren en te doen geloven in zichzelf. Bedankt. De rest van het proffenbestand van onze groep mag er ook zijn. Daniël De Zutter leidt de groep - en nu ook de vakgroep - met visie en enthousiasme en steekt met dat laatste iedereen aan. Luc Knockaert is de redder in nood van al wie zich onzeker voelt in de wereld van de Wiskunde. Hendrik Rogier, bedankt voor het aangename gezelschap op conferenties en de goede raad. Bedankt ook aan de IT-mensen, Kristien en Bert, want zonder jullie waren wij technisch werkloos. Bedankt Isabelle voor de hulp bij het nemen van allerlei administratieve en voor mij vaak onbegrijpelijke hindernissen. Bedankt vooral om dat altijd met een stralende lach te doen.

Dan kom ik bij de collega's. Ik begin met mijn ex-klasgenootjes. Ignace, wij hebben samen veel geproduceerd: een thesis en heel wat ideeën, maar vooral enorm veel gezever. Er is een human-beatbox-team, een cabaretduo, een gregoriaans koor en een stel Vlaamse zangers aan ons verloren gegaan. Aan iedereen op de gang die last had van geluidoverlast uit 13.B, sorry daarvoor. Bedankt Ignace om mij te doen volhouden tot het einde. Kristof, ik stond vaak zonder echt goede reden aan je bureau

in 13.A. Bedankt voor de oneindigheid aan interessante en grappige weetjes en opmerkingen die je mij dan iedere keer toestak. Roald, bedankt voor je goedgemutsheid en relativerende kijk op de dingen en voor de vele discussies tijdens de middagpauze. Lieven, jij bent al even weg uit de groep, maar dat maakt niet dat je geen dankwoordje verdient. Integendeel. De korte tijd in de HFHS meetruimte was hilarisch. Maar u moet ik vooral bedanken voor zaken die niets met mijn doctoraat te maken hebben en dus hier niet thuishoren. Sara, bedankt voor het gezelschap en de leuke gesprekken in Italië, Zuid-Frankrijk en Canada. Het ga je goed. Bedankt aan mijn bureaugenoten Gunther, Davy, Dirk en Dieter voor de leuke sfeer. Bedankt aan Jan en Joris van 13.A, waar ik bijna evenveel tijd doorbracht als aan mijn eigen computer gedurende de laatste maanden. Nu kunnen jullie weer ongestoord werken. Bedankt aan alle andere collega's: Dries, Frederick, Pieterjan, Thomas, Wouter, Francesco, Carla, Maria, Luigi en Ben. Ook Peter Lewyllie, die ondertussen al een eindje de groep verlaten heeft, wil ik bedanken. Enerzijds voor de hulp bij het verjagen van mijn informatica-nachtmerries en anderzijds voor het toffe en cultureel hoogstaande gezelschap in Turijn en Marseille. Bedankt ook aan de mensen van het Insitut Fresnel in Marseille. Vooral aan Jean-Michel Geffrin. Aangezien mijn Frans op niet veel trekt: Jean-Michel, thank you for offering me your full cooperation and your enthusiasm, for the useful suggestions and for inviting me over for dinner during the short visit of Peter and myself to the measurement facility in Marseille.

Aan mijn studietijd in Gent heb ik heel wat goede vrienden overgehouden. Lieven, Ignace, Kristof en Roald: jullie werden collega's en zijn reeds aan bod gekomen in dit dankwoord. Guillaume en Filip: wij gaan nog fantastisch slets geven in het repetitiekot en op het podium, maar ook bedankt voor de voorbije jaren. Jonathan en Wim, bedankt voor de nachtelijke discussies en de mannenklap en ik zou zeggen: wordt vervolgd. Tom en Kathy, An: ik weet jullie wonen. Bij uitbreiding bedankt aan al mijn andere klasgenootjes uit BN 1, 2 en 3, voor de leuke tijd. Vóór de proeven waren er de kandidaturen en vier jaar na het afstuderen blijft wat mij betreft de kern van ons toenmalige bende over: Bram, Christophe, Tom en Wim, als jullie me bellen, sta ik direct aan jullie deur ('t is te zeggen, voor Bram geldt dat enkel als hij eens ophoudt met voortdurend de hele wereld rond te crossen).

Tijdens mijn studententijd ontmoette ik nog iemand anders, in de Zuid-Franse Camargue dan nog. Ze zullen het mij ginder wel kwalijk nemen, maar ik heb een stukje zon mee naar huis genomen. Het heet Regina. Al zes jaar houdt ze het vol bij mij en ik hoop echt dat ze ook de rest van mijn leven wil regisseren. Bedankt Lieveke!

Maar al het bovenstaande was onbestaande geweest als ik niet de steun en de kansen had gekregen van mijn ouders. Mama en papa, ik ben jullie ongelooflijk dankbaar voor de warme thuis die Ruben, Jeroen en ikzelf hebben. Daarom draag ik dit doctoraat vooral aan jullie op.

Jurgen De Zaeytijd
Gent, 31 december, 2008

An expert is a man who has made all the mistakes, which can be made, in a very narrow field.

NIELS BOHR, PHYSICIST

Contents

Samenvatting

De term elektromagnetische inverse verstrooiing verwijst naar de technieken en processen die men gebruikt om informatie te winnen over bepaalde objecten uit de manier waarop ze elektromagnetische straling verstrooien. Elektromagnetische inverse verstrooiing is dus een voorbeeld van elektromagnetische beeldvorming. Wanneer hiervoor microgolfstraling wordt gebruikt, spreekt men van microgolfbeeldvorming, dat toepassingen heeft als medische beeldvorming, niet-destructief testen, geofysische exploratie, enzovoort. In een elektromagnetisch verstrooiingsexperiment wordt het studieobject belicht met een aantal gekende invallende elektromagnetische golven, waarbij de positie van de bron en vaak ook de frequentie gevarieerd wordt. Voor elk van deze belichtingen worden de verstrooide elektromagnetische velden gemeten in een aantal waarnemingspunten. Als de invallende velden en de meetpunten goed gekozen zijn, bevat deze vertrooiingsdata voldoende informatie om de vorm, de locatie en elektromagnetische materiaalparameters van het studieobject te bepalen.

Een elektromagnetische beeldvormingstechniek die deze objecteigenschappen uit de data haalt op een kwantitatieve manier, dus onder de vorm van hun numerieke waarden, wordt een kwantitatieve elektromagnetische beeldvormingstechniek genoemd. Over het algemeen is het een iteratieve methode die het niet-lineaire elektromagnetische inverse verstrooiingsprobleem oplost door het te formuleren als een optimalisatievraagstuk, waarbij een numeriek verstrooiingsmodel gefit wordt aan de data door de objectparameters te variëren. In de praktijk zal men een onderzoeksdomein bedekken met een rooster van voxels (een voxel is een 3D pixel) en zal men de materiaalparameters – in deze thesis de complexe permittiviteit – in elke voxel als optimalisatieveranderlijke beschouwen. Hoewel er andere methodes bestaan die enkel een lineair probleem oplossen in plaats van een niet-lineair optimalisatievraagstuk, zijn zulke methodes vaak gebaseerd op vereenvoudigingen van het verstrooiingsmodel en in elk geval geven ze alleen kwalitatieve informatie over de studieobjecten, meestal enkel over de vorm, de afmetingen en de positie. In deze thesis worden 3D kwantitatieve microgolfbeeldvormingsalgoritmes ontwikkeld met de nadruk op efficiëntie en reconstructiekwaliteit.

Een belangrijk onderdeel van de meeste kwantitatieve reconstructie-algoritmes is een voorwaartse simulator, die de verstrooiing van de gekende invallende golven aan een gegeven 3D complexe-permittiviteitsprofiel in het onderzoeksdomein berekent. Door de herhaalde oplossingen van het voorwaartse verstrooiingsprobleem en het grote aantal onbekenden daarin, is het oplossen van het elektromagnetische inverse

verstrooiingsprobleem een rekenintensieve taak en is er nood aan efficiënte voorwaartse simulatoren. In deze thesis werd een snelle simulator, die gebruik maakt van een volumeintegraalvergelijking, geïmplementeerd om het voorwaartse verstrooiingsprobleem op te lossen. Het oplossen van het resulterende lineaire stelsel gebeurt iteratief, omdat het stelsel teveel onbekenden heeft om het met directe inversiemethodes op te lossen. Om de iteratieve oplossing efficiënt te maken, worden twee strategieën gecombineerd. Enerzijds worden de matrix-vector-vermenigvuldigingen in elke stap van de iteratieve oplossing versneld door een combinatie van de Fast Fourier Transform (FFT) en het Multilevel Fast Multipole Algoritme (MLFMA) te gebruiken. Het wordt aangetoond dat deze hybride MLFMA-FFT methode het meest geschikt is voor verstrooiing aan geometrieën die groot zijn, maar veel lege ruimte bevatten. Anderzijds wordt het aantal benodigde iteraties gereduceerd door middel van een extrapolatietechniek die gepaste beginschattingen bepaalt, welke reeds dicht bij de oplossing liggen. Deze techniek combineert een stapschema in de bronpositie met een lineaire extrapolatie over de permittiviteit onder de vorm van een Born benadering. Zoals blijkt uit dit proefschrift, vertoont deze voorwaartse simulator inderdaad een verbeterde efficiëntie.

De snelle voorwaartse simulator werd geïncorporeerd in een optimalisatietechniek die het verschil tussen gemeten data en gesimuleerde data minimaliseert door het permittiviteitsprofiel aan te passen. In dit proefschrift wordt een Gauss-Newton methode met lijnoptimalisatie gebruikt om een kleinste kwadraten datafout-kostfunctie te minimaliseren waaraan een regularisatiemechanisme werd toegevoegd. Dit laatste is nodig door het slecht gesteld zijn van het inverse verstrooiingsprobleem, wat zich uit in het feit dat sommige aanzienlijke veranderingen in het permittiviteitsprofiel, meestal met hoge spatiale frequentie, enkel kleine afwijkingen in de verstrooiingsdata veroorzaken die niet kunnen geresolveerd worden als er meetruis op de data zit. Hierdoor kunnen zulke sterk oscillerende perturbaties de reconstructie van de permittiviteit verstoren en dit moet worden tegengegeaan met regularisatie. Een regularisatiemethode verwerkt bepaalde a priori informatie over het studieobject in de optimalisatie, bijvoorbeeld de afwezigheid van rimpels met hoge spatiale frequentie. Zo wordt het verlies aan informatie in de data gecompenseerd en de vervorming van de reconstructie vermeden.

Twee verschillende regularisatiemethodes werden ontwikkeld in dit onderzoek. De eerste regularisatietechniek straft sterke fluctuaties in de permittiviteit af door een gladheidsvoorwaarde op te leggen. Dit is een veel gebruikte aanpak voor inverse verstrooiing. Echter, in dit proefschrift wordt deze voorwaarde opgelegd op een multiplicatieve manier in plaats van op de gewoonlijke additieve manier. Dat wil zeggen dat het gewicht van de regularisatie in de totale kostfunctie afneemt als de data fit verbetert. Hierdoor past de regularisatie zichzelf aan aan het ruisniveau en wordt de keuze van een regularisatieparameter minder kritisch. De tweede regularisatiemethode is Value Picking (VP) regularisatie, een nieuwe methode ontwikkeld in dit onderzoek. Deze techniek is ontworpen om stuksgewijs homogene permittiviteitsprofie-

len te reconstrueren. Zulke profielen zijn moeilijk te reconstrueren omdat scherpe overgangen tussen gebieden met verschillende permittiviteit moeten bewaard blijven, terwijl andere sterke fluctuaties moeten onderdrukt worden. In plaats van hiervoor te werken op de ruimtelijke verdeling van de permittiviteit, zoals bestaande methodes voor het behoud van randen in de reconstructie, legt VP regularisatie de beperking op dat slechts een klein aantal verschillende permittiviteitswaarden in de reconstructie mogen voorkomen. Dit vermijdt een aantal problemen met de keuze van een gladheidsdrempel die voorkomen in andere methodes. De permittiviteitswaarden waarvan sprake moeten echter niet op voorhand gekend zijn en hun aantal wordt eveneens geoptimaliseerd in een stepwise relaxed VP (SRVP) regularisatieschema.

Beide regularisatietechnieken werden geïncorporeerd in het raamwerk van de Gauss-Newton minimalisatie en resulteren in sterk verbeterde kwaliteit van de reconstructies. De efficiëntie van het minimalisatiealgoritme kan ook worden verbeterd. In elke stap van de iteratieve optimalisatie moet er een lineair Gauss-Newton stelsel worden opgelost om de aanpassing van het permittiviteitsprofiel te berekenen. Dit is typisch een groot stelsel en daarom wordt het iteratief opgelost. Deze stelsels zijn echter slecht geconditioneerd ten gevolge van het slecht gesteld zijn van het inverse verstrooiingsprobleem. Gelukkig laten de vermelde regularisatiemethodes het gebruik toe van een LSQR methode met conditionering met behulp van deelruimtes, waarmee de Gauss-Newton stelsels efficiënt kunnen worden opgelost. Dit wordt in deze thesis aangetoond. Tenslotte werden grenzen op de permittiviteitswaarden in het algoritme opgenomen door het wijzigen van het pad in de lijnoptimalisatie, wat ervoor zorgt dat de voorwaarste problemen goed geconditioneerd blijven en het aantal voorwaarste iteraties beperkt.

Een andere bijdrage van dit onderzoek is het voorstel van een nieuwe methode, genaamd Consistentie Inversie (CI), die gebaseerd is op dezelfde principes als een andere goed gekende reconstructiemethode, de Constrast Source Inversion (CSI) methode. Deze laatste techniek beschouwt de contraststromen - equivalente stroombronnen die een veld veroorzaken dat identiek is aan het verstrooide veld - als fundamentele onbekenden naast de permittiviteit. In de CI methode worden de permittiviteitsonbekenden echter geëlimineerd uit de optimalisatie en worden ze slechts bepaald in een laatste stap. Dit vermijdt afwisselende updates van permittiviteit en contraststromen en kan daardoor resulteren in een snellere convergentie. De CI methode werd ook uitgerust met VP regularisatie, wat resulteert in de VPCI methode.

De kwantitatieve elektromagnetische beeldvormingsmethodes ontwikkeld in dit werk werden gevalideerd op zowel synthetische data als op experimentele data, voor zowel homogene als inhomogene objecten en in al deze gevallen is de kwaliteit van de reconstructies hoog. De succesvolle, volledig blinde reconstructie van een onbekend object uitgaande van gemeten data, ons geleverd door het Institut Fresnel in Marseille, Frankrijk, demonstreert in één klap de geldigheid van de voorwaartse simulator, de performantie van het reconstructiealgoritme en de kwaliteit van de metingen. De re-

constructie van een numeriek borstfantoom, gebaseerd op MRI beelden, is bemoedigend voor de verdere ontwikkeling van biomedische microgolfbeeldvorming en in het bijzonder borstkankerdetectie met microgolven.

Summary

The term electromagnetic inverse scattering refers to the techniques and processes used to obtain information about certain objects from the way in which they scatter electromagnetic radiation. Electromagnetic inverse scattering thus is an example of electromagnetic imaging. Microwave imaging is the special case of electromagnetic imaging that employs microwave radiation and has applications in medical imaging, non-destructive testing, geophysical exploration, etc. In an electromagnetic scattering experiment, the target under study is illuminated with a number of known incoming electromagnetic waves with varying position of the source antenna and often also with varying frequency. For each such illumination, the scattered electromagnetic fields are measured in a number of observation points. When the incident waves and measurement positions are properly chosen, these scattering data contain sufficient information to retrieve the shape, location and electromagnetic material parameters of the target.

An electromagnetic imaging method that extracts these object properties from the data in a quantitative way, i.e. it obtains their numerical values, is termed a quantitative electromagnetic imaging method. It generally is an iterative method which solves the non-linear electromagnetic inverse scattering problem by recasting it as an optimization problem, where a numerical scattering model is fitted to the data by tuning the object properties. In practice, the electromagnetic inverse scattering problem is most often solved by discretizing an investigation domain with a 3D voxel grid (a voxel is a 3D pixel) and by considering the electromagnetic material parameters – the complex permittivity in this thesis – in each voxel as optimization variables. Although other imaging methods exist which solve only a linear system instead of a non-linear optimization problem, such methods often rely on approximations of the scattering model and in any case they only give qualitative information on the targets, mostly only of its shape, size and location. In this thesis, 3D quantitative microwave imaging algorithms are developed with emphasis on efficiency of the algorithms and quality of the reconstruction.

An important part of most quantitative reconstruction algorithms is a forward simulator, which calculates the scattering of the known incident waves from a certain 3D profile of the complex permittivity in the investigation domain. Because of the repeated forward scattering problem solutions during the optimization and the large number of unknowns in this problem, solving the electromagnetic inverse scattering problem is a computationally challenging task and there is a need for efficient forward

simulators. In this thesis a fast simulation tool has been implemented which makes use of a volume integral equation (VIE) to solve the forward scattering problem. The solution of the resulting linear system is done iteratively, since it is a system with too many unknowns to solve it directly through matrix inversion. To do this efficiently, two strategies are combined. First, the matrix-vector multiplications needed in every step of the iterative solution are accelerated using a combination of the Fast Fourier Transform (FFT) method and the Multilevel Fast Multipole Algorithm (MLFMA). It is shown that this hybrid MLFMA-FFT method is most suited for large, sparse scattering problems. Secondly, the number of iterations is reduced by using an extrapolation technique to determine suitable initial guesses, which are already close to the solution. This technique combines a marching-on-in-source-position scheme with a linear extrapolation over the permittivity under the form of a Born approximation. It is shown that this forward simulator indeed exhibits a better efficiency.

The fast forward simulator is incorporated in an optimization technique which minimizes the discrepancy between measured data and simulated data by adjusting the permittivity profile. A Gauss-Newton optimization method with line search is employed in this dissertation to minimize a least squares data fit cost function with additional regularization. The latter is needed because of the ill-posedness of the inverse scattering problem, which is reflected in the fact that certain significant changes in the permittivity profile, mostly with high spatial frequency, yield only small deviations in the scattering data which cannot be resolved when the data is corrupted with measurement noise. As a result, such strongly oscillating perturbations can distort the permittivity reconstruction and this has to be remedied by regularization. A regularization method incorporates some a priori information on the target – for instance the absence of ripples with high spatial frequency in the permittivity profile – in the optimization process to compensate for the loss of information and to avoid distortion of the reconstruction.

Two different regularization methods were developed in this research. The first regularization method penalizes strong fluctuations in the permittivity by imposing a smoothing constraint, which is a widely used approach in inverse scattering. However, in this thesis, this constraint is incorporated in a multiplicative way instead of in the usual additive way, i.e. its weight in the cost function is reduced with an improving data fit. As a result, the regularization adapts itself automatically to the noise level, which renders the determination of a regularization parameter less critical. The second regularization method is Value Picking regularization, which is a new method proposed in this dissertation. This regularization is designed to reconstruct piecewise homogeneous permittivity profiles. Such profiles are hard to reconstruct since sharp interfaces between different permittivity regions have to be preserved, while other strong fluctuations need to be suppressed. Instead of operating on the spatial distribution of the permittivity, as certain existing methods for edge preservation do, it imposes the restriction that only a few different permittivity values should appear in

the reconstruction. This avoids some problems with the determination of a smoothing threshold that occur in other methods. The permittivity values just mentioned do not have to be known in advance, however, and their number is also updated in a stepwise relaxed VP (SRVP) regularization scheme.

Both regularization techniques have been incorporated in the Gauss-Newton optimization framework and yield significantly improved reconstruction quality. The efficiency of the minimization algorithm can also be improved. In every step of the iterative optimization, a linear Gauss-Newton update system has to be solved. This typically is a large system and therefore is solved iteratively. However, these systems are ill-conditioned as a result of the ill-posedness of the inverse scattering problem. Fortunately, the aforementioned regularization techniques allow for the use of a subspace preconditioned LSQR method to solve these systems efficiently, as is shown in this thesis. Finally, the incorporation of constraints on the permittivity through a modified line search path, helps to keep the forward problem well-posed and thus the number of forward iterations low.

Another contribution of this thesis is the proposal of a new Consistency Inversion (CI) algorithm. It is based on the same principles as another well known reconstruction algorithm, the Contrast Source Inversion (CSI) method, which considers the contrast currents – equivalent currents that generate a field identical to the scattered field – as fundamental unknowns together with the permittivity. In the CI method, however, the permittivity variables are eliminated from the optimization and are only reconstructed in a final step. This avoids alternating updates of permittivity and contrast currents, which may result in a faster convergence. The CI method has also been supplemented with VP regularization, yielding the VPCI method.

The quantitative electromagnetic imaging methods developed in this work have been validated on both synthetic and measured data, for both homogeneous and inhomogeneous objects and yield a high reconstruction quality in all these cases. The successful, completely blind reconstruction of an unknown target from measured data, provided by the Institut Fresnel in Marseille, France, demonstrates at once the validity of the forward scattering code, the performance of the reconstruction algorithm and the quality of the measurements. The reconstruction of a numerical MRI based breast phantom is encouraging for the further development of biomedical microwave imaging and of microwave breast cancer screening in particular.

List of Abbreviations

2D	Two-Dimensional
3D	Three-Dimensional
BFGS	Broyden-Fletcher-Goldfarb-Shanno
BICGSTAB	Bi-Conjugate Gradient
CG	Conjugate Gradient
CI	Consistency Inversion
CSI	Contrast Source Inversion
DCT	Discrete Cosine Transform
FFT	Fast Fourier Transform
FMM	Fast Multipole Method
(HF) MLFMA	(High Frequency) Multilevel Fast Multipole Algorithm
MoM	Method of Moments
MPDE	Mixed Potential Domain Equation
MS	Multiplicative Smoothing
SPLSQR	Subspace Preconditioned LSQR
SRRP	Stepwise Relaxed Region Picking
SRVP	Stepwise Relaxed Value Picking
TM	Transverse Magnetic
TV	Total Variation
VIE	Volume Integral Equation
RP	Region Picking
VP	Value Picking
VPCI	Consistency Inversion with Value Picking regularization

List of Symbols

Vectors and matrices

Vectors of general dimension are denoted by boldface lower case letters. Matrices of general dimensions as well as electromagnetic field vectors and dyadics are denoted by boldface upper case letters.

$\boldsymbol{r}$	The position vector in three dimensions
$\boldsymbol{\rho}$	The position vector in two dimensions
$\hat{\boldsymbol{x}}$	A unit vector in the positive x-direction
$\hat{\boldsymbol{y}}$	A unit vector in the positive y-direction
$\hat{\boldsymbol{z}}$	A unit vector in the positive z-direction
$\hat{\boldsymbol{u}}$	A unit vector with the same orientation as the vector $\boldsymbol{u}$
$\boldsymbol{I}_N$	The $N \times N$ unit matrix
$\mathbb{I}$	The identity dyadic in three dimensions

Operations on vectors and matrices and related concepts

$(\dots)^*$	Complex conjugate
$(\dots)^T$	Transpose
$(\dots)^H$	Conjugate transpose
$\sigma_l(\boldsymbol{A})$	The l-th singular vector of the matrix $\boldsymbol{A}$. Singular values decrease with increasing index
$\|\dots\|$	The L^2 norm, i.e. $\|\boldsymbol{u}\|^2 = \boldsymbol{u}^H\boldsymbol{u}$ for a vector $\boldsymbol{u}$ and $\|\boldsymbol{A}\| = \sigma_1(\boldsymbol{A})$ for a matrix $\boldsymbol{A}$
$[\boldsymbol{u}]_n$	n-th element of the general vector $\boldsymbol{u}$ (sometimes denoted as u_n)
$[\boldsymbol{A}]_{nm}$	nm-th element of the general matrix $\boldsymbol{A}$ (sometimes denoted as A_{nm})
$\cdot$	scalar (inner) product of 3-vectors, e.g. $\hat{\boldsymbol{x}} \cdot \hat{\boldsymbol{y}}$
$\boldsymbol{uv}$	tensor (outer) product of the general vectors $\boldsymbol{u}$ and $\boldsymbol{v}$: $[\boldsymbol{uv}]_{nm} = u_n v_m$
$\circ$	element-wise multiplication of general vectors: $[\boldsymbol{u} \circ \boldsymbol{v}]_n = u_n v_n$

Electromagnetic symbols

ϵ_0	The permittivity of vacuum
μ_0	The permeability of vacuum
ϵ	The complex permittivity

f	The frequency
ω	The angular frequency ($\omega = 2\pi f$)
ϵ_r	The real part of the relative permittivity
σ	The conductivity
k	The wave number $k = j\omega\sqrt{(}\epsilon\mu_0)$
χ	The permittivity contrast
ξ	The normalized permittivity contrast
$(\ldots)_\mathrm{b}$	Subscript to indicate a property of the background medium
$(\ldots)_0$	Subscript to indicate a property of vacuum
$\boldsymbol{E}$	The electric field vector
$\boldsymbol{H}$	The magnetic field vector
$\boldsymbol{D}$	The electric induction vector
$\boldsymbol{B}$	The magnetic induction vector
$\boldsymbol{J}$	The electric current density vector
G_b	The Green function of the background medium
$\boldsymbol{G}_\mathrm{b}$	The Green dyadic of the background medium
$\boldsymbol{G}_\mathrm{inh}$	The Green dyadic in an inhomogeneous background medium
$\mathcal{G}_\mathrm{b}^\mathcal{V}$	Green operator acting on a vector function with support $\mathcal{V}$
ρ	The electric charge density

Symbols related to the forward and inverse scattering algorithms

$\mathcal{D}$	The investigation domain
$\mathcal{D}^\epsilon$	The discretization grid for the permittivity
$\Phi_{f,g,h}$	A 3D pulse function which is 1 in cell (f,g,h) of the permittivity grid $\mathcal{D}^\epsilon$ and zero elsewhere
$\epsilon_{f,g,h}$	The relative permittivity in cell (f,g,h)
$\mathcal{C}_\nu$	A group of cells in the permittivity grid with index ν
ϵ_ν	A permittivity unknown; the permittivity of cell group $\mathcal{C}_\nu$
N^ϵ	The number of permittivity unknowns
$\boldsymbol{\varepsilon}$	The N^ϵ-dimensional vector containing the optimization variables ϵ_ν
N^I	The number of illuminations
N_i^R	The number of measurement points corresponding to illumination i
N	The number of field unknowns in the forward problem
N^S	The number of cubic subdomains in the MLFMA-FFT method
δ	The grid size of the forward grid
N^C	The number of cells in one subdomain in the MLFMA-FFT method
$\mathcal{D}^F$	The discretization grid for the electric flux density $\boldsymbol{D}$ or forward grid
F_α	The face with index α in the forward grid
$\boldsymbol{\Psi}_\alpha$	The vectorial rooftop function associated with F_α

$\boldsymbol{g}$	A (complex) gradient vector
$\boldsymbol{H}$	A (complex) Hessian matrix
$\boldsymbol{J}$	The Jacobian matrix of the scattered field vector with respect to the permittivity unknowns
T^N	The noise level
$\mathcal{F}^{LS}$	The least squares data fit cost function
$\mathcal{F}^{R}$	The smoothing regularizing function
$\mathcal{F}^{S}$	The cost function with multiplicative smoothing regularization
$\mathcal{F}^{VP}$	The cost function with Value Picking regularization
$\mathcal{F}^{P}$	The VP regularizing function with P VP values
f^P	The P-dimensional choice function

Special functions

$H_0^{(2)}$	Zeroth order Hankel function of the second kind
$h_l^{(2)}$	Spherical Hankel function of the second kind and order l
P_l	Legendre function of order l
j_l	Spherical Bessel function of order l

Miscellaneous

j	The imaginary unit, $j = \sqrt{-1}$
$\mathcal{O}(\cdot)$	Complexity measure: $\text{cost} = \mathcal{O}(x) = Cx$ with C a constant called the prefactor
$\mathbb{R}_+$	The set of non-negative real numbers

List of Publications

Articles in international journals

- J. De Zaeytijd, A. Franchois , C. Eyraud, J.M. Geffrin, "Full-wave three-dimensional microwave imaging with a regularized Gauss-Newton method – theory and experiment", *IEEE Transactions on Antennas and Propagation*, Vol. 55, No. 11, pp. 3279-3292, November 2007.

- J. De Zaeytijd, I. Bogaert, A. Franchois, "An efficient hybrid MLFMA-FFT solver for the volume integral equation in case of sparse 3-D inhomogeneous dielectric scatterers", *Journal of Computational Physics*, Vol. 227, No. 14, pp. 7052-7068, 2008.

- J. De Zaeytijd, A. Franchois, J.M. Geffrin, "A new value picking regularization strategy – application to the 3D electromagnetic inverse scattering problem", *Accepted for IEEE Transactions on Antennas and Propagation*.

- J. De Zaeytijd, A. Franchois, "A consistency inversion algorithm with value picking regularization for the 2D electromagnetic inverse scattering problem", *Submitted to IEEE Transactions Antennas and Propagation*.

- J. De Zaeytijd, A. Franchois, "3D Quantitative microwave imaging from measured data with multiplicative smoothing and value picking regularization", *Submitted to Inverse Problems*.

- J. De Zaeytijd, A. Franchois, "Three-dimensional vectorial quantitative microwave tomography for biomedical imaging: subspace preconditioning and regularization.", *Submitted to IEEE Transactions on Biomedical Engineering*.

Articles in conference proceedings

- J. De Zaeytijd, A. Franchois, F. Olyslager, "A fast HF MLFMA full-wave forward solver for 3-D lossy dielectric objects in a homogeneous background", *Proceedings of Joint 9th International Conference on Electromagnetics in Advanced Applications ICEAA'05 and 11th European Electromagnetic Structures Conference EESC'05*, Torino, Italy, 12-16 September 2005, pp. 413 - 416.

- J. De Zaeytijd, A. Franchois, F. Olyslager, "3-D electromagnetic scattering analysis of electrically large dielectric objects using MLFMA", *Workshop on inverse problems WIP 2005*, Marseille, France, pp. 73-76, December 2005.
- J. De Zaeytijd, A. Franchois, C. Eyraud and J.M. Geffrin, "Three dimensional complex permittivity reconstruction by means of Newton-type microwave imaging", *Proceedings of EUCAP 2006*, Nice, France, 6 - 10 November 2006, CD-ROM, session OA13.
- J. De Zaeytijd , A. Franchois, "Full-wave three-dimensional microwave imaging with a regularized Gauss-Newton method", *The 23rd Annual Review of Progress in Applied Computational Electromagnetics '2007 ACES*, Verona, Italy, 19-23 March 2007, pp. 667 - 674.
- J. De Zaeytijd, T. Maes, A. Franchois, "2-D real-time quantitative microwave imaging of reinforcement bars: simulations and experiments", *International Conference on Electromagnetics in Advanced Applications*, 17-21 September , 2007 Torino, Italy, CD-ROM.
- J. De Zaeytijd, A. Franchois, "3D quantitative microwave imaging with a regularized Gauss-Newton method for vreast cancer detection", *The 24th Annual Review of Progress in Applied Computational Electromagnetics '2008 ACES*, Niagara Falls, Canada, March 30 - April 4, pp. 467-472, 2008.
- J. De Zaeytijd, A. Franchois, "Breast cancer detection with a 3D microwave imaging reconstruction technique", *URSI Forum 2008*, Brussels, Belgium, May 30, pp. 23-25,2008.
- J. De Zaeytijd, C. L. Conmeaux, A. Franchois, "Three-dimensional linear sampling applied to microwave breast imaging", *The 29th General Assembly of the International Union of Radio Science (URSI)*, Chicago, USA, 7-16 August, 2008, CD-ROM.
- J. De Zaeytijd, A. Franchois, "A new value picking regularization method applied to the electromagnetic inverse scattering problem", *The 29th General Assembly of the International Union of Radio Science (URSI)*, Chicago, USA, 7-16 August, 2008, CD-ROM.

Conference abstracts

- F. Olyslager, J. De Zaeytijd, K. Cools, I. Bogaert, L. Meert, D. Vande Ginste en D. Pissoort, "Applications of complex coordinates to the MLFMA", *Proceedings of 2004 USNC/URSI National Radio Science Meeting*, Monterey, California, June 2004, p. 206.

- I. Bogaert, J. De Zaeytijd, D. Vande Ginste, D. Pissoort, F. Olyslager en E. Michielssen, "Simulation of extremely large 2-D electromagnetic problems", *5th UGent-FTW PhD Symposium*, Ghent, Belgium, December 2004.
- F. Olyslager, D. Pissoort, J. Fostier, I. Bogaert, J. De Zaeytijd en E. Michielssen, "Efficient and accurate techniques to simulate large electromagnetic crystals", *Proceedings of 2006 URSI National Radio Science Meeting*, Boulder, Colorado, January 2006, p. 58.
- P. Lewyllie, J. De Zaeytijd, A. Franchois, "Quantitative microwave imaging of 3D inhomogeneous objects", *2006 USNC/URSI National Radio Science Meeting, held in conjunction with the IEEE Antennas and Propagation Society International Symposium*, Albuquerque, USA, 9-14 July 2006, p. 177.
- J. De Zaeytijd, A. Franchois, "Full-vectorial 3D microwave inversion of inhomogeneous lossy dielectric objects", *URSI 2007 CNC/USNC North American Radio Science Meeting*, Ottawa, ON, Canada, 22-26 July 2007, ISBN: 978-0-9738425-2-4, CD-ROM B-20.
- A. Franchois, J. De Zaeytijd, "Three-dimensional quantitative microwave imaging", *GdR Ondes Runion gnrale "Interfrences d'ondes"*, Bordeaux, France, 21-23 November 2007.
- J. De Zaeytijd, A. Franchois, "3D quantitative microwave imaging of inhomogeneous dielectric objects", *8th FIRW PhD Symposium*, Ghent, Belgium, 5 December 2007, Interactive poster session, p. 101.
- J. De Zaeytijd, A. Franchois, "3D full-vectorial microwave reconstruction algorithm: application to medical imaging", *Progress in Electromagnetics Research Symposium (PIERS)*, 2-6 July, 2008 in Cambridge, USA.

Scientific awards

- Young Scientist Award for the XXIX URSI General Assembly in Chicago, USA, August 7-16, 2008.
- URSI Commision B Best Paper Prize for participation and presentation of the paper entitled "Three-dimensional linear sampling applied to microwave breast imaging" at the XXIX URSI General Assembly in Chicago, USA, August 7-16, 2008.

On the 3D electromagnetic quantitative inverse scattering problem: algorithms and regularization

CHAPTER 1

Introduction

1.1 Situation and history

Microwave imaging aims at characterizing an unknown object through electromagnetic scattering experiments. In such an experiment, the target is illuminated with different microwaves and the scattered electromagnetic fields are measured for each such illumination. From these scattering data one tries to determine certain object properties, such as shape, location and the distribution of electromagnetic material properties, such as the complex permittivity, inside the object. Possible applications include non-destructive testing, biomedical imaging and geophysical exploration. A variety of microwave imaging methods exist and the most distinctive differences among them can be found in the algorithms that extract unknown object properties from the scattering data. Based on the output of such an algorithm, one can distinguish two major classes of electromagnetic imaging methods. The methods in the first class are termed qualitative, because they do not provide quantitative information on the electromagnetic properties of the object under study. Instead they only give some idea about the support of the object, i.e. its shape and location and in case of multiple objects also their number. Microwave Diffraction Tomography [1–9], DORT (decomposition of the time reversal operator) [10–12], radar based techniques [13–16] including Confocal microwave imaging [17–19] and, more recently, the Linear Sampling method [20, 21] are examples of qualitative methods. The second class of methods is quantitative. They provide detailed information about all the relevant parameters that determine the interaction of an object with electromagnetic fields, i.e. its shape and location but also the values of its electromagnetic material parameters. The qualitative methods just mentioned are based on a linear or linearized model that relates the data and the reconstruction parameters (e.g. reflectivity, induced currents, permittivity,...), while quantitative methods solve the exact non-linear electromagnetic inverse scattering problem. Because the latter requires the solution of a system of non-linear equations, an iterative optimization procedure is generally applied. Therefore, quan-

titative imaging is both mathematically and computationally more challenging than qualitative imaging.

During the last two decades quantitative microwave imaging techniques were mainly developed for two-dimensional (2D), mostly Transverse Magnetic (TM)- polarized configurations [22–37]. In this 2D scalar framework various iterative reconstruction algorithms for different application-specific configurations [31, 32] as well as some experimental issues have been investigated [33, 34, 37]. Although an early implementation of the Newton-Kantorovich algorithm was applied to a simple 3D configuration by Joachimowicz et al. [23] in 1991, three-dimensional (3D) quantitative microwave imaging has not really been considered until the beginning of the new millennium. Bulyshev et al. [38] developed a 3D microwave tomography approach in a scalar approximation and Abubakar et al. [39] presented full-vectorial 3D inversion results using a multiplicative regularized contrast source inversion method, in both cases for biomedical applications. Other recent work on 3D inversion is reported in [40–47] and in [48], where 3D quantitative inversion is performed in the time domain. However, one can say that we only stand at the dawn of 3D quantitative microwave imaging and that a lot of ground has to be covered before such techniques can be successfully used in practical applications.

1.2 Problem formulation

It is the goal of this doctoral thesis to investigate and develop 3D complex permittivity reconstruction algorithms. The two main challenges associated with quantitative microwave imaging are the ill-posedness of the electromagnetic inverse scattering problem and its non-linearity. The former jeopardizes the robustness of the reconstruction algorithms and the quality of the results and the latter results in a high computational cost because it requires iterative optimization. A good algorithm for quantitative microwave imaging thus reduces the computational burden as much as possible and includes a proper regularization strategy to stabilize the reconstruction.

The type of quantitative microwave imaging algorithms that is considered in this dissertation attempts to recover the value of the complex permittivity in every point of an investigation domain. In the optimization approach to microwave imaging, a cost function, which depends on the permittivity distribution, is defined and then iteratively minimized. Most authors employ a least squares data fit cost function, which measures the difference between the measured field data and the scattered field computed for any given permittivity profile. Since the scattered field depends on two types of unknowns, the complex permittivity and the total field inside the object, two approaches for defining the cost function have been reported. In the first, “conventional”, approach, the total field unknown is eliminated by substitution, such that the cost function only depends on the complex permittivity. This approach involves the solution of a full forward scattering problem in each iteration of the optimization, i.e.

the numerical simulation of the scattering experiment for a given permittivity profile. Various Newton-type schemes [22, 23, 26, 29, 32] and a few global optimization techniques [24, 28] have been applied here. The Newton-based methods can be made to converge in a few iterations, but the forward problem solutions in each iteration can lead to long computation times. A second approach was presented by van den Berg et al. [27] and is called the contrast source inversion method (CSI). The method is a modification of the modified gradient method [25] and has been improved and extended [30, 39, 49, 50] since its introduction. With this kind of methods, the solution of the forward problems is eliminated by introducing a set of auxiliary variables – the contrast currents for the CSI method and the electric fields in the investigation domain for the modified gradient method – in a reformulated cost function. The larger number of unknowns, however, implies that efficient Newton-type optimization methods can no longer be used in this approach, because of memory limitations, and this results in a larger number of iterations. It is not clear yet whether and when the CSI and related methods outperform the conventional methods, but they have been applied by many authors during the last decade. In this thesis we investigate ways to improve the efficiency of both approaches.

Ill-posedness is typical for many inverse problems. Of the three criteria in Hadamard's definition of ill-posedness [51], non-uniqueness and instability are the two major burdens. The first problem stems from the combination of a limited information content in the data with a desire to reconstruct the complex permittivity profile with a high spatial resolution, which can introduce more reconstruction parameters than there are degrees of freedom in the data. The instability issue is the result of a low sensitivity of the scattered field to some fluctuations in the permittivity profile with high spatial frequency. Without precautions, such unwanted fluctuations can be amplified in the reconstruction, without noticeably degrading the data fit. To cope with these problems, a regularization strategy is indispensable. The purpose of regularization is to use some a priori information on the target to select a proper permittivity profile from the many that fit the data within the uncertainty introduced by noise. This is achieved by imposing extra constraints on the permittivity. This dissertation also studies new regularization methods.

1.3 Results of the research

The major part of this dissertation is devoted to 3D inversion algorithms that belong to the conventional approach. The basis of these methods is the Gauss-Newton minimization algorithm with line search, which is a variant of the Newton optimization algorithms. It exploits the specific form of the least squares cost function and requires no second order derivatives of the scattered fields with respect to the permittivity unknowns. The Gauss-Newton method has been modified in this work to include regularization by adding a regularizing function to the data fit function, which results

in reconstruction algorithms that provide high reconstruction quality and which converge rapidly. In this dissertation we propose two regularization strategies. The first one is a multiplicative smoothing (MS) regularization, which penalizes strong local variations in the permittivity profile by demanding that the reconstructed permittivity be sufficiently smooth. MS regularization operates on the spatial distribution of the permittivity in the investigation domain and adapts itself automatically to the level of noise on the data, i.e. there are no regularization parameters which strongly depend on this noise level. The MS regularization strategy is inspired by the work of mainly van den Berg and Abubakar [39, 49, 52, 53]. The second regularization method proposed in this thesis is a new type of regularization, which we have named Value Picking regularization or VP regularization. This regularization is most suited for permittivity profiles which are piecewise homogeneous or approximately so. Unlike most regularization methods, it does not operate on the spatial distribution of the permittivity, but imposes the constraint that the permittivity profile should consist of a limited number of different permittivity values. These values do not have to be known in advance, since they act as auxiliary optimization variables. Their number is also updated in a stepwise relaxed VP (SRVP) regularization strategy. To this end a new regularizing function is proposed and its properties are discussed. An extension of the VP regularization scheme to a Region Picking (RP) regularization scheme is finally suggested.

To reduce the computational cost, an efficient code has been developed to solve the forward problem iteratively. It is based on a combination of the Fast Fourier Transform (FFT) method [54–58] and the High Frequency Multilevel Fast Multipole Algorithm (HF MLFMA) [59–62], two methods that lower the memory use and the computation time in every iteration of the forward simulation. Moreover, since the forward problem has to be solved for varying source positions and permittivity profiles, an extrapolation procedure over these quantities can be used to determine a suitable initial guess for the iterative solution algorithm, which results in less forward iterations and thus also in an overall speed-up of the reconstruction [29, 63]. Apart from the forward simulation, there is another time-consuming component in Newton-based conventional reconstruction algorithms. That is the part where the Hessian matrix, or an approximate Hessian matrix, needs to be inverted. Since the dimensions of this matrix can become large in 3D inversion, it is not inverted directly. Rather, the associated linear system is again solved iteratively. However, due to the typical ill-conditioning of that system, its iterative solution converges very slowly. Therefore, in this thesis, a subspace preconditioning has been employed to solve these update systems more efficiently.

The resulting 3D inverse scattering algorithm has been validated extensively on both synthetic examples, where the data is generated through numerical simulation, and real world targets, where the data is actually measured in an experimental setup. The most popular future application of microwave imaging is medical imaging [64, 65]. Therefore, we present reconstructions of a number of biomedical phantoms from

synthetic data to examine the feasibility of microwave medical imaging. The most important of these examples is the reconstruction of a numerical breast phantom, which is encouraging for the use of microwave imaging in breast cancer detection. The implementation of a 3D Linear Sampling algorithm to find tumors in known breast tissue is also presented in this context. Since the most challenging test for reconstruction algorithms is their application to real measured data, we present numerous reconstructions from data which has been gathered in the bi-static polarimetric free-space measurement facility of Institut Fresnel, Marseille, France [66–68], and even a completely blind reconstruction of a mystery target. We were invited to contribute to a special issue in Inverse Problems on the testing of 3D reconstruction algorithms on experimental data, which is organized by the people of Institut Fresnel. Note that the successful inversion from measured data validates not only the reconstruction algorithm, but also the forward scattering code.

In the last part of this dissertation, an alternative, contrast source based approach is explored, which we denote as Consistency Inversion (CI). This method employs the same ideas as the CSI method, but the cost function is modified in order to eliminate the permittivity unknowns from the problem. In the original CSI method [27, 49, 50], the contrast currents and the permittivity unknowns are updated alternatingly, while in the CI method the contrast currents are the only optimization variables and hence the alternating updates of two sets of physically different quantities are avoided. Since it is known that alternating variable optimization methods can exhibit slow convergence [69], we think that the CI method may yield faster convergence than the CSI method. To test whether this is true, we tried both formulations in ideal circumstances on two test cases and conclude that the CI method indeed yields faster convergence on these examples and might do so in general. Finally, the VP regularization has also been incorporated in the CI method, yielding the VPCI method. This again greatly improves the reconstruction quality for piecewise constant permittivity profiles. The VPCI method has only been implemented so far for 2D TM reconstructions.

The organization of this thesis is as follows. In Chapter 2, inverse problems in general and the electromagnetic inverse scattering problem in particular are defined and some concepts and notations, necessary to understand the rest of the text, are introduced. Chapter 3 discusses the numerical solution of the forward scattering problem using a Volume Integral Equation (VIE). This chapter introduces the hybrid MLFMA-FFT method and the extrapolation procedure to determine the initial guesses for the iterative forward solutions. In Chapter 4 our 3D inverse scattering algorithms based on Gauss-Newton optimization are presented. Both types of regularization are proposed and discussed and various examples illustrate the performance of the algorithm. Further improvements to the general framework, namely the incorporation of constraints on the optimization variables by means of an adapted line search path and the use of subspace preconditioning, are also proposed. Chapter 5 is devoted to applications of the 3D reconstruction algorithm, i.e. biomedical imaging and reconstructions from

the Fresnel data. Finally, Chapter 6 explores the contrast source based approach to the inverse scattering problem by introducing the VPCI method for 2D TM inverse scattering problems.

Bibliography

[1] L.E. Larsen and J.H. Jacobi. Microwave scattering parameter imagery of an isolated canine kidney. *Med. Phys.*, 6:394–403, 1979.

[2] A.J. Devaney. A filtered backpropagation algorithm for diffraction tomography. *Ultrasonic Imag.*, 4:336–350, 1982.

[3] J.C. Bolomey, L. Jofre, C. Pichot, G. Peronnet, and M. Solaimani. Microwave diffraction tomography for biomedical applications. *IEEE Trans. Microw. Theory Tech.*, 30(11):1998–2000, 1982.

[4] A.J. Devaney. A computer simulation study of diffraction tomography. *IEEE Trans. Biomed. Eng.*, 30(7):377–386, 1983.

[5] C. Pichot, L. Jofre, G. Peronnet, and J.C. Bolomey. Active microwave imaging of inhomogeneous bodies. *IEEE Trans. Antennas Propagat.*, 33(4):416–423, 1985.

[6] G.T. Herman, H.K. Tuy, K.J. Langenberg, and P. Sabatier. *Basic methods of tomography and inverse problems*. Adam Hilger, Bristol, 1987.

[7] W. Tabbara, B. Duchêne, C. Pichot, D. Lesselier, L. Chommeloux, and N. Joachimowicz. Diffraction tomography: contribution to the analysis of some applications in microwaves and ultrasonics. *Inverse Problems*, 4(2):305–331, 1988.

[8] L. Jofre, M. Hawley, A. Broquetas, E. de los Reyes, M. Ferrando, and A. Elias. Medical imaging with a microwave tomographic scanner. *IEEE Trans. Biomed. Eng.*, 37(3):303–312, 1990.

[9] K.J. Langenberg, M. Brandfass, P. Fellinger, T. Gurke, and T. Kreuter. A unified theory of multidimensional electromagnetic vector inverse scattering within the Kirchoff or Born approximation. *Radar Target Imaging Berlin, Germany: Springer-Verlag*, pages 113–151, 1994.

[10] C. Prada and M. Fink. Eigenmodes of the time reversal operator: a solution to selective focusing in multiple-target media. *Wave Motion*, 20:151–163, 1994.

[11] C. Prada, S. Manneville, D. Spolianski, and M. Fink. Decomposition of the time reversal operator: detection and selective focusing on two scatterers. *Journal of the Acoustical Society of America*, 9:2067–2076, 1996.

[12] H. Tortel, G. Micolau, and M. Saillard. Decomposition of the time reversable operator for electromagnetic scattering. *Journal of electromagnetic Waves and Applications*, 13:687–719, 1999.

[13] X. Anguela and A. Broquetas. A near field 3D radar imaging technique. *23rd European Microwave Conference*, pages 377–379, 1993.

[14] J. Fortuny and A.J. Sieber. Three-dimensional synthetic aperture radar imaging of a fir tree: first results. *IEEE Trans. Geosci. Remote Sens.*, 37(2):1006–1014, 1999.

[15] T.B. Hansen and P.M. Johansen. Inversion scheme for ground penetrating radar that takes into account the planar air-soil interface. *IEEE Trans. Geosci. Remote Sens.*, 38(1):496–506, 2000.

[16] C.J. Leuschen and R.G. Plumb. A matched-filter-based reverse-time migration algorithm for ground-penetrating radar data. *IEEE Trans. Geosci. Remote Sens.*, 39(5):929–936, 2001.

[17] X. Li and S.C. Hagness. A confocal microwave imaging algorithm for breast cancer detection. *IEEE Microwave Guided Wave Lett.*, 11:130–132, 2001.

[18] E.C. Fear, X. Li, S.C. Hagness, and M.A. Stuchly. Confocal microwave imaging for breast tumor detection: Localization in three dimensions. *IEEE Trans. Biomed. Eng.*, 49:81–822, 2002.

[19] Y. Xie, B. Guo, J. Li, and P. Stoica. Novel multistatic adaptive microwave imaging methods for early breast cancer detection. *EURASIP Journal on Applied Signal Processing*, 2006:1–13, 2006.

[20] D. Colton and P. Monk. A linear sampling method for the detection of leukemia using microwaves. *SIAM J. Appl. Math.*, 58(3):926–941, 1998.

[21] D. Colton, H. Haddar, and M. Piana. The linear sampling method in inverse electromagnetic scattering theory. *Inverse problems*, 19:S105–S137, 2003.

[22] W.C. Chew and Y.M. Wang. Reconstruction of Two-Dimensional Permittivity Distribution Using the Distorted Born Iterative Method. *IEEE Trans. Med. Imaging*, 9(2), 1990.

[23] N. Joachimowicz, C. Pichot, and J. Hugonin. Inverse Scattering: An Iterative Numerical Method for Electromagnetic Imaging. *IEEE Trans. Antennas Propagat.*, 39(12):1742–1752, 1991.

[24] L. Garnero, A. Franchois, J. P. Hugonin, Ch. Pichot, and N. Joachimowicz. Microwave Imaging – Complex Permittivity Reconstruction by Simulated Annealing. *IEEE Trans. Microw. Theory Tech.*, 39:1801–1807, 1991.

[25] R.E. Kleinman and P.M. van den Berg. A Modified Gradient Method for Two-Dimensional Problems in Tomography. *J. Comput. Appl. Math.*, 42(1):17–35, 1992.

[26] A. Franchois and C. Pichot. Microwave Imaging - Complex Permittivity Reconstruction with a Levenberg-Marquardt Method. *IEEE Trans. Antennas Propagat.*, 45(2):203–215, 1997.

[27] P.M. van den Berg and R.E. Kleinman. A Contrast Source Inversion Method. *Inverse Problems*, 13(6):1607–1620, 1997.

[28] S. Caorsi, A. Massa, and M.A. Pastorino. A Computational Technique Based on a Real-Coded Genetic Algorithm for Microwave Imaging Purposes. *IEEE Trans. Geosci. Remote Sens.*, 38(4):1697–1708, 2000.

[29] A.G. Tijhuis, K. Belkebir, and A.C.S. Litman. Theoretical and Computational Aspects of 2-D Inverse Profiling. *IEEE Trans. Geosci. Remote Sens.*, 39(6):1316–1330, 2001.

[30] A. Abubakar, T.M. Habashy, P.M. van den Berg, and D. Gisolf. The Diagonalized Contrast Source Approach: an Inversion Method Beyond the Born Approximation. *Inverse Problems*, 21(2):685–702, 2005.

[31] T.J. Cui, W.C. Chew, A.A. Aydiner, and S. Chen. Inverse Scattering of Two-Dimensional Dielectric Objects Buried in a Lossy Earth Using the Distorted Born Iterative Method. *IEEE Trans. Geosci. Remote Sens.*, 39(2):339–345, 2001.

[32] A. Franchois and A.G. Tijhuis. A Quasi-Newton Reconstruction Algorithm for a Complex Microwave Imaging Scanner Environment. *Radio Science*, 38(2), 2003.

[33] A. Franchois, A. Joisel, C. Pichot, and J. C. Bolomey. Quantitative Microwave Imaging with a 2.45 GHz Planar Microwave Camera. *IEEE Trans. Med. Imaging*, 17(4):550–561, 1998.

[34] P.M. Meaney, K.D. Paulsen, and J.T. Chang. Nonactive Antenna Compensation for Fixed-Array Microwave Imaging: Part II - Imaging Results. *IEEE Trans. Med. Imaging*, 18(6):508–518, 1999.

[35] I.T. Rekanos, T.V. Yioultsis, and T.D. Tsiboukis. Inverse scattering using the finite-element method and a nonlinear optimization technique. *IEEE Trans. Microw. Theory Tech.*, 47(3):336–344, 1999.

[36] P.M. Meaney, K.D. Paulsen, B.W. Pogue, and M.I. Miga. Microwave image reconstruction utilizing log-magnitude and unwrapped phase to improve high-contrast object recovery. *IEEE Trans. Med. Imaging*, 20(2):104–116, 2001.

[37] O. Franza, N. Joachimowicz, and J.C. Bolomey. SICS: A Sensor Interaction Compensation Scheme for Microwave Imaging. *IEEE Trans. Antennas Propagat.*, 50(2):211–216, 2002.

[38] A.E. Bulyshev, A.E. Souvorov, S.Y. Semenov, R.H. Svenson, A.G. Nazarov, Y.E. Sizov, and G.P. Tatsis. Three-dimensional Microwave Tomography. Theory and Computer Experiments in Scalar Approximation. *Inverse Problems*, 16(3):863–875, 2000.

[39] A. Abubakar, P.M. van den Berg, and J.J. Mallorqui. Imaging of Biomedical Data Using a Multiplicative Regularized Contrast Source Inversion Method. *IEEE Trans. Microw. Theory Tech.*, 50(7):1761–1770, 2002.

[40] Z.Q. Zhang and Q.H. Liu. Three-Dimensional Nonlinear Image Reconstruction for Microwave Biomedical Imaging. *IEEE Trans. Biomed. Eng.*, 51(3):544–548, 2004.

[41] A.E. Bulyshev, A.E. Souvorov, S.Y. Semenov, V.G. Posukh, and Y.E. Sizov. Three-dimensional vector microwave tomography: theory and computational experiments. *Inverse Problems*, 20(4):1239–1259, 2004.

[42] S.Y. Semenov, A.E. Bulyshev, A. Abubakar, V.G. Posukh, Y.E. Sizov, A.E. Souvorov, P.M. van den Berg, and T.C. Williams. Microwave-Tomographic imaging of the high dielectric-contrast objects using different image-reconstruction approaches. *IEEE Trans. Microw. Theory Tech.*, 53(7):2284–2294, 2005.

[43] G. Franceschini, D. Franceschini, and A. Massa. Full-Vectorial Three-Dimensional Microwave Imaging through the Iterative Multiscaling Strategy - A Preliminary Assessment. *IEEE Trans. Geosci. Remote Sens. Letters*, 2(4):428–432, 2005.

[44] K. Belkebir, P.C. Chaumet, and A. Sentenac. Influence of Multiple Scattering on Three-Dimensional Imaging with Optical Diffraction Tomography. *J. Opt. Soc. Am. A.*, 23(3):586–595, 2006.

[45] T.J. Cui, Y. Qin, Y. Ye, J. Wu, G.L. Wang, and W.C. Chew. Efficient Low-Frequency Inversion of 3-D Buried Objects with Large Contrasts. *IEEE Trans. Geosci. Remote Sens.*, 44(1):3–9, 2006.

[46] I. Catapano, L. Crocco, M. D'Urso, and T. Isernia. A Novel Effective Model for Solving 3-D Nonlinear Inverse Scattering Problems in Lossy Scenarios. *IEEE Geosci. Remote Sens. Letters*, 3(3):302–306, 2006.

[47] Y. Yu and L. Carin. Three-Dimensional Bayesian Inversion with Application to Subsurface Sensing. *IEEE Trans. Geosci. Remote Sens.*, 45(5):1258–1270, 2007.

[48] T. Takenaka, H. Zhou, and T. Tanaka. Inverse Scattering for a Three-Dimensional Object in the Time Domain. *J. Opt. Soc. Am. A*, 20(10):1867–1874, 2003.

[49] P.M. van den Berg, A.L. van Broekhoven, and A. Abubakar. Extended Contrast Source Inversion. *Inverse Problems*, 15(5):1325–1344, 1999.

[50] P.M. van den Berg and A. Abubakar. Contrast source inversion method: state of the art. *PIER*, 34:189–218, 2001.

[51] J. Hadamard. *Sur les problemes aux derivees partielles et leur signification physique*. Princeton U. Bull., 1902.

[52] A. Abubakar and P.M. van den Berg. Total Variation as a Multiplicative Constraint for Solving Inverse Problems. *IEEE Transactions on Image Processing*, 10(9), 2001.

[53] T.M. Habashy and A. Abubakar. A general framework for constraint minimization for the inversion of electromagnetic measurements. *Progress in Electromagnetic Research*, 46:265–312, 2004.

[54] T.K. Sarkar, E. Sarvas, and S.M. Rao. Application of FFT and the Conjugate Gradient Method for the Solution of Electromagnetic Radiation from Electrically Large and Small Conducting Bodies. *IEEE Trans. Antennas Propagat.*, 34(5):635–640, 1986.

[55] C.C. Su. Electromagnetic Scattering by a Dielectric Body with Arbitrary Inhomogeneity and Anisotropy. *IEEE Trans. Antennas Propagat.*, 37(3):384–389, 1989.

[56] P. Zwamborn and P.M. van den Berg. The Three-Dimensional Weak Form of the Conjugate Gradient FFT Method for Solving Scattering Problems. *IEEE Trans. Microw. Theory Tech.*, 40(9):1757–1766, 1992.

[57] C.C. Su. The Three-Dimensional Algorithm of Solving the Electric Field Integral Equation using Face-Centered Node Points. *IEEE Trans. Microw. Theory Tech.*, 41(6):510–515, 1993.

[58] H. Gan and W.C. Chew. A Discrete BCG-FFT Algorithm for Solving 3D Inhomogeneous Scatterer Problems. *IEEE Trans. Antennas Propagat.*, 9(10):1339–1357, 1995.

[59] R. Coifman, V. Rokhlin, and S. Wandzura. The Fast Multipole Method for the Wave Equation: A Pedestrian Prescription. *IEEE Antennas Propagat. Mag.*, 35:7–12, 1993.

[60] C.C. Lu and W.C. Chew. A Multilevel Algorithm for Solving Boundary Integral Equations of Wave Scattering. *Microw. Opt. Tech. Lett.*, 7(10):466–470, 1994.

[61] J.M. Song, C.C. Lu, and W.C. Chew. Multilevel Fast-Multipole Algorithm for Electromagnetic Scattering by Large Complex Objects. *IEEE Trans. Antennas Propagat.*, 45(10):1488–1493, 1997.

[62] W.C. Chew, J. Jin, and . *Fast and Efficient Algorithms in Computational Electromagnetics*. Artech House, Boston, 2001.

[63] A.G. Tijhuis, M.C. van Beurden, and A.P.M. Zwamborn. Iterative Solution of Field Problems with a Varying Physical Parameters. *Turk J Elec Engin*, 10(2), 2002.

[64] A. Rosen, M.A. Stuchly, and A. Vander Vorst. Applications of RF/microwaves in medicine. *IEEE Trans. Microw. Theory Tech.*, 50(3):963–974, 2002.

[65] T. Rubaek, P.M. Meaney, P. Meincke, and K.D. Paulsen. Nonlinear microwave imaging for breast-cancer screening using GaussNewtons method and the CGLS inversion algorithm. *IEEE Trans. Antennas Propagat.*, 55(8):2320–2331, 2007.

[66] J.M. Geffrin, P. Sabouroux, and C. Eyraud. Free Space Experimental Scattering Database Continuation: Experimental Set-Up and Measurement Precision. *Inverse problems*, 21:117–130, 2005.

[67] C. Eyraud, J.M. Geffrin, P. Sabouroux, P. Chaumet, H. Tortel, H. Giovannini, and A. Litman. Validation of a 3D Bistatic Microwave Scattering Measurement Setup. *Radio Science*, doi:10.1029/2008RS003836, in press.

[68] J.M. Geffrin, P. Chaumet, C. Eyraud, K. Belkebir, and P. Sabouroux. Electromagnetic Three-Dimensional Reconstruction of Targets From Free Space Experimental Data. *Appl. Phys. Lett.*, 92:194102, 2008.

[69] R. Fletcher. *Practical Methods of Optimization*. John Wiley, New York, 1990.

CHAPTER 2

The electromagnetic inverse scattering problem

This chapter defines inverse problems in general and the electromagnetic inverse scattering problem in particular. Inverse problems are notorious for their ill-posedness. This concept is explained and the notions of regularization and optimization are briefly introduced. In order to clarify matters, a simple linear inverse problem is discussed, namely the volumetric inverse source problem in two dimensions. Next, the electromagnetic inverse problem is fully defined (in the form that will be used throughout this dissertation) and the relevant equations from electromagnetic theory are given.

2.1 Inverse problems in general

One of the major objectives of science is to build models of physical phenomena in order to understand these phenomena. With such a model one is able to make predictions, to foresee the consequences of a given cause. The cause, which is the input of the model, can be described as a collection of specific values of the *model parameters* and the consequences, the output of the model, are termed the *data*. The simulation of data using a certain model and starting from known model parameters is termed the *forward problem*. On the other hand, a model can also be used to determine the cause of a certain physical phenomenon, given its consequences. In such case, one starts from measured or observed data and tries to determine the model parameters that yield such data when the model is evaluated. This is commonly referred to as solving the *inverse problem*.

Inverse problems are typically ill-posed. Following the definition of Jacques Hadamard [1], this means that existence of a solution, uniqueness of the solution and stability cannot be simultaneously guaranteed. This makes the inverse problem far more challenging than the corresponding forward problem, which is typically well-posed.

The inverse scattering problem treated in this dissertation is also non-linear, which means that the data depends on the model parameters in a non-linear fashion. Unlike the linear case, not much general theory is available on non-linear inverse problems, which renders a rigorous mathematical treatment of such a problem very difficult and often impossible for practical applications.

Let us introduce a general notation

$$\boldsymbol{d} = F(\boldsymbol{u}), \tag{2.1}$$

where $\boldsymbol{d}$ represents the data vector (in general a complex vector), where $\boldsymbol{u}$ represents a vector containing the model parameters (also possibly complex) and where $F(\boldsymbol{u})$ is the (non-linear) model, evaluated in $\boldsymbol{u}$. The inverse problem then consists of determining $\boldsymbol{u}$ from knowledge of $\boldsymbol{d}$ and F. Problems with existence can occur when $\boldsymbol{d}$ is corrupted by measurement noise or when the model F contains certain (e.g. numerical) approximations, such that an exact data fit is not possible for any $\boldsymbol{u}$, in other words, $\boldsymbol{d}$ does not lie in the range of the operator F. This problem can be eliminated by recasting (2.1) as an optimization problem where one tries to minimize the least squares data error

$$\|\boldsymbol{d} - F(\boldsymbol{u})\|^2 \tag{2.2}$$

and defines the minimizer as the solution to the inverse problem. This way, a *least squares solution* is defined. Moreover, in case of non-linear inverse problems, iterative minimization of (2.2) is often the only way to solve them. Non-uniqueness is a more difficult problem for general non-linear inverse problems. Generally, this problem is related to overfitting, i.e. the situation that the degrees of freedom in parameter selection exceed the information content of the data. Providing as much non-redundant information as possible in the data is the common strategy to avoid problems with non-uniqueness. The stability condition, finally, is most often violated and occurs when the model output is not very sensitive to certain (possibly significant) changes in the model parameters, such that the subtle effects due to these changes are exceeded by the measurement noise and can no longer be resolved. In other words, information is lost in noise on the data and this again results in problems with overfitting. To solve the instability problem, regularization techniques are employed. This means that additional a priori information about the model parameters is incorporated in the optimization problem to compensate for the loss of information. Regularization often helps to counter non-uniqueness as well.

2.2 A linear example: the volumetric inverse source problem

To illustrate the general concepts outlined above, let us consider a simple two-dimensional (2D) linear inverse problem. The notations and concepts introduced in this section will furthermore be of use in the rest of this work.

Consider a time-harmonic (frequency f, angular frequency ω) current distribution, represented by its vectorial phasor [2] $J(\boldsymbol{\rho})\hat{\boldsymbol{z}}$, which only depends on the coordinates x and y ($\boldsymbol{\rho} = x\hat{\boldsymbol{x}} + y\hat{\boldsymbol{y}}$) and which is oriented along the z-axis. Suppose furthermore that $J(\boldsymbol{\rho})$ is embedded in a homogeneous and isotropic background medium with complex permittivity ϵ_b and permeability μ_0 (the permeability of vacuum) and that it is only non-zero inside a cylinder parallel to the z-axis with bounded cross section $\mathcal{S}$ in the xy-plane (Figure 2.1). This is a two-dimensional (2D) transverse magnetic (TM) problem, since $J(\boldsymbol{\rho})\hat{\boldsymbol{z}}$ only generates an electric field along the z-axis and a magnetic field parallel to the xy-plane [2]. In any point $\boldsymbol{\rho}$ outside $\mathcal{S}$, the electric field $\boldsymbol{E}(\boldsymbol{\rho}) = E(\boldsymbol{\rho})\hat{\boldsymbol{z}}$ is given by the integral equation

$$E(\boldsymbol{\rho}) = j\omega \int_{\mathcal{S}} G_\mathrm{b}(\boldsymbol{\rho} - \boldsymbol{\rho}')J(\boldsymbol{\rho}')\mathrm{d}\boldsymbol{\rho}', \tag{2.3}$$

where the 2D Green function G_b of the background medium is given by $G_\mathrm{b}(\boldsymbol{\rho}-\boldsymbol{\rho}') = \frac{j}{4}H_0^{(2)}(k_\mathrm{b}\|\boldsymbol{\rho}-\boldsymbol{\rho}'\|^2)$, in which $H_0^{(2)}$ is the zeroth order Hankel function of the second kind and $k_\mathrm{b} = \omega\sqrt{\mu_0\epsilon_\mathrm{b}}$ is the wave number of the background medium [2].

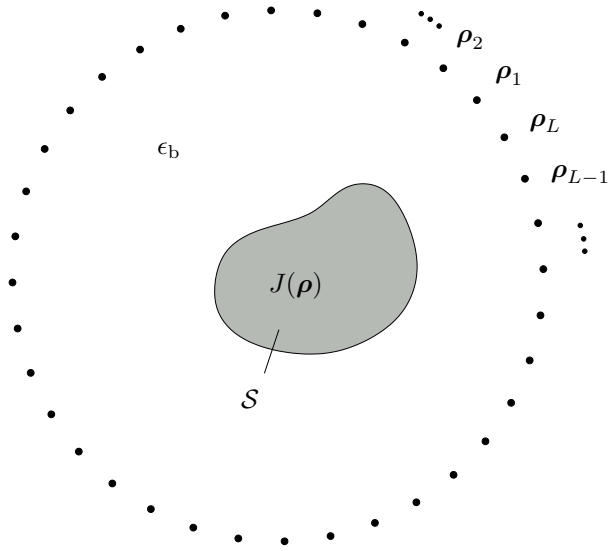

Figure 2.1: The configuration of the 2D volumetric inverse source problem.

The volumetric inverse source problem for the 2D TM case consists of determining the current $J(\boldsymbol{\rho})$ with support $\mathcal{S}$ that generates a measured field $E^{\text{meas}}(\boldsymbol{\rho}_l)$ in a number of observation points $\boldsymbol{\rho}_l, l = 1 \ldots L$, that lie, for example, on a circle around $\mathcal{S}$ (Figure 2.1). This problem is numerically solved after discretization of (2.3) (see Section 6.1), i.e. we have to solve the matrix system

$$\boldsymbol{e}^{\text{meas}} = \boldsymbol{A}\boldsymbol{j}, \tag{2.4}$$

where the L-dimensional vector $\boldsymbol{e}^{\text{meas}}$ contains the measured field values, where the N-dimensional vector $\boldsymbol{j}$ represents the discretized current and where $\boldsymbol{A}$ is a discretized Green operator (Section 6.1). Since typically the observation points lie on a curve around $\mathcal{S}$, while the current unknowns are distributed over the surface $\mathcal{S}$, the vector $\boldsymbol{j}$ contains much more elements than the vector $\boldsymbol{e}^{\text{meas}}$ (prior to discretization, there even is an infinitely large number of current unknowns, while there is only a finite number L of measurement points)[1]. As a consequence, the matrix $\boldsymbol{A}$ has less rows than columns, hence it has a null space, i.e. currents exist that do not generate a field in the measurement points. These currents are called invisible currents. It can be proven in general that continuous currents exist in $\mathcal{S}$ which generate a zero field everywhere outside $\mathcal{S}$ [2, 4]. These are called non-radiating currents.

Unless the field is heavily over-sampled on the measurement curve around $\mathcal{S}$, the rank of $\boldsymbol{A}$ is equal to L and there is no problem with existence of a solution, since any L-dimensional vector $\boldsymbol{e}^{\text{meas}}$ will lie in the range of $\boldsymbol{A}$. The existence of invisible currents, however, generates a problem with uniqueness: the current $\boldsymbol{j}_2 = \boldsymbol{j}_1 + \boldsymbol{j}^{INV}$, with $\boldsymbol{j}^{INV}$ an invisible current vector, yields the same field vector as $\boldsymbol{j}_1$. To restore uniqueness, one is forced to reformulate the problem. We could for example look for the current $\boldsymbol{j}^{MN}$, the unique current that yields the measured field $\boldsymbol{e}^{\text{meas}}$ and has minimal norm. This solution is given by

$$\boldsymbol{j}^{MN} = \boldsymbol{V}\boldsymbol{S}^{-1}\boldsymbol{U}^H\boldsymbol{e}^{\text{meas}}, \tag{2.5}$$

where the matrices $\boldsymbol{U}$, $\boldsymbol{S}$ and $\boldsymbol{V}$ form the thin Singular Value Decomposition (SVD) of $\boldsymbol{A}$, i.e.

$$\boldsymbol{A} = \boldsymbol{U}\boldsymbol{S}\boldsymbol{V}^H. \tag{2.6}$$

The dimensions of the matrices $\boldsymbol{U}$, $\boldsymbol{V}$ and $\boldsymbol{S}$ are $(L \times L)$, $(N \times L)$ and $(L \times L)$ respectively. Both $\boldsymbol{U}$ and $\boldsymbol{V}$ have orthonormal columns that span the range of $\boldsymbol{A}$ and the range of $\boldsymbol{A}^H$ respectively. $\boldsymbol{S}$ is a diagonal matrix that contains the non-zero singular values of $\boldsymbol{A}$, denoted as $\{\sigma_1, \ldots, \sigma_L\}$ with $\sigma_1 \geq \sigma_2 \geq \ldots \geq \sigma_L$.

[1] Electric fields outside a bounded source region are quasi-bandlimited, i.e. only a finite number of samples is needed to represent the field on any curve (in the 2D case) or surface (in the 3D case) outside the source region for a given numerical precision [3]. Typically the optimal sampling rate of the field (order half of a wavelength) is much lower than the sampling rate needed to represent the current distribution in $\mathcal{S}$ (order one tenth of a wavelength).

Finally there is the stability problem. In the inverse source problem, the Green operator has a low-pass effect [5]. Certain currents which vary over the domain $\mathcal{S}$ with high spatial frequencies can generate very small fields in the observation points. This typically is reflected in a rapid decrease of the singular value spectrum of $\boldsymbol{A}$ without sudden jumps in the spectrum. Since it is easily derived from (2.5) that

$$\|\boldsymbol{j}^{MN}\|^2 = \sum_{l=1}^{L} \frac{1}{\sigma_l^2} |\boldsymbol{u}_l^H \boldsymbol{e}^{\text{meas}}|^2, \tag{2.7}$$

where $\boldsymbol{u}_l$ is the l-th column of $\boldsymbol{U}$, we see that the norm of $\boldsymbol{j}^{MN}$ can only remain reasonably small if the projections $|\boldsymbol{u}_l^H \boldsymbol{e}^{\text{meas}}|$ follow the rapid decrease of the corresponding singular values. This is the case, for example for the ideal, noise free data vector $\boldsymbol{e}^{\text{ideal}}$. An arbitrary L-dimensional vector $\boldsymbol{v}$ can have projections $|\boldsymbol{u}_l^H \boldsymbol{v}|$ of comparable size for all l. Suppose now that the data is corrupted by noise, i.e. $\boldsymbol{e}^{\text{meas}} = \boldsymbol{e}^{\text{ideal}} + \boldsymbol{e}^{\text{noise}}$. Then the projections $|\boldsymbol{u}_l^H \boldsymbol{e}^{\text{meas}}| = |\boldsymbol{u}_l^H \boldsymbol{e}^{\text{ideal}} + \boldsymbol{u}_l^H \boldsymbol{e}^{\text{noise}}|$ will generally not decrease systematically, since it cannot be expected that the noise has smaller projections $\boldsymbol{u}_l^H \boldsymbol{e}^{\text{noise}}$ for larger l. This will cause the terms in (2.7) for large l to blow up, such that the norm of $\boldsymbol{j}^{MN}$ becomes much larger than in the case without noise. The reconstructed current will thus deviate much from the actual minimal norm current due to noise amplification. To counteract this noise amplification, a regularization strategy is employed. A frequently adopted regularization method is Tikhonov regularization [6]. Instead of looking for the exact minimum norm solution, which is a solution to the minimization problem

$$\boldsymbol{j}^{MN} = \underset{\boldsymbol{j}}{\text{argmin}} \quad \|\boldsymbol{e}^{\text{meas}} - \boldsymbol{A}\boldsymbol{j}\|^2, \quad \text{under the condition} \tag{2.8}$$

$$\|\boldsymbol{j}^{MN}\|^2 \quad \text{is minimal}, \tag{2.9}$$

a Tikhonov regularized solution satisfies

$$\boldsymbol{j}^{TI} = \underset{\boldsymbol{j}}{\text{argmin}} \quad \|\boldsymbol{e}^{\text{meas}} - \boldsymbol{A}\boldsymbol{j}\|^2 + \alpha\|\boldsymbol{j}\|^2, \tag{2.10}$$

where α is the positive regularization parameter. This allows for a trade-off between data fit and minimization of the norm. The idea is that the data is not perfect anyway, due to the noise, such that a perfect fit is not needed and there is some freedom which can be used to keep the norm small. Let us now first examine the solution to (2.10). First note that (2.10) can be rewritten as

$$\boldsymbol{j}^{TI} = \underset{\boldsymbol{j}}{\text{argmin}} \quad \|\boldsymbol{K}\boldsymbol{j} - \boldsymbol{y}\|^2, \tag{2.11}$$

where

$$\boldsymbol{K} = \begin{bmatrix} \boldsymbol{A} \\ \sqrt{\alpha}\boldsymbol{I}_N \end{bmatrix}, \quad \boldsymbol{y} = \begin{bmatrix} \boldsymbol{e}^{\mathrm{meas}} \\ \boldsymbol{0} \end{bmatrix}, \tag{2.12}$$

with $\boldsymbol{I}_N$ the $N \times N$ unit matrix. Since the dimensions of $\boldsymbol{K}$ are $(L+N) \times N$, (2.11) corresponds to an over-determined least squares problem (with rank N), the solution of which can be found by solving the normal equations

$$\boldsymbol{K}^H \boldsymbol{K} \boldsymbol{j} = \boldsymbol{K}^H \boldsymbol{y} \tag{2.13}$$

or, equivalently

$$\left(\boldsymbol{A}^H \boldsymbol{A} + \alpha \boldsymbol{I}_N \right) \boldsymbol{j} = \boldsymbol{A}^H \boldsymbol{e}^{\mathrm{meas}}. \tag{2.14}$$

Using the SVD decomposition (2.6) of $\boldsymbol{A}$ in this expression, one obtains

$$\left(\boldsymbol{S}^2 + \alpha \boldsymbol{I}_N \right) \boldsymbol{V}^H \boldsymbol{j} = \boldsymbol{S}\boldsymbol{U}^H \boldsymbol{e}^{\mathrm{meas}} \tag{2.15}$$

$$\boldsymbol{V}^H \boldsymbol{j} = \left(\boldsymbol{S}^2 + \alpha \boldsymbol{I}_N \right)^{-1} \boldsymbol{S}\boldsymbol{U}^H \boldsymbol{e}^{\mathrm{meas}}. \tag{2.16}$$

One solution of this last equation is given by

$$\boldsymbol{j} = \boldsymbol{V} \left(\boldsymbol{S}^2 + \alpha \boldsymbol{I}_N \right)^{-1} \boldsymbol{S}\boldsymbol{U}^H \boldsymbol{e}^{\mathrm{meas}}, \tag{2.17}$$

since the columns of $\boldsymbol{V}$ are orthonormal. This solution has no component in the null-space of $\boldsymbol{A}$, since it is a linear combination of the columns of $\boldsymbol{V}$. Since an invisible component in $\boldsymbol{j}$ has no influence on the first term in the right hand side of (2.10) and only increases the second term, (2.17) is *the* solution to (2.10). It is a visible current vector that more or less fits the data and has reasonable norm. Indeed, instead of (2.7), we obtain

$$\|\boldsymbol{j}^{TI}\|^2 = \sum_{l=1}^{L} \frac{\sigma_l^2}{(\sigma_l^2 + \alpha)^2} |\boldsymbol{u}_l^H \boldsymbol{e}^{\mathrm{meas}}|^2, \tag{2.18}$$

where we see that the noise amplification is avoided, since the factors $\sigma_l^2/(\sigma_l^2 + \alpha)^2$ approach σ_l^2/α^2 for small σ_l. For large σ_l, they become $1/\sigma_l^2$, which is the same as in (2.7).

Note that for $\alpha \to 0$ the minimum norm solution and thus a perfect data fit is again obtained. When the regularization parameter α is too large, however, too much emphasis will be put on a small solution norm, which will degrade the data fit too much. In order to choose a quasi-optimal value for α, the discrepancy principle can be used [6, 7]. This states that α is chosen as large as possible, and such that the data error is equal to the error introduced by the noise, which is the maximal acceptable error. This means that α is chosen such that

$$\|\boldsymbol{e}^{\mathrm{meas}} - \boldsymbol{A}\boldsymbol{j}^{TI}\|^2 = \|\boldsymbol{e}^{\mathrm{meas}} - \boldsymbol{e}^{\mathrm{ideal}}\|^2 = \|\boldsymbol{e}^{\mathrm{noise}}\|^2. \tag{2.19}$$

This, of course, requires an estimate of the noise level $\|\boldsymbol{e}^{\mathrm{noise}}\|^2$. Using the explicit expression for $\boldsymbol{j}^{TI}$, given by (2.17), (2.19) is transformed into

$$\sum_{l=1}^{L} \frac{\alpha^2}{(\sigma_l^2+\alpha)^2} |\boldsymbol{u}_l^H \boldsymbol{e}^{\mathrm{meas}}|^2 = \|\boldsymbol{e}^{\mathrm{noise}}\|^2, \tag{2.20}$$

which is a rational equation in α and can be quite easily solved using standard root finding algorithms.

2.3 The quantitative electromagnetic inverse scattering problem

2.3.1 Problem formulation

Consider an isotropic inhomogeneous, possibly lossy, dielectric object embedded in an isotropic homogeneous background with permittivity ϵ_{b} and permeability μ_0 (Figure 2.2). This background extends to infinity in all directions. Since the object is non-magnetic, its interaction with time harmonic electromagnetic fields is entirely determined by its complex permittivity ϵ, which is a function of the 3D position vector $\boldsymbol{r}$ and of the angular frequency ω:

$$\epsilon(\boldsymbol{r},\omega) = \epsilon_0 \epsilon_r(\boldsymbol{r},\omega) - j\frac{\sigma(\boldsymbol{r},\omega)}{\omega}, \tag{2.21}$$

where ϵ_r is the (real) dielectric permittivity of the object and σ is the conductivity. In the rest of this dissertation, only single frequency scattering will be regarded and the ω-dependency of the permittivity and the conductivity as well as the $e^{j\omega t}$ time dependency of all phasors (electromagnetic fields, currents, charges, etc.) will be omitted.

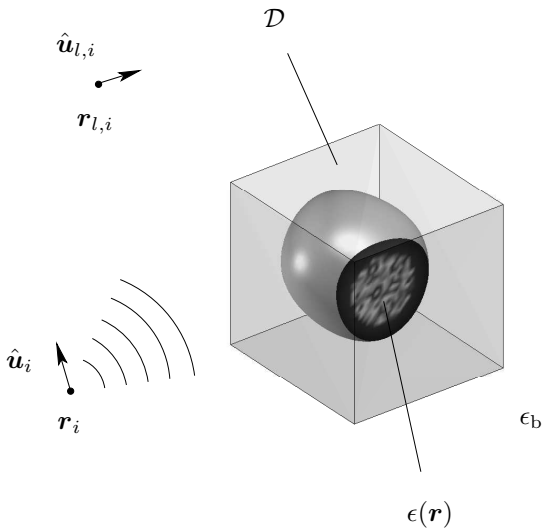

Figure 2.2: The 3D scattering configuration: general notations and definitions.

In this setting, it is the goal of the electromagnetic inverse scattering problem to reconstruct $\epsilon(\boldsymbol{r})$ within a bounded investigation domain $\mathcal{D}$ (which includes the unknown object) from multi-view scattering data. These data are collected as follows. The domain $\mathcal{D}$ is illuminated with a number of different incident fields $\boldsymbol{E}_i^{\mathrm{inc}}$ ($i = 1, \ldots, N^I$). An incident field is a field that would be present in the homogeneous background if the scattering object were absent. For each such illumination i, the scattered field, i.e. the difference between the total field $\boldsymbol{E}_i$ and the incident field, is measured in a number of measurement positions $\boldsymbol{r}_{l,i}$ ($l = 1, \ldots, N_i^R$) which are possibly different for different i (Figure 2.2). More specifically, we will restrict ourselves in this work to incident fields generated by elementary dipole current densities $\boldsymbol{J}_{\delta,i}$ at positions $\boldsymbol{r}_i$ and oriented along $\hat{\boldsymbol{u}}_i$:

$$\boldsymbol{J}_{\delta,i}(\boldsymbol{r}) = \delta(\boldsymbol{r} - \boldsymbol{r}_i)\hat{\boldsymbol{u}}_i, \tag{2.22}$$

where δ is the dirac distribution. On the other hand the measurement procedure for the scattered fields will be modelled simply by taking the component of $\boldsymbol{E}_i^{\mathrm{scat}}$ along the directions $\hat{\boldsymbol{u}}_{l,i}$ in the points $\boldsymbol{r}_{l,i}$, i.e. $\boldsymbol{E}_i^{\mathrm{scat}}(\boldsymbol{r}_{l,i}) \cdot \hat{\boldsymbol{u}}_{l,i}$. The position-orientation pairs $(\boldsymbol{r}_i, \hat{\boldsymbol{u}}_i)$ and $(\boldsymbol{r}_{l,i}, \hat{\boldsymbol{u}}_{l,i})$, respectively, will be frequently denoted as transmitting dipoles and receiving dipoles, respectively. The complete configuration of transmitting and receiving dipoles is referred to as the dipole configuration.

2.3.2 The scattering model

As mentioned in Section 2.1, an inverse problem is associated to a model. In the case of the electromagnetic inverse scattering problem, this model simulates the scattering

of an incident field $\boldsymbol{E}_i^{\text{inc}}$ from a given complex permittivity function $\epsilon(\boldsymbol{r})$ inside a domain $\mathcal{D}$. To build the model, we start from Maxwell's equations in an isotropic inhomogeneous dielectric medium, with a source current $\boldsymbol{J}_{\delta,i}$ (2.22)

$$\begin{aligned} \nabla \times \boldsymbol{E}_i &= -j\omega\mu_0 \boldsymbol{H}_i, && (2.23)\\ \nabla \times \boldsymbol{H}_i &= j\omega\epsilon \boldsymbol{E}_i + \boldsymbol{J}_{\delta,i}, && (2.24)\\ \nabla \cdot (\epsilon \boldsymbol{E}_i) &= \rho_{\delta,i}, && (2.25)\\ \mu_0 \nabla \cdot \boldsymbol{H}_i &= 0, && (2.26) \end{aligned}$$

where $\rho_{\delta,i}$ is the charge density corresponding to $\boldsymbol{J}_{\delta,i}$. Equations (2.24) and (2.25) can be rewritten as

$$\begin{aligned} \nabla \times \boldsymbol{H}_i &= j\omega\epsilon_{\text{b}} \boldsymbol{E}_i + \boldsymbol{J}_{\delta,i} + j\omega(\epsilon - \epsilon_{\text{b}})\boldsymbol{E}_i && (2.27)\\ \epsilon_{\text{b}} \nabla \cdot \boldsymbol{E}_i &= \rho_{\delta,i} - \frac{1}{j\omega} \nabla \cdot \left[j\omega(\epsilon - \epsilon_{\text{b}})\boldsymbol{E}_i \right]. && (2.28) \end{aligned}$$

From this and the law of charge conservation

$$\rho = -\frac{1}{j\omega} \nabla \cdot \boldsymbol{J} \tag{2.29}$$

it can be seen that a solution $(\boldsymbol{E}_i, \boldsymbol{H}_i)$ to (2.23)-(2.26) is also a solution to Maxwell's equations in a homogeneous background ϵ_{b} with an additional source current $\boldsymbol{J}_i^{\text{scat}}$, given by

$$\boldsymbol{J}_i^{\text{scat}}(\boldsymbol{r}) = j\omega(\epsilon(\boldsymbol{r}) - \epsilon_{\text{b}})\boldsymbol{E}_i(\boldsymbol{r}) = j\omega\chi(\boldsymbol{r})\boldsymbol{E}_i(\boldsymbol{r}), \tag{2.30}$$

which is denoted as the *contrast current*. The function χ is called the *contrast function*. Using the superposition principle, the total field $\boldsymbol{E}_i$ can be obtained as [2]

$$\boldsymbol{E}_i(\boldsymbol{r}) = -j\omega\mu_0 \left[\mathbb{I} + \frac{1}{k_{\text{b}}^2} \nabla\nabla \right] \cdot \int_{\mathbb{R}^3} G_{\text{b}}(\boldsymbol{r} - \boldsymbol{r}') \left[\boldsymbol{J}_{\delta,i}(\boldsymbol{r}') + \boldsymbol{J}_i^{\text{scat}}(\boldsymbol{r}') \right] \mathrm{d}\boldsymbol{r}', \tag{2.31}$$

where $\mathbb{I}$ is the 3×3 identity dyadic and

$$G_{\text{b}}(\boldsymbol{r} - \boldsymbol{r}') = \frac{e^{-jk_{\text{b}}\|\boldsymbol{r} - \boldsymbol{r}'\|}}{4\pi\|\boldsymbol{r} - \boldsymbol{r}'\|} \tag{2.32}$$

is the scalar Green's function of homogeneous space, which satisfies

$$\nabla^2 G_{\text{b}}(\boldsymbol{r} - \boldsymbol{r}') + k_{\text{b}}^2 G_{\text{b}}(\boldsymbol{r} - \boldsymbol{r}') = -\delta(\boldsymbol{r} - \boldsymbol{r}'). \tag{2.33}$$

To simplify the notations we introduce an operator $\mathcal{G}_{\text{b}}^{\mathcal{V}}$ that acts on a vector func-

tion $\boldsymbol{p}$ with support $\mathcal{V}$:

$$\left[\mathcal{G}_{\mathrm{b}}^{\mathcal{V}}(\boldsymbol{p})\right](\boldsymbol{r}) = -j\omega\mu_0\left[\mathbb{I} + \frac{1}{k_{\mathrm{b}}^2}\nabla\nabla\right] \cdot \int_{\mathcal{V}} G_{\mathrm{b}}(\boldsymbol{r}-\boldsymbol{r}')\,\boldsymbol{p}(\boldsymbol{r}')\mathrm{d}\boldsymbol{r}'. \tag{2.34}$$

Using this operator notation and the fact that the support of the contrast current is contained within $\mathcal{D}$ (the contrast function χ is zero outside $\mathcal{D}$) and that the source current $\boldsymbol{J}_{\delta,i}$ is non-zero only in $\boldsymbol{r}_i$, we can rewrite (2.31) as

$$\boldsymbol{E}_i(\boldsymbol{r}) = \boldsymbol{E}_i^{\mathrm{inc}}(\boldsymbol{r}) + \left[\mathcal{G}_{\mathrm{b}}^{\mathcal{D}}\left(j\omega\chi\boldsymbol{E}_i\right)\right](\boldsymbol{r}), \tag{2.35}$$

where the incident field $\boldsymbol{E}_i^{\mathrm{inc}}$ is given by

$$\boldsymbol{E}_i^{\mathrm{inc}}(\boldsymbol{r}) = \left[\mathcal{G}_{\mathrm{b}}^{\mathcal{S}_i}\left(\boldsymbol{J}_{\delta,i}\right)\right](\boldsymbol{r}), \tag{2.36}$$

with $\mathcal{S}_i$ an arbitrary volume which contains $\boldsymbol{r}_i$. Apparently, (2.35) is a second kind integral equation for the total field $\boldsymbol{E}_i$ inside $\mathcal{D}$ for fixed contrast χ. Once this equation, which is called the *domain equation*, has been solved and the field inside $\mathcal{D}$ is known, the contrast current (2.30) is known and (2.31) can be evaluated to yield the field everywhere in space. More specifically, the scattered field $\boldsymbol{E}_i^{\mathrm{scat}}$ is obtained through

$$\boldsymbol{E}_i^{\mathrm{scat}}(\boldsymbol{r}) = \left[\mathcal{G}_{\mathrm{b}}^{\mathcal{D}}\left(\boldsymbol{J}_i^{\mathrm{scat}}\right)\right](\boldsymbol{r}), \tag{2.37}$$

which is termed the *data equation*. Chapter 3 discusses the numerical solution of the domain equation and the evaluation of the data equation, in other words the solution of the forward problem. In Chapters 4 to 6, the inverse problem is solved.

Note that the data equation is a non-linear function of the permittivity. Indeed, although the relation (2.37) between $\boldsymbol{E}_i^{\mathrm{scat}}$ and $\boldsymbol{J}_i^{\mathrm{scat}}$ is linear, $\boldsymbol{J}_i^{\mathrm{scat}}$ itself is a product of the permittivity contrast and the total field $\boldsymbol{E}_i$ (2.30), which itself depends on the permittivity through (2.35). In some early attempts to solve the inverse scattering problem, the data equation was often linearized by putting $\boldsymbol{E}_i = \boldsymbol{E}_i^{\mathrm{inc}}$ in (2.30). This linearization is called the Born approximation [8, 9] and is valid if the contrast is small. In this work we attempt to solve the full non-linear inverse scattering problem and make no approximations in the forward scattering model.

2.3.3 The inverse problem

To obtain the complex permittivity $\epsilon(\boldsymbol{r})$ or, equivalently, the contrast $\chi(\boldsymbol{r})$ from knowledge of the scattered field measurements $\boldsymbol{E}_i^{\mathrm{meas}}(\boldsymbol{r}_{l,i}) \cdot \hat{\boldsymbol{u}}_{l,i}$, for $i = 1, \ldots, N^I$ and $l = 1, \ldots, N_i^R$, the inverse scattering problem (2.35),(2.37) is reformulated as an optimization problem in which a cost functional has to be minimized. The data equation (2.37) depends on the product of two unknowns, the contrast χ and the total field $\boldsymbol{E}_i$, which are related by the domain equation (2.35). Without considering regularization,

mainly two different approaches for defining the cost functional have been employed. The first one considers only the permittivity as the optimization variable in the cost functional. The field unknowns $\boldsymbol{E}_i$ are eliminated by substituting the solution to (2.35) into (2.37). This yields the least squares data fit cost functional

$$\mathcal{F}^{LS}(\epsilon) = \sum_{i=1}^{N^I} \sum_{l=1}^{N_i^R} \mid \boldsymbol{E}_i^{\mathrm{scat}}(\boldsymbol{r}_{l,i}) \cdot \hat{\boldsymbol{u}}_{l,i} - \boldsymbol{E}_i^{\mathrm{meas}}(\boldsymbol{r}_{l,i}) \cdot \hat{\boldsymbol{u}}_{l,i} \mid^2, \tag{2.38}$$

which is evaluated for a given permittivity function $\epsilon(\boldsymbol{r})$ by solving the domain equation (2.35) for $\boldsymbol{E}_i$, $i = 1, \ldots, N^I$, and by using the data equation (2.37) to calculate the scattered fields $\boldsymbol{E}_i^{\mathrm{scat}}$. An optimization algorithm is used to update the permittivity until (2.38) is minimized. Since this is historically the first approach, we call it the *conventional* approach to inverse scattering. It involves the solution of a multi-view forward scattering problem to calculate the total fields in every step of the optimization process.

In the second approach both the permittivity and the total fields $\boldsymbol{E}_i$ are considered as optimization variables. The cost functional then typically takes the following form

$$\begin{aligned} \mathcal{F}^{MG}(\epsilon) = {} & \textstyle\sum_{i=1}^{N^I} \sum_{l=1}^{N_i^R} \mid \boldsymbol{E}_i^{\mathrm{scat}}(\boldsymbol{r}_{l,i}) \cdot \hat{\boldsymbol{u}}_{l,i} - \boldsymbol{E}_i^{\mathrm{meas}}(\boldsymbol{r}_{l,i}) \cdot \hat{\boldsymbol{u}}_{l,i} \mid^2 \\ & + \lambda \textstyle\sum_{i=1}^{N^I} \int_{\mathcal{D}} \mathrm{d}\boldsymbol{r} \mid \boldsymbol{E}_i - \boldsymbol{E}_i^{\mathrm{inc}} - \left[\mathcal{G}_{\mathrm{b}}^{\mathcal{D}} \left(j\omega\chi \boldsymbol{E}_i\right)\right](\boldsymbol{r}) \mid^2, \end{aligned} \tag{2.39}$$

where an extra term has been added to the data fit cost functional, which expresses the constraint (2.35). When λ is the correct Lagrange multiplier [10], the minimizer of (2.39) exactly satisfies (2.35). Unfortunately, the Lagrange multiplier is not known in advance and is not easily obtained in this case where both the objective functional and the constraint are non-linear in the optimization variables. Although optimization schemes exist that iteratively update the lagrange multiplier [10], it is simpler to consider the second term in (2.39) as a penalty term and λ as a normalization constant which is either fixed or is adjusted heuristically throughout the minimization. Because of the large number of optimization variables (the permittivity and the field for each illumination in every point in the investigation domain), a conjugate gradient minimization [10] is usually employed to minimize (2.39), since this method is very memory efficient. The resulting approach is known as the Modified Gradient approach [11]. It avoids the solution of multi-view forward scattering problems, but due to the increased number of optimization variables, the optimization generally requires many iterations to converge. As an alternative to the Modified Gradient approach, van den Berg et al. [12] later proposed the Contrast Source Inversion (CSI) method, which considers the contrast currents $\boldsymbol{J}_i^{\mathrm{scat}}$ instead of the total fields as auxiliary variables

by using the cost functional

$$\mathcal{F}^{CSI}(\epsilon) = \sum_{i=1}^{N^I} \sum_{l=1}^{N_i^R} \mid \boldsymbol{E}_i^{\mathrm{scat}}(\boldsymbol{r}_{l,i}) \cdot \hat{\boldsymbol{u}}_{l,i} - \boldsymbol{E}_i^{\mathrm{meas}}(\boldsymbol{r}_{l,i}) \cdot \hat{\boldsymbol{u}}_{l,i} \mid^2 + \lambda \sum_{i=1}^{N^I} \int_{\mathcal{D}} \mathrm{d}\boldsymbol{r} \mid \boldsymbol{J}_i^{\mathrm{scat}} - j\omega\chi \boldsymbol{E}_i^{\mathrm{inc}} - j\omega\chi \left[\mathcal{G}_{\mathrm{b}}^{\mathcal{D}} \left(\boldsymbol{J}_i^{\mathrm{scat}}\right)\right](\boldsymbol{r}) \mid^2, \quad (2.40)$$

which results from multiplying the domain equation (2.35) with $j\omega\chi$ and by using the definition (2.30) for the contrast currents. Whereas, both (2.39) and (2.40) are minimized using a conjugate gradient approach (see Chapter 6), (2.38) can be minimized with the faster converging, but less memory efficient Newton type methods, since it involves less optimization variables (see [13] for an early application of the Newton-Kantorovich algorithm to inverse scattering). Chapter 4 is devoted to the conventional approach. It is the only approach we employ to solve the 3D electromagnetic inverse scattering. In Chapter 6, a modification of the CSI method is proposed, which is called the CI method.

2.3.4 Discretization of the inverse problem

Since a solution to the optimization problem has to be sought numerically, a parameter representation of the complex permittivity function $\epsilon(\boldsymbol{r})$ is needed to obtain a finite number of optimization variables. To formulate the discrete inverse scattering problem in a most general and simple way, we employ a cubic grid discretization. In Figure 2.3 this idea is illustrated: a permittivity grid $\mathcal{D}^{\epsilon}$ with $F \times G \times H$ cubic cells in the x-, y- and z-directions is laid over the investigation domain $\mathcal{D}$ and the value of the permittivity is assumed constant in each grid cell. The permittivity function is then approximated by

$$\epsilon(\boldsymbol{r}) \approx \sum_{f=0}^{F-1} \sum_{g=0}^{G-1} \sum_{h=0}^{H-1} \epsilon_{f,g,h} \epsilon_0 \Phi_{f,g,h}(\boldsymbol{r}), \quad (2.41)$$

where $\Phi_{f,g,h}$ is a 3D pulse function that assumes the value 1 in cell (f,g,h) and is zero elsewhere. The unknown coefficients $\epsilon_{f,g,h}$ represent relative complex permittivity values.

When some a priori information on the permittivity function is available, for example the knowledge of some region where the permittivity is constant, the cells in this region can be collected in a cell group with index ν. All cells (f,g,h) in this cell group then have the same relative permittivity $\epsilon_{f,g,h} = \epsilon_\nu$, which is the actual optimization variable. In general, the permittivity unknowns thus are denoted as ϵ_ν (the relative permittivity in cell group $\mathcal{C}_\nu$, which can be a single cell) and they are collected in the N^ϵ-dimensional ($N^\epsilon \leq FGH$) permittivity vector $\boldsymbol{\varepsilon}$. From the permittivity vector $\boldsymbol{\varepsilon}$, the relative permittivity $\epsilon_{f,g,h}$ in cell (f,g,h) is simply obtained by determining to which cell group this cell belongs.

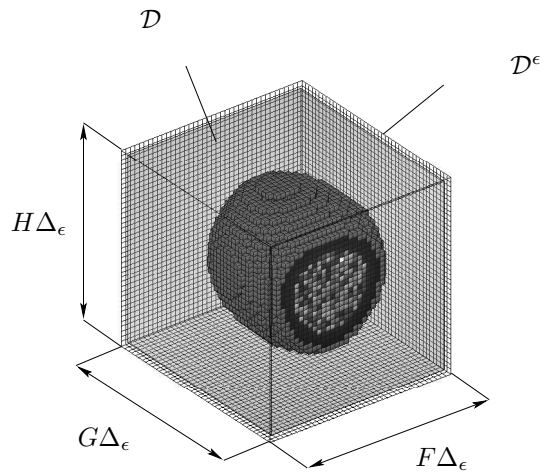

Figure 2.3: The piecewise constant approximation for the permittivity function of Figure 2.2.

The discretization of the electromagnetic field quantities which appear in the solution of the forward problem is discussed in Chapter 3.

2.3.5 Derivatives of the scattering model

In the optimization algorithms described in Chapter 4, which belong to the conventional approach, the derivatives of the forward scattering model with respect to the permittivity variables are needed. In this section it is shown that these derivatives are known when the domain equation (2.35) has been solved for illuminations with dipole sources $\boldsymbol{J}_{\delta,k}(\boldsymbol{r}) = \delta(\boldsymbol{r}-\boldsymbol{r}_k)\hat{\boldsymbol{u}}_k$, where the position-orientation pairs $(\boldsymbol{r}_k, \hat{\boldsymbol{u}}_k)$ include all illuminating dipole positions and orientations $(\boldsymbol{r}_i, \hat{\boldsymbol{u}}_i)$ $(i = 1, \ldots, N^I)$ *and* all measurement positions and orientations $(\boldsymbol{r}_{l,i}, \hat{\boldsymbol{u}}_{l,i})$ $(i = 1, \ldots, N^I,\ l = 1, \ldots, N_i^R)$. In most cases, large portions of the illuminating dipole configuration coincide with measurement position-orientation pairs and therefore the number of additional forward solutions (with respect to those already conducted to evaluate the scattered field for every illumination $i = 1, \ldots, N^I$) is limited.

We first define the Green's dyadic $\boldsymbol{G}_{\mathrm{inh}}$ of the total inhomogeneous dielectric space, such that $-j\omega\mu_0\boldsymbol{G}_{\mathrm{inh}}(\boldsymbol{r}, \boldsymbol{r}')\cdot\hat{\boldsymbol{u}}$ is the total field in $\boldsymbol{r}$ due to an elementary dipole source $\delta(\boldsymbol{r} - \boldsymbol{r}')\hat{\boldsymbol{u}}$ in the presence of both the homogeneous background medium and the scattering object. By linearity, the total field (2.35) then also is given by

$$\boldsymbol{E}_i(\boldsymbol{r}) = -j\omega\mu_0 \int_{\mathcal{S}_i} \boldsymbol{G}_{\mathrm{inh}}(\boldsymbol{r}, \boldsymbol{r}') \cdot \boldsymbol{J}_{\delta,i}(\boldsymbol{r}')\mathrm{d}\boldsymbol{r}'. \tag{2.42}$$

Taking the derivative of (2.37) — or equivalently of (2.35), since the incident field

$\boldsymbol{E}_i^{\mathrm{inc}}$ does not depend on the permittivity of the scattering object, by definition — with respect to the permittivity parameter ϵ_ν yields

$$\frac{\partial \boldsymbol{E}_i^{\mathrm{scat}}(\boldsymbol{r})}{\partial \epsilon_\nu} = \left[\mathcal{G}_{\mathrm{b}}^{\mathcal{D}}\left(j\omega\epsilon_0\Phi_\nu \boldsymbol{E}_i\right)\right](\boldsymbol{r}) + \left[\mathcal{G}_{\mathrm{b}}^{\mathcal{D}}\left(j\omega\chi\frac{\partial \boldsymbol{E}_i^{\mathrm{scat}}}{\partial \epsilon_\nu}\right)\right](\boldsymbol{r}), \tag{2.43}$$

where we have used (2.30) and (2.41) and where Φ_ν is the function which is 1 in the cell group ν and zero elsewhere (Φ_ν is the support function of cell group ν). It follows from (2.43) and (2.36) that $\partial \boldsymbol{E}_i^{\mathrm{scat}}/\partial\epsilon_\nu$ satisfies an equation as (2.35) corresponding to a source current $j\omega\epsilon_0\Phi_\nu \boldsymbol{E}_i$ in cell group ν. Following (2.42), the derivative of the scattered field thus can be written as

$$\frac{\partial \boldsymbol{E}_i^{\mathrm{scat}}}{\partial \epsilon_\nu}(\boldsymbol{r}) = k_0^2 \int_{\mathcal{D}} \Phi_\nu(\boldsymbol{r}')\, \boldsymbol{G}_{\mathrm{inh}}(\boldsymbol{r},\boldsymbol{r}') \cdot \boldsymbol{E}_i(\boldsymbol{r}')\mathrm{d}\boldsymbol{r}'. \tag{2.44}$$

The derivative of one measured scattered field value $\boldsymbol{E}_i^{\mathrm{scat}}(\boldsymbol{r}_{l,i}) \cdot \hat{\boldsymbol{u}}_{l,i}$ thus is given by

$$\frac{\partial \boldsymbol{E}_i^{\mathrm{scat}}}{\partial \epsilon_\nu}(\boldsymbol{r}_{l,i}) \cdot \hat{\boldsymbol{u}}_{l,i} = k_0^2 \int_{\mathcal{D}} \Phi_\nu(\boldsymbol{r}')\, \hat{\boldsymbol{u}}_{l,i} \cdot \boldsymbol{G}_{\mathrm{inh}}(\boldsymbol{r}_{l,i},\boldsymbol{r}') \cdot \boldsymbol{E}_i(\boldsymbol{r}')\mathrm{d}\boldsymbol{r}'. \tag{2.45}$$

Since it can be proven by reciprocity [2] that $\boldsymbol{G}_{\mathrm{inh}}(\boldsymbol{r}_{l,i},\boldsymbol{r}') = \boldsymbol{G}_{\mathrm{inh}}^T(\boldsymbol{r}',\boldsymbol{r}_{l,i})$ and with the definition

$$\boldsymbol{E}_{l,i}(\boldsymbol{r}') = -j\omega\mu_0 \boldsymbol{G}_{\mathrm{inh}}(\boldsymbol{r}',\boldsymbol{r}_{l,i}) \cdot \hat{\boldsymbol{u}}_{l,i}, \tag{2.46}$$

which is the field caused by a dipole current $\delta(\boldsymbol{r}-\boldsymbol{r}_{l,i})\hat{\boldsymbol{u}}_{l,i}$ in the measurement position $\boldsymbol{r}_{l,i}$, it follows that

$$\frac{\partial \boldsymbol{E}_i^{\mathrm{scat}}}{\partial \epsilon_\nu}(\boldsymbol{r}_{l,i}) \cdot \hat{\boldsymbol{u}}_{l,i} = j\omega\epsilon_0 \int_{\mathcal{D}} \Phi_\nu(\boldsymbol{r}')\, \boldsymbol{E}_i(\boldsymbol{r}') \cdot \boldsymbol{E}_{l,i}(\boldsymbol{r}')\mathrm{d}\boldsymbol{r}'. \tag{2.47}$$

Bibliography

[1] J. Hadamard. *Sur les problemes aux derivees partielles et leur signification physique*. Princeton U. Bull., 1902.

[2] J. Van Bladel. *Electromagnetic Fields, second edition*. John Wiley & Sons, Inc., New Jersey, 2007.

[3] O.M. Bucci, C. Gennarelli, and C. Savarese. Representation of Electromagnetic Fields over Arbitrary Surfaces by a Finite and Nonredundant Number of Samples. *IEEE Trans. Antennas Propagat.*, 46(3):351–359, 1998.

[4] A.J. Devaney and G.C. Sherman. Nonuniqueness in inverse source and scattering problems. *IEEE Trans. Antennas Propagat.*, 30(5):1034–1037, 1982.

[5] W.C. Chew, Y.M. Wang, G. Otto, D. Lesselier, and J.C. Bolomey. On The Inverse Source Method For Solving Inverse Scattering Problems. *Inverse Problems*, 10(3):547–553, 1994.

[6] M. Bertero, C. De Mol, and E.R. Pike. Linear inverse problems with discrete data: II. Stability and regularisation. *Inverse Problems*, 4(2):573–594, 1988.

[7] V.A. Morozov. On the solution of functional equations by the method of regularization. *Soviet Math. Dokl.*, 7:414–417, 1966.

[8] M. Slaney, A.C. Kak, and L.E. Larsen. Limitations of imaging with first-order diffraction tomography. *IEEE Trans. Microw. Theory Tech.*, 32(8):860–874, 1984.

[9] K.J. Langenberg, M. Brandfass, P. Fellinger, T. Gurke, and T. Kreuter. A unified theory of multidimensional electromagnetic vector inverse scattering within the Kirchoff or Born approximation. *Radar Target Imaging Berlin, Germany: Springer-Verlag*, pages 113–151, 1994.

[10] R. Fletcher. *Practical Methods of Optimization*. John Wiley, New York, 1990.

[11] R.E. Kleinman and P.M. van den Berg. A Modified Gradient Method for Two-Dimensional Problems in Tomography. *J. Comput. Appl. Math.*, 42(1):17–35, 1992.

[12] P.M. van den Berg and R.E. Kleinman. A Contrast Source Inversion Method. *Inverse Problems*, 13(6):1607–1620, 1997.

[13] A. Roger. A Newton-Kantorovich algorithm applied to an electromagnetic inverse problem. *IEEE Trans. Antennas Propagat.*, 29:232–238, 1981.

CHAPTER 3

Solving the forward problem

In this chapter, the numerical solution of the domain equation (2.35) is discussed. A Hybrid MLFMA-FFT solver is proposed to do this efficiently. The method is a hybridization of the FFT method and the High Frequency Multilevel Fast Multipole algorithm (HF MLFMA), which is especially useful for sparse inhomogeneous scattering configurations. These are configurations in which the investigation domain $\mathcal{D}$ contains much background medium and where the remainder is strongly inhomogeneous. This situation can be encountered in some specific inverse scattering problems, e.g. the reconstruction of an unknown object in an environment which contains a number of other, known objects that are scattered over a large area. Although the hybrid code has been incorporated in the 3D inverse solver of chapter 4, it is actually always used as a regular FFT solver in the chapters about inversion, since we did not treat sparse inverse scattering configurations in this thesis.

3.1 Introduction

Because the unknown of the domain equation (2.35) is a field quantity and because we wish to solve this equation numerically, a Method of Moments discretization of (2.35) is employed, yielding an algebraic linear system. In relation to the 3D electromagnetic inverse scattering problem, this system has a large dimension and a solution through direct methods is not feasible. Indeed, direct solution of an N-dimensional linear system has a $\mathcal{O}(N^3)$ computational complexity. Moreover, the memory needed to store the system's $N \times N$-matrix can easily exceed the available computer memory. Solving the system iteratively using, for example, a conjugate gradient (CG) or stabilized bi-conjugate gradient (BICGSTAB) solver reduces the computational complexity to $\mathcal{O}(N^F N^2)$, with N^F the number of iterations, but the system's matrix still has to be stored in this approach.

Two classes of methods that reduce the storage requirements and speed up the matrix-vector multiplications needed in every step of the iterative solver are the Fast

Fourier transform (FFT) based techniques and the Multilevel Fast Multipole algorithms (MLFMA's). The first class [1–5] uses the FFT to exploit the convolutional structure of the integral operator in the domain equation and has a computational complexity (for one matrix-vector multiplication) of $\mathcal{O}(N \log N)$ and a memory use of $\mathcal{O}(N)$. The methods in the second class, such as the High Frequency (HF) MLFMA [6–9], the Low Frequency MLFMA [10] and the Inhomogeneous or Stable Plane wave method [11,12], are based on efficient decompositions of the Green function. The major advantages of the FFT methods are their speed and easy implementation, thanks to the fast, reliable and widespread codes for calculating FFTs [13]. The MLFMA's on the other hand allow a more flexible meshing of the scattering geometry, since they can be applied to arbitrary meshes. For moderate to large volumetric problems with densely distributed mesh elements, the FFT methods are usually faster, thanks to their small prefactor, despite the lower computational complexity of MLFMA's ($\mathcal{O}(N)$) on such dense geometries.

In this chapter, a hybrid MLFMA-FFT method is proposed, which is particularly suited for large scattering configurations that show some sparsity. The method is a modification of the HF MLFMA that treats the interactions between nearby mesh elements using FFTs and the interactions between well-separated elements as in a regular HF MLFMA. It can also be regarded as a hybridization of the subdomain FFT method, which is proposed here as an FFT method for a collection of cubic subdomains. The subdomain meshing avoids the extension of the FFT grid over empty space between scatterers, as is necessary in the classical FFT method. It will be shown that the MLFMA-FFT method outperforms both the regular HF MLFMA and the FFT method on large sparse geometries and that it can have lower memory requirements even on large dense geometries.

The outline of this chapter is as follows. In section 3.2 the domain equation (2.35) is reformulated using a mixed potential approach and discretized with a MoM scheme. Section 3.3 proposes a subdomain FFT method to speed up the matrix-vector products needed for the iterative solution of the linear system. Section 3.4 starts by shortly revisiting the HF MLFMA. For a more thorough treatment, the reader is referred to [9]. Next, some improvements to the general MLFMA framework are presented. Specifically, the exploitation of symmetries in the subdomain mesh allows for a reduction of the memory cost of the MLFMA and the application of an FFT interpolation scheme for the vectorial MLFMA together with the use of vector spherical harmonics to represent the radiation patterns on the lowest level results in accurate and efficient aggregation and disaggregation stages. Section 3.5 presents the hybrid MLFMA-FFT method and discusses its relation to the FFT method and the HF MLFMA and in section 3.6 this hybrid method is validated and its performance tested. Finally, Sections 3.7 and 3.8 discuss the choice of the initial guess for the iterative solution of the MoM system and the discretization of the data equation (2.37) and its derivatives (2.47), respectively.

3.2 Problem reformulation and discretization

3.2.1 Mixed potential formulation

First, the normalized contrast function ξ is defined:

$$\xi(\boldsymbol{r}) = \frac{\epsilon(\boldsymbol{r}) - \epsilon_{\mathrm{b}}}{\epsilon(\boldsymbol{r})}. \tag{3.1}$$

Using this normalized contrast, the contrast current (2.30) and its associated charge density can be rewritten as (in this chapter, the illumination index i is mostly omitted)

$$\boldsymbol{J}^{\mathrm{scat}}(\boldsymbol{r}) = j\omega\xi(\boldsymbol{r})\boldsymbol{D}(\boldsymbol{r}), \tag{3.2}$$

$$\rho^{\mathrm{scat}}(\boldsymbol{r}) = \frac{-1}{j\omega}\nabla\cdot\boldsymbol{J}^{\mathrm{scat}}(\boldsymbol{r}), \tag{3.3}$$

where $\boldsymbol{D}$ represents the electric flux density $\boldsymbol{D} = \epsilon\boldsymbol{E}$. Next, the mixed potential formulation [14] is employed to rewrite (2.37) as

$$\boldsymbol{E}^{\mathrm{scat}}(\boldsymbol{r}) = -j\omega\boldsymbol{A}^{\mathrm{scat}}(\boldsymbol{r}) - \nabla\varphi^{\mathrm{scat}}(\boldsymbol{r}), \tag{3.4}$$

where $\boldsymbol{A}^{\mathrm{scat}}$ and φ^{scat}, respectively, represent the vector and scalar potentials, given by

$$\boldsymbol{A}^{\mathrm{scat}}(\boldsymbol{r}) = \mu_0\int_{\mathcal{D}} G_{\mathrm{b}}(\boldsymbol{r}-\boldsymbol{r}')\boldsymbol{J}^{\mathrm{scat}}(\boldsymbol{r}')\mathrm{d}\boldsymbol{r}' \tag{3.5}$$

$$\varphi^{\mathrm{scat}}(\boldsymbol{r}) = \frac{1}{\epsilon_{\mathrm{b}}}\int_{\mathcal{D}} G_{\mathrm{b}}(\boldsymbol{r}-\boldsymbol{r}')\rho^{\mathrm{scat}}(\boldsymbol{r}')\mathrm{d}\boldsymbol{r}'. \tag{3.6}$$

Finally, the domain equation (2.35) is recast as an integral equation for $\boldsymbol{D}$, which is called the *mixed potential domain equation* (MPDE)

$$\boldsymbol{E}^{\mathrm{inc}}(\boldsymbol{r}) = \frac{\boldsymbol{D}(\boldsymbol{r})}{\epsilon(\boldsymbol{r})} + j\omega\boldsymbol{A}^{\mathrm{scat}}(\boldsymbol{r}) + \nabla\varphi^{\mathrm{scat}}(\boldsymbol{r}). \tag{3.7}$$

The choice for the mixed potential formulation is motivated by the fact that the weak singularity in G_{b} allows for a simple numerical treatment, as opposed to the stronger singularity in the Green dyadic.

3.2.2 MoM discretization

To solve (3.7) numerically, a Galerkin Method of Moments (MoM) is applied. The electric flux density is expanded as

$$\boldsymbol{D}(\boldsymbol{r}) \approx \sum_{\alpha=1}^{N} d_\alpha \boldsymbol{\Psi}_\alpha(\boldsymbol{r}), \quad \forall \boldsymbol{r} \in \mathcal{D} \tag{3.8}$$

where $\boldsymbol{\Psi}_\alpha$ are vectorial basis functions and d_α are the unknown expansion coefficients. To define the functions $\boldsymbol{\Psi}_\alpha$, the domain $\mathcal{D}$ is built from a number of identical cubic subdomains D^a, $a = 1, \ldots, N^S$, which belong to a uniform cubic grid with grid parameter Δ. Each subdomain that contains only background medium is removed from $\mathcal{D}$ and every remaining subdomain D^a is divided in $N^C = P^3$ cubic cells with side δ (Figure 3.1). The resulting MoM grid is termed the *forward grid* and denoted by $\mathcal{D}^F$. The cell size δ and the position of the forward grid are chosen such that it is a subdivision of the permittivity grid $\mathcal{D}^\epsilon$, such that every cell has a constant permittivity. To every cell facet F_α in this grid, one basis function $\boldsymbol{\Psi}_\alpha = \Psi_\alpha \hat{\boldsymbol{u}}_\alpha$ is assigned, where $\hat{\boldsymbol{u}}_\alpha$ is the normal to F_α ($\hat{\boldsymbol{u}}_\alpha = \hat{\boldsymbol{x}},\ \hat{\boldsymbol{y}}$ or $\hat{\boldsymbol{z}}$) and Ψ_α is a 3D rooftop function that assumes the value 1 on F_α and linearly tends to zero along the directions $\pm\hat{\boldsymbol{u}}_\alpha$ over the two cells S_α^+ and S_α^- that share F_α (Figure 3.2). Such basis functions are also reported in [3,15] and a similar formulation on tetrahedral meshes is proposed in [16]. The support of Ψ_α is denoted $S_\alpha = S_\alpha^+ \cup S_\alpha^-$. With this choice for the basis functions, the normal component of $\boldsymbol{D}$ is continuous across all facets of the grid, as required by the boundary conditions. Furthermore, because the forward grid is a subdivision of the permittivity grid, the normalized contrast function ξ is a piecewise constant function which assumes one value per cell. In cell S_α^+ (respectively S_α^-) this value is denoted as ξ_α^+ (respectively ξ_α^-).

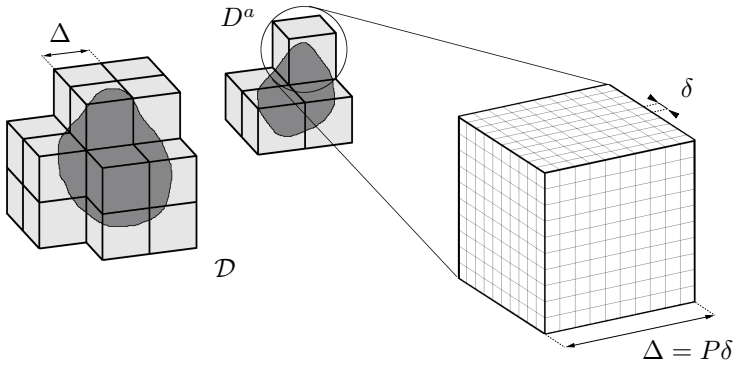

Figure 3.1: The construction of the domain $\mathcal{D}$ from a number of identical cubic subdomains D^a, meshed with a uniform cubic grid.

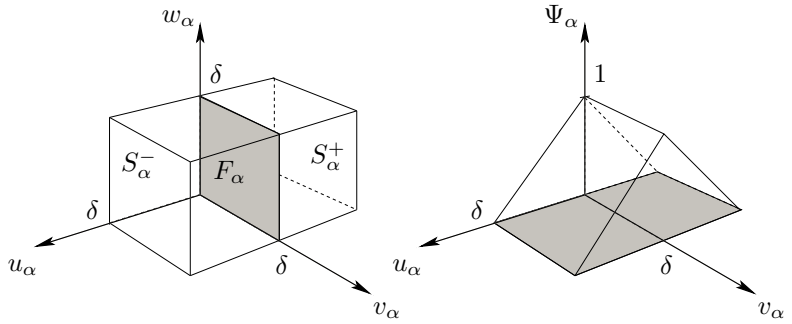

Figure 3.2: Graphical representation of the rooftop function Ψ_α associated to facet F_α: (a) definition of the support cells S_α^+ and S_α^- and a local reference system $(\hat{\boldsymbol{u}}_\alpha, \hat{\boldsymbol{v}}_\alpha, \hat{\boldsymbol{w}}_\alpha)$, where $\hat{\boldsymbol{u}}_\alpha$ is the normal to F_α, and (b) Ψ_α as a function of u_α and v_α for every w_α: $0 \leq w_\alpha \leq \delta$.

After substituting the expansion (3.8) in the domain equation (3.7), the same vectorial rooftop functions are used to test the equation. To illustrate the MoM procedure, consider $\boldsymbol{A}_\alpha^{\mathrm{scat}}$, $\phi_\alpha^{\mathrm{scat}}$ and $\boldsymbol{E}_\alpha$, respectively the potentials due to and the total electric field corresponding to one term $d_\alpha \boldsymbol{\Psi}_\alpha(\boldsymbol{r})$ in (3.8). Testing $\boldsymbol{A}_\alpha^{\mathrm{scat}}$ and $\nabla\phi_\alpha^{\mathrm{scat}}$ with $\boldsymbol{\Psi}_\beta$ yields

$$\begin{aligned}
&\int_{S_\beta} \boldsymbol{\Psi}_\beta(\boldsymbol{r}) \cdot \boldsymbol{A}_\alpha^{\mathrm{scat}}(\boldsymbol{r}) \mathrm{d}\boldsymbol{r} \\
&\qquad = j\omega\mu_0\, d_\alpha \left[\xi_\alpha^+ \int_{S_\beta} \mathrm{d}\boldsymbol{r} \boldsymbol{\Psi}_\beta(\boldsymbol{r}) \cdot \int_{S_\alpha^+} \mathrm{d}\boldsymbol{r}' G_{\mathrm{b}}(\boldsymbol{r}-\boldsymbol{r}') \boldsymbol{\Psi}_\alpha(\boldsymbol{r}') \right. \\
&\qquad\quad \left. + \xi_\alpha^- \int_{S_\beta} \mathrm{d}\boldsymbol{r} \boldsymbol{\Psi}_\beta(\boldsymbol{r}) \cdot \int_{S_\alpha^-} \mathrm{d}\boldsymbol{r}' G_{\mathrm{b}}(\boldsymbol{r}-\boldsymbol{r}') \boldsymbol{\Psi}_\alpha(\boldsymbol{r}') \right]
\end{aligned} \tag{3.9}$$

and

$$\int_{S_\beta} \boldsymbol{\Psi}_\beta(\boldsymbol{r}) \cdot \nabla\phi_\alpha^{\mathrm{scat}}(\boldsymbol{r}) \mathrm{d}\boldsymbol{r} = -\int_{S_\beta} \phi_\alpha^{\mathrm{scat}}(\boldsymbol{r}) \nabla \cdot \boldsymbol{\Psi}_\beta(\boldsymbol{r}) \mathrm{d}\boldsymbol{r}, \tag{3.10}$$

where we have used Gauss' theorem and the fact that $\boldsymbol{\Psi}_\beta$ is zero outside S_β. The expression for $\phi_\alpha^{\mathrm{scat}}$ in (3.10) is given by

$$\begin{aligned}
\phi_\alpha^{\mathrm{scat}}(\boldsymbol{r}) \;=\; & -\frac{1}{\epsilon_{\mathrm{b}}} d_\alpha \left[\xi_\alpha^+ \int_{S_\alpha^+} G_{\mathrm{b}}(\boldsymbol{r}-\boldsymbol{r}') \nabla' \cdot \boldsymbol{\Psi}_\alpha(\boldsymbol{r}') \mathrm{d}\boldsymbol{r}' \right. \\
& + \xi_\alpha^- \int_{S_\alpha^-} G_{\mathrm{b}}(\boldsymbol{r}-\boldsymbol{r}') \nabla' \cdot \boldsymbol{\Psi}_\alpha(\boldsymbol{r}') \mathrm{d}\boldsymbol{r}' \\
& \left. + \left(\xi_\alpha^- - \xi_\alpha^+\right) \int_{F_\alpha} G_{\mathrm{b}}(\boldsymbol{r}-\boldsymbol{r}') \mathrm{d}\boldsymbol{r}' \right],
\end{aligned} \tag{3.11}$$

where the last term represents the contribution of the surface charges that arise from the discontinuities in the discretized contrast currents across the facets of the grid. The testing of $\boldsymbol{E}_\alpha$ with $\boldsymbol{\Psi}_\beta$ results in

$$\int_{S_\beta} \boldsymbol{\Psi}_\beta(\boldsymbol{r}) \cdot \boldsymbol{E}_\alpha(\boldsymbol{r}) \mathrm{d}\boldsymbol{r} = \frac{d_\alpha}{\epsilon_\mathrm{b}} \left[(1-\xi_\alpha^+) \int_{S_\beta \cap S_\alpha^+} \mathrm{d}\boldsymbol{r} \boldsymbol{\Psi}_\beta(\boldsymbol{r}) \cdot \boldsymbol{\Psi}_\alpha(\boldsymbol{r}) + (1-\xi_\alpha^-) \int_{S_\beta \cap S_\alpha^-} \mathrm{d}\boldsymbol{r} \boldsymbol{\Psi}_\beta(\boldsymbol{r}) \cdot \boldsymbol{\Psi}_\alpha(\boldsymbol{r}) \right]. \quad (3.12)$$

Note that we use complete rooftop functions $\boldsymbol{\Psi}_\beta$ in (3.9), (3.10) and (3.12) to test the MPDE. Strictly speaking this generates a problem in (3.12) when the facets F_β and F_α coincide on the boundary of $\mathcal{D}$. In this case S_α^+ $(= S_\beta^+)$ or S_α^- $(= S_\beta^-)$ lies outside $\mathcal{D}$, where the expansion (3.8) is not defined. We therefore extend the validity of (3.8) over one cell-width exterior to $\mathcal{D}$ by replacing the half rooftop Ψ_α outside $\mathcal{D}$ with the constant unity function, i.e. $\boldsymbol{\Psi}_\alpha(\boldsymbol{r}) = \hat{\boldsymbol{u}}_\alpha$. This means we assume that keeping $\boldsymbol{D}(\boldsymbol{r}) \cdot \hat{\boldsymbol{u}}_\alpha$ constant and equal to its value on F_α is a good approximation over a distance δ outside $\mathcal{D}$.

Collecting the tested incident field in the N-dimensional vector $\boldsymbol{e}^\mathrm{inc}$ and introducing N-dimensional vectors $\boldsymbol{d}_\xi^\pm$ with elements $\xi_\alpha^\pm d_\alpha$ and $\boldsymbol{d}$ with elements d_α, we finally obtain the following set of N linear equations in N unknowns d_α

$$\boldsymbol{e}^\mathrm{inc} = \boldsymbol{W}_\xi \boldsymbol{d} + \boldsymbol{Z}^+ \boldsymbol{d}_\xi^+ + \boldsymbol{Z}^- \boldsymbol{d}_\xi^- \quad (3.13)$$

or, in short,

$$\boldsymbol{e}^\mathrm{inc} = \boldsymbol{L}_\xi \boldsymbol{d} \quad (3.14)$$

The elements of the $N \times N$ matrices $\boldsymbol{Z}^\pm$ consist of double integrals with the Green function and at most two linear functions in the integrand, as appears from (3.9)-(3.11). These integrals are computed numerically using Gaussian quadrature and the $1/r$-singularity of the Green function is handled by singularity subtraction [17]. The sparse matrix $\boldsymbol{W}_\xi$ is derived from (3.12). The integrals involved in this are easily obtained analytically. Note that the elements of the dense matrices $\boldsymbol{Z}^\pm$ do not depend on the contrast. This way, they need to be calculated only once for a series of scattering simulations with varying contrast, for example in an inverse scattering problem, where the voxel permittivities are iteratively updated until the simulated forward scattering matches the measured data.

3.3 The subdomain FFT method

Since N is usually quite large, we solve (3.13) iteratively with a stabilized bi-conjugate gradient (BICGSTAB) routine [18]. To speed up the evaluations of the matrix-vector

multiplications in (3.13), we focus on the most time consuming part, i.e. the multiplications with $\boldsymbol{Z}^{\pm}$. By denoting with $\boldsymbol{v}_a$ the part of an N-dimensional vector $\boldsymbol{v}$ that corresponds to basis or testing functions in the subdomain D^a, we can write

$$\left(\boldsymbol{Z}^{+}\boldsymbol{d}_{\xi}^{+}+\boldsymbol{Z}^{-}\boldsymbol{d}_{\xi}^{-}\right)_{b}=\sum_{a}\boldsymbol{Z}_{ba}^{+}\boldsymbol{d}_{\xi,a}^{+}+\sum_{a}\boldsymbol{Z}_{ba}^{-}\boldsymbol{d}_{\xi,a}^{-},\quad\forall b\in\{1,\ldots,N^{S}\},\tag{3.15}$$

where the matrices $\boldsymbol{Z}_{ba}^{\pm}$ describe the interaction between two subdomains D^a and D^b. The matrix-vector products $\boldsymbol{Z}_{ba}^{+}\boldsymbol{d}_{\xi,a}^{+}$ and $\boldsymbol{Z}_{ba}^{-}\boldsymbol{d}_{\xi,a}^{-}$ can be cast as 3D discrete convolutions, since the convolutional symmetry in (3.5) - (3.6) is conserved thanks to the chosen discretization. Therefore, the index α and the notation F_α are replaced by the quintet $(p,q,r;a;u)$ and the notation $F_{p,q,r}^{a,u}$. The indices p, q and r determine the position of S_α^-, or equivalently $S_{p,q,r}^{a,-}$, in the x-, y- and z-direction respectively within the subdomain D^a and the superscript $u=1,\ 2$ or 3 discriminates between the three faces $F_{\alpha'}$ for which $S_{\alpha'}^-=S_\alpha^-$. With this labelling we write $[\boldsymbol{Z}_{ba}^{+}]_{\beta\alpha}=\mathcal{Z}_{ba}^{+}(p-p',q-q',r-r';u;u')$ and

$$\left[\boldsymbol{Z}_{ba}^{+}\boldsymbol{d}_{\xi,a}^{+}\right]_{\beta}=\sum_{u'}\sum_{p'}\sum_{q'}\sum_{r'}\mathcal{Z}_{ba}^{+}(p-p',q-q',r-r';u;u')\,\xi_{p',q',r'}^{a,u',+}d_{p',q',r'}^{a,u'}.\tag{3.16}$$

After performing a 3D FFT of size $(2P+1)\times(2P+1)\times(2P+1)$, the discrete convolution in this expression is transformed into a simple diagonal multiplication, as is well known. We denote this method, where the total mesh consists of cubic subdomains D^a, as the subdomain FFT method. The computational complexity of an evaluation of (3.13) in the subdomain FFT method (Figure 3.3) is dominated by the calculation of the FFTs of $\boldsymbol{d}_{\xi,a}^{\pm}$ for every subdomain and the diagonal multiplications for every combination of subdomains. Thus it is $\mathcal{O}(c_1N^SN^C\log N^C+c_2(N^S)^2N^C)$ and the memory use is bounded above by $\mathcal{O}(d_1(N^S)^2N^C+d_2N^SN^C)$ (for storing the spectra of $\mathcal{Z}_{ba}^{+}$, which are calculated in the setup time of the algorithm, and of $\boldsymbol{d}_{\xi,a}^{\pm}$), where c_1, c_2, d_1 and d_2 are constant prefactors. In practice the memory use is smaller, because some interactions $\mathcal{Z}_{ba}^{+}$ are identical due to translation symmetry.

3.4 The HF MLFMA

3.4.1 Basic equations

The Multilevel Fast Multipole Algorithm (MLFMA) is a multilevel extension of the Fast Multipole Method (FMM). In this thesis, a vectorial FMM is employed. This means that the mixed potential formulation (3.4) is replaced by the electric field inte-

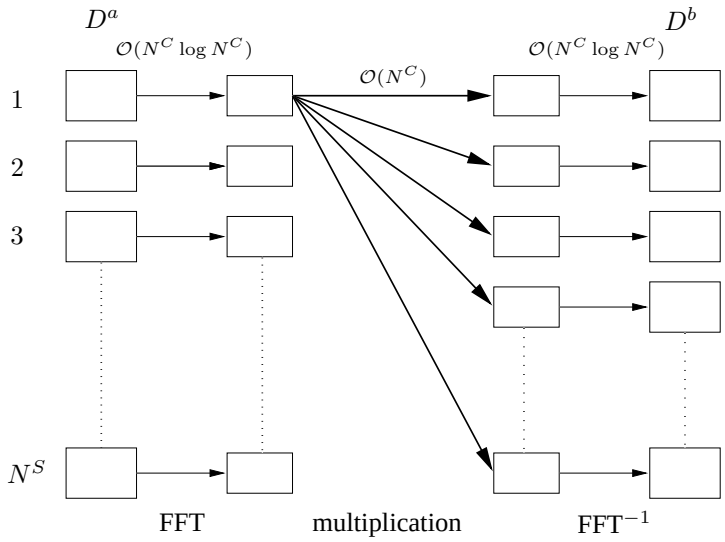

Figure 3.3: Illustration of the computational complexity of the subdomain FFT method.

gral formulation

$$\boldsymbol{E}^{\mathrm{scat}}(\boldsymbol{r}) = -j\omega\mu_0 \int_{\mathcal{D}} \left(\mathbb{I} + \frac{1}{k_b^2} \nabla\nabla \right) G_{\mathrm{b}}(\boldsymbol{r} - \boldsymbol{r}') \cdot \boldsymbol{J}^{\mathrm{scat}}(\boldsymbol{r}') \mathrm{d}\boldsymbol{r}' \tag{3.17}$$

and the diagonal addition theorem for the Green dyadic is used (see [9], chapter 3, and [19]). Note that we have put the operator $\left(\mathbb{I} + \frac{1}{k_b^2} \nabla\nabla \right)$ under the integral sign (compare with (2.31)). This is, strictly speaking, only valid if the point $\boldsymbol{r}$ does not belong to the integration domain [1]. Since it will become clear in a moment that the self-interaction (the interaction of $\boldsymbol{r}$ with the points in its immediate surroundings) will not be calculated with (3.17), there is no problem here.

The FMM requires a division of the basis functions in a number of non-overlapping FMM-groups. In our implementation the FMM-groups conveniently coincide with the cubic subdomains D^a, which are introduced in section 3.2.2. Let $\boldsymbol{E}_a^{\mathrm{scat}}$ be the scattered electric field, caused by the contrast currents in subdomain D^a. The HF FMM computes $\boldsymbol{E}_a^{\mathrm{scat}}$, tested with a basis function $\boldsymbol{\Psi}_\beta$ belonging to subdomain D^b as

$$\begin{aligned} &\int_{\mathcal{D}} \boldsymbol{\Psi}_\beta(\boldsymbol{r}) \cdot \boldsymbol{E}_a^{\mathrm{scat}}(\boldsymbol{r}) \mathrm{d}\boldsymbol{r} \\ &\approx -\frac{j k_b^3}{(4\pi)^2 \epsilon_{\mathrm{b}}} \int_0^{\pi} \mathrm{d}\theta \int_0^{2\pi} \mathrm{d}\phi \boldsymbol{V}_{\beta,b}(\theta,\phi) \cdot T_{ba}(\theta,\phi) \sin\theta \; \boldsymbol{U}_a(\theta,\phi). \end{aligned} \tag{3.18}$$

[1] In the other case, a *depolarizing dyadic* must be added, as outlined in [14]

Note that (3.18) represents one element of $-(\boldsymbol{Z}^+_{ba}\boldsymbol{d}^+_{\xi,a} + \boldsymbol{Z}^-_{ba}\boldsymbol{d}^-_{\xi,a})$ in (3.15). The diagonal translation operator T_{ba} is calculated as

$$T_{ba}(\theta,\phi) = \sum_{l=0}^{L}(-j)^l(2l+1)h_l^{(2)}(k_\mathrm{b}r_{ba})P_l(\hat{\boldsymbol{k}}(\theta,\phi)\cdot\hat{\boldsymbol{r}}_{ba}), \tag{3.19}$$

where $h_l^{(2)}$ is the spherical Hankel function of the second kind and order l, P_l is the Legendre function of order l, $r_{ba} = \|\boldsymbol{r}_{ba}\| = \|\boldsymbol{r}^b_c - \boldsymbol{r}^a_c\|$ is the distance between the centers of the subdomains, $\hat{\boldsymbol{r}}_{ba} = \boldsymbol{r}_{ba}/r_{ba}$ and $\hat{\boldsymbol{k}}(\theta,\phi) = \hat{\boldsymbol{x}}\sin\theta\cos\phi + \hat{\boldsymbol{y}}\sin\theta\sin\phi + \hat{\boldsymbol{z}}\cos\theta$ is a vector on the unit sphere. The radiation patterns $\boldsymbol{U}_a$ and $\boldsymbol{V}_{\beta,b}$ are given by

$$\begin{aligned}
\boldsymbol{U}_a(\theta,\phi) &= \sum_{\alpha\in I_a^+}\xi^+_\alpha d_\alpha \int_{\mathcal{S}^+_\alpha} e^{j\boldsymbol{k}_\mathrm{b}\cdot(\boldsymbol{r}'-\boldsymbol{r}^a_c)}\left(\mathbb{I}-\hat{\boldsymbol{k}}\hat{\boldsymbol{k}}\right)\cdot\boldsymbol{\Psi}_\alpha(\boldsymbol{r}')\mathrm{d}\boldsymbol{r}' \\
&+ \sum_{\alpha\in I_a^-}\xi^-_\alpha d_\alpha \int_{\mathcal{S}^-_\alpha} e^{j\boldsymbol{k}_\mathrm{b}\cdot(\boldsymbol{r}'-\boldsymbol{r}^a_c)}\left(\mathbb{I}-\hat{\boldsymbol{k}}\hat{\boldsymbol{k}}\right)\cdot\boldsymbol{\Psi}_\alpha(\boldsymbol{r}')\mathrm{d}\boldsymbol{r}' \qquad (3.20)\\
\boldsymbol{V}_{\beta,b}(\theta,\phi) &= \int_{\mathcal{S}_\beta} e^{-j\boldsymbol{k}_\mathrm{b}\cdot(\boldsymbol{r}-\boldsymbol{r}^b_c)}\left(\mathbb{I}-\hat{\boldsymbol{k}}\hat{\boldsymbol{k}}\right)\cdot\boldsymbol{\Psi}_\beta(\boldsymbol{r})\mathrm{d}\boldsymbol{r}, \qquad (3.21)
\end{aligned}$$

where $\boldsymbol{k}_\mathrm{b} = k_\mathrm{b}\hat{\boldsymbol{k}}$. The set $I_a^\pm$ in (3.20) contains indices α of basis functions $\boldsymbol{\Psi}_\alpha$ for which $S_\alpha^\pm$ lies in D^a. Note that these patterns only have transverse components $U^u_a = \boldsymbol{U}_a\cdot\hat{\boldsymbol{u}}$ and $V^u_{\beta,b} = \boldsymbol{V}_{\beta,b}\cdot\hat{\boldsymbol{u}}$ with $u=\phi$ or $u=\theta$. Equation (3.18) can be shown to be valid up to arbitrary precision as long as r_{ba} is sufficiently large, i.e. D^a and D^b have to be well-separated [9]. In general, this is expressed as $r_{ab} > \beta R$, where β is the separation parameter and R is the radius of the subdomains.

3.4.2 Numerical implementation

Integration and interpolation

To evaluate the integrals in (3.18) numerically and to perform the interpolations needed to extend the FMM to the MLFMA, we follow an approach, similar to that of Sarvas [20]. In this approach, the radiation patterns are presented in a Fourier basis rather than with the usual spherical harmonics and interpolations are done with FFTs. The difference is that the FMM in [20] is scalar, while ours is vectorial. We use the transverse components of the radiation patterns, which are not bandlimited in terms of spherical harmonics, in contrast to the cartesian components. However, the functions U^u_a and $V^u_{\beta,b}$ do have exponentially decaying Fourier spectra when their definition domain is extended from $[0,\pi]\otimes[0,2\pi]$ to $[0,2\pi]\otimes[0,2\pi]$ using the formula

$$F(\theta,\phi) = -F(2\pi-\theta,\phi+\pi) \tag{3.22}$$

for $F = U_a^u$ or $F = V_{\beta,b}^u$, as can easily be verified. The integral in (3.18) then is replaced by

$$\int_{\mathcal{D}} \boldsymbol{\Psi}_\beta(\boldsymbol{r}) \cdot \boldsymbol{E}_a^{\text{scat}}(\boldsymbol{r}) \mathrm{d}\boldsymbol{r} \approx -\frac{1}{2} \frac{jk_b^3}{(4\pi)^2 \epsilon_\text{b}} \int_0^{2\pi} \mathrm{d}\theta \int_0^{2\pi} \mathrm{d}\phi \boldsymbol{V}_{\beta,b}(\theta,\phi) \cdot T_{ba}(\theta,\phi) |\sin\theta| \boldsymbol{U}_a(\theta,\phi) \quad (3.23)$$

where the definition domain of the spherical function T_{ba} is extended with

$$T_{ba}(\theta,\phi) = T_{ba}(2\pi - \theta, \phi + \pi). \quad (3.24)$$

Formula (3.22) thus allows the extension of the FFT approach of [20] to the vectorial case. In the Fourier representation, $N_0(2M_0+1)$ samples of the radiation patterns, uniformly spaced in θ and ϕ within the domain $[0,\pi] \otimes [0,2\pi]$, are needed to perform the integration in (3.23). The numbers M_0 and N_0 depend on the subdomain radius R and the desired accuracy. We chose $M_0 = L_0, N_0 = L_0 + 1$ where L_0 is determined numerically together with L in (3.19) on a worst case scenario in such a way that the desired accuracy is achieved with the minimum number of samples. L_0 turns out to be much smaller than L, usually somewhat larger than $\frac{L}{2}$. Further differences with the implementation of [20] involve the recursive calculation of the truncated Fourier spectrum of $T_{ba}(\theta,\phi)|\sin\theta|$ using a recursion formula for the Legendre function (see Appendix A) and the use of a (trivial) 2D extension of Theorem 4.1 in [20] to anterpolate the product $T_{ba}(\theta,\phi)|\sin\theta|\boldsymbol{U}_a(\theta,\phi)$.

More efficient aggregation and disaggregation

The evaluation of (3.20) in $N_0(2M_0+1)$ uniformly spaced sample points, referred to as aggregation towards the lowest level, can be cast into a matrix operation:

$$\boldsymbol{\mathcal{U}}_a^u = \boldsymbol{\mathcal{A}}^{+,u} \boldsymbol{d}_{\xi,a}^+ + \boldsymbol{\mathcal{A}}^{-,u} \boldsymbol{d}_{\xi,a}^-, \quad u = \theta \text{ or } \phi. \quad (3.25)$$

$\boldsymbol{\mathcal{U}}_a^u$ is a $N_0(2M_0+1)$-dimensional vector containing the samples of U_a^u and $\boldsymbol{\mathcal{A}}^{+,u}$ and $\boldsymbol{\mathcal{A}}^{-,u}$ are the aggregation matrices. After interpolation, translation and anterpolation, the incoming pattern $\boldsymbol{R}_b(\theta,\phi) = \sum_a T_{ba}(\theta,\phi)\boldsymbol{U}_a(\theta,\phi)|\sin\theta|$ of every group D^b is multiplied in (3.23) with $\boldsymbol{V}_{\beta,b}$ and integrated for every $\boldsymbol{\Psi}_\beta$ in D^b. Since the integration is performed numerically by a summation over samples, this can also be written as a matrix operation:

$$\boldsymbol{e}_{b,FMM}^{\text{scat}} = \boldsymbol{\mathcal{D}}^\theta \boldsymbol{\mathcal{R}}_b^\theta + \boldsymbol{\mathcal{D}}^\phi \boldsymbol{\mathcal{R}}_b^\phi \quad (3.26)$$

where $\boldsymbol{e}_{b,FMM}^{\text{scat}}$ contains the weighted scattered field in subdomain D^b, due to all well-separated subdomains D^a and $\boldsymbol{\mathcal{R}}_b^u$ contains the samples of $\boldsymbol{R}_b(\theta,\phi)\cdot\hat{\boldsymbol{u}}$. The matrices $\boldsymbol{\mathcal{D}}^\theta$ and $\boldsymbol{\mathcal{D}}^\phi$ are the disaggregation matrices and this step in the algorithm is denoted

as disaggregation from the lowest level.

Again the contributions of S_α^+ and S_α^- are separated in (3.25) in order to make the aggregation matrices independent of the contrast. Because of this and because of the identical geometry of all subdomains, the aggregation and disaggregation matrices are the same for every subdomain and have to be stored only once. This saves a lot of memory compared to a HF MLFMA applied to arbitrary meshes, where these matrices have to be stored per FMM-group or subdomain.

Although using uniform samples in θ and ϕ allows for an elegant FFT interpolation, combining global exact interpolation with efficiency, it is suboptimal with respect to the aggregation toward and disaggregation from the lowest level. The cost of these stages can be reduced by choosing the samples more optimally [21] or by temporarily switching to another, more economic representation of the radiation patterns. The latter approach has been employed in [22], where the cartesian components of the radiation patterns are represented in a spherical harmonics basis on the lowest level. After aggregation to this basis, the uniform samples are still needed to proceed with the diagonal translations and the interpolations towards higher levels, where the patterns are stored in the usual k-space representation. In this dissertation a similar strategy is adopted, but we use vector spherical harmonics to represent only the transverse components of the radiation patterns. For example:

$$\boldsymbol{U}_a(\theta,\phi) = \sum_{l=0}^{L_0}\sum_{m=-l}^{l} (\gamma_a)_{lm}\, \boldsymbol{X}_{lm}(\theta,\phi) + \sum_{l=0}^{L_0}\sum_{m=-l}^{l} (\kappa_a)_{lm}\, \boldsymbol{\Phi}_{lm}(\theta,\phi). \tag{3.27}$$

Here, $\boldsymbol{X}_{lm}$ and $\boldsymbol{\Phi}_{lm} = \hat{\boldsymbol{k}} \times \boldsymbol{X}_{lm}$ are vector spherical harmonics as defined in [23]. The multipole coefficients $(\gamma_a)_{lm}$ and $(\kappa_a)_{lm}$ are determined as

$$\begin{aligned}
(\gamma_a)_{lm} &= 4\pi j^l \sum_{\alpha\in I_a^+} \xi_\alpha^+ d_\alpha \int_{\mathcal{S}_\alpha^+} \mathrm{d}\boldsymbol{r}\, \boldsymbol{\Psi}_\alpha(\boldsymbol{r}) \cdot \boldsymbol{m}_{lm}^{(1)*}(\boldsymbol{r}-\boldsymbol{r}_c^a) \\
&+ 4\pi j^l \sum_{\alpha\in I_a^-} \xi_\alpha^- d_\alpha \int_{\mathcal{S}_\alpha^-} \mathrm{d}\boldsymbol{r}\, \boldsymbol{\Psi}_\alpha(\boldsymbol{r}) \cdot \boldsymbol{m}_{lm}^{(1)*}(\boldsymbol{r}-\boldsymbol{r}_c^a) \qquad (3.28) \\
(\kappa_a)_{lm} &= 4\pi j^{l-1} \sum_{\alpha\in I_a^+} \xi_\alpha^+ d_\alpha \int_{\mathcal{S}_\alpha^+} \mathrm{d}\boldsymbol{r}\, \boldsymbol{\Psi}_\alpha(\boldsymbol{r}) \cdot \boldsymbol{n}_{lm}^{(1)*}(\boldsymbol{r}-\boldsymbol{r}_c^a) \\
&+ 4\pi j^{l-1} \sum_{\alpha\in I_a^-} \xi_\alpha^- d_\alpha \int_{\mathcal{S}_\alpha^-} \mathrm{d}\boldsymbol{r}\, \boldsymbol{\Psi}_\alpha(\boldsymbol{r}) \cdot \boldsymbol{n}_{lm}^{(1)*}(\boldsymbol{r}-\boldsymbol{r}_c^a) \qquad (3.29)
\end{aligned}$$

where $\boldsymbol{m}_{lm}^{(1)}(\boldsymbol{r}) = j_l(k_0 r)\boldsymbol{X}_{lm}(\hat{\boldsymbol{r}})$ and $\boldsymbol{n}_{lm}^{(1)}(\boldsymbol{r}) = \frac{1}{k_0}\nabla\times\boldsymbol{m}_{lm}^{(1)}(\boldsymbol{r})$, with j_l the spherical Bessel function of order l, are the standing wave vector solutions with zero divergence of the Helmholtz equation as defined in [23]. $\boldsymbol{m}_{lm}^{(1)*}$ and $\boldsymbol{n}_{lm}^{(1)*}$ denote the complex conjugate of $\boldsymbol{m}_{lm}^{(1)}$ and $\boldsymbol{n}_{lm}^{(1)}$ respectively. The advantage of this approach is

that we only need to calculate $2 \times (L_0+1)^2$ multipole coefficients to represent $\boldsymbol{U}_a$, which is half the amount of uniform samples that are needed, $2 \times (2L_0+1)(L_0+1)$. The matrix version of (3.28) and (3.29) which now replaces (3.25) is

$$\boldsymbol{\gamma}_a = \boldsymbol{\mathcal{M}}^+ \boldsymbol{d}^+_{\xi,a} + \boldsymbol{\mathcal{M}}^- \boldsymbol{d}^-_{\xi,a} \tag{3.30}$$

$$\boldsymbol{\kappa}_a = \boldsymbol{\mathcal{N}}^+ \boldsymbol{d}^+_{\xi,a} + \boldsymbol{\mathcal{N}}^- \boldsymbol{d}^-_{\xi,a} \tag{3.31}$$

where $\boldsymbol{\gamma}_a$ and $\boldsymbol{\kappa}_a$ are vectors containing the multipole coefficients of $\boldsymbol{U}_a$. $\boldsymbol{\mathcal{M}}^{\pm}$ and $\boldsymbol{\mathcal{N}}^{\pm}$ are the new aggregation matrices, which are still independent of the domain index a. Since these matrices are only half as large as the original aggregation matrices in (3.25), the aggregation to multipole coefficients will be twice as fast. The overall gain factor, however, will be smaller than 2, because we still have to evaluate the multipole expressions for the radiation patterns in the $N_0(2M_0+1)$ uniform sample points with (3.27). However, this can be done efficiently. First of all note that $\boldsymbol{\Phi}_{lm} \cdot \hat{\boldsymbol{\theta}} = -\boldsymbol{X}_{lm} \cdot \hat{\boldsymbol{\phi}}$ and $\boldsymbol{\Phi}_{lm} \cdot \hat{\boldsymbol{\phi}} = \boldsymbol{X}_{lm} \cdot \hat{\boldsymbol{\theta}}$. Then let us rewrite (3.27) using a block matrix notation:

$$\begin{bmatrix} \boldsymbol{\mathcal{U}}^{\theta}_a \\ \boldsymbol{\mathcal{U}}^{\phi}_a \end{bmatrix} = \begin{bmatrix} \boldsymbol{\mathcal{X}}_{\theta} & -\boldsymbol{\mathcal{X}}_{\phi} \\ \boldsymbol{\mathcal{X}}_{\phi} & \boldsymbol{\mathcal{X}}_{\theta} \end{bmatrix} \begin{bmatrix} \boldsymbol{\gamma}_a \\ \boldsymbol{\kappa}_a \end{bmatrix}. \tag{3.32}$$

It appears that four matrix-vector multiplications (with matrices of much smaller dimension than the aggregation matrices) have to be carried out. This can be avoided, however, since (3.32) can be diagonalized:

$$\begin{bmatrix} \boldsymbol{\mathcal{U}}^{\theta}_a \\ \boldsymbol{\mathcal{U}}^{\phi}_a \end{bmatrix} = \frac{1}{2} \begin{bmatrix} \boldsymbol{I}_0 & \boldsymbol{I}_0 \\ j\boldsymbol{I}_0 & -j\boldsymbol{I}_0 \end{bmatrix} \begin{bmatrix} \boldsymbol{\mathcal{X}}_{\theta} - j\boldsymbol{\mathcal{X}}_{\phi} & 0 \\ 0 & \boldsymbol{\mathcal{X}}_{\theta} + j\boldsymbol{\mathcal{X}}_{\phi} \end{bmatrix} \begin{bmatrix} \boldsymbol{\gamma}_a - j\boldsymbol{\kappa}_a \\ \boldsymbol{\gamma}_a + j\boldsymbol{\kappa}_a \end{bmatrix}, \tag{3.33}$$

where $\boldsymbol{I}_0$ represents the unit matrix of dimension $N_0(2M_0+1)$. This way, only two matrix-vector products and some simple recombinations remain. Note that in [22] three matrix-vector products are required to calculate the three cartesian components of the radiation patterns. Furthermore the summations over m in (3.27) can be carried out efficiently by using FFTs. It can be shown that $\boldsymbol{X}_{lm} \cdot \hat{\boldsymbol{\theta}}$ and $\boldsymbol{X}_{lm} \cdot \hat{\boldsymbol{\phi}}$ depend on ϕ only through a factor $e^{jm\phi}$, such that the typical summation is of the form

$$\sum_{l=0}^{L_0} \sum_{m=-l}^{l} F_{lm}(\theta) e^{jm\phi_q} \gamma_{lm} = \sum_{m=-L_0}^{L_0} \sum_{l=|m|}^{L_0} F_{lm}(\theta) e^{jm\phi_q} \gamma_{lm} \tag{3.34}$$

$$= \sum_{m=-L_0}^{L_0} e^{jm\frac{2\pi}{2L_0+1}q} \left(\sum_{l=|m|}^{L_0} F_{lm}(\theta) \gamma_{lm} \right) \tag{3.35}$$

where we have assumed the form $\phi_q = q\frac{2\pi}{2L_0+1} = q\frac{2\pi}{2M_0+1}$ for the samples in the ϕ-direction. The outer summation in (3.35) is a discrete Fourier transform and hence can be calculated by an FFT.

$\boldsymbol{V}_{\beta,b}$ is also expanded in multipoles and by substituting this expansion in (3.18) and by interchanging the integration and the summation in the multipole expansion, a disaggregation procedure with multipoles is readily obtained similar to the aggregation procedure outlined above. The gain in speed obtained by the aggregation and disaggregation via multipoles will be discussed in Section 3.6.2.

A last improvement to the aggregation towards and disaggregation from the lowest level is a purely technical one. The matrix operations (3.30) and (3.31) have to be carried out for every subdomain. Since the aggregation and disaggregation matrices are the same for all the groups, the vectors $\boldsymbol{d}^{+}_{\xi,a}$ for all a, for example, can be stored columnwise in a large matrix with N^S columns. This matrix can be multiplied as a whole with the appropriate aggregation matrix using Level 3 Basic Linear Algebra Subprograms (BLAS) [24, 25], which reduces the CPU time considerably. This will also be illustrated in Section 3.6.2.

3.5 The hybrid MLFMA-FFT method

The hybrid MLFMA-FFT method consists of applying the HF MLFMA of Section 3.4 to the cubic mesh of Section 3.2.2 and treating the interactions (3.15) between subdomains that are not well-separated – the near interactions – with the use of FFTs (3.16). The resulting method is an improvement with respect to both the HF MLFMA and the subdomain FFT method. With regard to the MLFMA, treating the near interactions with FFTs is rewarding, because the $\mathcal{O}((N^C)^2)$ near interactions of the HF MLFMA are replaced by more efficient $\mathcal{O}(N^C)$ diagonal multiplications (Figure 3.4). With regard to the subdomain FFT method, the hybrid MLFMA-FFT method replaces the diagonal multiplication in the Fourier domain with the diagonal translation of the FMM for well-separated subdomains. Because the dimension of the former is proportional to N^C and thus to the volume of the subdomains, while the dimension of the latter is generally smaller (only proportional to the surface area of the subdomains when these are large enough), this can reduce the computation time and memory use, even in a two-level FMM. Furthermore, in the multilevel scheme, the computational complexity of the MLFMA-FFT method is $\mathcal{O}(N)$ to $\mathcal{O}(N \log^2 N)$, while the subdomain FFT method scales as $(N^S)^2 N^C = N^2/N^C$ for a fixed size of the subdomains.

For a more in depth study of the method, the subdomain size is the most important parameter. For a fixed separation parameter β (which determines the reachable accuracy) it determines the height of the MLFMA tree (we add levels until there are no more far interactions on the level to add) and the efficiency of the multilevel scheme. To investigate the influence of the subdomain size, consider first a very large dense scattering configuration. In such a situation, the number of near interactions for a given subdomain (i.e. the number of subdomains with a center that lies within a radius βR from the center of the considered subdomain) is independent of the subdomain size. To see what happens when the subdomain size is increased, consider a

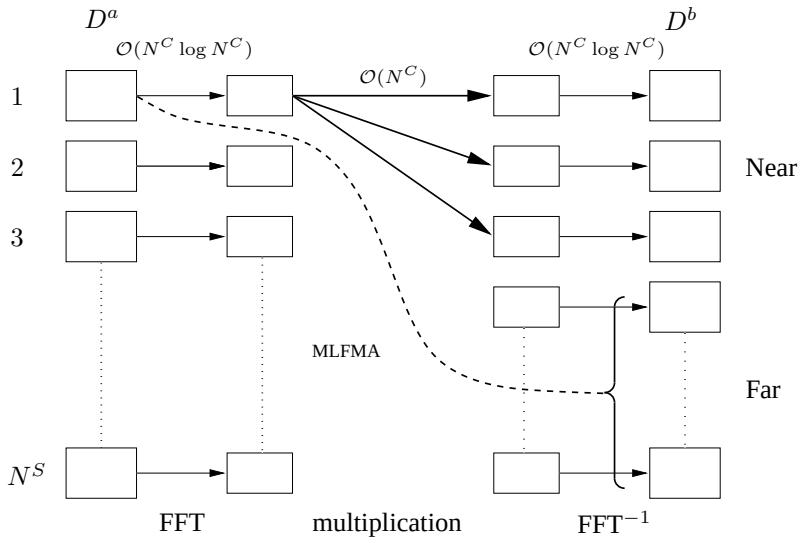

Figure 3.4: Illustration of the computational complexity of the MLFMA-FFT method.

doubling of this size:

- The number of cells N^C per subdomain is multiplied by 8.
- The number of subdomains is divided by 8.
- The cost of calculating the FFTs for every subdomain increases slightly from $N^C \ln(N^C)$ to $N^C \ln(8N^C)$.
- The cost of the diagonal multiplications in the Fourier domain for the near interactions is unaltered, since the increase in cells per subdomain and the decrease in number of subdomains balance each other.
- The cost of the translations and interpolations/anterpolations is seriously reduced, because we lose a level and nothing changes for the remaining levels.
- The cost of the aggregation toward and disaggregation from the lowest level is increased, because L_0 is increased. For subdomain sizes of about one wavelength or less, the increase is practically negligible, but for larger subdomains, L_0 increases linearly with the subdomain size.

One can conclude that unless the subdomains become very large ($k_b R \gg 1$), an increase in subdomain size reduces the cost and memory usage. For sparse configurations, the behaviour is less predictable, but apart from some exotic configurations the

same conclusion stands. This is an important difference with the original MLFMA, where the cost of the near interactions is multiplied by 8 when the subdomain size is doubled. Therefore, in the MLFMA there generally is an optimal subdomain size, smaller than the background wavelength, which balances the load between near and far interactions optimally, but the use of FFTs shifts this optimum in the MLFMA-FFT method to much larger subdomains.

Our main goal is to examine for which type of configurations the MLFMA-FFT method outperforms the FFT method in terms of CPU time or memory consumption. On dense problems it is well known that the MLFMA, and thus also the MLFMA-FFT method, is $\mathcal{O}(N)$. However, it appears from numerical tests that despite this lower computational complexity, the MLFMA-FFT method is slower than the FFT method even for fairly large problems, due to the small prefactor of the FFT method. It will be shown in section 3.6, though, that it uses substantially less memory. Another situation is encountered when considering sparse scattering configurations, such as the one in Figure 3.5(a). When the FFT method is used to calculate the scattering from this geometry, the cubic grid has to be extended to the bounding box $\mathcal{D}^{\mathrm{C}}$ of the domain $\mathcal{D}$ as in Figure 3.5(b). This implies that the CPU time and the memory needed for the calculation of (3.13) are the same as for a dense configuration in $\mathcal{D}^{\mathrm{C}}$. In this case the MLFMA-FFT or even the subdomain FFT method can yield a faster matrix-vector multiplication because they discretize the geometry more economically (Figure 3.5(c)). If we do not want the grid to extend over regions of empty space, the maximal subdomain size is dictated by the sparsity of the configuration. Combining this with the main conclusion of the previous paragraph, we state the following rule of thumb: if the maximal subdomain size, determined by the sparsity of the geometry, is not much larger then a wavelength, use this maximal subdomain size and the MFLMA-FFT method. For very large maximal subdomain sizes, the aggregation and disaggregation steps become unwieldy and it might be appropriate to use the subdomain FFT on the maximal subdomains or the MLFMA-FFT method with smaller subdomains, depending on the specific geometry. In general, however, the MLFMA-FFT method will consume less memory on any large problem, as will be demonstrated in Section 3.6.

3.6 Validation and performance analysis

In this section the proposed MLFMA-FFT method is validated and its performance is investigated and compared to that of the FFT-method and the HF MLFMA on a number of test cases. All computations are carried out in double precision arithmetics on a 64 bit computer with 2GHz Dual Core AMD Opteron processor and 8GB RAM. All FFTs are computed using FFTW, the Fastest Fourier Transform in the West, a collection of fast C routines for computing the discrete Fourier transform [13]. No parallelizing or multi-threading of any kind are used.

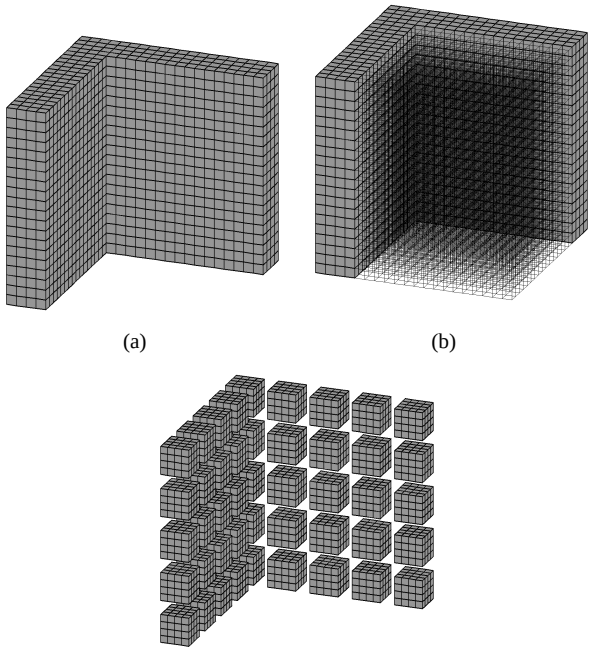

Figure 3.5: Two ways of handling a sparse cubic mesh (a): extension to the bounding box D^C (b), and division in identical cubic subdomains (c).

3.6.1 Validation

The scattering from a homogeneous sphere is considered to first validate the subdomain FFT method. The sphere has a radius $R = \lambda_\mathrm{b}$ of one background wavelength and a permittivity $\epsilon = (2 - 2j)\epsilon_\mathrm{b}$ and is illuminated with an x-polarized plane wave traveling in the $+z$-direction:

$$\boldsymbol{E}^\mathrm{inc}(\boldsymbol{r}) = e^{-jk_\mathrm{b}z}\hat{\boldsymbol{x}}. \tag{3.36}$$

The sphere is contained in a cubic domain $\mathcal{D}$ with side $2\lambda_\mathrm{b}$. The grid on this domain has a cell size $\delta = 0.05\lambda_\mathrm{b}$, which results in 196800 unknowns. Such a fine grid is chosen to reduce the staircasing error. We solve the MPDE in two ways: firstly we consider $\mathcal{D}$ as one cubic subdomain, which means that we employ a classical FFT method, and secondly we divide $\mathcal{D}$ in 64 subdomains and apply the subdomain FFT method. Both methods needed 39 BICGSTAB iterations to converge to an accuracy of 10^{-6}. Figure 3.6 compares the scattered fields with the analytical solution provided by the MIE series [14]. The agreement is very good.

We now compare the scattered fields computed by the MLFMA-FFT method and

the subdomain FFT-method for the sparse scattering configuration of Figure 3.7. A homogeneous sphere with a radius $R = 2\lambda_\mathrm{b}$ and a permittivity $\epsilon = (2 - 2j)\epsilon_\mathrm{b}$ is surrounded by 50 cubes with side λ_b and permittivity $\epsilon = 1.5\epsilon_\mathrm{b}$, that are randomly distributed in a cubic domain $\mathcal{D}$ with side $10\lambda_b$. The cell size is $0.1\lambda_\mathrm{b}$. This problem yields 344100 unknowns and is solved by both methods in 67 iterations to an accuracy of 10^{-6}. The results are shown in Figure 3.8. The parameters for the MLFMA are chosen such that the relative error on the FMM-formula (3.18) is less than 10^{-5} and Figure 3.8 (b) shows that the relative difference between both solutions stays below this value.

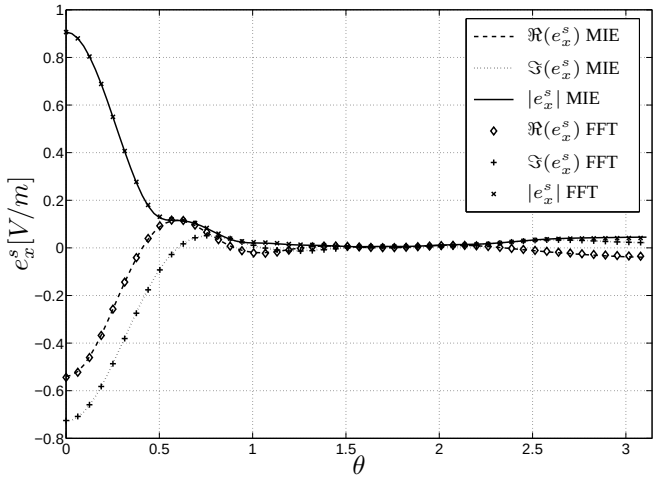

(a)

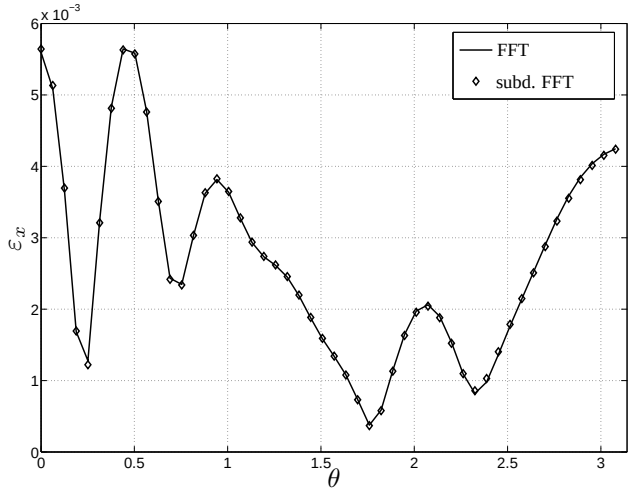

(b)

Figure 3.6: Scattering from a homogeneous sphere with radius $R = \lambda_\mathrm{b}$ and permittivity $\epsilon = (2 - 2j)\epsilon_\mathrm{b}$: comparison between MIE series and results from the FFT and subdomain FFT methods. Figure (a) shows the x-component of the scattered field on a semicircle $S = \{\boldsymbol{r} : \boldsymbol{r} = R_m \sin\theta\hat{\boldsymbol{x}} + R_m \cos\theta\hat{\boldsymbol{z}}\}$, with $R_m = 4\lambda_\mathrm{b}$ and $\theta \in [0, \pi[$. Figure (b) shows the error defined as $\varepsilon_x(\boldsymbol{r}) = \|e_x^s(\boldsymbol{r}) - e_{x,MIE}^s(\boldsymbol{r})\| / \max_{\boldsymbol{r}\in S} \|e_{x,MIE}^s(\boldsymbol{r})\|$ for both the FFT and subdomain FFT methods.

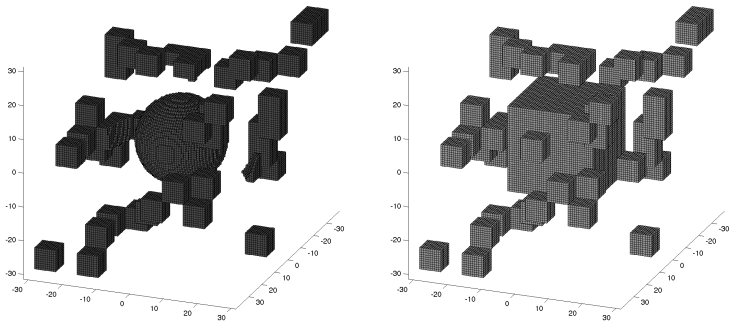

(a) (b)

Figure 3.7: A homogeneous sphere with $R = 2\lambda_{\mathrm{b}}$ and $\epsilon = (2 - 2j)\epsilon_{\mathrm{b}}$, surrounded by 50 particles with side λ_{b} and $\epsilon = 1.5\epsilon_{\mathrm{b}}$, randomly distributed over a cubic domain $\mathcal{D}^C$ with side $10\lambda_{\mathrm{b}}$. Figure (a) shows the actual scatterers and Figure (b) represents the mesh used by the MLFMA-FFT and subdomain FFT methods. The cell size is $\delta = 0.1\lambda_{\mathrm{b}}$.

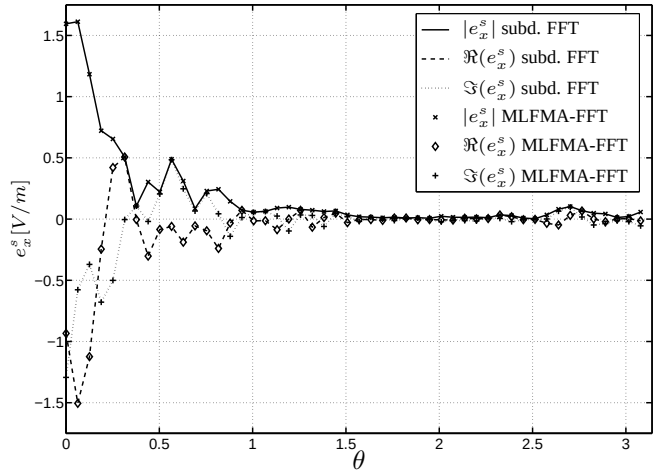

(a)

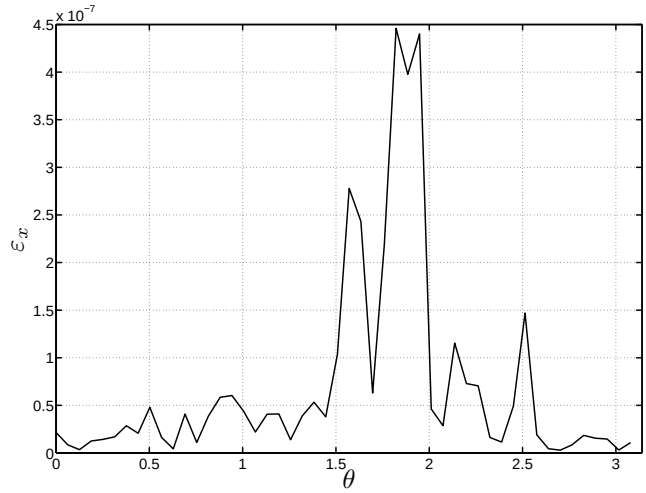

(b)

Figure 3.8: Scattering from the scatterers depicted in Figure 3.7. Figure (a) shows the x-component of the scattered field on a semicircle $S = \{\boldsymbol{r} : \boldsymbol{r} = R_m \sin\theta\hat{\boldsymbol{x}} + R_m \cos\theta\hat{\boldsymbol{z}}\}$, with $R_m = 10\lambda_\mathrm{b}$ and $\theta \in [0, \pi[$. Figure (b) shows the error defined as $\varepsilon_x(\boldsymbol{r}) = \|e^s_{x,2}(\boldsymbol{r}) - e^s_{x,1}(\boldsymbol{r})\|/\|e^s_{x,1}(\boldsymbol{r})\|$ between the subdomain FFT method ($e^s_{x,1}$) and the hybrid MLFMA-FFT method ($e^s_{x,2}$).

3.6.2 Performance analysis

We first demonstrate the acceleration of the aggregation towards and the disaggregation from the lowest level, introduced by the techniques of section 3.4.2, in Table 3.1. Three sizes of the subdomains ($0.5\lambda_\mathrm{b}$, $0.8\lambda_\mathrm{b}$ and λ_b) are considered. The values of L_0 and N^a determine the size of the aggregation and disaggregation matrices. N^a is the number of basis functions in a subdomain if it is filled with a uniform cubical grid with $\delta = 0.1\lambda_\mathrm{b}$. L_0 is determined together with L (not shown in Table 3.1) such that the relative error on the FMM-formula (3.18) does not exceed 10^{-5} when the separation parameter β is set to 4. It can be seen that by performing the aggregation towards and disaggregation from the lowest level via multipoles (M) instead of with uniform samples (US), the CPU time for these stages can be reduced by 40% to 45%. Moreover, with the use of Level 3 BLAS routines (MB) the total reduction factor ranges from 3 for a subdomain size of $0.5\lambda_\mathrm{b}$ to 5 for a subdomain size of λ_b. The number of subdomains N^S, once it is large enough, does not seem to have a significant influence on these gain factors.

subdomain size (in λ_b)	L_0	N^a	N^S	US	M	MB
0.5	11	450	1000	5.00	3.16	1.66
0.5	11	450	500	2.62	1.61	0.85
0.8	15	1728	1000	45.88	24.64	9.32
0.8	15	1728	500	17.74	10.03	4.70
1.0	17	3300	1000	112.34	61.25	21.29
1.0	17	3300	500	56.26	30.77	10.79

Table 3.1: Comparison of CPU times (in seconds) for the aggregation and disaggregation towards and from the lowest level using uniform samples (US), multipoles (M) and multipoles and Level 3 BLAS (MB). Results are given for different subdomain sizes and for two values of N^D, the number of subdomains. The values of L_0 yield an FMM-accuracy of 10^{-5}.

Next, the performances in terms of CPU time and storage requirements of all the methods described in this chapter are investigated and compared. Table 3.2 shows the CPU time for one evaluation of (3.13) and the memory needed to solve the MPDE for a number of test geometries. These geometries are all contained in a cubic bounding box $\mathcal{D}^C$ with side $10\lambda_\mathrm{b}$ and are meshed with a uniform cubic grid with cell size $\delta = 0.1\lambda_\mathrm{b}$. For the FFT method, the complete bounding box $\mathcal{D}^C$ has to be discretized, irrespective of the actual permittivity profile and geometry inside $\mathcal{D}^C$. This yields the test grid "full". The subdomain FFT method and the MLFMA-FFT method can be used on sparse subdomain grids. The test grid "clutN^P" thus refers to grids like the one of Figure 3.7(b), where N^P is the number of particles that surround a central cube of side $4\lambda_\mathrm{b}$. All particles are cubes with side λ_b and coincide with one subdomain each in all test grids, except for "clut45/2". The test grid "clut45/2" is identical to "clut45", but the size of its subdomains is twice as small ($0.5\lambda_\mathrm{b}$) and hence their number is eight

times larger than with "clut45". Finally the test grid "corner" indicates a mesh like the one in Figure 3.5(a) with a wall thickness of λ_{b} and outer dimensions of $10\lambda_{\mathrm{b}}$. The subdomains for the test grids "full" and "corner", when using MLFMA-FFT or subdomain FFT, also have a size λ_b.

problem	method	f_V	N	CPU-time	memory
full	FFT	1.0	$3,030,000$	38.92 s	$+7$ GB
	MLFMA-FFT	1.0	$3,030,000$	310.88 s	2951 MB
clut45	MLFMA-FFT	0.07	$343,900$	12.91 s	940 MB
	subdomain FFT	0.07	$343,900$	29.87 s	>7.3 GB
clut45/2	MLFMA-FFT	0.07	$343,900$	32.04 s	720 MB
	MLFMA	0.07	$343,900$	142.89 s	1570 MB
clut87	MLFMA-FFT	0.11	$487,300$	20.83 s	1059 MB
clut127	MLFMA-FFT	0.15	$610,700$	25.12 s	1156 MB
clut173	MLFMA-FFT	0.19	$758,400$	34.38 s	1267 MB
corner	MLFMA-FFT	0.18	$591,900$	19.33 s	943 MB

Table 3.2: Comparison between the different methods in terms of memory requirements and CPU-time per evaluation of (3.13). f_V is the volume fraction of the scatterers in the surrounding cube $\mathcal{D}^C$ with side $10\lambda_{\mathrm{b}}$. Whenever the MLFMA or the subdomain FFT method is not mentioned for one of the test cases, this means that the available memory was not sufficient for that method.

We first note that the subdomain FFT method is less efficient than the FFT method in case of dense geometries like the test grid "full", due to a higher complexity. In fact, on the test grid "full" and on all other test grids except for "clut45", the subdomain FFT method could not even be used, because it required more memory than the available 8 GB. On the sparse test grid "clut45", the subdomain FFT method yields a faster matrix vector product than the FFT method, but even here the memory requirements are close to the limit.

When we compare the MLFMA-FFT method with the subdomain FFT method on the test grid "clut45", the gain in CPU time and especially in memory use of the hybrid method is obvious. In comparison to the FFT method (test grid "full"), the MLFMA-FFT method clearly performs better on all sparse test grids. The matrix-vector multiplication is faster and the reduction of the storage needs is even more explicit. Even on the dense problem of test grid "full" the MLFMA-FFT method requires less memory than the FFT-method, but it is defeated in terms of CPU time. Note that most of the $+7$ GB used by the FFT-method is needed to store the FFT-vectors and is therefore not affected by how sparse the actual permittivity profile on the grid is. Because of the $\mathcal{O}(N)$ storage complexity of both the MLFMA-FFT method and the FFT method on dense problems like the test grid "full", the hybrid method will always require less memory than the FFT method on electrically large problems.

Finally the MLFMA-FFT method and the MLFMA are compared on the same

cubic mesh and using the same parameters. The MLFMA exploits the symmetry to reuse the aggregation and disaggregation matrices. When not doing so, the aggregation and disaggregation matrices of only 78 subdomains with side λ_b could be stored in the available 8 GB of RAM. However, even the symmetry adjusted MLFMA could only be used on the sparsest test grid "clut45/2" with the smallest subdomains, since the other test grids required too much memory to store the near interaction matrices. For this test grid, the hybrid MLFMA-FFT is almost 5 times as fast as the MLFMA and memory requirements are less than half. It follows that the hybrid MLFMA-FFT method is applicable to a much wider range of volumetric problems than the MLFMA and that it also performs better. The test case "clut45/2" illustrates that dividing the mesh in smaller subdomains beyond what is necessary to account for the sparsity of the scatterers is not beneficial in terms of CPU time of the MLFMA-FFT method. On this example it does reduce the memory use, but this behavior strongly depends on the geometry and is not a fundamental property.

3.7 Choice of the initial guess

Since the total solution time is also proportional to the number of iterations needed to solve (3.14), it is important that this number N^F is kept low. Often in computational electromagnetics, a large number of iterations results from the ill-conditioning of the forward problem. A remedy in such a case is the use of some kind of preconditioning. The domain equation (3.7) is an integral equation of the second kind and as a result is reasonably well-conditioned in general (if the contrast in permittivity is not too extreme) and it is not so much the large number of iterations for one solution of (3.14) that is the problem as the fact that solving the inverse scattering problem requires the solution of a large number of forward problems (for a varying permittivity vector $\boldsymbol{\varepsilon}$ and with each of those for varying illumination i).

Therefore, a more appropriate strategy makes use of the repeated forward problem solutions. In [26, 27] it is shown that the number of iterations N^F to solve (3.14) can be significantly reduced by means of a "marching-on-in-anything-technique" provided that the desired accuracy is not much lower than the relative error introduced by noise and the discretization [28]. This technique proposes an adequate choice for the initial guess $\boldsymbol{d}_i^0$ for the solution corresponding to illumination i based on available solutions which correspond to slightly different illumination and/or object configurations.

Suppose we have a few vectors $\boldsymbol{x}_m$, $m = 1 \ldots M$, that can be regarded as approximations for $\boldsymbol{d}_i$. The initial guess $\boldsymbol{d}_i^0$ then is calculated as the linear combination

$$\boldsymbol{d}_i^0 = \sum_{m=1}^{M} a_m \, \boldsymbol{x}_m \tag{3.37}$$

which minimizes the error $\|\boldsymbol{L}_\xi \boldsymbol{d}_i^0 - \boldsymbol{e}_i^{\mathrm{inc}}\|^2$ between the LHS and RHS of (3.14). The

coefficients a_m thus are a solution of the linear system

$$\sum_{m=1}^{M} \left[\boldsymbol{L}_\xi \, \boldsymbol{x}_{m'}\right]^H \boldsymbol{L}_\xi \, \boldsymbol{x}_m \, a_m = \left[\boldsymbol{L}_\xi \, \boldsymbol{x}_{m'}\right]^H \boldsymbol{e}_i^{\mathrm{inc}} \qquad m' = 1, \ldots, M. \tag{3.38}$$

which is a small system, since $M = 3$ or $M = 4$ is usually sufficient.

In this thesis we propose to use as the approximations $\boldsymbol{x}_m$ to $\boldsymbol{d}_i$ on the one hand a few solutions $\boldsymbol{d}_{i'}$, that were computed for the same permittivity vector but for nearby transmitter positions—so-called "marching-on-in-illumination" [28]—and on the other hand a Distorted Born approximation $\boldsymbol{d}_i^{\mathrm{DB}}$, which is calculated as

$$\boldsymbol{d}_i^{\mathrm{DB}} = \boldsymbol{W}_\xi^{-1} \left(\boldsymbol{e}_i^{\mathrm{inc}} - \boldsymbol{Z}^+ \boldsymbol{j}_i^{\mathrm{DB},+} - \boldsymbol{Z}^- \boldsymbol{j}_i^{\mathrm{DB},-} \right), \tag{3.39}$$

where the vectors $\boldsymbol{j}_i^{\mathrm{DB},\pm}$ have elements

$$j_{i,\alpha}^{\mathrm{DB},\pm} = \xi_\alpha^{\mathrm{DB},\pm} d'_{i,\alpha} \tag{3.40}$$

$$= \frac{\epsilon_\alpha^\pm - \epsilon_{\mathrm{b}}}{\left(\epsilon_\alpha^\pm\right)'} d'_{i,\alpha}. \tag{3.41}$$

The Distorted Born approximation $\boldsymbol{d}_i^{\mathrm{DB}}$ thus is the discretized flux density which corresponds to the total field $\boldsymbol{E}_i^{\mathrm{DB}}(\boldsymbol{r})$ in the investigation domain, generated by the source current and the contrast current

$$\boldsymbol{J}_i^{\mathrm{DB}}(\boldsymbol{r}) = j\omega\chi(\boldsymbol{r})\boldsymbol{E}'_i(\boldsymbol{r}) = j\omega\frac{\chi(\boldsymbol{r})}{\epsilon'(\boldsymbol{r})}\boldsymbol{D}'_i(\boldsymbol{r}) = j\omega\xi^{\mathrm{DB}}(\boldsymbol{r})\boldsymbol{D}'_i(\boldsymbol{r}), \tag{3.42}$$

which is the product of the new contrast function χ (corresponding to the new permittivity ϵ) and the total field $\boldsymbol{E}'_i$ obtained for a previous contrast function χ' (corresponding to a previous permittivity ϵ') and for the same illumination i. This approximation actually represents a linearization of scattering model as a function of the permittivity around the permittivity profile ϵ'. Since the matrix $\boldsymbol{W}_\xi$ is sparse and since the multiplications $\boldsymbol{Z}^\pm \boldsymbol{j}_i^{\mathrm{DB},\pm}$ can be done with FFT's, the calculation of $\boldsymbol{d}_i^{\mathrm{DB}}$ is fast. Note further that in (3.38) only the multiplication of $\boldsymbol{L}_\xi$ with $\boldsymbol{d}_i^{\mathrm{DB}}$ needs to be done, since the other products $\boldsymbol{L}_\xi \boldsymbol{d}_{i'} = \boldsymbol{e}_{i'}^{\mathrm{inc}}$ are just the incoming field vectors which are readily available. The inclusion of the Distorted Born solution in the marching-on scheme allows for a simple extrapolation over the permittivity without having to store multiple solution vectors for a number of different permittivity profiles as would be the case in a "marching-on-in-permittivity" scheme.

3.8 Numerical evaluation of the scattered field

So far the focus was on solving the domain equation (2.35) or (3.7) for the total field inside the domain $\mathcal{D}$. After this, the scattered field still has to be computed in a number of observation points outside $\mathcal{D}$, i.e. the data equation (2.37) has to be evaluated. Since there is no problem with the singularity in the Green's dyadic, we can use (3.17) for this task. Using the expression (3.2) for the contrast current and the expansion (3.8) in (3.17), we can write down the scattered field, due to one term $d_\alpha \boldsymbol{\Psi}_\alpha(\boldsymbol{r})$ in (3.8):

$$\begin{aligned} \boldsymbol{E}^{\mathrm{scat}}_\alpha(\boldsymbol{r}_{l,i}) &= \omega^2\mu_0 d_\alpha \left[\xi^+_\alpha \int_{\mathcal{S}^+_\alpha} \mathrm{d}\boldsymbol{r}' \boldsymbol{G}_{\mathrm{b}}(\boldsymbol{r}_{l,i},\boldsymbol{r}')\cdot\boldsymbol{\Psi}_\alpha(\boldsymbol{r}') \right. && (3.43)\\ &\quad \left. + \xi^-_\alpha \int_{\mathcal{S}^-_\alpha} \mathrm{d}\boldsymbol{r}' \boldsymbol{G}_{\mathrm{b}}(\boldsymbol{r}_{l,i},\boldsymbol{r}')\cdot\boldsymbol{\Psi}_\alpha(\boldsymbol{r}')\right], && (3.44) \end{aligned}$$

where we have used the notation $\boldsymbol{G}_{\mathrm{b}}$ for the electric Green's dyadic of the background medium

$$\boldsymbol{G}_{\mathrm{b}}(\boldsymbol{r},\boldsymbol{r}') = \left(\mathbb{I} + \frac{1}{k_b^2}\nabla\nabla\right) G_{\mathrm{b}}(\boldsymbol{r}-\boldsymbol{r}'). \tag{3.45}$$

$\boldsymbol{G}_{\mathrm{b}}(\boldsymbol{r},\boldsymbol{r}')$ can be conveniently computed as

$$\begin{aligned} \boldsymbol{G}_{\mathrm{b}}(\boldsymbol{r},\boldsymbol{r}') &= G_{\mathrm{b}}(\boldsymbol{r}-\boldsymbol{r}')\left[\left(\frac{2j}{k_{\mathrm{b}}R} + \frac{2}{(k_{\mathrm{b}}R)^2}\right)\hat{\boldsymbol{R}}\hat{\boldsymbol{R}} \right. && (3.46)\\ &\quad \left. + \left(1 - \frac{1}{k_{\mathrm{b}}R} - \frac{1}{(k_{\mathrm{b}}R)^2}\right)(\mathbb{I}-\hat{\boldsymbol{R}}\hat{\boldsymbol{R}})\right], && (3.47) \end{aligned}$$

where $R = \|\boldsymbol{r}-\boldsymbol{r}'\|$ and $\hat{\boldsymbol{R}} = (\boldsymbol{r}-\boldsymbol{r}')/R$.

When the scattered field has to be evaluated in a lot of observation points, the MLFMA can be used to do this. It is easy to see that the evaluation of $\boldsymbol{E}^{\mathrm{scat}}(\boldsymbol{r}_{l,i})_a \cdot \hat{\boldsymbol{u}}$, the component along $\hat{\boldsymbol{u}}$ of the scattered field caused by the contrast currents in subdomain D^a, can be obtained with (3.18) if $\boldsymbol{\Psi}_\beta(\boldsymbol{r})$ is replaced by $\delta(\boldsymbol{r}-\boldsymbol{r}_{l,i})\hat{\boldsymbol{u}}$ and the integration domain $\mathcal{D}$ in the left hand side by $\mathbb{R}^3$. The same has to be done in (3.21). To make the process more efficient, the observation points $\boldsymbol{r}_{l,i}$ should also be organized in an FMM-tree and a multilevel scheme should be adopted. This ensures that a minimal number of translations have to be carried out.

Finally, the expression (2.47) for the derivatives of the scattered fields, can be discretized by noting that

$$\begin{aligned} \boldsymbol{E}(\boldsymbol{r}) &= \frac{\boldsymbol{D}(\boldsymbol{r})}{\epsilon(\boldsymbol{r})} && (3.48)\\ &\approx \sum_{\alpha=1}^{N} \frac{d_\alpha}{\epsilon_{\mathrm{b}}}\left[(1-\xi^+_\alpha)\boldsymbol{\Psi}^+_\alpha(\boldsymbol{r}) + (1-\xi^-_\alpha)\boldsymbol{\Psi}^-_\alpha(\boldsymbol{r})\right], && (3.49) \end{aligned}$$

where $\mathbf{\Psi}_\alpha^\pm$ is the half of $\mathbf{\Psi}_\alpha$ on $\mathcal{S}_\alpha^\pm$. Since the forward grid $\mathcal{D}^F$ is a subdivision of the permittivity grid $\mathcal{D}^\epsilon$, the integration with Φ_ν in (2.47) becomes particularly simple and can be done analytically.

3.9 Conclusions

In this chapter the numerical solution of (2.35) has been discussed. To this end, a new hybrid MLFMA-FFT method was presented. The method combines the advantages of the HF MLFMA and the FFT method on volumetric scattering problems which can be meshed using a uniform grid. A flexible subdomain meshing of sparse scatterers was introduced and the symmetry in this mesh was exploited to make some of the more time and memory consuming stages in the HF MLFMA more efficient. Also, a novel approach employing vector spherical harmonics to represent the radiation patterns on the lowest level in combination with an FFT interpolation scheme for the vectorial MLFMA was introduced. It was finally shown that the resulting hybrid method is a valuable supplement to the existing fast methods, because it is more efficient on sparse scattering configurations and it can easily be used as a regular FFT solver on dense problems. Furthermore, when memory is an issue, the method's low storage requirements provide a means to tackle very large problems which would otherwise be out of reach.

Although the MLFMA-FFT method reduces the computational and memory costs of one matrix-vector multiplication in the iterative solution of the forward problem, it is desirable to also keep the number of iterations low. To this end, the hybrid MLFMA-FFT method was supplemented with a marching-on scheme to determine an initial guess for the iterative solution of the MoM-system. This scheme is based on a marching-on-in-source-position strategy, combined with a Distorted Born approximation to allow for a simple (linear) extrapolation over the permittivity.

Bibliography

[1] T.K. Sarkar, E. Sarvas, and S.M. Rao. Application of FFT and the Conjugate Gradient Method for the Solution of Electromagnetic Radiation from Electrically Large and Small Conducting Bodies. *IEEE Trans. Antennas Propagat.*, 34(5):635–640, 1986.

[2] C.C. Su. Electromagnetic Scattering by a Dielectric Body with Arbitrary Inhomogeneity and Anisotropy. *IEEE Trans. Antennas Propagat.*, 37(3):384–389, 1989.

[3] P. Zwamborn and P.M. van den Berg. The Three-Dimensional Weak Form of the Conjugate Gradient FFT Method for Solving Scattering Problems. *IEEE Trans. Microw. Theory Tech.*, 40(9):1757–1766, 1992.

[4] C.C. Su. The Three-Dimensional Algorithm of Solving the Electric Field Integral Equation using Face-Centered Node Points. *IEEE Trans. Microw. Theory Tech.*, 41(6):510–515, 1993.

[5] H. Gan and W.C. Chew. A Discrete BCG-FFT Algorithm for Solving 3D Inhomogeneous Scatterer Problems. *IEEE Trans. Antennas Propagat.*, 9(10):1339–1357, 1995.

[6] R. Coifman, V. Rokhlin, and S. Wandzura. The Fast Multipole Method for the Wave Equation: A Pedestrian Prescription. *IEEE Antennas Propagat. Mag.*, 35:7–12, 1993.

[7] C.C. Lu and W.C. Chew. A Multilevel Algorithm for Solving Boundary Integral Equations of Wave Scattering. *Microw. Opt. Tech. Lett.*, 7(10):466–470, 1994.

[8] J.M. Song, C.C. Lu, and W.C. Chew. Multilevel Fast-Multipole Algorithm for Electromagnetic Scattering by Large Complex Objects. *IEEE Trans. Antennas Propagat.*, 45(10):1488–1493, 1997.

[9] W.C. Chew, J. Jin, and . *Fast and Efficient Algorithms in Computational Electromagnetics*. Artech House, Boston, 2001.

[10] J.S. Zhao, W.C. Chew, and . Three Dimensional Multilevel Fast Multipole Algorithm from Static to Electrodynamic. *Microw. Opt. Tech. Lett.*, 26(1):43–48, 2000.

[11] B. Hu and W.C. Chew. Fast Inhomogeneous Plane Wave Algorithm for Scattering from Objects Above the Multilayered Medium. *IEEE Trans. Geosci. Remote Sens.*, 39(5), 2001.

[12] E. Darve and P. Havé. A Fast Multipole Method for Maxwell Equations Stable at all Frequencies. *Phil. Trans. R. Soc. Lond. A*, 362(1816):603–628, 2004.

[13] M. Frigo and S.G. Johnson. The Design and Implementation of FFTW3. *Proceedings of the IEEE 93*, (2):216–231, 2005.

[14] J. Van Bladel. *Electromagnetic Fields, second edition*. John Wiley & Sons, Inc., New Jersey, 2007.

[15] A.F. Peterson, S.L. Ray, and R. Mittra. *Computational Methods for Electromagnetics*. Wiley-IEEE Press, 1997.

[16] D.H. Schaubert, D.R. Wilton, and A.W. Glisson. A Tetrahedral Modeling Method for Electromagnetic Scattering by Arbitrarily Shaped Inhomogeneous Dielectric Bodies. *IEEE Trans. Antennas Propagat.*, 32(1):77–85, 1984.

[17] D.R. Wilton, S.M. Rao, A.W. Glisson, D.H. Schaubert, O.M. Al-Bundak, and C.M. Butler. Potential Integrals for Uniform and Linear Source Distributions on Polygonal and Polyhedral Domains. *IEEE Trans. Antennas Propagat.*, 32(3):276–281, 1984.

[18] R.D. da Cunha and T. Hopkins. The Parallel Iterative Methods (PIM) Package for the Solution of Systems of Linear Equations on Parallel Computers. *Appl. Num. Math.*, 19(1-2):33–50, 1995.

[19] W.C. Chew, S. Koc, J.M. Song, C.C. Lu, and E. Michielssen. A Succinct Way to Diagonalize the Translation Matrix in Three Dimensions. *Microw. Opt. Tech. Lett.*, 15(3):144–146, 1997.

[20] J. Sarvas. Performing Interpolation and Anterpolation Entirely by Fast Fourier Transform in the 3-D Multilevel Fast Multipole Algorithm. *SIAM J. Num. Anal.*, 41(6):2180–2196, 2003.

[21] O. M. Bucci, C. Gennarelli, and C. Savarese. Optimal Interpolation of Radiated Fields over a Sphere. *IEEE Trans. Antennas Propagat.*, 39(11):1633–1643, 1991.

[22] T.F. Eibert. A Diagonalized Multilevel Fast Multipole Method With Spherical Harmonics Expansion of the k-space integrals. *IEEE Trans. Antennas Propagat.*, 53(2):814–817, 2005.

[23] R.C. Wittman. Spherical Wave Operators and the Translation Formulas. *IEEE Trans. Antennas Propagat.*, 36(8):1078–1087, 1988.

[24] C.L. Lawson, R.J. Hanson, D. Kincaid, and F.T. Krogh. Basic Linear Algebra Subprograms for FORTRAN usage. *ACM Trans. Math. Soft.*, 5:308–323, 1979.

[25] L.S. Blackford, J. Demmel, J. Dongarra, I. Duff, S. Hammarling, G. Henry, M. Heroux, L. Kaufman, A. Lumsdaine, A. Petitet, R. Pozo, K. Remington, and R.C. Whaley. An Updated Set of Basic Linear Algebra Subprograms (BLAS). *ACM Trans. Math. Soft.*, 28(2):131–151, 2002.

[26] A.G. Tijhuis, K. Belkebir, and A.C.S. Litman. Theoretical and Computational Aspects of 2-D Inverse Profiling. *IEEE Trans. Geosci. Remote Sens.*, 39(6):1316–1330, 2001.

[27] A.G. Tijhuis, M.C. van Beurden, and A.P.M. Zwamborn. Iterative Solution of Field Problems with a Varying Physical Parameters. *Turk J Elec Engin*, 10(2), 2002.

[28] A. Franchois and A.G. Tijhuis. A Quasi-Newton Reconstruction Algorithm for a Complex Microwave Imaging Scanner Environment. *Radio Science*, 38(2), 2003.

CHAPTER 4

Newton-based inverse scattering

This chapter presents quantitative reconstruction algorithms for the 3D inverse scattering problem, which belong to the conventional approach (Section 2.3.3). The algorithms in this chapter are based on the Gauss-Newton minimization of a cost function which includes both the least squares data fit cost function and a regularization term. Quasi-Newton optimization using the Broyden-Fletcher-Goldfarb-Shanno (BFGS) update formula is also investigated, but it is concluded that this method is outperformed by the Gauss-Newton method.

Two different regularization strategies are proposed. The first one is a multiplicative smoothing (MS) constraint, which is appropriate when little a priori information is available on the scatterers and on the amount of noise on the data. It is also suited for the reconstruction of strongly inhomogeneous objects, such as the ones encountered in biomedical applications. The second regularization method is the newly developed value picking (VP) regularization, which is very effective for the reconstruction of piecewise (quasi-) homogeneous scatterers, such as man-made objects in industrial or security applications of inverse scattering.

The rest of the chapter is devoted to two important improvements on the basic algorithm: the incorporation of constraints on the permittivity with minimal changes to the algorithm and the use of a subspace preconditioned LSQR algorithm to solve the ill-conditioned Gauss-Newton update systems.

4.1 The basic optimization problem

4.1.1 The least squares cost function

Let $\boldsymbol{e}^{\mathrm{scat}}(\boldsymbol{\varepsilon})$ be the vector that contains the simulated scattered field components $\boldsymbol{E}_i^{\mathrm{scat}}(\boldsymbol{r}_{l,i})\cdot\hat{\boldsymbol{u}}_{l,i}$ (see Section 2.3.1) for all combinations of illuminations ($i = 1, \ldots, N^I$) and measurements ($l = 1, \ldots, N_i^R$) and for a given permittivity vector $\boldsymbol{\varepsilon}$. This vector has dimension $N^D = \sum_{i=1}^{N^I} N_i^R$. Furthermore, let the N^D-dimensional vector $\boldsymbol{e}^{\mathrm{meas}}$ contain the measured data. The least squares data fit cost function then is defined as

$$\mathcal{F}^{LS}(\boldsymbol{\varepsilon}) = \frac{1}{\mathcal{N}^{LS}} \|\boldsymbol{e}^{\mathrm{scat}}(\boldsymbol{\varepsilon}) - \boldsymbol{e}^{\mathrm{meas}}\|^2, \tag{4.1}$$

where $\mathcal{N}^{LS} = \|\boldsymbol{e}^{\mathrm{meas}}\|^2$ is a normalization constant, such that $\mathcal{F}^{LS} = 1$ for $\epsilon_\nu = \epsilon_{\mathrm{b}}/\epsilon_0$, $\forall\nu$. Note that, due to the non-linear relation between the permittivity and the scattered fields, $\mathcal{F}^{LS}$ is not quadratic in $\boldsymbol{\varepsilon}$. Note further that, to evaluate $\mathcal{F}^{LS}$ for a given permittivity vector $\boldsymbol{\varepsilon}$, a multi-view forward problem has to be solved, i.e. one has to solve the domain equation (2.35) for each transmitting dipole. To calculate derivatives of $\mathcal{F}^{LS}$, (2.35) possibly has to be solved for a number of additional excitations by receiving dipoles (see Section 2.3.5).

A straightforward approach to the inverse scattering problem would be to minimize the bare least squares cost function (4.1). Because the number of optimization variables can become large in 3D inverse scattering problems and because the evaluation of the cost function $\mathcal{F}^{LS}$ is computationally expensive, a global minimization approach is not feasible, since it would require too many cost function evaluations. Therefore, we have to resort to a local minimization approach, i.e. a minimization method that relies on local derivatives, although this introduces the risk of getting trapped in local minima in addition to the risk of ending up in the wrong global minimum in case of non-uniqueness.

4.1.2 Newton and Gauss-Newton minimization

Newton's iterative method for local optimization approximates a non-linear cost function with a quadratic model based on the function's first and second order derivatives (the gradient and the Hessian matrix) at the current iterate and chooses the stationary point of this model as the next iterate. It has the attractive fundamental property of super-linear convergence if the initial guess is close enough to the solution [1]. However, when starting further away from the solution, the Newton correction may lead to an increase in the cost function, if at its stationary point the model is no longer a good approximation to the function or if the Hessian matrix is not positive definite (i.e. the quadratic approximation does not have positive curvature and hence no (unique) minimum). Furthermore, for large optimization problems the computation of second order derivatives is usually very expensive. A variety of Newton-type methods that

try to deal with these issues are described in the literature, but in this dissertation we focus on one of these: the Gauss-Newton method with line search.

Let us first give a few definitions. Consider a general cost function $\mathcal{F}(\boldsymbol{\varepsilon})$. This function is a real-valued function of the N^ϵ complex variables $\epsilon_\nu = \epsilon'_\nu - j\epsilon''_\nu$. We define a gradient

$$\boldsymbol{g} = \begin{bmatrix} \frac{\partial \mathcal{F}}{\partial \epsilon_\nu} \\ \frac{\partial \mathcal{F}}{\partial \epsilon^*_\nu} \end{bmatrix} = \begin{bmatrix} \boldsymbol{g}_c \\ \boldsymbol{g}_{cc} \end{bmatrix} \tag{4.2}$$

with $\boldsymbol{g}_c = \boldsymbol{g}^*_{cc}$, because $\mathcal{F}$ is real, and a Hessian matrix

$$\boldsymbol{H} = \begin{bmatrix} \frac{\partial^2 \mathcal{F}}{\partial \epsilon_\nu \partial \epsilon_\upsilon} & \frac{\partial^2 \mathcal{F}}{\partial \epsilon_\nu \partial \epsilon^*_\upsilon} \\ \frac{\partial^2 \mathcal{F}}{\partial \epsilon^*_\nu \partial \epsilon_\upsilon} & \frac{\partial^2 \mathcal{F}}{\partial \epsilon^*_\nu \partial \epsilon^*_\upsilon} \end{bmatrix} \tag{4.3}$$

with derivatives with respect to ϵ_ν and its complex conjugate ϵ^*_ν. These definitions are equivalent with the use of ϵ'_ν and ϵ''_ν as independent variables [2], and lead to simplified notations in the following. For sums of squares the gradient and Hessian matrix take particular forms. For the least-squares data error $\mathcal{F}^{LS}$ the gradient is

$$\boldsymbol{g}^{LS} = \frac{1}{\mathcal{N}^{LS}} \begin{bmatrix} \boldsymbol{J}^T \left[\boldsymbol{e}^{\text{scat}} - \boldsymbol{e}^{\text{meas}}\right]^* \\ \boldsymbol{J}^H \left[\boldsymbol{e}^{\text{scat}} - \boldsymbol{e}^{\text{meas}}\right] \end{bmatrix}, \tag{4.4}$$

where $\boldsymbol{J}$ is the $N^D \times N^\epsilon$ Jacobian matrix containing the first order derivatives of the scattered field components, $J_{d\nu} = \partial e^{\text{scat}}_d / \partial \epsilon_\nu$. The Hessian matrix is

$$\boldsymbol{H}^{LS} = \frac{1}{\mathcal{N}^{LS}} \begin{bmatrix} \boldsymbol{B} & \boldsymbol{J}^T \boldsymbol{J}^* \\ \boldsymbol{J}^H \boldsymbol{J} & \boldsymbol{B}^* \end{bmatrix}, \tag{4.5}$$

where $\boldsymbol{B}$ is a $N^\epsilon \times N^\epsilon$ matrix containing products of second order derivatives of the scattered field with the data residues,

$$B_{\nu\upsilon} = \left(\frac{\partial^2 \boldsymbol{e}^{\text{scat}}}{\partial \epsilon_\nu \partial \epsilon_\upsilon} \right)^T \left[\boldsymbol{e}^{\text{scat}} - \boldsymbol{e}^{\text{meas}}\right]^* \tag{4.6}$$

In a Newton optimization scheme the complex permittivity vector is iteratively updated as

$$\boldsymbol{\varepsilon}_{k+1} = \boldsymbol{\varepsilon}_k + \boldsymbol{s}_k, \tag{4.7}$$

where $\boldsymbol{s}_k$ is the permittivity correction at iterate k, given by

$$\begin{bmatrix} \boldsymbol{s}_k \\ \boldsymbol{s}^*_k \end{bmatrix} = -\boldsymbol{H}_k^{-1} \boldsymbol{g}_k. \tag{4.8}$$

To enlarge the convergence domain, it is better to use this correction as a search direc-

tion along which the next iterate is located as

$$\boldsymbol{\varepsilon}_{k+1} = \boldsymbol{\varepsilon}_k + \beta_k \boldsymbol{s}_k, \tag{4.9}$$

where the positive line parameter β_k is determined with an approximate line search, i.e. β_k is chosen such that $\mathcal{F}(\boldsymbol{\varepsilon}_k + \beta_k \boldsymbol{s}_k)$ is close to a local minimum of $\mathcal{F}$ along the search direction $\boldsymbol{s}_k$. In this work, the line search is performed with the algorithm described in [1]. This algorithm requires that the search direction is a descent direction, i.e.

$$\begin{aligned} \left.\frac{\partial \mathcal{F}}{\partial \beta_k}\right|_{\beta_k=0} &= \left.\sum_{\nu=1}^{N^\epsilon} \left(\frac{\partial \mathcal{F}}{\partial \epsilon_\nu} s_{\nu,k} + \frac{\partial \mathcal{F}}{\partial \epsilon_\nu^*} s_{\nu,k}^* \right) \right|_{\beta_k=0} \\ &= \begin{bmatrix} \boldsymbol{s}_k^T & \boldsymbol{s}_k^H \end{bmatrix} \boldsymbol{g}_k \\ &= 2\Re\left(\boldsymbol{s}_k^T \boldsymbol{g}_{c,k} \right) \\ &< 0 \end{aligned} \tag{4.10}$$

In [1] it is proven that an optimization method that searches successively along different descent paths using the aforementioned approximate line search converges to a (local) minimizer provided that the search directions are uniformly bounded away from orthogonality with the steepest descent direction $-\boldsymbol{g}_k$.

A widely used alternative for the Newton method in case of sums of squares of non-linear functions, such as the data error $\mathcal{F}^{LS}$, is the Gauss-Newton method. It consists of linearizing the function $\boldsymbol{e}^{\mathrm{scat}}$ in (4.1) around the current iterate as

$$\Delta \boldsymbol{e}_k^{\mathrm{scat}} = \boldsymbol{e}^{\mathrm{scat}}\left(\boldsymbol{\varepsilon}_k + \boldsymbol{s}_k\right) - \boldsymbol{e}^{\mathrm{scat}}\left(\boldsymbol{\varepsilon}_k\right) \approx \boldsymbol{J}_k \boldsymbol{s}_k. \tag{4.11}$$

From (4.11), by identifying $\boldsymbol{e}^{\mathrm{scat}}\left(\boldsymbol{\varepsilon}_k + \boldsymbol{s}_k\right) = \boldsymbol{e}^{\mathrm{meas}}$ and by solving the resulting system in the least squares sense, the Gauss-Newton correction for $\mathcal{F}^{LS}$ is given by

$$\boldsymbol{s}_k = -\left(\boldsymbol{J}_k^H \boldsymbol{J}_k \right)^{-1} \boldsymbol{J}_k^H \left[\boldsymbol{e}_k^{\mathrm{scat}} - \boldsymbol{e}^{\mathrm{meas}} \right]. \tag{4.12}$$

Equation (4.12) is obtained as well from the Newton correction (4.8) by neglecting the matrix $\boldsymbol{B}$ in the Hessian matrix (4.5). No second order derivatives of the scattered fields thus are needed. Also, the hermitian matrix $\boldsymbol{J}^H \boldsymbol{J}$ is at least positive semi-definite, hence the update direction (4.12) is never uphill. Indeed, (4.12) is of the form

$$\boldsymbol{s}_k = -\boldsymbol{A}\boldsymbol{g}_{cc,k} = -\boldsymbol{A}\boldsymbol{g}_{c,k}^*, \tag{4.13}$$

which satisfies

$$\boldsymbol{s}_k^T \boldsymbol{g}_{c,k} = -\boldsymbol{g}_{c,k}^H \boldsymbol{A}^T \boldsymbol{g}_{c,k} \leq 0, \tag{4.14}$$

because $\boldsymbol{A}$ is hermitian and positive semi-definite. Therefore the condition (4.10) for a

descent direction is either satisfied or the search direction $\boldsymbol{s}_k$ lies along a level contour of the cost function $\mathcal{F}$.

However, the linearization (4.11) may be too bad an approximation far from the solution, possibly resulting in an increase of the cost function when the update is done with (4.7). Also, the condition number of $\boldsymbol{J}^H\boldsymbol{J}$ typically is large, because the singular value spectrum of $\boldsymbol{J}$ decays rapidly. This is a symptom of the ill-posedness of the inverse scattering problem (see Section 4.1.4). In some cases $\boldsymbol{J}^H\boldsymbol{J}$ is even singular. This situation occurs when the inverse problem is under-determined, i.e. when the dimension N^D of the data vector is smaller than the number of unknowns N^ϵ. Even when $N^D \geq N^\epsilon$, the system can be under-determined with respect to the physically independent data due to redundancy in the data vector caused by reciprocity, i.e. if both $\boldsymbol{E}_i^{\mathrm{scat}}(\boldsymbol{r}_{l,i}) \cdot \hat{\boldsymbol{u}}_{l,i}$ and $\boldsymbol{E}_{l,i}^{\mathrm{scat}}(\boldsymbol{r}_i) \cdot \hat{\boldsymbol{u}}_i$ occur in the data vector. Theoretically, both numbers should be equal and although their measured values are probably different due to noise on the data (or due to modelling errors when the data is simulated), the corresponding rows of the jacobian matrix $\boldsymbol{J}$ are *identical*, as can be seen from (2.47) (by interchanging i and (l,i)). This rank deficiency can prevent convergence, because update-directions can be orthogonal to the steepest descent vector ($\boldsymbol{s}_k^T\boldsymbol{g}_{c,k} = 0$). In [3] the convergence of the Gauss-Newton method was improved with a Levenberg-Marquardt trust-region approach, which ensures a positive definite and better conditioned approximate Hessian matrix and which keeps the step size $\|\boldsymbol{s}_k\|$ sufficiently small. The use of a line search, as in this dissertation, also remedies the problem of a step size which is too large (even if the linearization is no longer valid in $\boldsymbol{\varepsilon}_k + \beta_k\boldsymbol{s}_k$, we know that the cost function will be reduced), but it does not solve the problem of a rank-deficient Hessian matrix. The regularization strategies, proposed in Sections 4.2 and 4.3 will take care of that.

Finally, what is meant by an *iteration* in the rest of the text, is the calculation of an update direction and the execution of a line search along this search direction, regardless of the iterative algorithm that is used.

4.1.3 Quasi-Newton minimization

The quasi-Newton method consists in approximating the Hessian matrix in the Newton correction (4.8) with a matrix that does not involve the explicit computation of second order derivatives. In each iteration this approximated Hessian matrix is updated based on the change in the gradient with respect to the previous iteration. In this thesis we consider the Broyden-Fletcher-Goldfarb-Shanno (BFGS) update formula for the inverse Hessian matrix $\boldsymbol{H}_k^{-1}$,

$$\tilde{\boldsymbol{H}}_{k+1} = \tilde{\boldsymbol{H}}_k + \left(1 + \frac{\boldsymbol{\gamma}_k^T\tilde{\boldsymbol{H}}_k\boldsymbol{\gamma}_k}{\boldsymbol{\delta}_k^T\boldsymbol{\gamma}_k}\right)\frac{\boldsymbol{\delta}_k\boldsymbol{\delta}_k^T}{\boldsymbol{\delta}_k^T\boldsymbol{\gamma}_k} - \left(\frac{\boldsymbol{\delta}_k\boldsymbol{\gamma}_k^T\tilde{\boldsymbol{H}}_k + \tilde{\boldsymbol{H}}_k\boldsymbol{\gamma}_k\boldsymbol{\delta}_k^T}{\boldsymbol{\delta}_k^T\boldsymbol{\gamma}_k}\right), \quad (4.15)$$

where $\boldsymbol{\delta}_k = \boldsymbol{\varepsilon}_{k+1} - \boldsymbol{\varepsilon}_k$, $\boldsymbol{\gamma}_k = \boldsymbol{g}_{k+1} - \boldsymbol{g}_k$ and where $\tilde{\boldsymbol{H}}_k$ is a symmetric matrix for which $\boldsymbol{g}_k^T \tilde{\boldsymbol{H}}_k \boldsymbol{g}_k > 0$, which means that the updates

$$\begin{bmatrix} \boldsymbol{s}_k \\ \boldsymbol{s}_k^* \end{bmatrix} = -\tilde{\boldsymbol{H}}_k \boldsymbol{g}_k \tag{4.16}$$

are descent directions. For the first iteration we choose $\tilde{\boldsymbol{H}}$ equal to the identity matrix. It is expected that after a sufficient number of iterations the matrices $\tilde{\boldsymbol{H}}_k$ become close approximations to $\boldsymbol{H}_k^{-1}$ [1]. Since (4.15) directly approximates the inverse Hessian matrix, only one matrix-vector multiplication is needed to compute the quasi-Newton correction (4.16). This could be an advantage over the Gauss-Newton method, where the solution of a linear system of order N^ϵ (see (4.12)), even if this is done iteratively, can increase the computation time substantially. Unfortunately, we observed a much slower rate of convergence with this BFGS quasi-Newton implementation than with the modified Gauss-Newton implementation. This will be illustrated in Section 4.2.3.

4.1.4 The necessity of regularization

Basically, all problems with the ill-posedness of the inverse scattering problem are related to overfitting. Since electromagnetic fields, measured on any surface outside the source region, essentially have a limited number of degrees of freedom in finite precision [4], the information content of the data vector is always limited and cannot be increased beyond a certain point by adding more illuminations and measurement positions. On the other hand, the requirement of a high resolution in the reconstruction results in a small cell size for the permittivity grid $\mathcal{D}^\epsilon$ and therefore a high number of optimization variables or model parameters. It is clear that increasing the resolution will eventually result in overfitting. On top of this, as already mentioned in Section 2.1, noise on the data results in an extra loss of information, which already leads to overfitting with a smaller number of unknowns. In practice, mainly changes in the permittivity function with high spatial frequencies cannot be well resolved and therefore such fluctuations can grow almost unbounded in the reconstruction. This results in instability and should be remedied by proper regularization.

To illustrate the seriousness of the problem, we consider a 2D permittivity profile in a setting which will be treated more extensively in Chapter 6. The target under study is a circular cylinder parallel to the z-axis with radius $0.5\lambda_\mathrm{b}$ (λ_b is the background wavelength) and permittivity $2\epsilon_0$, which is enclosed in a larger circular cylinder with radius λ_b and permittivity $1.5\epsilon_0$. The background medium is air ($\epsilon_\mathrm{b} = \epsilon_0$). This object is illuminated with 29 line sources parallel to the z-axis, evenly distributed on a circle with radius $3\lambda_\mathrm{b}$ around the target and for each illumination, the TM-field is measured in the same positions. The scattering from such a 2D object can be simulated using a volume integral equation, much like the one used in 3D (see Section 6.1). After simulating the data, Gaussian noise is added to simulate measurement noise. Let us

define the signal-to-noise ratio (SNR) as

$$\mathrm{SNR} = 10 \log_{10} \frac{\|\boldsymbol{e}^{\mathrm{meas}}\|^2}{2N^D \sigma^2} \mathrm{dB}, \tag{4.17}$$

where σ^2 is the variance of the Gaussian white noise, which is calculated as

$$\sigma^2 = \frac{1}{2N^D - 1} \|\boldsymbol{e}^{\mathrm{scat}}(\boldsymbol{\varepsilon}^0) - \boldsymbol{e}^{\mathrm{meas}}\|^2. \tag{4.18}$$

Here, $\boldsymbol{\varepsilon}^0$ is the discrete relative permittivity distribution which, within the applied discretization, yields the closest approximation to the true relative permittivity distribution. We also define the *noise level* T^N as the data fit error obtained for $\boldsymbol{\varepsilon}^0$: $T^N = \mathcal{F}^{LS}(\boldsymbol{\varepsilon}^0)$ (this definition thus encompasses both measurement noise and discretization errors). In the present example the SNR is 20 dB, which corresponds to a noise level $T^N \approx 0.01$ (approximately 10% error on the data). Figures 4.1 and 4.2 show two discretized permittivity profiles. Figure 4.1 shows the ideal profile $\boldsymbol{\varepsilon}^0$ ($\mathcal{F}^{LS} = 0.0104$) and Figure 4.2 shows a profile which deviates significantly from $\boldsymbol{\varepsilon}^0$ but yields an almost identical data fit ($\mathcal{F}^{LS} = 0.0108$). The difference between the two permittivity profiles is a radially symmetric ripple of the form $\sin(a\rho)/\rho$, where ρ is the distance to the origin and a is some constant. It is clear that this perturbation with high spatial frequency goes almost unnoticed in the scattering measurements. In order to exclude such large pixel-to-pixel fluctuations we need regularization.

The purpose of regularization can be formulated as follows. It adds information to compensate for the information that is lost due to noise or just to increase the overall information content. By doing this, it reduces the freedom in the optimization space and prevents overfitting. The overall result of regularization is the choice of (ideally) one profile among the many that fit the data within the uncertainty introduced by the noise. A good regularization then yields a permittivity profile close to $\boldsymbol{\varepsilon}^0$.

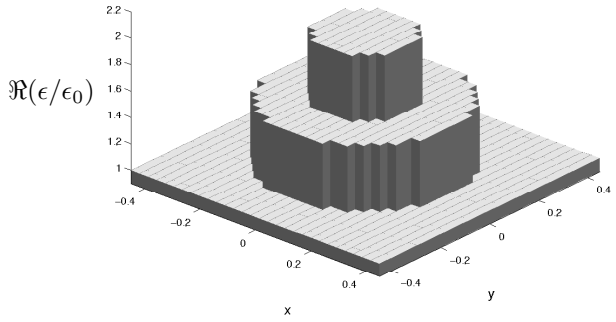

Figure 4.1: A permittivity profile $\boldsymbol{\varepsilon}^0$.

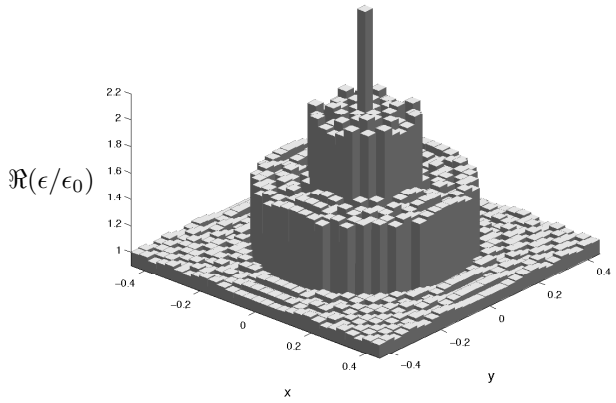

Figure 4.2: A profile that yields the same data fit as the profile of Figure 4.1, but exhibits a perturbation with high spatial frequency.

4.2 Multiplicative smoothing regularization

We proposed the multiplicative smoothing regularization in [5] as a regularization which adapts itself to the amount of noise on the data, without knowledge of the noise level. The idea is related to the work of van den Berg and Abubakar [6–8] on multiplicative regularization for the contrast source inversion method. Habashy and Abubakar also also incorporated a multiplicative regularizer in the Gauss-Newton

framework [9], but not in exactly the same manner as the one presented below.

4.2.1 Modification of the cost function

When using multiplicative smoothing regularization, the solution of the inverse problem is sought by minimizing the cost function

$$\mathcal{F}^S(\boldsymbol{\varepsilon}) = \mathcal{F}^{LS}(\boldsymbol{\varepsilon})\left[1 + \alpha\mathcal{F}^R(\boldsymbol{\varepsilon})\right], \tag{4.19}$$

where $\mathcal{F}^R$ is a smoothing function, given by

$$\begin{aligned}\mathcal{F}^R(\boldsymbol{\varepsilon}) &= \sum_{f=0}^{F}\sum_{g=0}^{G-1}\sum_{h=0}^{H-1}|\epsilon_{f,g,h} - \epsilon_{f-1,g,h}|^2 \\ &+ \sum_{f=0}^{F-1}\sum_{g=0}^{G}\sum_{h=0}^{H-1}|\epsilon_{f,g,h} - \epsilon_{f,g-1,h}|^2 \\ &+ \sum_{f=0}^{F-1}\sum_{g=0}^{G-1}\sum_{h=0}^{H}|\epsilon_{f,g,h} - \epsilon_{f,g,h-1}|^2,\end{aligned} \tag{4.20}$$

which is proportional to a discrete version of the expression

$$\frac{1}{\epsilon_0^2}\int_{\mathcal{D}}|\nabla\epsilon(\boldsymbol{r})|^2\,\mathrm{d}\boldsymbol{r}. \tag{4.21}$$

Whenever the triplet (f, g, h) in (4.20) indicates a cell outside $\mathcal{D}^\epsilon$ (i.e. $f = -1$, $f = F$, $g = -1$, $g = G$, $h = -1$ or $h = H$), the corresponding value of $\epsilon_{f,g,h}$ is equal to some fixed relative permittivity value ϵ^R. The most logical choice in most applications is $\epsilon^R = \epsilon_\mathrm{b}/\epsilon_0$.

The addition of a smoothing term to the least squares data fit cost function as in

$$\mathcal{F}^{LS}(\boldsymbol{\varepsilon}) + \alpha\mathcal{F}^R(\boldsymbol{\varepsilon}), \tag{4.22}$$

has the result that the reconstruction algorithm will favor smooth profiles over non-smooth profiles, much like the extra term $\|\boldsymbol{j}\|^2$ in (2.10) favors current vectors with a small norm. Therefore such a regularization reduces the number of degrees of freedom in the optimization space, since strongly fluctuating permittivity perturbations, which would otherwise distort the reconstruction, are excluded. However, as explained in Section 2.2, the regularization parameter α has to be chosen carefully in (4.22) to provide an optimal trade-off between data fit and smoothness of the permittivity profile. The discrepancy principle, as used in Section 2.2, could be used here as well, in which

case α is determined such that the corresponding minimum ε^α of (4.22) satisfies

$$\mathcal{F}^{LS}(\varepsilon^\alpha) = T^N. \tag{4.23}$$

However, since the inverse scattering problem is non-linear and the solution ε^α has to be determined through an iterative minimization technique, a simple equation as (2.20) is no longer available and the value for α given by the discrepancy principle can only be obtained via a lot of experimentation. Moreover, an estimate of the noise level T^N has to be available for this. Other methods for choosing the regularization parameter exist, such as Generalized cross validation [10–12] and the L-curve criterion [13], which do not assume knowledge of the noise level. However, these methods still use some a posteriori criteria to determine whether a certain choice for the regularization parameter is suitable and hence it is not clear how to avoid repetitive solution of full optimization problems in their application to non-linear inverse problems (see for example [14]), which increases the computation time.

The incorporation of the smoothing function in a multiplicative way as in (4.19), avoids these problems. In (4.19), the weight of the regularization term is proportional to $\mathcal{F}^{LS}$, the effect of which is twofold:

- An adaptive regularization scheme is obtained, where the choice of the positive regularization parameter α is less critical than with additive regularization. With additive regularization, the weight of the regularizing term has to be chosen large enough to provide enough smoothing in the final reconstruction, but small enough to allow for a data fit on the noise level, i.e. $\mathcal{F}^{LS} \approx T^N$, according to the discrepancy principle. With multiplicative smoothing, the probability of overregularization is reduced, because the regularization is relaxed as long as $\mathcal{F}^{LS}$ is reduced during the minimization of (4.19). It has been observed in all our numerical experiments involving inversion of noise-corrupted synthetic data that $\mathcal{F}^{LS}$ is allowed to reach the noise level for choices of α in a wide range of values and that this function is not much further minimized once this happens. The weight of the regularization thus stays practically constant from this point on and if α is chosen rather large, an appropriately smoothed reconstruction is obtained.

- The optimization space is restricted initially to very smooth profiles and gradually increased to allow for more and more detail in the reconstruction. When the optimization is started from a smooth profile (e.g. a domain $\mathcal{D}$ filled with background medium), $\mathcal{F}^R$ has to be increased to obtain less smooth profiles, which restricts the step size in the initial stages of the non-linear iterative minimization when the weight of the regularization is still large. This improves the convergence (the Gauss-Newton linearization becomes more valid).

Note that, in the extreme case of no noise and no discretization errors ($T^N = 0$), the

cost function $\mathcal{F}^S$ can be reduced to zero and in such case the regularization completely vanishes, as required by the discrepancy principle.

4.2.2 Incorporation in the Gauss-Newton framework

To incorporate the multiplicative smoothing regularization in the Gauss-Newton minimization framework, we start again from Newton's method. The gradient and Hessian of the smoothing function $\mathcal{F}^R$ are given by

$$\boldsymbol{g}^{\mathcal{R}} = \begin{bmatrix} \boldsymbol{\Omega} \\ \boldsymbol{\Omega}^* \end{bmatrix}, \tag{4.24}$$

with $\Omega_\nu = \partial \mathcal{F}^R / \partial \epsilon_\nu$ and

$$\boldsymbol{H}^{\mathcal{R}} = \begin{bmatrix} 0 & \boldsymbol{\Sigma} \\ \boldsymbol{\Sigma} & 0 \end{bmatrix}, \tag{4.25}$$

where $\boldsymbol{\Sigma}$ is a real and constant matrix with $\Sigma_{\nu\upsilon} = \partial^2 \mathcal{F}^R / \partial \epsilon_\nu \partial \epsilon_\upsilon^*$. The explicit expressions for the elements of $\boldsymbol{\Omega}$ and $\boldsymbol{\Sigma}$ are

$$\frac{\partial \mathcal{F}^R}{\partial \epsilon_\nu} = \sum_{(f,g,h)\in\mathcal{C}_\nu} \frac{\partial \mathcal{F}^R}{\partial \epsilon_{f,g,h}} \tag{4.26}$$

$$\frac{\partial^2 \mathcal{F}^R}{\partial \epsilon_\nu \partial \epsilon_\upsilon^*} = \sum_{(f,g,h)\in\mathcal{C}_\nu} \sum_{(f',g',h')\in G_\upsilon} \frac{\partial^2 \mathcal{F}^R}{\partial \epsilon_{f,g,h} \partial \epsilon^*_{f',g',h'}} \tag{4.27}$$

with

$$\frac{\mathcal{F}^R}{\partial \epsilon_{f,g,h}} = 6\epsilon^*_{f,g,h} - \sum_{(f',g',h')\in B_{f,g,h}} \epsilon^*_{f',g',h'} \tag{4.28}$$

$$\frac{\partial^2 \mathcal{F}^R}{\partial \epsilon_{f,g,h} \partial \epsilon^*_{f',g',h'}} = \begin{cases} 6 & \text{if } (f,g,h) = (f',g',h'), \\ -1 & \text{if } (f',g',h') \in B_{f,g,h}, \\ 0 & \text{else.} \end{cases} \tag{4.29}$$

$B_{f,g,h}$ in these expressions represents the set of neighboring cells of cell (f,g,h), i.e. the cells that share a face with cell (f,g,h). These also include the virtual neighboring cells just outside $\mathcal{D}^\epsilon$ when (f,g,h) is on the border of $\mathcal{D}^\epsilon$. As mentioned before, the permittivity value for those cells is ϵ^R.

Combined with (4.4) and (4.5), the gradient and Hessian matrix of the regularized cost-function $\mathcal{F}^S$ can be written as

$$\boldsymbol{g}^S = \boldsymbol{g}^{LS}(1 + \alpha \mathcal{F}^R) + \mathcal{F}^{LS} \alpha \boldsymbol{g}^R \tag{4.30}$$

and

$$\boldsymbol{H}^S = \frac{1}{\mathcal{N}^{LS}} \begin{bmatrix} \boldsymbol{B}' & \boldsymbol{A}^* \\ \boldsymbol{A} & \boldsymbol{B}'^* \end{bmatrix}, \tag{4.31}$$

where $\boldsymbol{H}^S$ is a complex symmetric matrix with

$$\begin{aligned} \boldsymbol{B}' &= \boldsymbol{B}(1+\alpha\mathcal{F}^R) + \alpha\boldsymbol{J}^T \left[\boldsymbol{e}^{\text{scat}} - \boldsymbol{e}^{\text{meas}}\right]^* \boldsymbol{\Omega}^T \\ &\quad +\alpha\boldsymbol{\Omega} \left[\boldsymbol{e}^{\text{scat}} - \boldsymbol{e}^{\text{meas}}\right]^H \boldsymbol{J}, \qquad (4.32) \\ \boldsymbol{A} &= \boldsymbol{J}^H\boldsymbol{J}(1+\alpha\mathcal{F}^R) + \alpha\boldsymbol{J}^H \left[\boldsymbol{e}^{\text{scat}} - \boldsymbol{e}^{\text{meas}}\right] \boldsymbol{\Omega}^T \\ &\quad +\alpha\boldsymbol{\Omega}^* \left[\boldsymbol{e}^{\text{scat}} - \boldsymbol{e}^{\text{meas}}\right]^H \boldsymbol{J} + \alpha\mathcal{N}^{LS}\mathcal{F}^{LS}\boldsymbol{\Sigma}. \qquad (4.33) \end{aligned}$$

Applying the Newton formula (4.8) to $\mathcal{F}^S$ yields (the index k is omitted in the following)

$$\boldsymbol{A}\boldsymbol{s} + \boldsymbol{B}'^*\boldsymbol{s}^* = -\boldsymbol{J}^H \left[\boldsymbol{e}^{\text{scat}} - \boldsymbol{e}^{\text{meas}}\right](1+\alpha\mathcal{F}^R) - \alpha\mathcal{N}^{LS}\mathcal{F}^{LS}\boldsymbol{\Omega}^*. \tag{4.34}$$

Using (4.32) and (4.33) and introducing the linearization (4.11), we obtain for the left hand side of (4.34)

$$\begin{aligned} \boldsymbol{A}\boldsymbol{s} + \boldsymbol{B}'^*\boldsymbol{s}^* &= \boldsymbol{J}^H\boldsymbol{J}(1+\alpha\mathcal{F}^R)\boldsymbol{s} + \alpha\boldsymbol{J}^H \left[\boldsymbol{e}^{\text{scat}} - \boldsymbol{e}^{\text{meas}}\right] \left[\boldsymbol{\Omega}^T\boldsymbol{s} + \boldsymbol{\Omega}^H\boldsymbol{s}^*\right] \\ &+ \alpha\boldsymbol{\Omega}^* \left\{ \left[\boldsymbol{e}^{\text{scat}} - \boldsymbol{e}^{\text{meas}}\right]^H \Delta\boldsymbol{e}^{\text{scat}} + \left[\boldsymbol{e}^{\text{scat}} - \boldsymbol{e}^{\text{meas}}\right]^T \Delta\boldsymbol{e}^{\text{scat}*} \right\} \\ &+ \alpha\mathcal{N}^{LS}\mathcal{F}^{LS}\boldsymbol{\Sigma}\boldsymbol{s}. \qquad (4.35) \end{aligned}$$

The optimization is usually started from a constant initial permittivity ϵ^R, i.e. $\epsilon_{f,g,h} = \epsilon^R \; \forall f,g,h$. This permittivity vector is the minimizer of $\mathcal{F}^R$ and yields zero for $\boldsymbol{\Omega}$. Consequently, the second and third terms in the right hand side of (4.35) are zero in the first iteration (and may remain small in a few subsequent iterations). The data residu $\Delta\boldsymbol{e}^{\text{meas}} = [\boldsymbol{e}^{\text{meas}} - \boldsymbol{e}^{\text{scat}}]$ eventually becomes small due to the minimization, such that all terms except the first one in the right hand side of (4.35) become negligible. Given this behavior at the beginning and end of the optimization, we choose to keep only the first and the last terms. The modified Gauss-Newton correction thus is a solution of the linear system

$$\left(\boldsymbol{J}^H\boldsymbol{J} + \lambda^2\boldsymbol{\Sigma}\right)\boldsymbol{s} = -\left(\boldsymbol{J}^H \left[\boldsymbol{e}^{\text{scat}} - \boldsymbol{e}^{\text{meas}}\right] + \lambda^2\boldsymbol{\Omega}^*\right), \tag{4.36}$$

with $\lambda^2 = \alpha\mathcal{N}^{LS}\mathcal{F}^{LS}/(1+\alpha\mathcal{F}^R)$.

The matrix $\boldsymbol{J}^H\boldsymbol{J} + \lambda^2\boldsymbol{\Sigma}$ in (4.36) is always positive definite for $\lambda^2 \neq 0$, since $\boldsymbol{\Sigma}$ can be proven to be strictly positive definite, and the right hand side of (4.36) is proportional to $-\left(\boldsymbol{g}_c^S\right)^*$. The presence of $\lambda^2\boldsymbol{\Sigma}$ thus ensures a strict descent direction. Therefore, the algorithm will converge towards a minimum of the regularized cost function, whether the approximations that led to (4.36) were good approximations or

not.

Some additional insight in the effect of the regularization can be obtained by observing that the update (4.36) is the solution to the following regularized linear least squares problem:

$$\min_{\boldsymbol{s}} \quad \|\boldsymbol{J}\boldsymbol{s} - \Delta\boldsymbol{e}^{\text{meas}}\|^2 + \lambda^2\|\boldsymbol{L}^T\boldsymbol{s} + \boldsymbol{L}^{-1}\boldsymbol{\Omega}^*\|^2, \tag{4.37}$$

where $\boldsymbol{L}$ is the Cholesky factor of $\boldsymbol{\Sigma} = \boldsymbol{L}\boldsymbol{L}^T$. The second term in (4.37) can be interpreted as a generalized Tikhonov regularization term [15] (see Section 2.2). It is minimized when $\boldsymbol{\Sigma}\boldsymbol{s} = -\boldsymbol{\Omega}^*(\boldsymbol{\varepsilon})$, hence also when $\boldsymbol{\Omega}^*(\boldsymbol{\varepsilon} + \boldsymbol{s}) = 0$, since $\boldsymbol{\Sigma}\boldsymbol{s} = \boldsymbol{\Omega}^*(\boldsymbol{\varepsilon} + \boldsymbol{s}) - \boldsymbol{\Omega}^*(\boldsymbol{\varepsilon})$ ($\mathcal{F}^R$ is a quadratic function). This term thus tries to minimize $\mathcal{F}^R$, or fluctuations in the permittivity $\boldsymbol{\varepsilon}$, which seems to be more appropriate than smoothing the correction $\boldsymbol{s}$, as was done by several authors with regular Tikhonov regularization, e.g. [3, 16, 17]. The regularization parameter λ^2 in (4.37) is proportional to the data error $\mathcal{F}^{LS}$ — see [17] for a similar strategy in case of regular Tikhonov regularization — hence the regularization term has a larger influence in the beginning of the minimization.

4.2.3 Examples

In this section some early 3D reconstructions from simulated and measured data are shown, which were presented in [5]. In Chapter 5, some more realistic and more challenging reconstructions will be presented.

Reconstruction of a heterogeneous lossy dielectric cube

We consider a lossless dielectric cube in air, hence $\epsilon_{\text{b}} = \epsilon_0$, at a frequency $f = 47,7$ MHz ($\lambda_0 = 2\pi$ m). It has side $0.6\lambda_0$ (3.77 m) and permittivity $\epsilon = 1.5\epsilon_0$ and contains a smaller, lossy cube with side $0.3\lambda_0$ (1.89 m) and permittivity $\epsilon = (2-2j)\epsilon_0$. The origin of the reference system coincides with the center of the larger cube and the center of the smaller cube has coordinates ($-0.05\lambda_0$, $-0.05\lambda_0$, $-0.05\lambda_0$) or (-0.31 m, -0.31 m, -0.31 m). For the inversion domain $\mathcal{D}$ we choose a cube with side λ_0 (6.28 m), that is centered on the origin. Figure 4.3 shows the relative complex permittivity in three orthogonal slices through $\mathcal{D}$. We perform reconstructions for two dipole configurations: one yielding many and one yielding few data. In the first, "many data", configuration, shown in Figure 4.4 (a), there are 12 dipole positions regularly spaced on each of 6 meridional circles with radii $R = 2\lambda_0$ (12.57 m). In each position, a transmitter is oriented along two polarizations, the θ- and φ-polarizations, and for each illumination the scattered field is measured along these two polarizations on receivers in all positions. In the second, "few data", configuration, shown in Figure 4.4 (b), only 3 meridional circles and only the θ-polarization are used. This results in $N_1^D = 20736$ data for the first and $N_2^D = 1296$ data for the second configuration.

In this paragraph, these data are simulated using the same forward solver as the one employed in the reconstruction algorithm, and the discretization grids for the inverse and forward problems coincide. This allows us to test the convergence behavior in ideal conditions. We choose $F = G = H = 10$, and consider the permittivity in each cell as an unknown, hence the number of reconstruction variables is $N^\epsilon = 1000$ and the number of field-unknowns in the forward problem is $N = 3300$. With the "few data" configuration the number of data thus is barely larger than the number of unknowns, $N_2^D \approx N^\epsilon$. Moreover, there is some redundancy in the data due to reciprocity, so the "few data" configuration is actually under-determined. The "many data" configuration is well over-determined, $N_1^D \gg N^\epsilon$. For all reconstructions in this paragraph, the regularization parameter is $\alpha = 10^{-4}$ and the initial guess is air ($\epsilon^R = 1$).

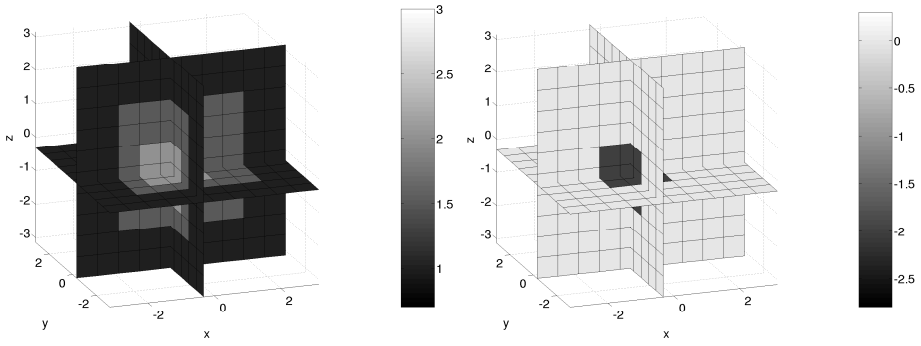

(a) Real part

(b) Imaginary part

Figure 4.3: The exact relative permittivity along orthogonal cross-sections of the heterogeneous lossy dielectric cube.

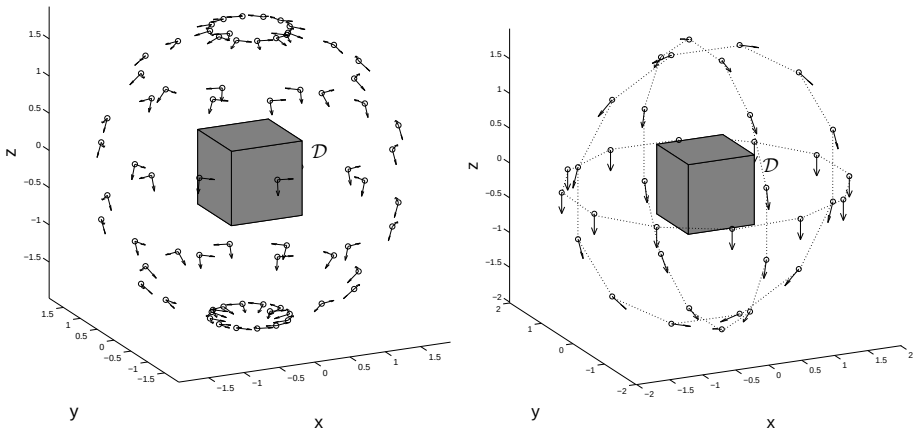

(a) Configuration 1 (b) Configuration 2

Figure 4.4: The dipole configurations for the heterogeneous lossy dielectric cube.

Figure 4.5 shows the root mean square relative reconstruction error $\Delta\epsilon^{RMS}$, defined as

$$\Delta\epsilon^{RMS} = \sqrt{\frac{1}{N^{\epsilon}} \sum_{\nu=1}^{N^{\epsilon}} \frac{|\epsilon_{\nu} - \epsilon_{\nu}^{0}|^2}{|\epsilon_{\nu}^{0}|^2}}, \tag{4.38}$$

and the regularized cost function $\mathcal{F}^S$ as a function of the number of iterations. Let us first discuss the reconstructions from noise-free data. The threshold for the forward iterative solver BICGSTAB is set to a relative accuracy of 10^{-6}, both for the computation of the simulated data and for the reconstructions. The reconstruction iterations are stopped when the cost function is very small, $\mathcal{F}^S \leq 10^{-8}$. It can be seen on Figure 4.5(b) that the cost function rapidly decreases when applying the modified Gauss-Newton method, for both the "many data" (plain line) and "few data" (dashed line) configurations . However, Figure 4.5(a) shows that the reconstruction error decreases more slowly for the "few data" configuration. After as few as 11 iterations, the "many data" configuration yields an almost exact reconstruction ($\Delta\epsilon^{RMS} < 0.01$) of both the real and imaginary parts of the complex permittivity. This is illustrated with images along the three orthogonal slices in Figures 4.6(a)-(b). With the "few data" configuration the images and profile show small artifacts, see Figures 4.6(c)-(d) and the profiles along the x-axis in Figure 4.7, respectively.

Let us now consider data with 30dB additive Gaussian noise, which corresponds to a realistic SNR. The threshold for the forward iterative solver BICGSTAB is now increased to 10^{-3}, since it would be a waste of effort to solve the forward problem to an accuracy far beyond the noise level. With the modified Gauss-Newton method, the reconstruction error $\Delta\epsilon^{RMS}$ decreases and then starts to increase again at a cer-

tain point, as shown by the plain and dashed curves with crosses in Figure 4.5. This happens when the data error (or least-squares cost function) reaches the noise level, i.e. $\mathcal{F}^{LS} \approx 10^{-3}$. The regularized cost function $\mathcal{F}^S$ hardly decreases from this point on and the tiny reductions are accompanied by an increase in the regularizing function $\mathcal{F}^R$. This behavior is often called "semi-convergence". In the presence of noise on the data, we thus conclude that the stopping criterium should be based on the least squares cost function and the noise level or on the loss of convergence when considering the regularized cost function, since this allows for the detection of the semi-convergence point during the reconstruction. In the examples presented here, the reconstructions thus are achieved after 3 iterations only. From the images and profile in Figures 4.6(e)-(h) and Figure 4.7, respectively, it appears that the noise does degrade the reconstructions, but the boundaries of the outer and inner cubes are still well reconstructed and valuable quantitative information on both the real and imaginary parts of the complex permittivity can still be retrieved. Note again that in Figure 4.5 the cost functions of both dipole configurations coincide, and that the reconstruction error behaves better for the "many data" than for the "few data" configuration.

Figure 4.5 also shows a result obtained with the BFGS quasi-Newton algorithm, applied to the regularized cost function $\mathcal{F}^S$, for exact data and the "few data" configuration. The algorithm converges very slowly in comparison with the modified Gauss-Newton method: after 100 iterations the reconstruction error is still 10% and the cost function is reduced to 10^{-4} only. Such behavior was noticed in all our inversions with the BFGS-method, as well as in earlier 2D work [18]. The advantage of not having to solve a linear system to obtain an update direction thus is completely annihilated by the large number of iterations required to converge to the desired accuracy.

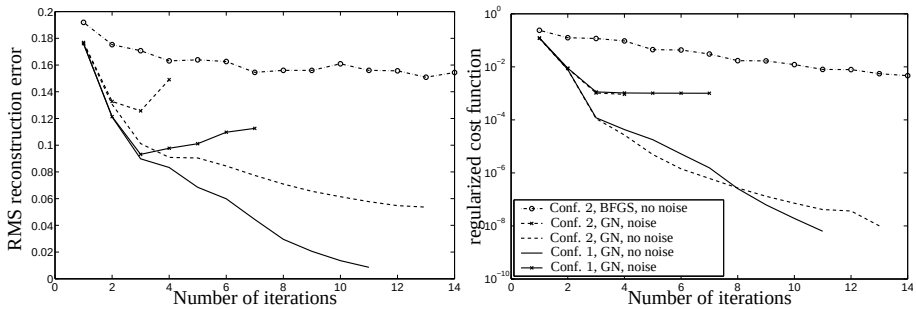

Figure 4.5: The RMS relative reconstruction error (a) and the regularized cost function (b) versus the number of iterations for the reconstructions of the heterogeneous lossy dielectric cube, for the "many data" (Conf. 1) and "few data" (Conf. 2) dipole configurations, with the modified Gauss-Newton (GN) and the BFGS quasi-Newton (BFGS) methods using exact or noisy (SNR = 30 dB) data.

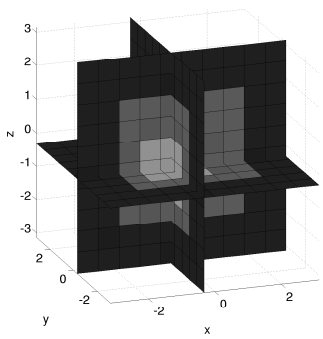

(a) Conf. 1, GN, no noise, real part

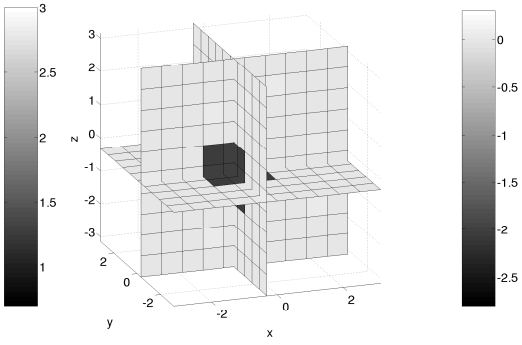

(b) Conf. 1, GN, no noise, imaginary part

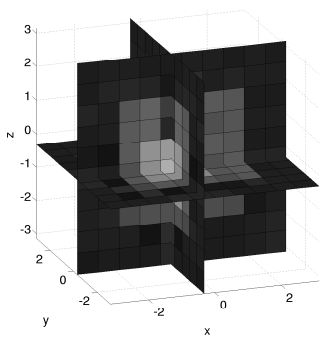

(c) Conf. 2, GN, no noise, real part

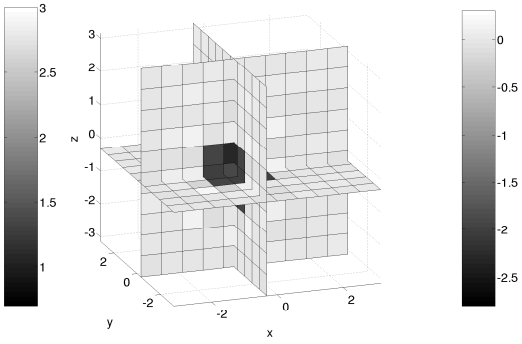

(d) Conf. 2, GN, no noise, imaginary part

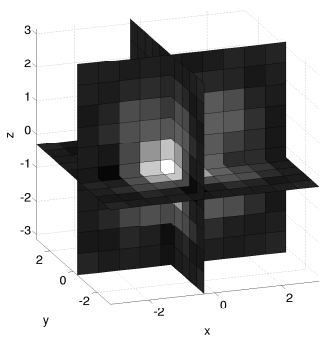

(e) Conf. 1, GN, noise, real part

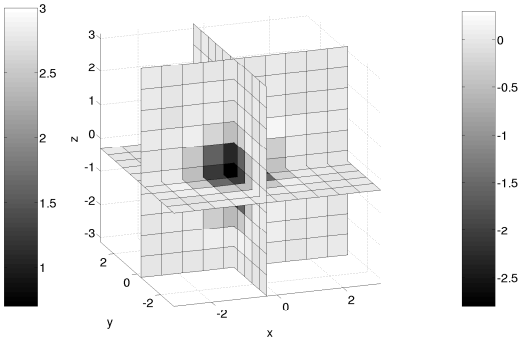

(f) Conf. 1, GN, noise, imaginary part

Figure 4.6: Reconstructed relative permittivity corresponding to the curves in Figure 4.5.

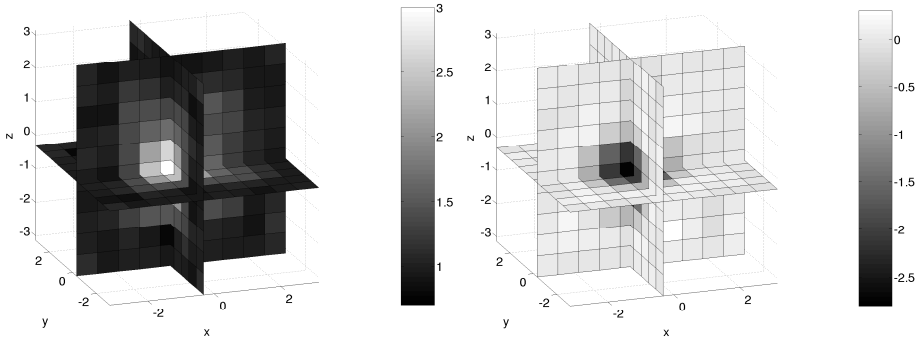

(h) Conf. 2, GN, noise, real part

(i) Conf. 2, GN, noise, imaginary part

Figure 4.6: Reconstructed relative permittivity corresponding to the curves in Figure 4.5, continued.

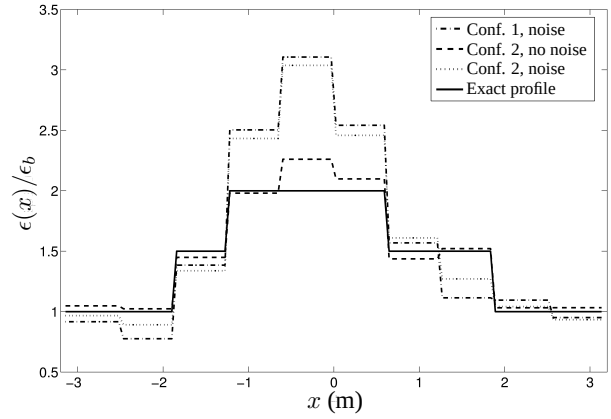

(a) Real part

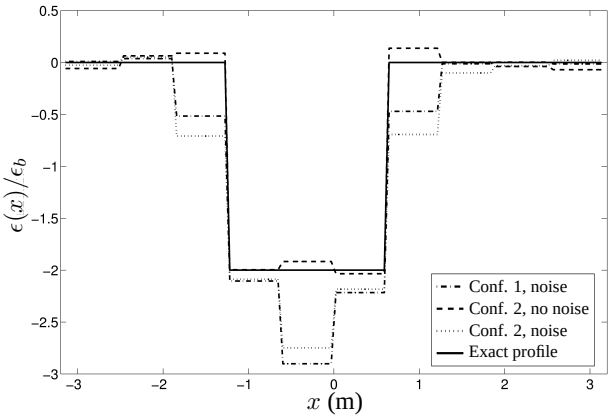

(b) Imaginary part

Figure 4.7: Profiles of the relative permittivity along the x-axis for the reconstructions of Figure 4.6.

Reconstruction of a homogeneous dielectric sphere

We now consider a lossless homogeneous dielectric sphere in air with a radius $0.25\lambda_0$ or 1.57 m (again $f = 47,7$ MHz) and permittivity $\epsilon = 2\epsilon_0$. The origin of the reference system and the center of the sphere coincide. For the inversion domain $\mathcal{D}$ we again choose a cube with side λ_0 (6.28 m), that is centered on the origin. A dipole configuration identical to the "many data" configuration 1 from the previous paragraph is used, except that the radius of the meridional circles now is divided by a

factor 2, $R = \lambda_0$ (6.28 m). The total number of scattered field data thus is again $N^D = 20736$. These data are now simulated using the full-vectorial analytic MIE solution, thus avoiding "inverse crime" [1]. We choose again the same discretization grids for the forward and inverse problems with $F = G = H = 20$, hence the number of reconstruction variables is $N^\epsilon = 8000$ and the number of field-unknowns in the forward problem is $N = 25200$. This discretization is actually too fine in terms of the wavelength, as $\delta = \frac{\lambda}{10}$ usually is recommended for a forward solution, but we did so to reduce the discretization noise introduced by the spherical boundary. This discretization noise was estimated by comparing the analytic and discretized scattered field solutions, yielding a SNR of 27dB. The threshold for the forward iterative solver BICGSTAB is set to 10^{-3} and the stopping criterion for the modified Gauss-Newton optimization is chosen as $\mathcal{F}^{LS} \leq 2 \cdot 10^{-3}$. The regularization parameter again is $\alpha = 10^{-4}$ and the initial guess is air.

Figure 4.8 shows the reconstructed images along the orthogonal cross sections, obtained after as few as 3 iterations, comprising a total of 6 multi-view forward problem solutions, including the line-search iterations. The shape, dimensions and real part of the permittivity are well reconstructed and the imaginary part of the permittivity is small, as expected. This also appears from the profiles along the x-axis in Figure 4.9.

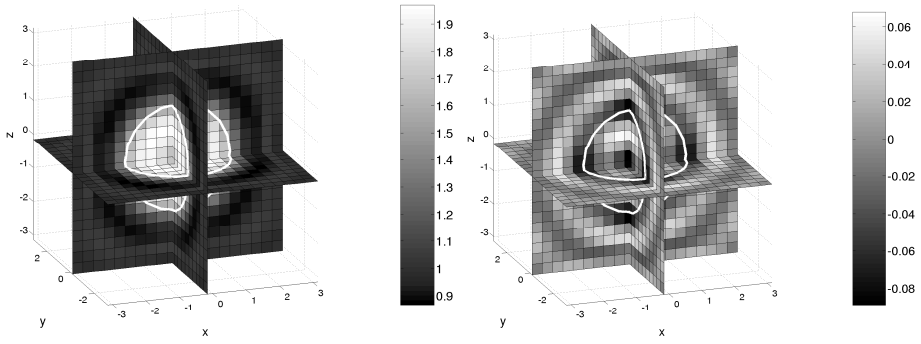

(a) Real part (b) Imaginary part

Figure 4.8: Reconstructed relative permittivity after 3 iterations of a homogeneous dielectric sphere ($\epsilon = 2\epsilon_0$) with radius $0.25\lambda_b$ from analytic data. The white contour shows the boundaries of the actual sphere.

[1] The term "inverse crime" is used to describe a numerical inversion experiment where the data is generated with the same forward model (same formulation, same discretization, etc.) as is used in the inversion algorithm. Such an experiment might not reveal systematic errors in de forward model.

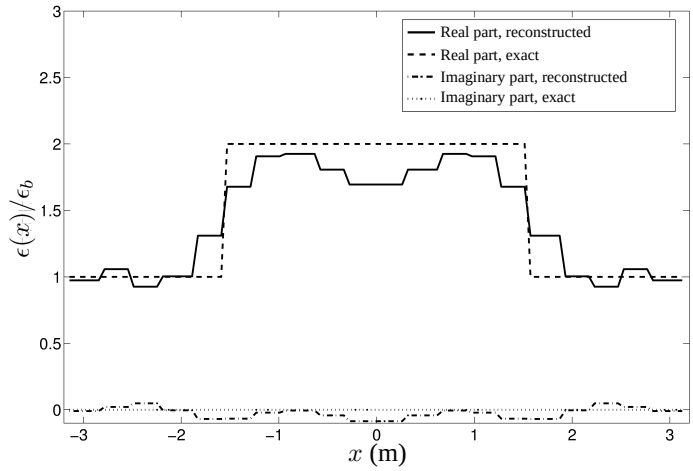

Figure 4.9: Profiles of the relative permittivity along the x-axis for the reconstruction of Figure 4.8.

A homogeneous cube: reconstructions from experimental data

We now present reconstruction results from experimental data for a homogeneous polyethylene cube with permittivity $\epsilon = 2.4\epsilon_0$ and side 8 cm, surrounded with air. The scattered fields were measured in the bi-static polarimetric free-space measurement facility of Institut Fresnel, Marseille, France, as part of a first measurement campaign conducted on 3D objects, after the successful completion of an experimental database for quasi-2D objects [19]. We refer the reader to [20] for a detailed description of the Fresnel measurement set-up. In this section, the available data are limited to measurements of the z-component of the scattered field along an arc of a circle in the xy-plane with radius $R = 167$ cm and centered on the center of the cube. The z-polarized transmitting antenna also moves on this circle. Figure 4.10 (a) shows the 5 transmitter positions, at angles $\varphi_{\mathrm{T},k} = k\pi/8$ for $k \in \{-2, -1, 0, 1, 2\}$ and Figure 4.10 (b) shows the receiving arc for a transmitter at $\varphi_{\mathrm{T},0}$. For a transmitter at $\varphi_{\mathrm{T},k}$, the receiver positions range from $\varphi_{\mathrm{T},k} + \pi/3$ to $\varphi_{\mathrm{T},k} + 4\pi/3$ in steps of 1 degree, or $\Delta\varphi_{\mathrm{R}} = \pi/180$.

In earlier work [21] we found a good agreement between these measured data and simulations obtained with a 3D-BICGSTAB-FFT solver for different frequencies. The transmitter was modeled as an elementary dipole and a calibration factor for each frequency was derived from the comparison of the simulated and measured incident fields in one point, i.e. in the receiver position $\varphi_{\mathrm{R}} = \pi$ opposite to the transmitter position $\varphi_{\mathrm{T}} = 0$. Also, a SNR ≈ 30 dB at 2 GHz and SNR ≈ 23 dB at 4 GHz was determined by comparing the calibrated measured and simulated scattered fields.

The limited data on a circle in one plane as described above are not sufficient for a successful 3D inversion. However, since we know that the scatterer is a cube,

we have exploited symmetries to extend the measurements by rotation with respect to the origin to two additional circles in the xz- and yz-planes, and for each of the circles to extend the illuminations to 16 transmitter positions with $\Delta\varphi_{\mathrm{T}} = \pi/8$. Of course the polarization of the dipoles is rotated together with the circles. Also, for every transmitter position, we use only 43 receiver positions, with $\Delta\varphi_{\mathrm{R}} = \pi/32$. The resulting antenna configuration is shown in Figure 4.11, where $N^I = 48$ and $N_i^I = 43, \forall i$.

The inversion domain $\mathcal{D}$ is a cube with side 15 cm and it is discretized into cells with side 1 cm, hence $F = G = H = 15$. The number of reconstruction variables thus is $N^\epsilon = 3375$. Since the number of data is only $N^D = 2064$, the problem is under-determined. Therefore data at two different frequencies, at 2 GHz and 4 GHz, are used. At 2 GHz the grid for the forward problem coincides with the permittivity grid, resulting in $N = 10800$ field unknowns, but at 4 GHz the grid for the forward problem is twice as fine, with $\delta = 0.5$ cm. This gives $N = 83700$ field unknowns. The threshold of the BICGSTAB iterative solver for the forward problem is set to 10^{-3}. The initial estimate is again air.

At 2 GHz the algorithm, now with $\alpha = 10^{-5}$, needed 3 iterations to reach the stopping criterion $\mathcal{F}^{LS} \leq 10^{-3}$. At this point the reconstruction error was $\Delta\epsilon^{RMS} = 0.19$ and further iterations yielded no improvements. Images along the orthogonal cross sections of the reconstructions at 2 GHz are given in Figure 4.12. The total execution time was about 10 minutes and a total of 6 multiview forward problems was solved. Next, this result was used as an initial estimate for a subsequent reconstruction at 4 GHz (Figure 4.13), which took only 1 iteration to reach a reconstruction error of $\Delta\epsilon^{RMS} = 0.17$ and the stopping criterion $\mathcal{F}^{LS} \leq 5 \cdot 10^{-3}$, which again proved to be sufficient since further iterations did not reduce $\Delta\epsilon^{RMS}$. This time, because of the greater number of field unknowns, the execution time was much longer: about 1 hour and 50 minutes for three multiview forward problems. Figure 4.14 shows the relative permittivity profiles along the x-axis and Figure 4.15 displays the evolution of the reconstruction error along the complete reconstruction. Although only limited experimental data is used in this example, the modified Gauss-Newton method yields an encouraging result.

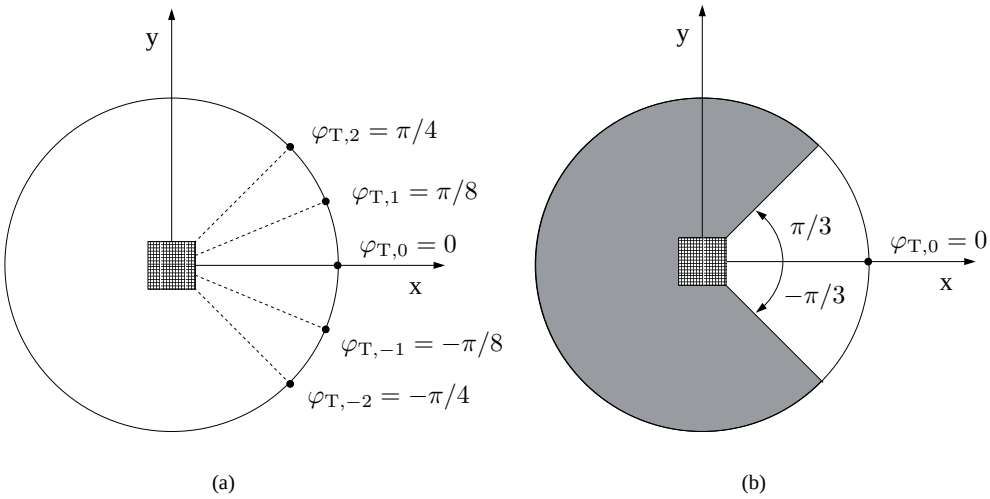

Figure 4.10: Source positions (a) and range of receiver positions in grey for the source at $\varphi = 0$ (b) used to collect the experimental data.

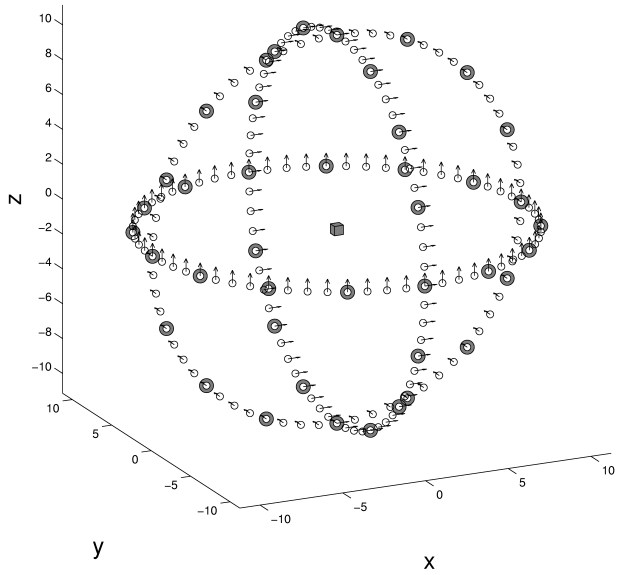

Figure 4.11: Antenna configuration used for the inversion from experimental data. The encircled antennas act as both emitter and receiver.

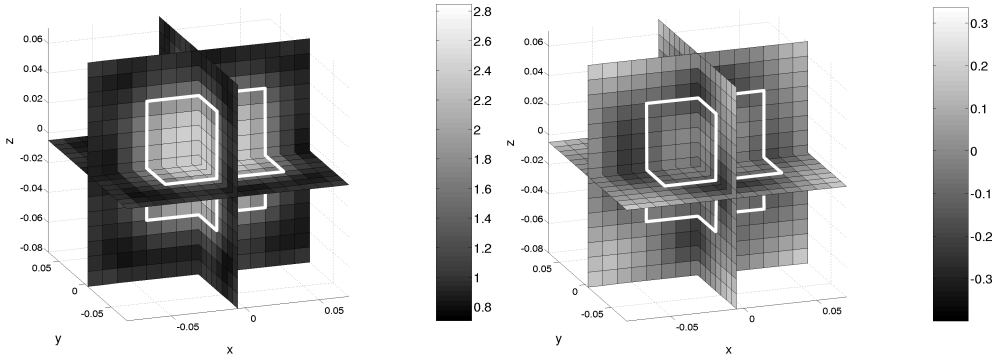

(a) Real part (b) Imaginary part

Figure 4.12: Reconstructed relative permittivity of a polyethylene cube ($\epsilon = 2.4\epsilon_0$) with side 8 cm from experimental data at 2 GHz, after 3 iterations with $\alpha = 10^{-5}$. The white contour shows the boundaries of the actual polyethylene cube.

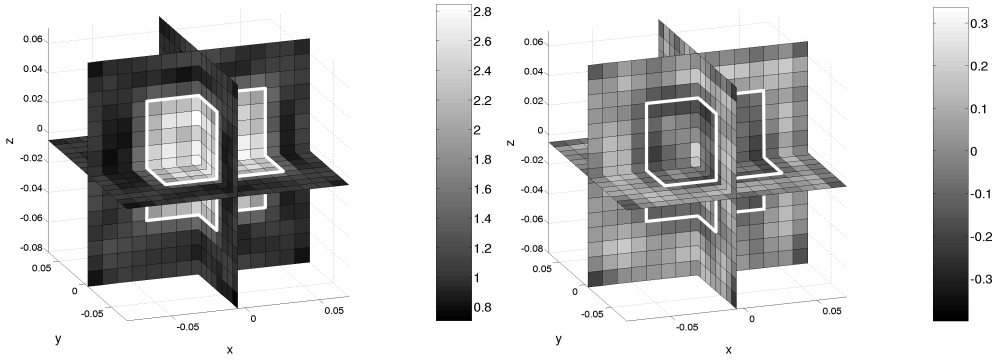

(a) Real part (b) Imaginary part

Figure 4.13: Reconstructed relative permittivity, starting from the result of Figure 4.12, after 1 iteration at 4 GHz and with $\alpha = 10^{-5}$. The white contour shows the boundaries of the actual polyethylene cube.

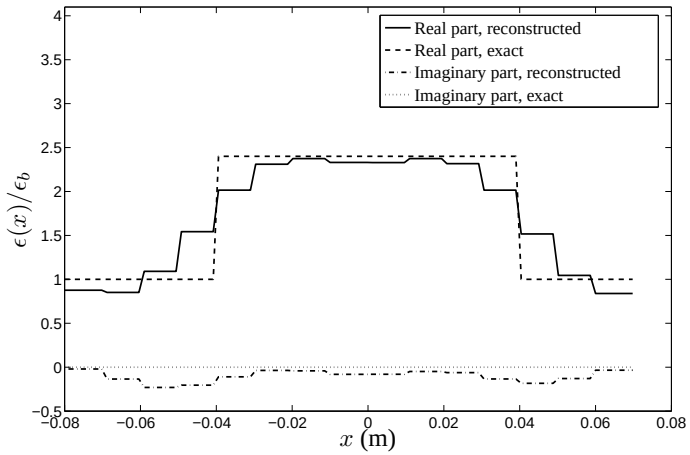

(a)

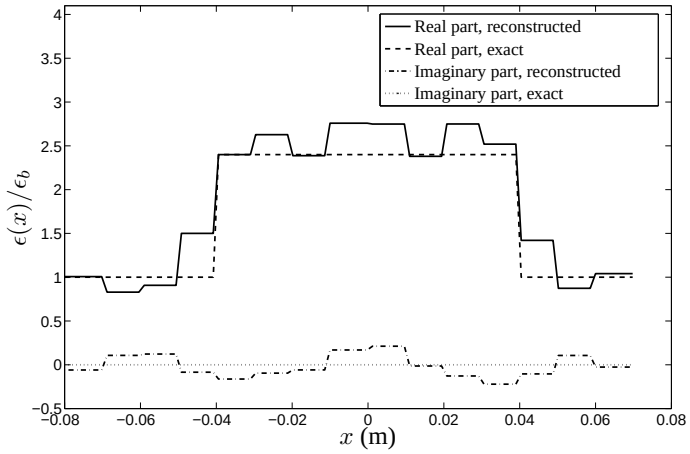

(b)

Figure 4.14: Profiles of the relative permittivity along the x-axis for the reconstructions of a homogeneous dielectric cube from experimental data, at 2 GHz (a) and 4 GHz (b).

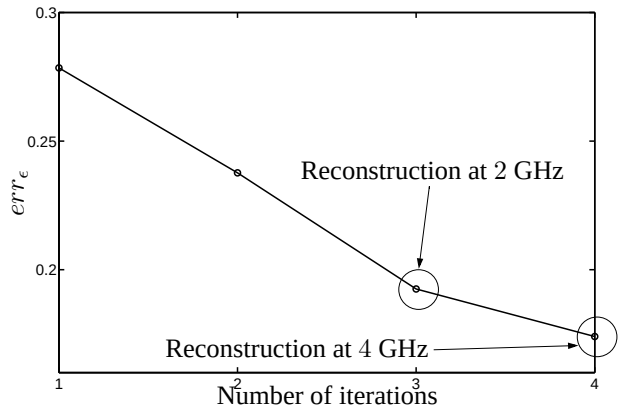

Figure 4.15: Evolution of the reconstruction error for the inversion, corresponding to Figures 4.12 and 4.13.

4.3 Value picking regularization

The multiplicative regularization strategy of the previous section reduces the freedom in the optimization space, but it does so by keeping the reconstruction smooth, which is not very suitable for piecewise homogeneous permittivity profiles such as the ones presented above, since the sharp interfaces in such profiles are smoothed away. The level of smoothness depends on the noise level – lower noise levels allow for less smooth profiles – but for realistic noise levels, the reconstructions, by their smoothness, deviate relatively much from the actual permittivity profile.

Regularization methods that allow edges in the reconstruction while still mitigating unwanted fluctuations in homogeneous regions have been developed for image processing and can be applied to the electromagnetic inverse scattering problem as well. Total variation (TV) regularization [6, 7, 22, 23] is one example. It satisfies a set of unifying criteria, proposed by Charbonnier et al. [24], which determine whether a regularization function is edge preserving. Such edge preserving regularization methods are closely related to Markov Random field approaches [25] and have been used in microwave imaging [26,27]. Also methods based on level set techniques are used in inverse scattering [28, 29]. Both approaches effectively allow for piecewise constant reconstructions, but achieve this in different ways. Edge preserving regularization, for example, penalizes pixel-to-pixel differences unless they are large enough, in which case it is assumed that they correspond to edges in the profile. There is no distinct threshold below which differences are smoothed out and above which they are allowed to exist, but rather there is a transitional region which is encoded in potential functions. Level set techniques on the other hand implicitly only optimize for permittivity profiles that consist of regions of constant permittivity and therefore naturally

allow for edges in the profile. Both methods have been used with success, but some possible disadvantages may be noted. On the one hand, the definition of the potential functions in edge preserving regularization generally implies the choice of some free parameter which tunes the aforementioned transitional region, such as δ in the TV scheme of [6], β in [23], δ in [24] and δ_R and δ_I in [27]. On the other hand, it appears to us that the use of level set methods in situations with more than two different permittivities is somewhat complicated.

In this dissertation, we propose a new regularization scheme, that we call Value Picking (VP) regularization. It combines simplicity of implementation with an ability to reconstruct piecewise constant, or approximately piecewise constant permittivity profiles. Moreover, there is no need to determine additional parameters apart from the regularization parameter. The idea is to provide a limited number of reference permittivity values, the VP values, from which the regularization has to pick one for each permittivity unknown in the inverse problem. The choice for particular VP values is made through the minimization of a choice function for every permittivity unknown, constrained by the simultaneous minimization of a classical least squares data fit cost function. This basic idea also has been explored in [30–32] for binary objects [30, 31] or for one extra permittivity value [32]. However, the choice function in this dissertation is different from the one used in those previous works, there is no limitation on the number of permittivity values and we do not assume the VP values to be known in advance. Rather, they act as auxiliary variables which are also optimized for. Even the number of VP values is updated in the course of the iterations. Starting from a severe restriction with only one VP value, more VP values are gradually added in a stepwise relaxed VP (SRVP) regularization scheme until a number is reached which allows for both a good data fit and a reconstruction which is close to piecewise constant. Because the VP regularizing function is "less than quadratic", it can be elegantly incorporated in the Gauss-Newton algorithm through a sequence of quadratic approximations. This yields a simple half quadratic minimization algorithm, similar to the one in [24]. It will be shown that the VP regularization scheme yields accurate reconstructions. Further research is needed to find out how it compares with various types of edge preserving regularization, but an advantage may be that it relies on a totally different principle. Indeed, VP regularization does not operate on the spatial distribution of the permittivity. Instead it clusters permittivity values in the complex plane. Therefore, it might also be useful in cases where one applies a different, non-pixel-based parameterization of the permittivity. Moreover, the framework naturally allows for the incorporation of a priori knowledge on the permittivity values.

4.3.1 Modification of the cost function

The VP regularized cost function proposed in this work is

$$\mathcal{F}^{VP}(\boldsymbol{\varepsilon}, \boldsymbol{c}) = \mathcal{F}^{LS}(\boldsymbol{\varepsilon}) + \gamma \mathcal{F}^{P}(\boldsymbol{\varepsilon}, \boldsymbol{c}), \tag{4.39}$$

where γ is a positive regularization parameter. The Value Picking regularizing function $\mathcal{F}^P$ is given by

$$\mathcal{F}^P(\boldsymbol{\varepsilon}, \boldsymbol{c}) = \frac{1}{N^\epsilon} \sum_{\nu=1}^{N^\epsilon} f^P(\mid \epsilon_\nu - c_1 \mid^2, \ldots, \mid \epsilon_\nu - c_P \mid^2), \tag{4.40}$$

where f^P is the P-dimensional ($P \ll N^\epsilon$) choice function and where the auxiliary variables c_p are denoted the VP values. One of these VP values, more specifically c_P, is fixed to the known relative background permittivity, i.e. $c_P = \epsilon_\mathrm{b}/\epsilon_0$, and the $P-1$ other VP values are collected in the vector $\boldsymbol{c}$. The cost function is minimized for both $\boldsymbol{\varepsilon}$ and $\boldsymbol{c}$.

The choice function of dimension P, $f^P : \mathbb{R}_+^P \to \mathbb{R}_+$ ($\mathbb{R}_+$ is the set of non-negative real numbers), is defined as

$$f^P(u_1, \ldots, u_P) = F^P(u_1, \ldots, u_P; 0), \tag{4.41}$$

where F^P is defined and evaluated through the recursion formula

$$F^P(u_1, \ldots, u_P; x) = (u_P + x) \frac{F^{P-1}(u_1, \ldots, u_{P-1}; x)}{F^{P-1}(u_1, \ldots, u_{P-1}; u_P + x)}, \tag{4.42}$$

and

$$F^1(u_1; x) = u_1 + x. \tag{4.43}$$

For example, the cases with $P = 1$, $P = 2$ and $P = 3$ yield:

$$f^1(u_1) = u_1 \tag{4.44}$$

$$f^2(u_1, u_2) = \frac{u_1 u_2}{u_1 + u_2} \tag{4.45}$$

$$f^3(u_1, u_2, u_3) = \frac{u_1 u_2 u_3 (u_1 + u_2 + u_3)}{(u_1 + u_2)(u_1 + u_3)(u_2 + u_3)}. \tag{4.46}$$

The definition of the choice function is discussed in more detail in Appendix B, where its relevant properties are also proven.

As is readily seen from expressions (4.44)-(4.46) and for general P from Theorem B.4 of Appendix B, the VP function $\mathcal{F}^P$ is minimal when VP values c_p can be found such that every optimization variable ϵ_ν is equal to one of these VP values, i.e. $\mathcal{F}^P = 0$ for permittivity profiles with at most P different permittivity values. The minimization of (4.39) thus favors this kind of permittivity profiles. To our knowledge, the choice function (4.41)-(4.43) has not been used elsewhere. Its definition is the result of three major demands: (i) it should be zero if and only if one or more of its arguments are zero, (ii) it should be symmetric in its arguments and (iii), for ease of use in optimization algorithms, its order should not increase for increasing P, i.e.

the function should be bounded by a polynomial function with a fixed degree, independent of P. A function like $f^P = u_1 \cdot u_2 \ldots \cdot u_P$, as is used in [8], does not satisfy the third demand. Because of Conjecture B.1, the function f^P, defined in (4.41), is less than linear and hence the function $\mathcal{F}^P$ is less than quadratic.

When approaching the minimum of (4.39) during the optimization, a specific VP value is picked from $\{c_1, \ldots, c_P\}$ for every permittivity unknown ϵ_ν and the difference $\mid \epsilon_\nu - c_p \mid^2$ between the considered permittivity unknown and the chosen VP value c_p is minimized. Thanks to the particular form of the choice function, these choices are made in an intuitively attractive way. To investigate this, the VP function (4.40) is rewritten using Theorem B.11:

$$\mathcal{F}^P(\boldsymbol{\varepsilon}, \boldsymbol{c}) = \frac{1}{N^\epsilon} \sum_{\nu=1}^{N^\epsilon} \sum_{p=1}^{P} b_{p,\nu}^P(\boldsymbol{\varepsilon}, \boldsymbol{c}) \mid \epsilon_\nu - c_p \mid^2, \tag{4.47}$$

which can be seen as a weighted sum of the penalty functions $\mid \epsilon_\nu - c_p \mid^2$ where the weights $b_{p,\nu}^P$ are calculated with the weight functions defined in (B.39)

$$b_{p,\nu}^P(\boldsymbol{\varepsilon}, \boldsymbol{c}) = B_p^P(\mid \epsilon_\nu - c_1 \mid^2, \ldots, \mid \epsilon_\nu - c_P \mid^2). \tag{4.48}$$

Following observations can be made:

- Every time the difference $\mid \epsilon_\nu - c_p \mid$ between the permittivity unknown ϵ_ν and the VP value c_p becomes much larger than the differences $\mid \epsilon_\nu - c_{p'} \mid$ between ϵ_ν and the other VP values $c_{p'}$ ($p' \neq p$), the corresponding term $b_{p,\nu}^P \mid \epsilon_\nu - c_p \mid^2$ vanishes in (4.47). This is a direct result of (B.25). It also implies that the weight $b_{p,\nu}^P$ approaches zero and that c_p does not contribute to the regularization of ϵ_ν.

- If $\mid \epsilon_\nu - c_p \mid \ll \mid \epsilon_\nu - c_{p'} \mid$, $\forall p' \neq p$, only the term $b_{p,\nu}^P \mid \epsilon_\nu - c_p \mid^2$ is retained in (4.47) and we have $b_{p,\nu}^P \approx b_{p,\nu}^1 = 1$ and $b_{p',\nu}^P \approx 0$, for $p' \neq p$, which is compatible with Theorem B.9. This means that the regularization will try to force $\epsilon_\nu = c_p$.

- If k differences $\mid \epsilon_\nu - c_p \mid$, for $p \in I \subset \{1, \ldots, P\}$, are of comparable size, but much smaller than the differences of ϵ_ν with the other VP values, only k terms $b_{p,\nu}^k \mid \epsilon_\nu - c_p \mid^2$ will remain in the summation (4.47) with weights $b_{p,\nu}^k$ somewhere between 0 and 1. Moreover, it can be derived from Theorem B.10 that

  $$\sum_{p' \in I} b_{p',\nu}^k \mid \epsilon_\nu - c_{p'} \mid^2 \leq \mid \epsilon_\nu - c_p \mid^2, \quad \forall p \in I, \tag{4.49}$$

  which means that the sum of all the penalty terms corresponding to ϵ_ν contributes less to (4.47) than a single penalty term with unit weight does. This way, the regularization will not force a decision too soon if the data fit does not provide enough driving force for it.

- It is possible that two or more VP values merge in the course of the minimization. P thus can be larger than the actual number of different permittivities.

Summarizing, whenever a permittivity variable becomes closer to one specific VP value than to the other VP values in course of the optimization, the regularization will try to force equality with this VP value. When there is no clear preference, no choice will be made apart from disregarding VP values that are clearly far away from the considered optimization variable. The 3D plot of the weights $b_{p,\nu}^P$ on the permittivity grid can be considered as a *choice map*, where values close to 1 indicate a choice for the VP value c_p and values close to 0 indicate that c_p has been disregarded in that position on the grid.

4.3.2 Incorporation in the Gauss-Newton framework

The minimization of the cost function (4.39) is performed by alternately updating the permittivity profile and the VP values. To update the permittivity vector $\boldsymbol{\varepsilon}$, an approximate line search [1] is performed along a modified Gauss-Newton descent direction. The VP values, subject to upper and lower bounds on real and imaginary parts, are then updated using a sequence of active set minimizations of quadratic functions that bound the VP function $\mathcal{F}^P$ from above.

The Gauss-Newton Descent Direction for the permittivity

Starting from the permittivity profile $\boldsymbol{\varepsilon}_k$ and the VP vector $\boldsymbol{c}_k$ in iteration k of the minimization process, a search direction $\boldsymbol{s}_k$ is calculated for $\boldsymbol{\varepsilon}$, by applying a Gauss-Newton method. This search direction, however, is not directly computed from the cost function (4.39), but from a modified cost function

$$\mathcal{F}^Q(\boldsymbol{\varepsilon}, \boldsymbol{c}; \boldsymbol{\varepsilon}_k, \boldsymbol{c}_k) = \mathcal{F}^{LS}(\boldsymbol{\varepsilon}) + \gamma \mathcal{Q}^P(\boldsymbol{\varepsilon}, \boldsymbol{c}; \boldsymbol{\varepsilon}_k, \boldsymbol{c}_k), \tag{4.50}$$

with

$$\mathcal{Q}^P(\boldsymbol{\varepsilon}, \boldsymbol{c}; \boldsymbol{\varepsilon}_k, \boldsymbol{c}_k) = \frac{1}{N^\epsilon} \sum_{\nu=1}^{N^\epsilon} \sum_{p=1}^{P} b_{p,\nu}^P(\boldsymbol{\varepsilon}_k, \boldsymbol{c}_k) \mid \epsilon_\nu - c_p \mid^2 . \tag{4.51}$$

The difference between (4.51) and (4.47) is that in (4.51) the weights $b_{p,\nu}^P$ are computed in $(\boldsymbol{\varepsilon}_k, \boldsymbol{c}_k)$ and then kept fixed when $(\boldsymbol{\varepsilon}, \boldsymbol{c})$ changes. Because of Theorem B.11 and Conjecture B.1, $\mathcal{Q}^P$ bounds $\mathcal{F}^P$ from above and touches with $\mathcal{F}^P$ in $(\boldsymbol{\varepsilon}_k, \boldsymbol{c}_k)$. Therefore, taking a reduction step in $(\boldsymbol{\varepsilon}_k, \boldsymbol{c}_k)$ based on $\mathcal{F}^Q$ will also reduce $\mathcal{F}^{VP}$. The use of (4.50) instead of (4.39) facilitates the incorporation of the VP regularization in the Gauss-Newton framework. The gradient $\boldsymbol{g}^Q$ and Hessian matrix $\boldsymbol{H}^Q$ of

$\mathcal{F}^Q$ are given by

$$\boldsymbol{g}^Q = \boldsymbol{g}^{LS} + \gamma \boldsymbol{g}^P \tag{4.52}$$

$$\boldsymbol{H}^Q = \boldsymbol{H}^{LS} + \gamma \boldsymbol{H}^P, \tag{4.53}$$

where the gradient vector $\boldsymbol{g}^{LS}$ and Hessian matrix $\boldsymbol{H}^{LS}$ of the least squares data fit are given by (4.4) and (4.5). The gradient vector $\boldsymbol{g}^P$ and Hessian matrix $\boldsymbol{H}^P$ of the function $\mathcal{Q}^P$ are given by

$$\boldsymbol{g}^P = \begin{bmatrix} \boldsymbol{\Omega}^P \\ \left(\boldsymbol{\Omega}^P\right)^* \end{bmatrix} \tag{4.54}$$

$$\boldsymbol{H}^P = \begin{bmatrix} \boldsymbol{0} & \boldsymbol{\Sigma}^P \\ \boldsymbol{\Sigma}^P & \boldsymbol{0} \end{bmatrix}, \tag{4.55}$$

with

$$\left[\boldsymbol{\Omega}^P\right]_\nu = \frac{\partial \mathcal{Q}^P}{\partial \epsilon_\nu}(\boldsymbol{\varepsilon}, \boldsymbol{c}; \boldsymbol{\varepsilon}_k, \boldsymbol{c}_k) = \frac{1}{N^\epsilon} \sum_{p=1}^{P} b^P_{p,\nu}(\boldsymbol{\varepsilon}_k, \boldsymbol{c}_k) \left(\epsilon_\nu - c_p\right)^*, \tag{4.56}$$

$$\left[\boldsymbol{\Sigma}^P\right]_{\nu v} = \frac{\partial^2 \mathcal{Q}^P}{\partial \epsilon_\nu \partial \epsilon_v^*}(\boldsymbol{\varepsilon}, \boldsymbol{c}; \boldsymbol{\varepsilon}_k, \boldsymbol{c}_k) = \delta_{\nu,v} \frac{1}{N^\epsilon} \sum_{p=1}^{P} b^P_{p,\nu}(\boldsymbol{\varepsilon}_k, \boldsymbol{c}_k). \tag{4.57}$$

Applying Newton's method yields an equation for the search direction $\boldsymbol{s}_k$ in iteration k

$$\boldsymbol{H}^Q_k \begin{bmatrix} \boldsymbol{s}_k \\ \boldsymbol{s}_k^* \end{bmatrix} = -\boldsymbol{g}^Q_k, \tag{4.58}$$

where the subscript k indicates quantities evaluated in $(\boldsymbol{\varepsilon}, \boldsymbol{c}) = (\boldsymbol{\varepsilon}_k, \boldsymbol{c}_k)$. In the Gauss-Newton approximation, Newton's formula (4.58) is applied after a linearization of the scattered field $\boldsymbol{e}^{\mathrm{scat}}$ as a function of $\boldsymbol{\varepsilon}$, i.e. the matrix $\boldsymbol{B}$ in (4.5) is neglected. This yields the Gauss-Newton update system

$$\left(\boldsymbol{J}^H_k \boldsymbol{J}_k + \lambda^2 \boldsymbol{\Sigma}^P_k\right) \boldsymbol{s}_k = -\left(\boldsymbol{J}^H_k \left[\boldsymbol{e}^{\mathrm{scat}}_k - \boldsymbol{e}^{\mathrm{meas}}\right] + \lambda^2 \left(\boldsymbol{\Omega}^P_k\right)^*\right), \tag{4.59}$$

where the trade-off parameter λ^2 is given by $\lambda^2 = \gamma \|\boldsymbol{e}^{\mathrm{meas}}\|^2 = \mathcal{N}^{LS}$. Since $\boldsymbol{J}^H_k \boldsymbol{J}_k$ is at least positive semi-definite, and since $\boldsymbol{\Sigma}^P_k$ is a diagonal matrix with strictly positive diagonal entries, $\boldsymbol{s}_k$ again is a strict descent direction. Moreover, towards the end of the minimization, when VP choices have been made for every permittivity variable, the matrix $\boldsymbol{\Sigma}^P_k$ approaches $(1/N^\epsilon)\boldsymbol{I}_{N^\epsilon}$, where $\boldsymbol{I}$ is the $N^\epsilon \times N^\epsilon$ unity matrix.

Note that, although the search direction is derived from the function $\mathcal{F}^Q$, the line search along this direction is performed on the actual cost function $\mathcal{F}$.

Updating the VP values

After updating $\boldsymbol{\varepsilon}_k$ to $\boldsymbol{\varepsilon}_{k+1}$ as described above, an optimization for $\boldsymbol{c}$ to obtain $\boldsymbol{c}_{k+1}$ is conducted. This step reduces the VP regularizing function in (4.39) without modifying the data fit $\mathcal{F}^{LS}$. The optimization for $\boldsymbol{c}$ is done by generating a sequence of VP vectors $\{\boldsymbol{c}_l\}$, starting from $\boldsymbol{c}_0 = \boldsymbol{c}_k$, where $\boldsymbol{c}_{l+1}$ is the solution of the constrained quadratic minimization problem

$$\boldsymbol{c}_{l+1} = \underset{\boldsymbol{c}}{\operatorname{argmin}} \quad \mathcal{Q}^P(\boldsymbol{\varepsilon}_{k+1}, \boldsymbol{c}; \boldsymbol{\varepsilon}_{k+1}, \boldsymbol{c}_l), \tag{4.60}$$

subject to the upper and lower bounds

$$(p, r, u): \qquad \Re(c_p) \le c^r_{p,u}, \quad p = 1, \ldots, P-1, \tag{4.61}$$
$$(p, r, l): \qquad \Re(c_p) \ge c^r_{p,l}, \quad p = 1, \ldots, P-1, \tag{4.62}$$
$$(p, i, u): \qquad \Im(c_p) \le c^i_{p,u}, \quad p = 1, \ldots, P-1, \tag{4.63}$$
$$(p, i, l): \qquad \Im(c_p) \ge c^i_{p,l}, \quad p = 1, \ldots, P-1. \tag{4.64}$$

Since $\mathcal{Q}^P(\boldsymbol{\varepsilon}_{k+1}, \boldsymbol{c}; \boldsymbol{\varepsilon}_{k+1}, \boldsymbol{c}_l)$ touches $\mathcal{F}^P$ in the point $(\boldsymbol{\varepsilon}_{k+1}, \boldsymbol{c}_l)$ and since $\mathcal{Q}^P(\boldsymbol{\varepsilon}_{k+1}, \boldsymbol{c}; \boldsymbol{\varepsilon}_{k+1}, \boldsymbol{c}_l) \ge \mathcal{F}^P(\boldsymbol{\varepsilon}_{k+1}, \boldsymbol{c})$, every step in this scheme will reduce $\mathcal{F}^P$. The iterations are terminated for $l = L$, such that $\|\boldsymbol{c}_L - \boldsymbol{c}_{L-1}\| \le T^C$, some small threshold. We then conclude with $\boldsymbol{c}_{k+1} = \boldsymbol{c}_L$.

The minimization problem (4.60)-(4.64) for every l is solved using a simple active set method which is a problem-specific reformulation of the general quadratic active set method described in [1]. The iterations of this method generate a sequence $\{\boldsymbol{c}_m\}$ which starts from $\boldsymbol{c}_0 = \boldsymbol{c}_{l-1}$ and the associated vector $\boldsymbol{\Lambda}^P_{l,0}$ and matrix $\boldsymbol{\Xi}^P_l$, which for general m are defined as

$$\begin{aligned}
\left[\boldsymbol{\Lambda}^P_{l,m}\right]_p &= \frac{\partial \mathcal{Q}^P}{\partial c_p}(\boldsymbol{\varepsilon}_{k+1}, \boldsymbol{c}_m; \boldsymbol{\varepsilon}_{k+1}, \boldsymbol{c}_l) \\
&= -\frac{1}{N^\epsilon} \sum_{\nu=1}^{N^\epsilon} b^P_{p,\nu}(\boldsymbol{\varepsilon}_{k+1}, \boldsymbol{c}_l) \left(\epsilon_{k+1,\nu} - c_{m,p}\right)^*, \qquad (4.65) \\
\left[\boldsymbol{\Xi}^P_l\right]_{pq} &= \frac{\partial^2 \mathcal{Q}^P}{\partial c_p \partial c^*_q}(\boldsymbol{\varepsilon}_{k+1}, \boldsymbol{c}_m; \boldsymbol{\varepsilon}_{k+1}, \boldsymbol{c}_l) \\
&= \delta_{p,q} \frac{1}{N^\epsilon} \sum_{\nu=1}^{N^\epsilon} b^P_{p,\nu}(\boldsymbol{\varepsilon}_{k+1}, \boldsymbol{c}_l). \qquad (4.66)
\end{aligned}$$

The iterations proceed as follows:

1. Determine the set of active constraints I_A. A constraint is said to be active if it yields an equality in (4.61)-(4.64).

2. Calculate $\Delta \boldsymbol{c}_m$ with

$$\Delta c_{m,p} = -\frac{\left[\boldsymbol{\Lambda}_{l,m}^P\right]_p^*}{\left[\boldsymbol{\Xi}_l^P\right]_{pp}}, \tag{4.67}$$

$$\Re(\Delta c_{m,p}) = 0, \quad \text{if} \quad (p,r,u) \in I_A \quad \text{or} \quad (p,r,l) \in I_A, \tag{4.68}$$

$$\Im(\Delta c_{k,p}) = 0, \quad \text{if} \quad (p,i,u) \in I_A \quad \text{or} \quad (p,i,l) \in I_A, \tag{4.69}$$

   where (4.68) and (4.69) possibly overwrite the result of (4.67). The first line returns the update $\Delta \boldsymbol{c}_m$ such that the VP vector $\boldsymbol{c} = \boldsymbol{c}_{l-1} + \Delta \boldsymbol{c}_m$ with $m = 0$ is the solution to the optimization problem (4.60) if no constraints are imposed.

3. Determine the smallest positive value of β, let it be β_m, such that the line

$$\boldsymbol{c}(\beta) = \boldsymbol{c}_m + \beta \Delta \boldsymbol{c}_m \tag{4.70}$$

   violates a presently inactive constraint and determine the corresponding constraint (p,a,b), with $a = r$ or $a = i$ and $b = u$ or $b = l$.

4. If $\beta_m < 1$, put $\boldsymbol{c}_{m+1} = \boldsymbol{c}_m + \beta_m \Delta \boldsymbol{c}_m$. Then calculate $\boldsymbol{\Lambda}_{l,m+1}^P$ and add (p,a,b) to I_A. Return to 2.

5. If $\beta_m \geq 1$ (including infinity), put $\boldsymbol{c}_{m+1} = \boldsymbol{c}_m + \Delta \boldsymbol{c}_m$ and calculate $\boldsymbol{\Lambda}_{l,m+1}^P$. Then, for every constraint in I_A, calculate the projection of $-(\boldsymbol{\Lambda}_{l,m+1}^P)^*$ on the direction in the complex plane, which is perpendicular to that constraint and pointing outward from the constrained optimization domain. If the smallest of these projection values is positive or equal to zero, terminate with $\boldsymbol{c}_{l+1} = \boldsymbol{c}_{m+1}$. Else, remove the corresponding constraint from I_A and return to 2.

Note that the VP values can be initialized at random within their constraints (4.61)-(4.64). The only limitation is that their initial values should not coincide. The presented algorithm treats identical VP values (with the same constraints) in an identical fashion, so once merged, two coinciding VP values will remain identical during the rest of the reconstruction.

Further analysis

In this work, the assumption that the desired permittivity vector $\boldsymbol{\varepsilon}^0$ consists of only a few different permittivity values is used to regularize the inverse scattering problem and is not strictly imposed throughout the minimization, as is the case, for example, in inverse scattering algorithms using level set methods. As a result, the condition $\mathcal{F}^P = 0$ generally is not satisfied exactly for the final reconstruction. Indeed, it is

possible to prove the following statement (see Appendix B.3)

$$\nabla \mathcal{F}^P(\boldsymbol{\varepsilon}, \boldsymbol{c}) = 0 \quad \Leftrightarrow \quad \mathcal{F}^P(\boldsymbol{\varepsilon}, \boldsymbol{c}) = 0, \tag{4.71}$$

which means that a stationary point of $\mathcal{F}^P$ always is a global minimum of $\mathcal{F}^P$. Therefore, in a minimum of the cost function (4.39) where $\nabla \mathcal{F}^{VP} = \nabla \mathcal{F}^{LS} + \gamma \nabla \mathcal{F}^P = 0$, there are two possibilities:

a) $\nabla \mathcal{F}^P = 0$ and therefore $\nabla \mathcal{F}^{LS} = 0$ and $\mathcal{F}^P = 0$.

b) $\nabla \mathcal{F}^P \neq 0$ and therefore $\nabla \mathcal{F}^{LS} \neq 0$ and $\mathcal{F}^P \neq 0$.

Case a) implies that the minimum of the total cost function is also a minimum of the least squares data fit and exactly consists of at most P different permittivity values. This is not very likely to happen when the data is noisy, especially with $P \ll N^\epsilon$. The resulting reconstruction thus is a trade-off between data fit and the condition $\mathcal{F}^P = 0$, as is expressed by case b). As a result the permittivity unknowns will not perfectly coincide with the VP values, but will rather be clustered around those VP values in the complex plane.

4.3.3 Stepwise relaxed VP regularization

The algorithm described in section 4.3.2 can become trapped in local minima above the noise level. Such spurious minima are likely to be introduced in the cost function since the VP regularizing function $\mathcal{F}^P$ has multiple (global) minimizers: every permittivity profile consisting of only P different permittivity values that lie within the constraints imposed on $\boldsymbol{\varepsilon}$ and $\boldsymbol{c}$ yields $\mathcal{F}^P = 0$. To avoid this problem, one could use the VP regularization as a post processing step which starts from a reasonable initial estimate, obtained for example with the multiplicative smoothing regularization as described in Section 4.2. In such approach it is crucial that the data fit which corresponds to this initial estimate is sufficiently larger than the noise level such that the data fit cost function can guide the value picking process during the further minimization. However, it is then necessary to find a good criterion for switching from smoothing to VP regularization.

We propose a different strategy. Let us first consider the extreme cases $P = N^\epsilon$ and $P = 1$, where the optimization for $\boldsymbol{c}$ is straightforward. The case $P = N^\epsilon$ yields $c_\nu = \epsilon_\nu$, for every ν, which results in $\mathcal{F}^P = 0$, $\boldsymbol{\Omega}^P = 0$ and $\boldsymbol{\Sigma}^P = (1/N^\epsilon)\boldsymbol{I}_{N^\epsilon}$. As a result, the update system (4.59) is reduced to

$$\left(\boldsymbol{J}_k^H \boldsymbol{J}_k + \frac{\lambda^2}{N^\epsilon} \boldsymbol{I}_{N^\epsilon} \right) \boldsymbol{s}_k = -\boldsymbol{J}_k^H \left[\boldsymbol{e}_k^{\mathrm{scat}} - \boldsymbol{e}^{\mathrm{meas}} \right]. \tag{4.72}$$

This update equation has been used by many authors, e.g. [3, 16, 17]. It results from minimizing the non-regularized least squares cost function $\mathcal{F}^{LS}$ instead of (4.39) and

applying a regularization only to the linear Gauss-Newton subproblems. This approach can be regarded as a Levenberg-Marquardt minimization algorithm [1, 3] applied to $\mathcal{F}^{LS}$. Since the minimum of $\mathcal{F}^{LS}$ generally is not well defined, the performance of this algorithm is significantly reduced in the presence of noise. We could say that this approach does not yield an actual regularized solution. The case $P = 1$ requires no optimization for $\boldsymbol{c}$, because the only VP value c_1 is kept fixed and equal to $\epsilon_\mathrm{b}/\epsilon_0$. It results in the cost function

$$\mathcal{F}^{VP}(\boldsymbol{\varepsilon}, \boldsymbol{c}) = \mathcal{F}^{LS}(\boldsymbol{\varepsilon}) + \frac{\gamma}{N^\epsilon}\|\boldsymbol{\varepsilon} - \boldsymbol{\varepsilon}_\mathrm{b}\|^2, \tag{4.73}$$

where the second term is a classical Tikhonov regularization [15] and where $\boldsymbol{\varepsilon}_\mathrm{b}$ is the N^ϵ-dimensional vector with $[\boldsymbol{\varepsilon}_\mathrm{b}]_\nu = \epsilon_\mathrm{b}/\epsilon_0, \forall\nu$. The corresponding update system is

$$\left(\boldsymbol{J}_k^H\boldsymbol{J}_k + \frac{\lambda^2}{N^\epsilon}\boldsymbol{I}_{N^\epsilon}\right)\boldsymbol{s}_k = -\left(\boldsymbol{J}_k^H\left[\boldsymbol{e}_k^\mathrm{scat} - \boldsymbol{e}^\mathrm{meas}\right] + \frac{\lambda^2}{N^\epsilon}\left(\boldsymbol{\varepsilon}_k - \boldsymbol{\varepsilon}_\mathrm{b}\right)\right). \tag{4.74}$$

The regularization (4.73) imposes a strong restriction on the permittivity vector $\boldsymbol{\varepsilon}$. From these two extreme cases $P = 1$ (strong restriction) and $P = N^\epsilon$ (no restriction) and from Theorem B.10 of Appendix B, we can conclude that increasing the number of VP values relaxes the regularization.

Since, according to the discrepancy principle, it is desirable to have as much regularization as possible without preventing the least squares data fit from reaching the noise level, we propose the following strategy. The iterations start with $P = 1$ and a fairly large value of the regularization parameter γ and proceed until a local minimum is reached, i.e. the gradient of the cost function is small enough, or until $\mathcal{F}^{LS}$ increases again. The latter case implies that the VP regularization is making decisions that are not guided by the data fit. When γ is large enough, this first step is terminated with $\mathcal{F}^{LS}$ above the noise level. Then, the regularization is relaxed by adding an extra VP value and the optimization continues until the same stopping criterion is met. New VP values are added this way until $\mathcal{F}^{LS}$ reaches the noise level or a threshold derived from an estimate of the noise level. Ofcourse, when the actual permittivity profile consists of P_0 different permittivity values, the algorithm should ideally reach the noise level when $P = P_0$. To this end γ has to be chosen properly. When it is too large, the algorithm typically stops with $P > P_0$, since the large weight given to the regularization term has to be compensated by adding more VP values, such that the regularization is sufficiently relaxed and allows for a data fit on the noise level. When it is too small, there is no strong restriction on the optimization and $\mathcal{F}^{LS}$ will easily reach the noise level, even with a few VP values. The choice of γ has been done by numerical experimentation so far. However, this does not require knowledge of the object. When the algorithm stops, i.e. when $\mathcal{F}^{LS} \approx T^N$, we check for sufficient clustering of the permittivity unknowns around the VP values. We try to achieve this with as few VP values as possible. If the final reconstruction shows insufficient

clustering, we restart with larger γ. If, on the other hand the clustering is sufficient, we try a smaller γ too see if we can achieve a comparable clustering with fewer VP values. The addition of an extra VP value in every step of the stepwise relaxed VP scheme is performed by randomly initializing the VP value (making sure it does not coincide with already present VP values) and performing the minimization of section 4.3.2 before proceeding with the updates of the permittivity.

Finally, note that the stepwise relaxed VP (SRVP) regularization strategy can be seen as a minimization of the fixed cost function $\mathcal{F} = \mathcal{F}^{LS} + \gamma\mathcal{F}^{N^\epsilon}$, where in a step with P VP values $N^\epsilon - P$ VP values are frozen at infinity. This is a result of Theorem B.2. In this perspective the cost function thus remains unaltered, but the optimization domain is restricted initially and gradually increased. We want to stress that the VP regularization assumes that a reconstruction is possible with $P << N^\epsilon$. If P approaches N^ϵ, there is no real regularization, as pointed out earlier.

4.3.4 Examples

To validate the proposed stepwise relaxed VP regularization algorithm, some reconstructions from synthetic data are presented. Throughout the rest of the section all targets are embedded in free space (i.e. $\epsilon_b = \epsilon_0$) and the operating frequency is 8 GHz, which yields a background wavelength $\lambda_\mathrm{b} = 0.0375$ m.

The first target is a numerical phantom consisting of a cube with side $0.6\lambda_\mathrm{b}$ (0.0225 m) and permittivity $(2.5 - j)\epsilon_0$, which is embedded in a sphere with radius $0.75\lambda_\mathrm{b}$ (0.0281 m) and permittivity $1.8\epsilon_0$. The sphere and cube are centered at the origin and at the point $(-0.15\lambda_\mathrm{b}, -0.15\lambda_\mathrm{b}, -0.15\lambda_\mathrm{b})$ or (-0.0056 m, -0.0056 m, -0.0056 m), respectively, in a reference system with axes parallel to the edges of the cube. The dipole configuration for the reconstruction of this target is depicted in Figure 4.16. The dipole positions and orientations are indicated with dots and arrows, respectively. All 144 dipoles in the configuration are distributed over 6 meridional circles on a sphere with radius $3\lambda_\mathrm{b}$ (0.1125 m) that is centered at the origin. One half of the dipoles is oriented along the ϕ direction, while the other half is oriented along the θ direction. For this first example each dipole is used to illuminate the target and the scattered field is measured in every dipole position and along each dipole direction. This yields a total of $N^D = 20736$ data points.

The investigation domain $\mathcal{D}$ is a cube with side $1.5\lambda_\mathrm{b}$ (0.0562 m), centered at the origin and with edges parallel to the coordinate axes (Figure 4.16), and the permittivity grid on this domain has a cell size $0.075\lambda_\mathrm{b}$ (0.0028 m), which yields 20 cells in each direction and thus a total of $N^\epsilon = 8000$ permittivity unknowns. The synthetic data are obtained by solving the forward scattering problem with the same FFT-accelerated volume integral equation technique as is used in the inverse scattering algorithm. Since the discretization grids for the fields and the permittivity in this forward simulation coincide with the grids used in the inversion algorithm, it is possi-

ble in principle to exactly reconstruct the target from these data and therefore this first reconstruction is a test under ideal circumstances. Gaussian noise with an SNR of 30 dB is added to the data, which results in a noise level $T^N = 10^{-3}$.

Figures 4.17 (a) and (b) show the exact permittivity profile $\boldsymbol{\varepsilon}^0$ in two slices through the investigation domain and the reconstructions of this profile are depicted in Figures 4.18 (a)-(f). For all these reconstructions, the optimization starts from the background permittivity in $\mathcal{D}$ using the following physical constraints on the VP values:

$$\Re(c_p) \geq 1.0, \quad \forall p \tag{4.75}$$

$$\Im(c_p) \leq 0.0, \quad \forall p. \tag{4.76}$$

Figures 4.18 (a) and (b) show a reconstruction with the multiplicative smoothing regularization of [5], which is obtained in 7 iterations. Figures 4.18 (c) and (d) show the reconstruction with SRVP regularization ($\gamma = 0.1$) after the step with $P = 3$ and 9 iterations in total. The iterations in each step of the stepwise relaxed VP scheme are terminated if $\|\boldsymbol{g}^Q\| \leq \sqrt{2} \cdot 10^{-4}$ or when the data fit increases again. The final reconstruction yields a data fit on the noise level, see Figure 4.19 (a), and a permittivity profile which is close to piecewise constant. Therefore, the algorithm can be terminated with $P = 3$ with a result that is clearly very close to the actual permittivity profile (the final VP values are $\{2.45 - 0.94j, 1.79 - 0.01j, 1\}$). Figure 4.19 (b) shows the reconstruction error $\Delta\epsilon(\boldsymbol{\varepsilon})$, defined as

$$\Delta\epsilon(\boldsymbol{\varepsilon}) = \frac{\|\boldsymbol{\varepsilon} - \boldsymbol{\varepsilon}^0\|}{\|\boldsymbol{\varepsilon}^0\|}, \tag{4.77}$$

which is smallest for the reconstruction with VP regularization.

When an extra VP value is added ($P = 4$), the result of Figures 4.18 (e) and (f) is obtained, which visually hardly can be distinguished from the result with $P = 3$. The VP values now are $\{2.48 - 0.97j, 1.80, 1.73 - 0.01j, 1\}$. The third VP value is close to the second one and mainly corresponds to cells along the surface of the sphere. The data fit for this result, which is obtained after only one additional iteration, has decreased negligibly (a reduction of $5 \cdot 10^{-4}$). This justifies a posteriori the termination with 3 VP values. Figure 4.20 shows the "swarm plot" of the complex permittivity values in the complex permittivity plane for all the reconstructions of Figure 4.18. The clustering in the reconstructions with VP regularization is apparent in these plots as opposed to the spreading of the permittivity values when using multiplicative smoothing.

Next, two more challenging targets are considered. The permittivity profiles are shown in Figures 4.21 (a) and (b) and in Figures 4.22 (a) and (b). The investigation domain is now a cuboid with dimensions $4\lambda_\mathrm{b} \times 2\lambda_\mathrm{b} \times 2\lambda_\mathrm{b}$ ($0.15 \times 0.075 \times 0.075$ m) and there are three objects with different permittivities: a cube with side $0.6\lambda_\mathrm{b}$ (0.0225 m), embedded in a sphere with radius $0.75\lambda_\mathrm{b}$ (0.0281 m) and an additional

cube with side λ_b (0.0375 m). For the target of Figure 4.21, the permittivities of these objects are $(2-j)\epsilon_0$, $1.5\epsilon_0$ and $1.8\epsilon_0$, respectively, and for the target of Figure 4.22, these permittivities become $(1.5-j)\epsilon_0$, $2\epsilon_0$ and $1.6\epsilon_0$, respectively. The dipole configuration is the same as the one used for the first example, except that the radius of the sphere on which the dipoles are located is now $4\lambda_b$ (0.15 m). Again, Gaussian noise with an SNR of 30 dB is added to the data and the grid for the data generation is now twice as fine as the inversion grid. The cell size of the inversion grid is $0.1\lambda_b$ (0.0037 m) and the number of permittivity unknowns is $N^\epsilon = 16000$.

The reconstructions with multiplicative smoothing and with SRVP regularization of the target of Figures 4.21 (a) and (b) are shown in Figures 4.21 (c) and (d) and Figures 4.21 (e) and (f), respectively. The VP regularization uses $\gamma = 0.5$ and reaches the noise level with $P = 4$ and 13 iterations. The final VP values are $\{1.95 - 1.00j, 1.82, 1.56, 1.0\}$. Both reconstructions yield almost exactly the same data fit, but from the reconstructions and from the swarm plots of Figure 4.23, it is clear that the VP reconstruction yields a better defined and more accurate estimation of the permittivity values and the shape of the objects. Due to the misfit between the grids for the data generation and the inversion algorithm, the sphere cannot be perfectly reconstructed and this apparently results in a slight overestimation of its permittivity and in the introduction of some stray cells with background permittivity inside it.

The reconstructions of the target of Figures 4.22 (a) and (b) are shown in Figures 4.22 (c)-(f). This time, the SRVP regularization, with $\gamma = 1.0$, reaches the noise level with $P = 5$ and 25 iterations. The final VP values are $\{2.01 - 0.01j, 1.64, 1.54 - 1.01j, 1.45, 1.0\}$. The extra VP value apparently has to be added to define an intermediate permittivity level along the outside of the sphere. Lowering the regularization parameter, does not remedy this. Probably, the intermediate permittivity level is needed to compensate for the staircasing error in the coarser reconstruction grid. Indeed, no such intermediate level occurs around the larger cube in Figure 4.21, which also has a relatively high permittivity. However, from Figures 4.22 and 4.24, it can be concluded once more that the VP result provides more quantitative information on the original permittivity profile than the result obtained with multiplicative smoothing.

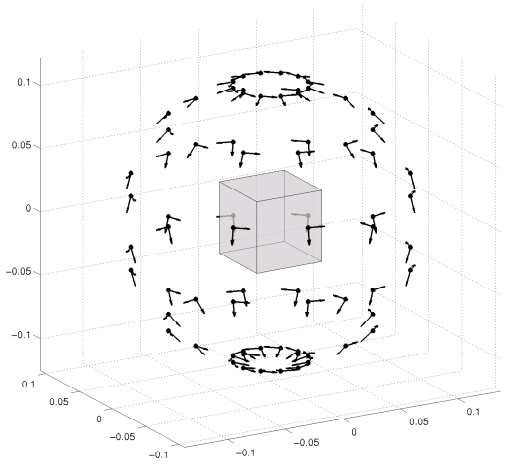

Figure 4.16: A view of the dipole configuration and the investigation domain $\mathcal{D}$ which are used in the first reconstruction from simulated data. 144 dipoles are placed on a sphere with radius 11.2 cm and are oriented along the θ and ϕ directions. For each illumination, the scattered field is measured in all the dipole positions along the θ and ϕ directions.

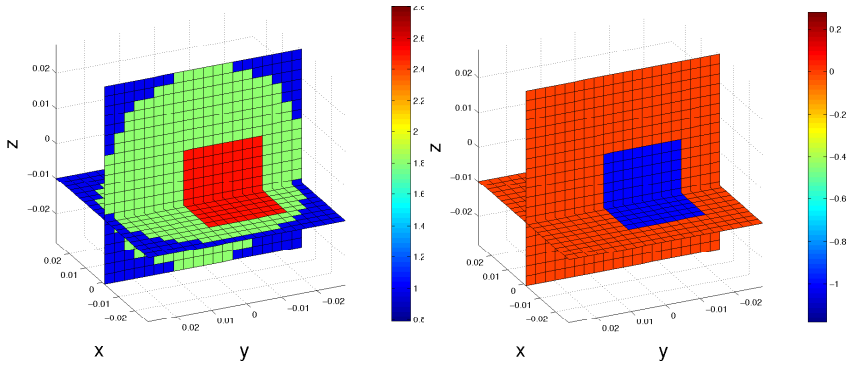

(a) (b)

Figure 4.17: Real (a) and imaginary (b) part of the permittivity of the first synthetic target in two slices through the investigation domain $\mathcal{D}$.

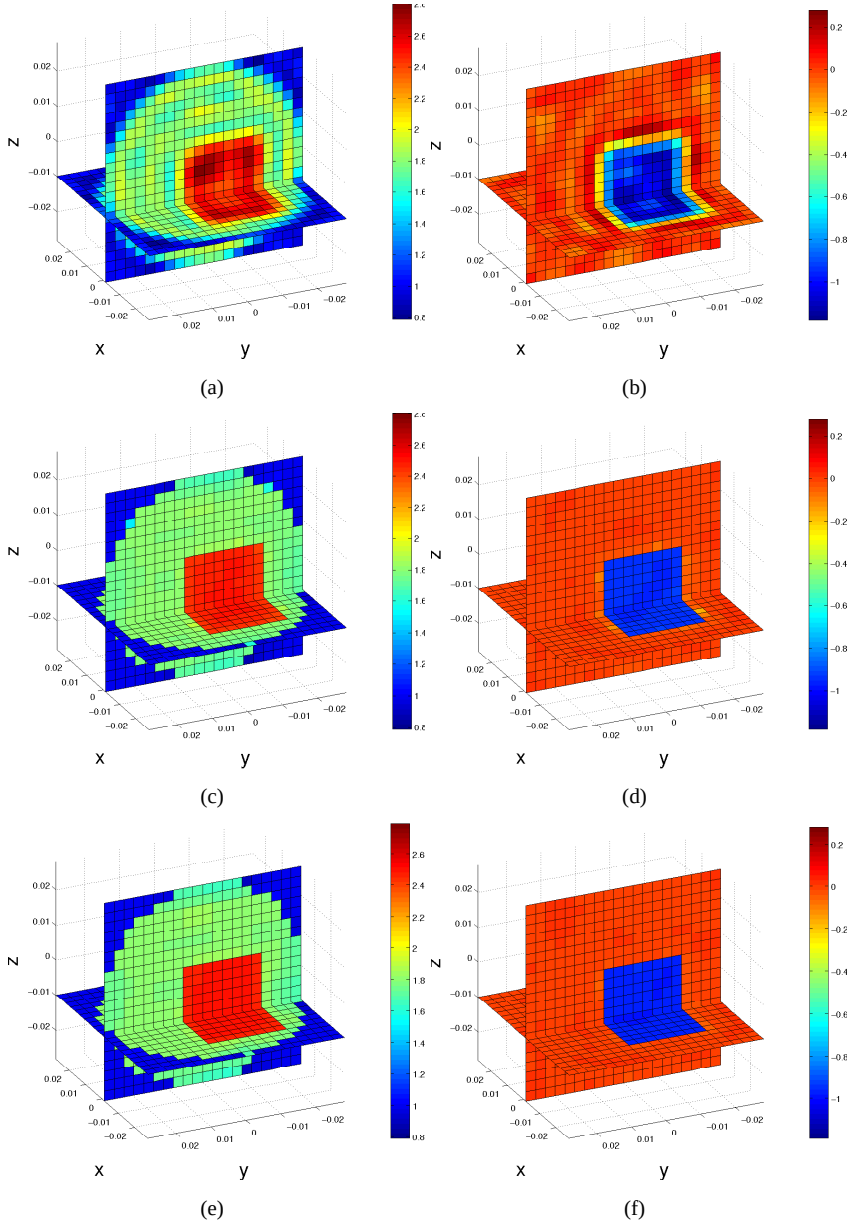

Figure 4.18: Reconstruction of the first synthetic target at 8 GHz: Real (left) and imaginary (right) part of the permittivity in two slices through the investigation domain $\mathcal{D}$. (a) and (b): reconstruction with multiplicative smoothing regularization. (c) and (d): reconstruction with SRVP regularization with $P = 3$. (e) and (f): reconstruction with SRVP regularization with $P = 4$.

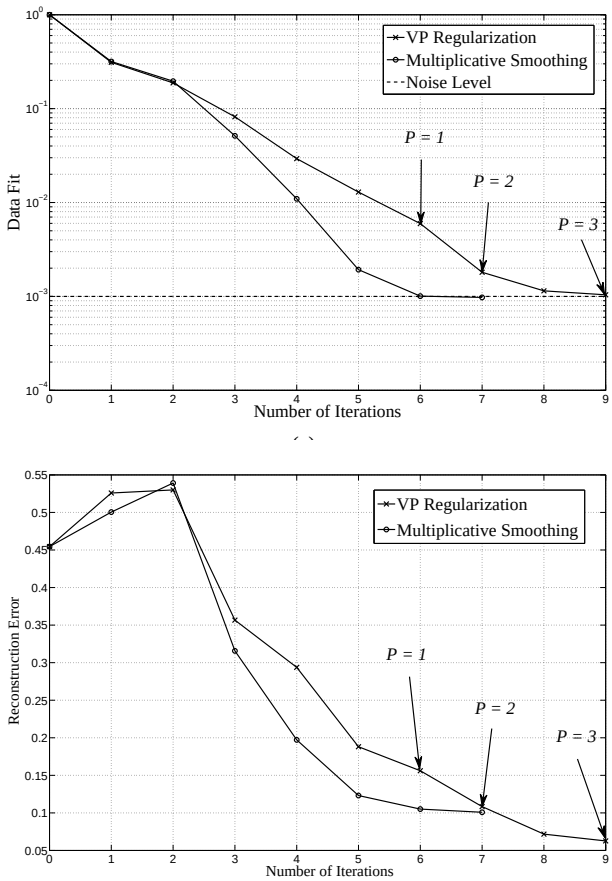

(b)

Figure 4.19: The data fit cost function $\mathcal{F}^{LS}$ (a) and the reconstruction error $\Delta\epsilon$ (b) versus the number of iterations during the reconstructions of the first synthetic target. The end of each step in the stepwise relaxed VP regularization scheme is indicated with an arrow. An extra VP value is added when $\|\boldsymbol{g}^Q\| \leq \sqrt{2} \cdot 10^{-4}$ or when the data fit cost function $\mathcal{F}^{LS}$ increases again.

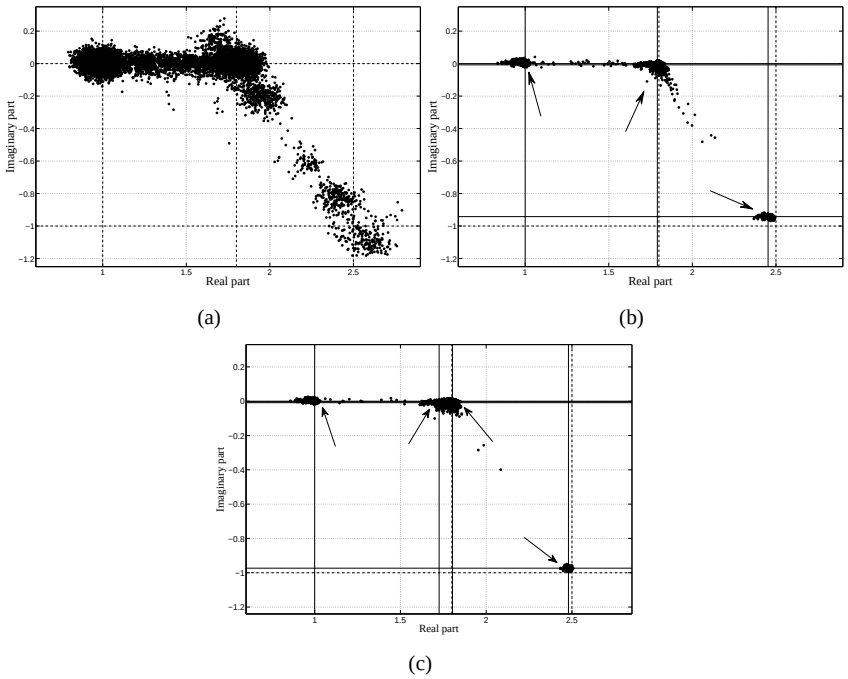

Figure 4.20: Swarm plot of the N complex permittivity values on the grid, represented with dots in the complex plane, for the reconstructions of the target of Figure 4.18. Reconstructions: (a) of Figure 4.18 (c),(d) with multiplicative smoothing; (b) of Figure 4.18 (e),(f) with SRVP regularization and $P = 3$; (c) of Figure 4.18 (g) and (h) with SRVP regularization and $P = 4$. The VP values are indicated as the intersections of the solid horizontal and vertical lines marked by arrows and the exact permittivity values lie at the nearby intersections of the dashed lines.

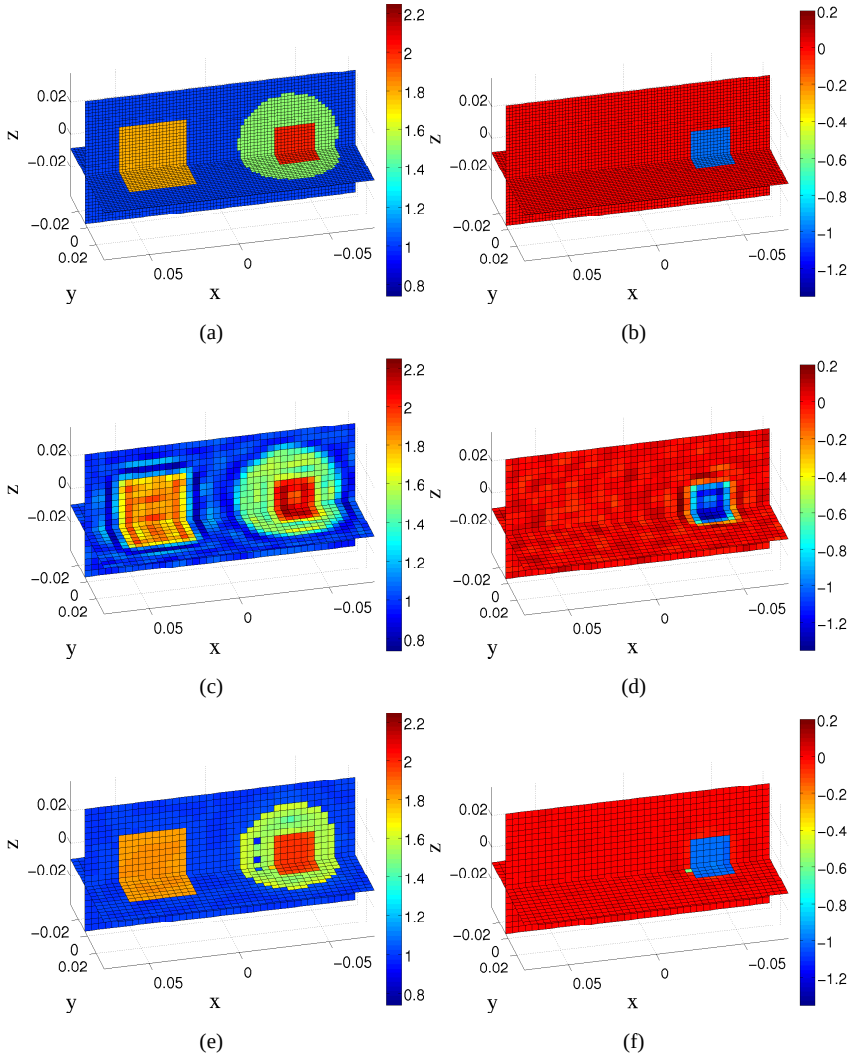

Figure 4.21: Reconstruction of the second synthetic target at 8 GHz: Real (left) and imaginary (right) part of the permittivity in two slices through the investigation domain $\mathcal{D}$. (a) and (b): exact permittivity profile. (c) and (d): reconstruction with multiplicative smoothing regularization. (e) and (f): reconstruction with SRVP regularization.

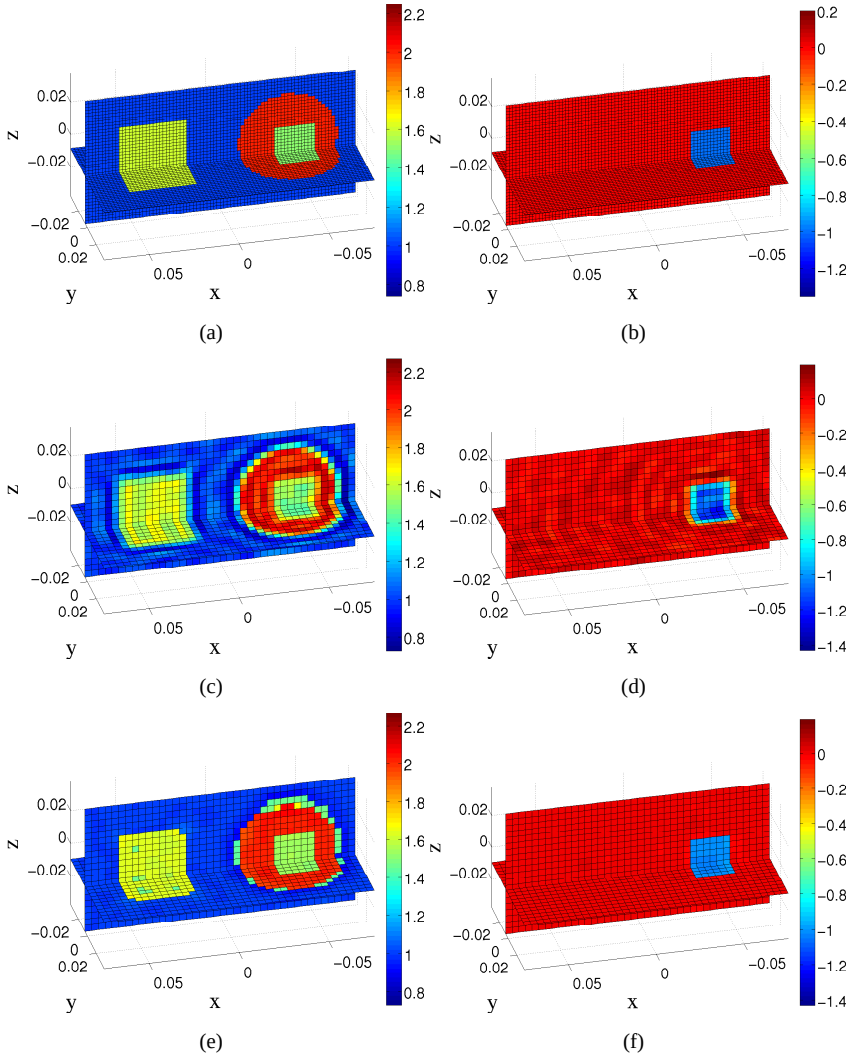

Figure 4.22: Reconstruction of the third synthetic target at 8 GHz: Real (left) and imaginary (right) part of the permittivity in two slices through the investigation domain $\mathcal{D}$. (a) and (b): exact permittivity profile. (c) and (d): reconstruction with multiplicative smoothing regularization. (e) and (f): reconstruction with SRVP regularization.

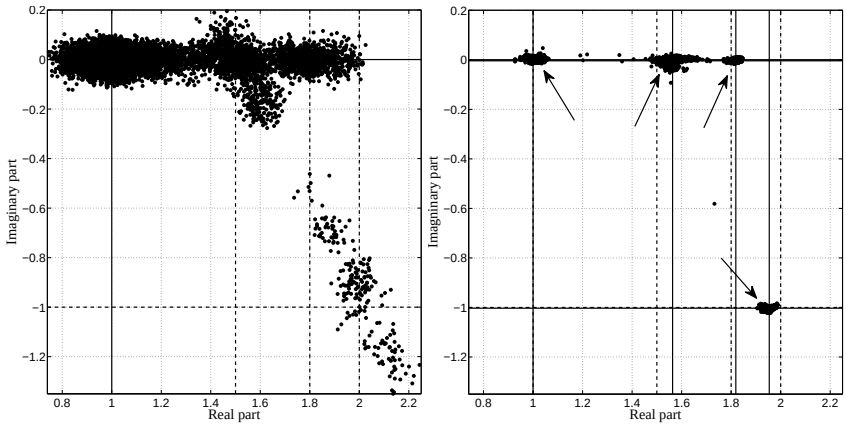

(a) (b)

Figure 4.23: Swarm plot of the N complex permittivity values on the grid, represented with dots in the complex plane, for the reconstructions of the target of Figure 4.21. Reconstructions: (a) of Figure 4.21 (c),(d) with multiplicative smoothing; (b) of Figure 4.21 (e),(f) with SRVP regularization. The VP values are indicated as the intersections of the solid horizontal and vertical lines marked by arrows and the exact permittivity values lie at the nearby intersections of the dashed lines.

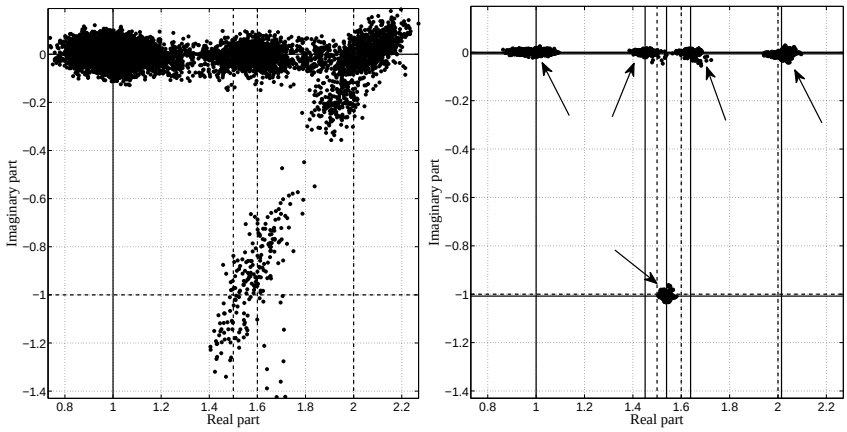

(a) (b)

Figure 4.24: Swarm plot of the N complex permittivity values on the grid, represented with dots in the complex plane, for the reconstructions of the target of Figure 4.22. Reconstructions: (a) of Figure 4.22 (c),(d) with multiplicative smoothing; (b) of Figure 4.22 (e),(f) with SRVP regularization. The VP values are indicated as the intersections of the solid horizontal and vertical lines marked by arrows and the exact permittivity values lie at the nearby intersections of the dashed lines.

4.4 Further improvements to the algorithm

4.4.1 Constraints on the permittivity

In order to improve the convergence of the optimization technique, but mainly to prevent the permittivity and conductivity values from becoming non-physical or too high to handle with the chosen forward discretization δ, it is recommended to include a priori knowledge concerning the expected upper and lower bounds on the complex permittivity by means of constraints. If the optimization variables violate these constraints, the conditioning of the forward problem can become problematic. Let us denote the upper and lower bounds by $\epsilon^r_{\max}$ and $\epsilon^r_{\min}$, respectively, for the real part of the optimization variables and by $\epsilon^i_{\max}$ and $\epsilon^i_{\min}$, respectively, for the imaginary part, i.e.

$$\epsilon^r_{\min} < \Re(\epsilon_\nu) < \epsilon^r_{\max}, \qquad \forall \nu \tag{4.78}$$

$$\epsilon^i_{\min} < \Im(\epsilon_\nu) < \epsilon^i_{\max}, \qquad \forall \nu. \tag{4.79}$$

Such constraints can be incorporated in the Gauss-Newton framework using a nonlinear transformation that maps the constrained permittivity values on new, unconstrained optimization variables [9]. Here, we follow an approach which is inspired by the use of parameter transformations, but which is only used in the line search. More specifically, we propose to replace the search path in the line search (4.9) with a smooth, constrained path that entirely lies within the constraints, if the starting point $\boldsymbol{\varepsilon}_k$ does so, and which starts along a descent direction. With this constrained path, it is sure that the cost function will be reduced if $\boldsymbol{\varepsilon}_k$ is not a local minimizer, and that the constraints will not be violated. The path is defined as

$$\boldsymbol{\varepsilon}_{k+1}(\beta_k) = \boldsymbol{f}\left(\beta_k, \Re(\boldsymbol{s}), \Re(\boldsymbol{\varepsilon}_k), \epsilon^r_{\min}, \epsilon^r_{\max}\right) + j\boldsymbol{f}\left(\beta_k, \Im(\boldsymbol{s}), \Im(\boldsymbol{\varepsilon}_k), \epsilon^i_{\min}, \epsilon^i_{\max}\right), \tag{4.80}$$

where $\boldsymbol{s}$ is the solution of (4.36) or (4.59) and where the vector function $\boldsymbol{f}$ is defined as

$$\begin{aligned} &f_\nu\left(\beta, \boldsymbol{x}, \boldsymbol{\xi}, \xi_{\min}, \xi_{\max}\right) \\ &\quad = \xi_{\max} - (\xi_{\max} - \xi_\nu)\exp\left(-\beta\frac{x_\nu}{\xi_{\max} - \xi_\nu}\right), \quad x_\nu \geq 0 \qquad (4.81) \\ &\quad = \xi_{\min} + (\xi_\nu - \xi_{\min})\exp\left(\beta\frac{x_\nu}{\xi_\nu - \xi_{\min}}\right), \quad x_\nu < 0. \qquad (4.82) \end{aligned}$$

The path (4.80) only considers the constraints that can be violated along the path (4.9) with $\beta_k > 0$, hence the distinction between the cases $x_\nu \geq 0$ and $x_\nu < 0$ in (4.81)-(4.82). For small β_k (4.9) and (4.80) coincide, but in the vicinity of the constraints, the path (4.80) is bent away from (4.9) and it has a limit point on the

constraints, as is illustrated in Figure 4.25 (a) for a problem with only one complex optimization variable. Although theoretically the optimization variables can never reach their bounds with this procedure and the path always starts along a descent direction, it is possible that no progress is made if one or more variables are very close to one or more of their bounds (in finite precision, they can actually be *on* their bounds). Indeed, in such a situation, the line search path deviates from its initial direction $\boldsymbol{s}$ already for very small β-values and starts to run along the projection of $\boldsymbol{s}$ on the nearest boundaries of the constrained optimization domain as is illustrated in Figure 4.25 (b). It is possible that although $\boldsymbol{s}$, calculated with (4.36) or (4.59), is a descent direction, its projection on these boundaries is not and the cost function starts to increase again for very small values of β. In this case the line search is terminated after only a negligible reduction of the cost function, without necessarily implying that a local minimum is reached. If $\boldsymbol{s}$ is the steepest descent direction, it can easily be shown that its projection on boundaries like the ones considered here (i.e. upper and lower bounds on the optimization variables) remains a descent direction. Therefore, in our implementation it is possible to switch temporarily to the steepest descent update when the above mentioned problems with the constraints are encountered.

Note that the use of the new search path implements the constrained optimization in an elegant way, without requiring any adjustments to the update systems and the line search algorithm. It also avoids sequences of time consuming minimizations of reduced problems, as is needed in active set methods. However, the mapping (4.80) is highly non-linear and a large step in β can correspond to a negligible step in the actual optimization domain and a corresponding negligible reduction of the cost function when a lot of optimization variables are close to their boundaries. Therefore, the line search algorithm can require many steps and many forward problem simulations before a local minimum along the search path is reached. Although the extrapolation over the permittivity provided by the Born approximation in Section 3.7 will result in a rapid solution of the additional forward problems when the permittivity profile changes little (eventually only one iteration per solution of (3.13) will be needed), the large number of forward problem solutions can increase the total computation time significantly. Together with the fact that local optimization can get trapped against the constraints even if they are handled in an ideal way, we recommend to avoid constraints as much as possible. For example, instead of demanding that the imaginary part of the permittivity is not positive, as required by the passivity condition, we will only require that it does not become too positive, because this would prevent convergence in the forward problem. Note finally that we could use different upper and lower bounds per permittivity unknown, if that would be appropriate, for instance if some region-specific a priori information on the permittivity is available.

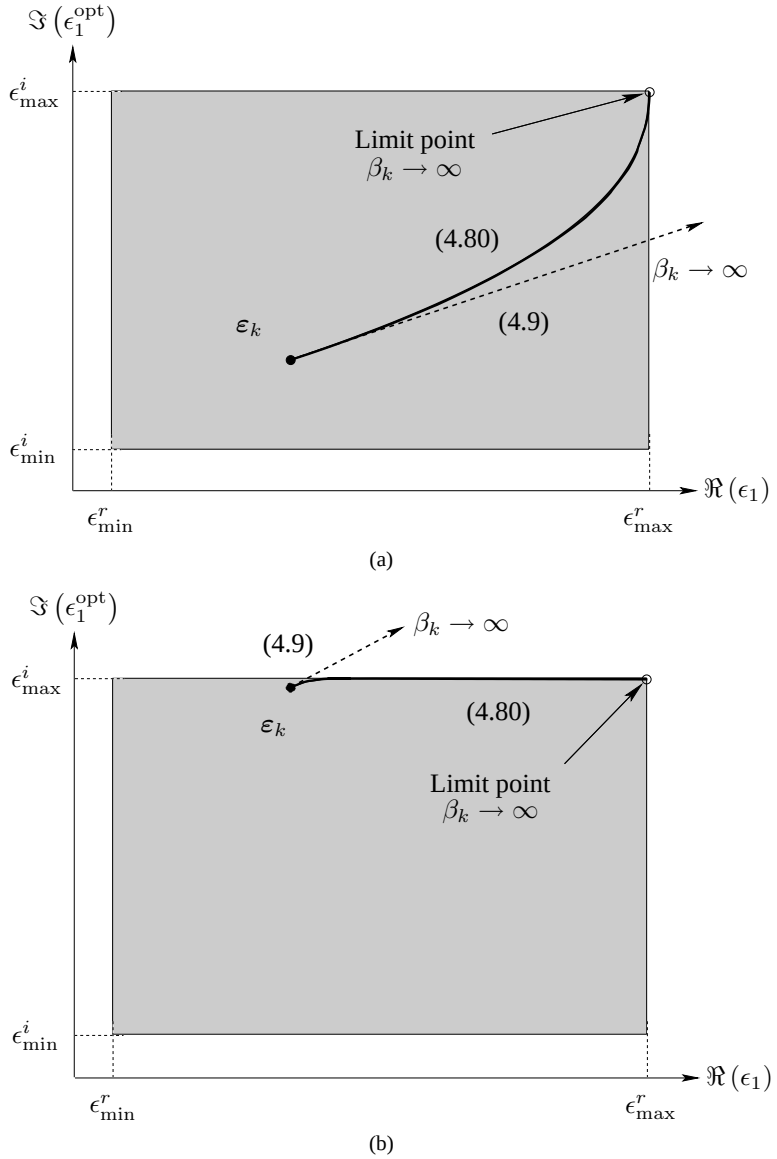

Figure 4.25: Illustration of the constrained line search path: (a) the starting point ε_k lies far from the boundaries of the optimization domain, such that the new line search path (4.80) coincides with the original path (4.9) up to large β_k; (b) the starting point ε_k lies close to a boundary of the optimization domain, such that the new line search path (4.80) starts running along the projection of (4.9) on this boundary already for small β_k.

4.4.2 Subspace preconditioning of the update systems

The solution of system (4.36) or (4.59) for the Gauss-Newton update $\boldsymbol{s}$ by means of a direct inversion method would require $\mathcal{O}((N^{\epsilon})^3)$ operations and since the number of unknowns N^{ϵ} easily grows large in a 3D inverse problem, this would be computationally very demanding. Moreover, the calculation of the product $\boldsymbol{J}^H\boldsymbol{J}$ would require $\mathcal{O}(N^{\mathrm{D}}(N^{\epsilon})^2))$ operations. It is therefore more efficient to solve (4.36) and (4.59) iteratively, which requires per iteration one multiplication of an N^{ϵ}-dimensional vector with $\boldsymbol{J}$, followed by one multiplication of an N^{D}-dimensional vector with $\boldsymbol{J}^H$. The computational complexity then is $\mathcal{O}(PN^{\epsilon}N^{\mathrm{D}})$, which is much less than a direct inversion provided that the number of iterations P can be kept small. However, the condition number of $\boldsymbol{J}$ — and therefore of $\boldsymbol{J}^H\boldsymbol{J}$ — generally is very large. Even with the well-conditioned regularization term $\lambda^2\boldsymbol{\Sigma}$ in (4.36) or $\lambda^2\boldsymbol{\Sigma}^P$ in (4.59), the conditioning of the system matrix remains problematic and even worsens towards the end of the optimization in case of multiplicative smoothing regularization, since λ^2 then is proportional to the least squares data error.

We therefore propose to solve (4.36) and (4.59) with the iterative subspace preconditioned LSQR algorithm (SPLSQR) of Jacobsen, et al. [33], which is specifically designed for regularized linear least squares problems such as (4.36) and (4.59). Since this algorithm has been conceived for real system matrices, the problem (4.36) or (4.59) is first reformulated (dropping the subscript k for convenience) as the minimization problem

$$\boldsymbol{x} = \underset{\boldsymbol{x}'}{\operatorname{argmin}} \quad \|\boldsymbol{K}\boldsymbol{x}' - \boldsymbol{y}\|^2 = \underset{\boldsymbol{x}'}{\operatorname{argmin}} \quad \|\boldsymbol{J}^r\boldsymbol{x}' - \boldsymbol{y}_1\|^2 + \lambda^2\|\boldsymbol{L}^r\boldsymbol{x}' - \boldsymbol{y}_2\|^2, \tag{4.83}$$

where

$$\boldsymbol{K} = \begin{bmatrix} \Re(\boldsymbol{J}) & -\Im(\boldsymbol{J}) \\ \Im(\boldsymbol{J}) & \Re(\boldsymbol{J}) \\ \lambda\boldsymbol{L} & \boldsymbol{0} \\ \boldsymbol{0} & \lambda\boldsymbol{L} \end{bmatrix} = \begin{bmatrix} \boldsymbol{J}^{\mathrm{r}} \\ \lambda\boldsymbol{L}^{\mathrm{r}} \end{bmatrix}, \quad \boldsymbol{y} = \begin{bmatrix} \Re(\Delta\boldsymbol{e}^{\mathrm{meas}}) \\ \Im(\Delta\boldsymbol{e}^{\mathrm{meas}}) \\ -\lambda\boldsymbol{L}^{-1}\Re(\Omega) \\ \lambda\boldsymbol{L}^{-1}\Im(\Omega) \end{bmatrix} = \begin{bmatrix} \boldsymbol{y}_1 \\ \boldsymbol{y}_2 \end{bmatrix},$$

$$\boldsymbol{x} = \begin{bmatrix} \Re(\boldsymbol{s}) \\ \Im(\boldsymbol{s}) \end{bmatrix},$$

where $\Re$ and $\Im$ stand for the real and imaginary parts, respectively, and where $\boldsymbol{L}$ is the Cholesky factor of $\boldsymbol{\Sigma} = \boldsymbol{L}\boldsymbol{L}^T$ or $\boldsymbol{\Sigma}^P = \boldsymbol{L}\boldsymbol{L}^T$ and $\Delta\boldsymbol{e}^{\mathrm{meas}} = \boldsymbol{e}^{\mathrm{meas}} - \boldsymbol{e}^{\mathrm{scat}}$. As can be seen in Figure 4.26 for a generic (but relatively small) inverse problem, the singular value spectrum of the matrix $\boldsymbol{K}$ with $\lambda = 0$, i.e. without regularization, generally decreases over a wide range of values without showing a clear threshold were this spectrum could be truncated. For $\lambda \neq 0$, on the other hand, the spectrum of $\boldsymbol{K}$ shows a platform at the lower end, which is introduced by the regularization. Nonetheless the conditioning of $\boldsymbol{K}$ clearly is still not very good, because of the rapidly decreasing

singular values in the first part of the spectrum.

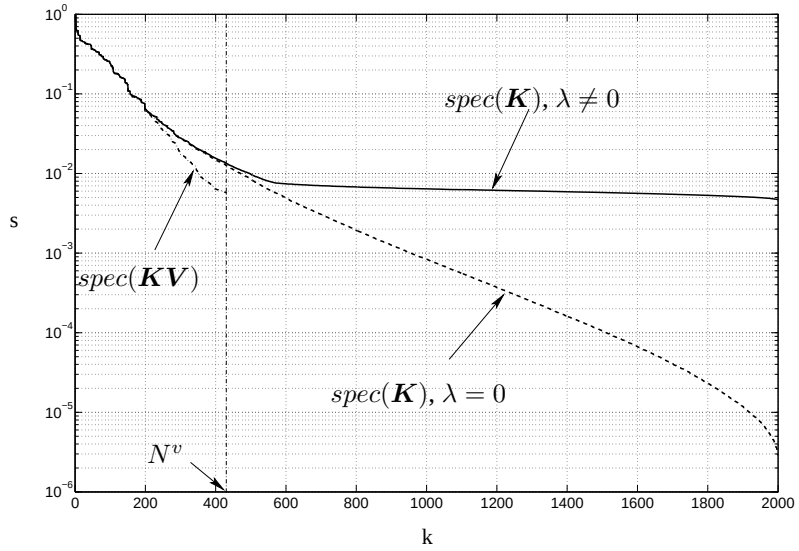

Figure 4.26: The singular value spectra of the matrix $\boldsymbol{K}$ without regularization ($\lambda = 0$) and with regularization ($\lambda \neq 0$) for a generic inverse scattering problem with 2000 permittivity unknowns. The spectrum of the matrix $\boldsymbol{KV}$ where $\boldsymbol{V}$ contains the truncated 3D discrete cosine basis corresponding to $N^\nu = 432$.

The key idea of the subspace preconditioned LSQR algorithm is a splitting of the solution space $\mathcal{S}$ into two orthogonally complementary subspaces, $\mathcal{S}^v$ and $\mathcal{S}^w$, respectively spanned by the columns of the orthogonal matrices $\boldsymbol{V}$ and $\boldsymbol{W}$. This means we look for a solution $\boldsymbol{x} = \boldsymbol{V}\boldsymbol{v} + \boldsymbol{W}\boldsymbol{w}$. It is furthermore desirable that $\mathcal{S}^v$ has a small dimension N^v and that the conditioning of $\boldsymbol{KW}$ is much better than the conditioning of $\boldsymbol{K}$. Indeed, introducing the QR factorization

$$\boldsymbol{KV} = \boldsymbol{QR} = \begin{bmatrix} \boldsymbol{Y} & \boldsymbol{Z} \end{bmatrix} \begin{bmatrix} \boldsymbol{R} \\ \boldsymbol{0} \end{bmatrix} = \boldsymbol{YR}, \tag{4.84}$$

where $\boldsymbol{Q}$ is orthogonal and $\boldsymbol{R}$ is square and upper triangular, it easily can be shown that

$$\|\boldsymbol{Kx} - \boldsymbol{y}\|^2 = \|\boldsymbol{Rv} - \boldsymbol{Y}^T (\boldsymbol{y} - \boldsymbol{KW}\boldsymbol{w}) \|^2 + \|\boldsymbol{Z}^T\boldsymbol{KW}\boldsymbol{w} - \boldsymbol{Z}^T\boldsymbol{y}\|^2. \tag{4.85}$$

Because $\boldsymbol{K}$ has full rank, the same holds for $\boldsymbol{R}$ and the first term in the RHS of (4.85)

can be made zero for every $\boldsymbol{w}$. Therefore, (4.83) is equivalent to

$$\boldsymbol{w} = \underset{\boldsymbol{w}'}{\operatorname{argmin}} \quad \|\boldsymbol{Z}^T\boldsymbol{K}\boldsymbol{W}\boldsymbol{w}' - \boldsymbol{Z}^T\boldsymbol{y}\|^2, \tag{4.86}$$

$$\boldsymbol{v} = \boldsymbol{R}^{-1}\boldsymbol{Y}^T\left(\boldsymbol{y} - \boldsymbol{K}\boldsymbol{W}\boldsymbol{w}\right). \tag{4.87}$$

Since (4.87) is a small $N^v \times N^v$- dimensional and upper-triangular system, it is solved conveniently for $\boldsymbol{v}$ by back substitution. The solution of (4.86) for $\boldsymbol{w}$ is done with the LSQR algorithm [34], which, although mathematically equivalent, is numerically more stable than the CGLS method. Moreover, this iterative algorithm can be formulated directly in terms of $\boldsymbol{p} = \boldsymbol{W}\boldsymbol{w}$, thereby avoiding the construction of and multiplications with the large matrix $\boldsymbol{W}$ [33]. Calculating the QR factorization (4.84) and performing the multiplications with $\boldsymbol{Z}$ or $\boldsymbol{Z}^T$ is relatively cheap if done with Householder transformations, because N^v is small.

With an appropriate choice of $\boldsymbol{V}$ (and $\boldsymbol{W}$) the number of LSQR iterations to solve (4.86) can be kept small. If, for instance, $\boldsymbol{V}$ consists of the N^v principal right singular vectors of $\boldsymbol{K}$, then the spectrum of $\boldsymbol{K}\boldsymbol{V}$, denoted as $spec(\boldsymbol{K}\boldsymbol{V})$, will coincide with $spec(\boldsymbol{K})$ up to σ_{N^v}, the N^v-th singular value of $\boldsymbol{K}$. On the other hand, since $\boldsymbol{W}$ is orthogonal to $\boldsymbol{V}$, the subspace $\mathcal{S}^w$ is spanned by the $2N^\epsilon - N^v$ least significant right singular vectors of $\boldsymbol{K}$ and $spec(\boldsymbol{K}\boldsymbol{W})$ will coincide with $(\sigma_{N^v+1}, \ldots, \sigma_{2N^\epsilon})$. It can be seen from Figure 4.26 that, if N^v is large enough, $spec(\boldsymbol{K}\boldsymbol{W})$ will practically completely lie within the plateau in $spec(\boldsymbol{K})$, introduced by the regularization. This means that the conditioning of $\boldsymbol{K}\boldsymbol{W}$ in this situation will be very good. It also implies that $\boldsymbol{K}\boldsymbol{V}$ inherits the ill-conditioning of $\boldsymbol{K}$, but since (4.87) is solved directly, this does not pose any problem. However, it is computationally too expensive to construct this SVD subspace, and therefore a subspace that 'resembles' it is chosen. It is well-known that for most applications the right singular vectors of an ill-posed problem become more oscillatory as the corresponding singular values decrease. Therefore, we propose in this thesis a truncated 3D discrete cosine basis (the DCT-II basis from [35]), defined on the cubic grid $\mathcal{D}^\epsilon$, which is used for the real and imaginary part of the complex update vector $\boldsymbol{s}$ separately, i.e. the matrix $\boldsymbol{V}$ has the form

$$\boldsymbol{V} = \begin{bmatrix} \boldsymbol{V}_c & \boldsymbol{0} \\ \boldsymbol{0} & \boldsymbol{V}_c \end{bmatrix}, \tag{4.88}$$

where $\boldsymbol{V}_c$ contains per column one of the N^v DCT basis vectors with the lowest spatial frequencies in x-, y- and z-directions. In this case the multiplication of $\boldsymbol{K}$ with $\boldsymbol{V}$ can be evaluated efficiently by performing 3D discrete cosine transforms [35] on the rows of $\boldsymbol{K}$ (actually on the first and the second half of these rows separately) and retaining only the N^v components with the lowest spatial frequencies. This subspace can be considered as a coarse grid approximation to the actual solution space. Figure 4.26 shows $spec(\boldsymbol{K}\boldsymbol{V})$ for this subspace and it can be seen that it indeed coincides

with $spec(\boldsymbol{K})$ for large singular values. The reduction in computation time obtained with this subspace preconditioned LSQR algorithm for the solution of (4.36), when compared with standard iterative solvers, such as the CG method, is considerable, as will be demonstrated in Section 5.1.2.

4.5 Region picking regularization

In this section, the concept of Value Picking regularization is extended to the more abstract concept of *Region Picking* (RP) regularization. VP regularization assumes that the permittivity is piecewise constant. One could think of such a permittivity profile as built from a number of homogeneous regions. Such a region does not have to be simply connected or compact, but is just characterized by the value of its complex permittivity. The difference $|\epsilon_\nu - c_p|$ between the permittivity ϵ_ν of a certain cell group $\mathcal{C}_\nu$ and the permittivity (or VP value) c_p of region p then is a measure of how much $\mathcal{C}_\nu$ belongs to region p.

A more general permittivity profile could consist of different types of *regions*, which are areas in the optimization domain with certain characteristics and for which a *distance* between a given cell group and the region can be defined. Examples are:

- the homogenous region with index p, already used in VP regularization. This region is solely characterized by a VP value c_p and the distance between cell group $\mathcal{C}_\nu$ and the region is given by $u^H_{p,\nu} = |\epsilon_\nu - c_p|^2$.
- the small-scatterer region with index t. This region is characterized by a permittivity value d_t and a position vector $\boldsymbol{R}_t$. The distance between cell group $\mathcal{C}_\nu$ and the small-scatterer region is given by

$$u^{SS}_{t,\nu} = \mid \epsilon_\nu - d_t \mid^2 + \frac{\lambda^{SS}}{N^\nu} \sum_{(f,g,h)\in\mathcal{C}_\nu} \|\boldsymbol{r}_{f,g,h} - \boldsymbol{R}_t\|^2, \tag{4.89}$$

  where λ^{SS} is a normalization constant, where $\boldsymbol{r}_{f,g,h}$ is the midpoint of cell (f,g,h) and where N^ν is the number of cells in cell group $\mathcal{C}_\nu$. This definition thus also includes a physical distance to the small scatterer.

- the smooth region with index s. This region is characterized by some parameter representation $\epsilon_s(\boldsymbol{r}, a_1, ..., a_M)$ of the complex permittivity on the investigation domain, which depends linearly on a limited number M of parameters a_m. This representation could be the expansion of the permittivity in a truncated Fourier or cosine basis, such that it can only represent smooth permittivity profiles. The distance of cell group $\mathcal{C}_\nu$ to this smooth region then is

$$u^S_{s,\nu} = \frac{1}{N^\nu} \sum_{(f,g,h)\in\mathcal{C}_\nu} \mid \epsilon_{f,g,h} - \epsilon_s(\boldsymbol{r}_{f,g,h}, a_1, ..., a_M) \mid^2 . \tag{4.90}$$

The idea behind RP regularization is that in the course of the reconstruction, a choice for a certain region is made for every permittivity unknown ϵ_ν. As in VP regularization, the characteristics of the regions (c_p,d_t,$\boldsymbol{R}_t$,a_m,...) are considered as auxiliary variables, which are included in the optimization process. Figure 4.27 shows a 2D permittivity profile, consisting of a homogeneous background region, a smooth region and a small-scatterer region. During the reconstruction, some permittivity cells are assigned the background permittivity and form the plateau in the profile. The profile of the smooth region results from a fitting of the parameter representation $\epsilon_1(\boldsymbol{r}, a_1, ..., a_M)$ (Figure 4.27 (b)) to the permittivities of the cells that were chosen to belong the the smooth region. Finally, cells in the vicinity of the small scatterer take on the permittivity of that small scatterer. The permittivity and position of the small scatterer again are the result of a fitting to the permittivities and the positions of the corresponding permittivity cells.

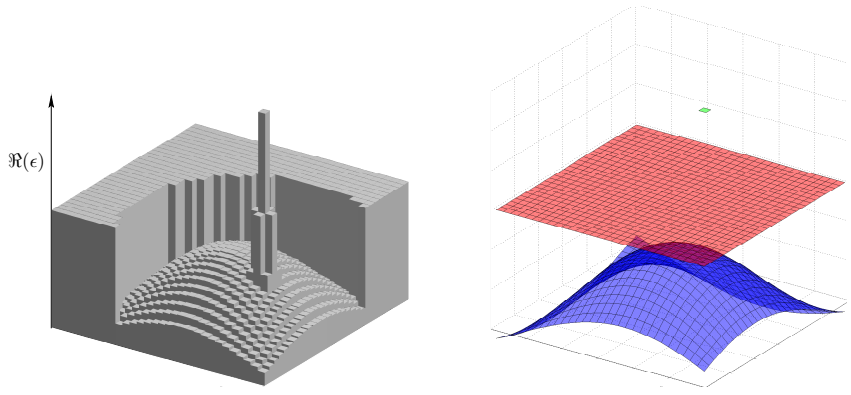

(a) (b)

Figure 4.27: The principle of RP regularization. Left: a real permittivity profile after a reconstruction with RP regularization with three different regions: a homogeneous region, a smooth region and a small-scatterer region. Right: a visual representation of the characteristics of the three regions: the position-independent permittivity value of the homogeneous region (red), the smooth parameter representation of the smooth region (blue) and the permittivity of the small scatterer, which corresponds to one position only (green).

This whole adaptive mechanism can again be contained within the definition of one cost function. If there are $K = P + T + S$ regions, i.e. P homogeneous regions, T small scatterers and S smooth regions, the RP cost function is defined as

$$\mathcal{F}^{RP} = \mathcal{F}^{LS} + \gamma \mathcal{F}^{K}, \tag{4.91}$$

where $\mathcal{F}^K$ is defined as

$$\mathcal{F}^K = \frac{1}{N^\epsilon} \sum_{\nu=1}^{N^\epsilon} f^K(u^H_{1,\nu}, \ldots, u^H_{P,\nu}, u^{SS}_{1,\nu}, \ldots, u^{SS}_{T,\nu}, u^S_{1,\nu}, \ldots, u^S_{S,\nu}). \tag{4.92}$$

Again, f^K is the K-dimensional choice function. The same techniques of Section 4.3.2 can be used to obtain a half-quadratic minimization scheme, both for updating the permittivity unknowns with a Gauss-Newton scheme, as for updating the characteristics of the regions in repeated quadratic minimization steps, which alternate with the permittivity updates.

Finally, a stepwise relaxed scheme is again expected to yield the best results. In such a scheme, different regions are gradually added to the reconstruction in order to relax the regularization. One could for example start with only the homogeneous background region. This would again be equivalent to a Tichonov regularization of the cost function. Then one could add one or more homogeneous regions or smooth regions and finally the small scatterers.

The stepwise relaxed RP (SRRP) regularization could be of use when reconstructing biomedical targets, such as the ones presented in Chapter 5. A human breast, for example, consists of a skin layer, which more or less is a homogeneous region; generally a larger volume of adipose-based tissue, which has low permittivity but is not entirely homogeneous and could be modelled by a smooth region; and finally some scattered fibro-glandular inhomogeneities and possibly tumors that are small-scale scatterers with high permittivity. The SRRP regularization has not been implemented yet and it remains to be investigated how feasible this approach really is.

4.6 Conclusion

In this Chapter, novel 3D microwave imaging algorithms were developed. These algorithms consist of the Gauss-Newton minimization of the least squares data fit cost function with additional regularization. Two regularization strategies were proposed in this Chapter. The multiplicative smoothing regularization imposes a smoothness constraint on the permittivity, but does that in an adaptive way. Less smoothing is automatically applied if the noise level is low. Knowledge of the noise level is therefore not needed for multiplicative smoothing. The new stepwise relaxed Value Picking regularization allows for the very accurate reconstruction of piecewise homogeneous permittivity profiles with minimal a priori information except for the piecewise homogeneity itself. This property is exploited by clustering the permittivity values in the complex plane around a number of VP values, which are treated as auxiliary optimization variables. The number of VP values is also adjusted in a stepwise relaxed VP regularization scheme. VP regularization can be easily incorporated in the Gauss-Newton framework thanks to a half-quadratic updating scheme. Extension of the VP

regularization to a Region Picking regularization is also possible and is expected to be a flexible regularization tool for the reconstruction of all sorts of permittivity profiles.

The combination of Gauss-Newton updates with an approximate line search proves to be an efficient and reliable minimization scheme. Although the Gauss-Newton update systems are generally ill-conditioned, they can be efficiently solved using a subspace preconditioned LSQR algorithm. This algorithm exploits the specific form of the singular value spectrum of the system matrix that arises when the Gauss-Newton method is supplemented with the above regularization methods. The SPLSQR algorithm relies on a splitting of the solution space in a coarse subspace and its orthogonal complement. The system, projected on the coarse subspace, is still ill-conditioned, but has small dimension. Therefore it can be solved directly without being affected by the ill-conditioning. The component of the solution in the remaining subspace is obtained through the iterative solution of a larger, but better conditioned system. Finally, when constraints have to be imposed on the permittivity variables, the line search path can be modified as described in Section 4.4.1, a feature which requires minimal adjustments to the core of the algorithm.

Bibliography

[1] R. Fletcher. *Practical Methods of Optimization.* John Wiley, New York, 1990.

[2] A. van den Bos. Complex Gradient and Hessian. *Vision, Image and Signal Processing, IEE Proceedings*, 141(6):380–383, 1994.

[3] A. Franchois and C. Pichot. Microwave Imaging - Complex Permittivity Reconstruction with a Levenberg-Marquardt Method. *IEEE Trans. Antennas Propagat.*, 45(2):203–215, 1997.

[4] O.M. Bucci, C. Gennarelli, and C. Savarese. Representation of Electromagnetic Fields over Arbitrary Surfaces by a Finite and Nonredundant Number of Samples. *IEEE Trans. Antennas Propagat.*, 46(3):351–359, 1998.

[5] J. De Zaeytijd, A. Franchois, C. Eyraud, and J. M. Geffrin. Full-Wave Three-Dimensional Microwave Imaging With a Regularized GaussNewton Method Theory and Experiment. *IEEE Trans. Antennas Propagat.*, 55(11):3279–3292, 2007.

[6] P.M. van den Berg, A.L. van Broekhoven, and A. Abubakar. Extended Contrast Source Inversion. *Inverse Problems*, 15(5):1325–1344, 1999.

[7] A. Abubakar and P.M. van den Berg. Total Variation as a Multiplicative Constraint for Solving Inverse Problems. *IEEE Transactions on Image Processing*, 10(9), 2001.

[8] A. Abubakar, P.M. van den Berg, and J.J. Mallorqui. Imaging of Biomedical Data Using a Multiplicative Regularized Contrast Source Inversion Method. *IEEE Trans. Microw. Theory Tech.*, 50(7):1761–1770, 2002.

[9] T.M. Habashy and A. Abubakar. A general framework for constraint minimization for the inversion of electromagnetic measurements. *Progress in Electromagnetic Research*, 46:265–312, 2004.

[10] G.H. Golub, M. Heath, and G. Wahba. Generalized cross validation as a method for choosing a good ridge parameter. *Technometr.*, 21:215–223, 1997.

[11] M. Bertero, C. De Mol, and E.R. Pike. Linear inverse problems with discrete data: II. Stability and regularisation. *Inverse Problems*, 4(2):573–594, 1988.

[12] G. Wahba. *Spline models for observational data*. SIAM, Philadelphia, 1990.

[13] P.C. Hansen. Analysis of discrete ill-posed problems by means of the L-curve. *SIAM Review*, 34(4):561–580, 1992.

[14] C.R. Vogel. Numerical solution of a non-linear ill-posed problem arising in inverse scattering. *Inverse Problems*, 1(4):393–403, 1985.

[15] A.N. Tikhonov and V.Y. Arsenine. *Solutions of Ill-Posed Problems*. Winston, Washington DC, 1977.

[16] W.C. Chew and Y.M. Wang. Reconstruction of Two-Dimensional Permittivity Distribution Using the Distorted Born Iterative Method. *IEEE Trans. Med. Imaging*, 9(2), 1990.

[17] N. Joachimowicz, C. Pichot, and J. Hugonin. Inverse Scattering: An Iterative Numerical Method for Electromagnetic Imaging. *IEEE Trans. Antennas Propagat.*, 39(12):1742–1752, 1991.

[18] A. Franchois and A.G. Tijhuis. A Quasi-Newton Reconstruction Algorithm for a Complex Microwave Imaging Scanner Environment. *Radio Science*, 38(2), 2003.

[19] K. Belkebir and M. Saillard. Testing Inversion Algorithms Against Experimental Data: Inhomogeneous Targets. *Inverse Problems*, 21(6):S1–S3, 2005.

[20] J.M. Geffrin, P. Sabouroux, and C. Eyraud. Free Space Experimental Scattering Database Continuation: Experimental Set-Up and Measurement Precision. *Inverse problems*, 21:117–130, 2005.

[21] P. Lewyllie, A. Franchois, C. Eyraud, and J.M. Geffrin. Testing a 3D BCGS-FFT solver against experimental data. *Proceedings of ICEAA'05*, (421–424), 2005.

[22] P.M. van den Berg and R.E. Kleinman. A total variation enhanced modified gradient algorithm for profile reconstruction. *Inverse Problems*, 11:5–10.

[23] C.R. Vogel and M.E. Oman. Fast, Robust Total Variation-Based Reconstruction of Noisy, Blurred Images. *IEEE Transactions on Image Processing*, 7(6):813–824, 1998.

[24] P. Charbonnier, L. Blanc-Féraud, G. Aubert, and M. Barlaud. Deterministic Edge-Preserving Regularization in Computed Imaging. *IEEE Trans. Image Process.*, 6(2), 1997.

[25] S. Geman and D. Geman. Stochastic relaxation, Gibbs distributions and the Bayesian restoration of images. *IEEE Trans. Pattern Anal. Machine Intell.*, PAMI-6:721–741, 1984.

[26] P. Lobel, C. Pichot, L. Blanc-Féraud, and M. Barlaud. Microwave imaging: Reconstructions from experimental data using conjugate gradient and enhancement by edge-preserving regularization. *International Journal of Imaging Systems and Technology*, 8(4):337–342, 1997.

[27] P. Lobel, C. Pichot, L. Blanc-Féraud, and M. Barlaud. Conjugate-gradient algorithm with edge-preserving regularization for image reconstruction from Ipswich data for mystery objects. *IEEE Antennas Propagat. Mag.*, 39(2):12–14, 1997.

[28] A. Litman, D. Lesselier, and F. Santosa. Reconstruction of a two-dimensional binary obstacle by controlled evolution of a level-set. *Inverse Problems*, 14:685–706, 1998.

[29] A. Litman. Reconstruction by level sets of n-ary scattering obstacles. *Inverse Problems*, 21:131–152, 2005.

[30] D. Colton and P. Monk. A modified dual space method for solving the electromagnetic inverse scattering problem for an infinite cylinder. *Inverse Problems*, 10:87–107, 1994.

[31] L. Crocco and T. Isernia. Inverse scattering with real data: detecting and imaging homogeneous dielectric objects. *Inverse Problems*, 17(6):1573–1583, 2001.

[32] A. Abubakar and P.M. van den Berg. The contrast source inversion method for location and shape reconstructions. *Inverse Problems*, 18:495–510, 2002.

[33] M. Jacobsen, P.C. Hansen, and M.A. Saunders. Subspace preconditioned LSQR for discrete ill-posed problems. *BIT Numerical Mathematics*, 43(5):975–989, 2003.

[34] C.C. Paige and M.A. Saunders. LSQR: An algorithm for sparse linear equations and sparse least squares. *ACM Trans. Math. Software*, 8:43–71, 1982.

[35] G. Strang. The discrete cosine transform. *SIAM Rev.*, 41:135–147, 1999.

CHAPTER 5

Applications of the 3D reconstruction algorithm

In this chapter some applications of the reconstruction algorithms developed in Chapter 4 are discussed, which are more realistic than the examples presented so far. In Section 5.1, the added realism comes from the application to biomedical imaging. This is not to say that the presented examples are entirely realistic. Due to the simplifications in our model – the homogeneous background medium, the fact that the antenna configuration is idealized by only considering non-interacting elementary dipoles – it is not yet applicable to real-world applications and the presented results are simulation studies. However, they are encouraging the further development of microwave medical imaging, which is gaining interest as an alternative or supplement to existing modalities, such as X-ray imaging, mainly because of the non-ionizing nature of microwaves and because the interaction of microwaves with biological tissue is governed by other material parameters. In Section 5.2, the realism comes from the data: in this section, real measurement data from the Fresnel Institute in Marseille are inverted.

Because biomedical targets are usually highly inhomogeneous, the multiplicative smoothing regularization is employed in 5.1. In contrast, the real world targets of the Fresnel Institute are perfect examples of piecewise homogeneous profiles with a small number of different permittivity values and the best results for these targets are obtained with SRVP regularization.

5.1 Biomedical examples

5.1.1 Synthetic arm phantom

The first example consists of a simplified model of a child's arm immersed in water. The phantom, together with the investigation domain $\mathcal{D}$ and the dipole configuration

is depicted in Figure 5.1. It consists of an oblique cylinder of muscle material with radius 3 cm and permittivity $(49.6 - 40.4j)\epsilon_0$ in which a simple bone structure with permittivity $(8.0-3.2j)\epsilon_0$ is contained. The bone is modelled with a cylinder of radius 1 cm and a sphere with radius 2 cm. For simplicity, we only consider the portion of this arm model that falls within the domain $\mathcal{D}$, which is a cube with side 10 cm. The rest of the arm is simply neglected. We want to reconstruct this phantom using microwaves with a frequency of 1 GHz. We chose a permittivity of $(77.3 - 21.2j)\epsilon_0$ for the water, which yields a background wavelength of $\lambda_\mathrm{b} = 3.38$ cm. All the permittivities are adopted from [1].

For the data generation, the domain $\mathcal{D}$ is discretized using $30 \times 30 \times 30$ cells in x-, y and z-directions both for the permittivity grid $\mathcal{D}^\epsilon$ and for the forward field grid $\mathcal{D}^\mathrm{F}$, which yields a cell size of 3.33 mm or $0.0987\lambda_\mathrm{b}$. The phantom is illuminated by 120 elementary dipole fields, radiated by elementary dipoles that are evenly distributed over 5 horizontal circles with radius 10.14 cm or $3\lambda_\mathrm{b}$, which have a vertical spacing of 2.36 cm or $0.7\lambda_\mathrm{b}$ (Figure 5.1). One half of the dipole orientations $\hat{\boldsymbol{u}}_i$ is oriented along the positive z-direction and the other half is oriented along the ϕ-direction (the azimuthal direction). For all these illuminations, the scattered field is calculated in the same dipole positions, along the same polarization directions $\hat{\boldsymbol{u}}_i$. In the notations of Section 2.3.1, we have $N^I = 120$, $N_i^R = 120$, $\forall i$, which results in $N^\mathrm{D} = 14400$.

For the reconstruction of the phantom, the domain $\mathcal{D}$ is discretized with $25 \times 25 \times 25$ cells in order to avoid committing an inverse crime. This corresponds to a total of $N^\epsilon = 15625$ permittivity unknowns. The problem thus is under-determined ($N^\epsilon > N^\mathrm{D}$), even more so when the redundancy in the data due to reciprocity is taken into account. The regularization thus has the additional role of keeping the problem solvable, since without it, the update system (4.36) would become singular. Indeed, the rank of the jacobian matrix $\boldsymbol{J}$ is smaller than N^ϵ. When the iterations proceed, the parameter λ_k in (4.36) becomes smaller and the system evolves toward a singular system, which provides extra motivation for the use of the subspace preconditioning of Section 4.4.2. Note that in practice, due to noise on the data or – in our simulation study – due to the misfits of the simulation grids for the data generation and the reconstruction, a perfect data fit is not possible and the system (4.36) never becomes singular. The SPLSQR algorithm is used with $N^v = 512$, which is the result of retaining only the discrete cosine basis vector with the 8 lowest spatial frequencies in the x-, y- and z-directions.

The inversion is started from a domain $\mathcal{D}$ filled with background medium and with a value $\alpha = 10^{-6}$ for the regularization parameter in (4.19). The result of Figures 5.2 and 5.3 is obtained in 7 iterations (i.e. 7 solutions of the update system (4.36)) after a total excecution time of about 5 hours and 45 minutes (on our computing modalities: a 64 bit computer with 2 GHz Dual Core AMD Opteron processor and 8 GB RAM) if the relative accuracy of the forward solver is set to 0.001. The data fit at this point is $\mathcal{F}^{LS} = 2.1 \cdot 10^{-4}$ and is not significantly reduced by proceeding with the iterations.

The constraints that were imposed on the permittivity unknowns were $1.0 < \Re(\epsilon_n) < 85.0$ and $-50.0 < \Im(\epsilon_n) < 1.0$. The fact that we allow for slightly positive imaginary parts is motivated by the observation that too severe constraints can stall or even stop the convergence by introducing local minima. From Figures 5.2 and 5.3 it can be concluded that a nice reconstruction is obtained, where the structures in the arm are clearly visible in the correct permittivity ranges. It deviates from the actual profile by its smoother appearance, which is due to the type of regularization we employed and the large influence of this regularization when the system is under-determined.

The marching-on technique of Section 3.7 has been used on this example with $M = 4$, i.e. the initial guess for a forward problem solution is obtained as a linear combination of the Born approximation (3.39) and the solutions for three previous transmitter positions on the same horizontal circle in Figure 5.1. There is no extrapolation over different dipole circles. Without the marching-on scheme, the total solution for the present example increases to about 8 hours, an increase of about 40%.

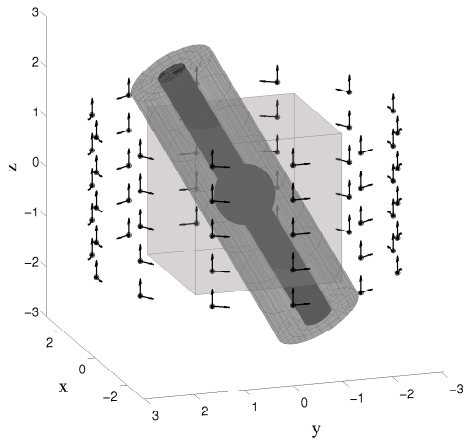

Figure 5.1: A view on the numerical Arm phantom, the investigation domain $\mathcal{D}$ (the cube in the figure) and the dipole configuration. Dipole positions are indicated by black dots and dipole orientations by arrows. All dipoles act as transmitter and receiver. Distances are expressed in background wavelengths.

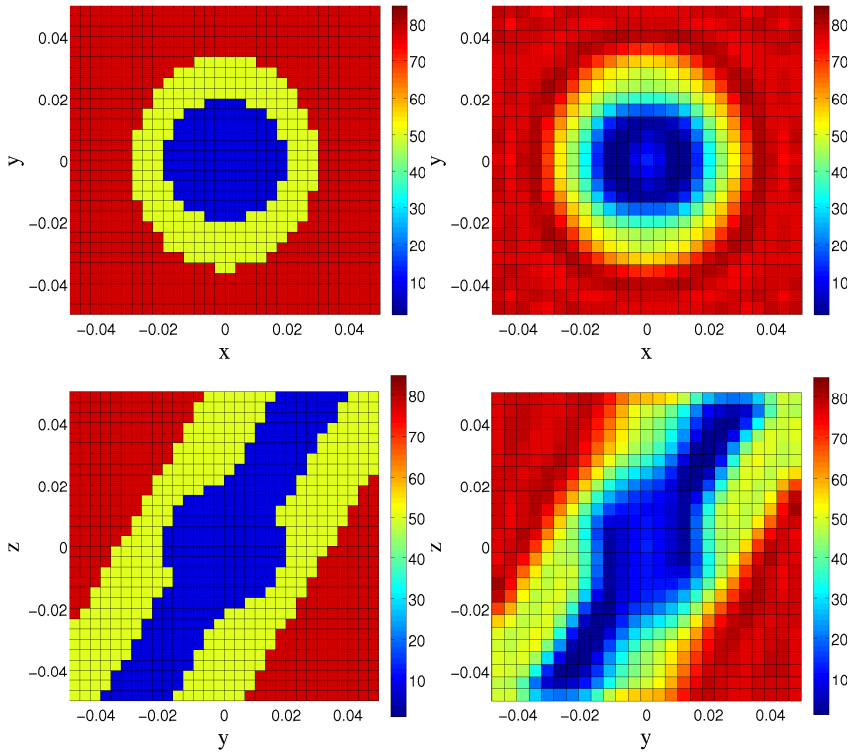

Figure 5.2: Reconstruction of the synthetic arm phantom with $\alpha = 10^{-6}$ in two planes through the center of the investigation domain $\mathcal{D}$, one parallel to the xy-plane and one parallel to the yz-plane. The left column shows the real part of the permittivity profile used to simulate the data and the right column shows the real part of the reconstructed permittivity on the coarser reconstruction grid.

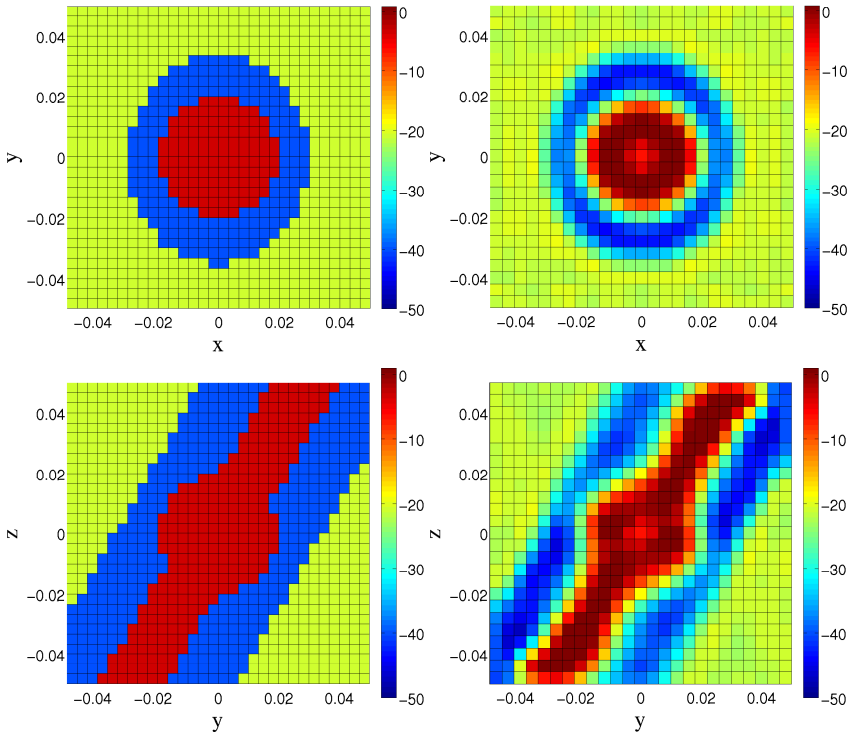

Figure 5.3: Reconstruction of the synthetic arm phantom with $\alpha = 10^{-6}$ in two planes through the center of the investigation domain $\mathcal{D}$, one parallel to the xy-plane and one parallel to the yz-plane. The left column shows the imaginary part of the permittivity profile used to simulate the data and the right column shows the imaginary part of the reconstructed permittivity on the coarser reconstruction grid.

5.1.2 MRI-based breast phantom

The second example is a numerical breast phantom, which is adopted from the online repository of the Department of Electrical and Computer Engineering at the University of Wisconsin-Madison (UWCEM). This online repository (see the web site http://uwcem.ece.wisc.edu/home.htm) provides a database of anatomically realistic MRI-based numerical breast phantoms, which capture the structural heterogeneity of normal breast tissue and incorporate the realistic dispersive dielectric properties of normal breast tissue from 0.5 to 20 GHz reported by Lazebnik et al [2, 3]. The phantom we consider in this thesis is Phantom 1 from ACR class 1 which is a mostly fatty breast phantom with some glandular and fibro-connective inhomogeneities. The complex permittivity in a slice through the breast phantom at a frequency of 2 GHz is depicted in Figure 5.4. As background medium in which the breast is immersed, we chose a material with permittivity $(10.0 - 2.0j)\epsilon_0$, which yields a background

wavelength $\lambda_{\mathrm{b}} = 4.72$ cm.

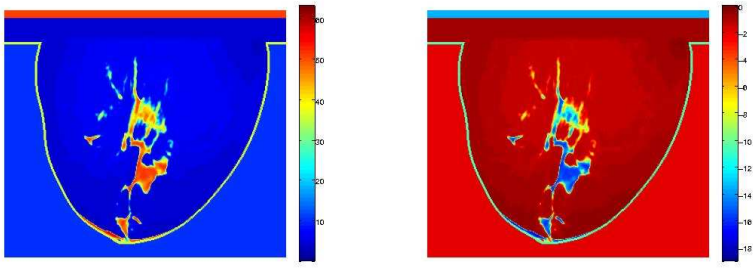

Figure 5.4: A view of the permittivity in a slice through the full-resolution MRI-based breast phantom from the online UWCEM repository at 2 GHz: (a) real part and (b) imaginary part.

Since the resolution of the MRI-based breast phantom is very high (it has a cell size of 0.5 mm) and since such a high resolution is not needed at the considered frequency, nor desirable due to the high memory needs and computation times, we derived a coarser permittivity model with cell size 2.5 mm ($0.053\lambda_{\mathrm{b}}$) from this phantom by local averaging. This coarser model is depicted in Figure 5.5 in the same slice. An artificial spherical tumor with permittivity $(50.0-10.0j)\epsilon_0$ and a radius of 1 cm is also added and rather close to the chest wall to make its detection even more challenging. We also removed the muscle layer from the original phantom, since in our free-space measurement setup this thin high-contrast layer would cause too much scattering at its (non-realistic) interfaces with the background medium. Although the present example is not entirely realistic due to the fact that it is a free-standing breast, not attached to a human body, the problem is challenging as it is.

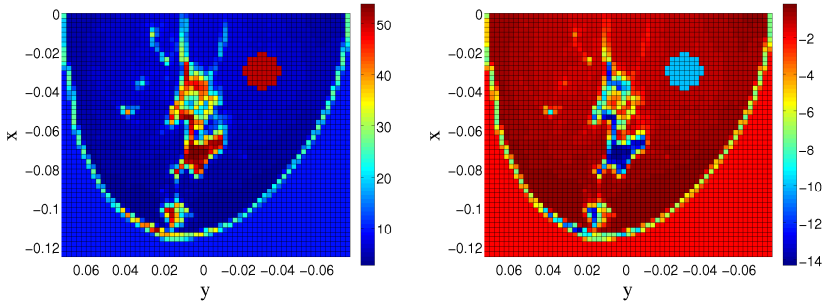

Figure 5.5: A view of the permittivity in a slice through the discretized breast phantom for the data generation. The cell size is 2.5 mm, an artificial tumor has been added to the phantom and the muscle layer has been removed: (a) real part and (b) imaginary part.

The dipole configuration which is used to generate the data is depicted in Figure

5.6. It consists of 168 dipoles on an ellipsoidal surface around the front side of the breast with polarizations in two orthogonal directions tangential to this surface. All these dipoles are used to sample the field, but only 48 of them (indicated with the larger black dots) are used to illuminate the phantom because of memory limitations (increasing the number of illuminations increases the size of the jacobian matrix too much). This yields a total of $N^D = 8064$ data points.

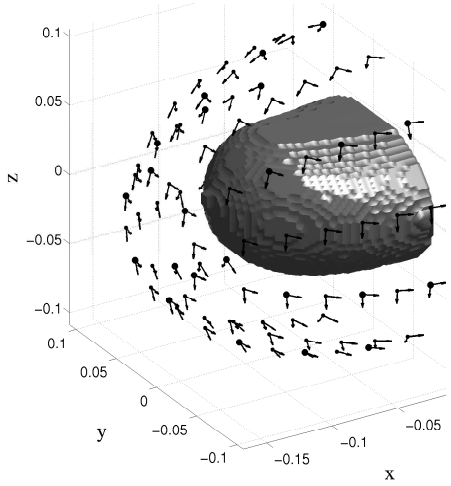

Figure 5.6: A view of the dipole configuration used to reconstruct the breast phantom. Dipole positions are indicated by black dots and dipole orientations by arrows. All dipoles act as receiver and transmitting dipoles are indicated with larger black dots. The gray shape represents the outline of the breast phantom. Distances are in meters.

The permittivity grid $\mathcal{D}^\epsilon$ for the reconstruction as well as the forward field grid $\mathcal{D}^F$ has cell size 5 mm ($0.106\lambda_\mathrm{b}$) with $25 \times 30 \times 21$ cells, which yields 15 750 permittivity unknowns. This means the problem is heavily under-determined and the regularization and subspace preconditioning are indispensable. For this example, the subspace dimension is $N^v = 560$, using the cosine base with respectively the 8, 10 and 7 lowest spatial frequencies in the x-, y- and z-directions, thus a coarse grid approximation with roughly one third of the resolution of the full permittivity grid. To test the abilities of the method, we perform a complete blind reconstruction, i.e. we do not use knowledge of the breast contour, as is sometimes suggested in the literature about microwave breast cancer imaging, and the initial estimate is just background medium. To keep the forward problems well-conditioned, the constraints on the permittivity were $1.0 < \Re(\epsilon_n) < 55.0$ and $-50.0 < \Im(\epsilon_n) < 1.0$. The result after 13 iterations and 18 hours and 25 minutes using a regularization parameter $\alpha = 10^{-5}$ is depicted in Figure 5.7. The marching-on scheme is again used with the same parameters as for the previous example. After 13 iterations the changes in the permittivity profile are less than

1 percent. The shape of the breast and the overall structure of the inhomogeneities are clearly visible in the reconstruction. The tumor is located correctly as well. Even the small lump of fibro-glandular tissue near the nipple can be resolved. However, the reconstructed permittivity and conductivity values of the inhomogeneities are too low. This is probably the result of the strong smoothing effect that is present in the reconstruction. The fact that the inverse problem is so heavily under-determined gives a lot of importance to the smoothing regularization. Nonetheless, despite its limitations, this reconstruction is a promising result for microwave imaging in biomedical applications.

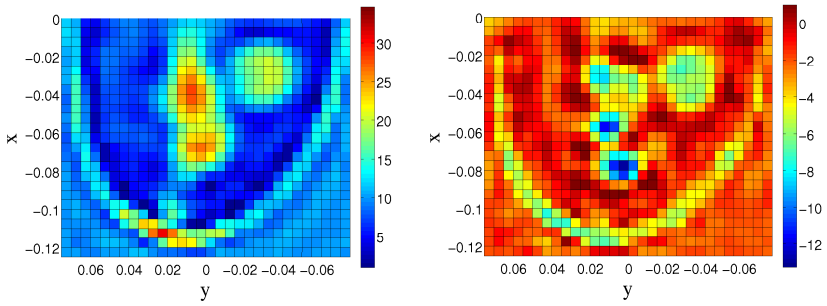

Figure 5.7: A view of the reconstructed permittivity in a slice through the investigation domain. (a) real part and (b) imaginary part.

Finally, we employ this example to illustrate the effect of the subspace preconditioning. We compare the efficiency of the SPLSQR algorithm to the efficiency of a conventional iterative solver without preconditioning in solving (4.36). The conventional solver is the Stabilized Bi-Conjugate Gradient method (BICGSTAB) [4]. For the first ($k = 0$) and the final ($k = 12$) Gauss-Newton iteration, we let the SPLSQR algorithm, with the same parameters as mentioned earlier, solve (4.86) to a relative accuracy of 10^{-4} and calculate the resulting accuracy on the original system (4.36). We then let BICGSTAB solve (4.36) to that accuracy and compare the number of iterations and the time needed by both methods. The comparison is summarized in Table 5.1. In the beginning of the optimization, the SPLSQR algorithm is more then 4 times faster then BICGSTAB and towards the end of the optimization, when the preconditioning becomes more crucial due to the decrease of the parameter λ in (4.36), the speed-up factor approaches 20. The reduction in solution time is less then the reduction in the number of iterations in the case $k = 0$, since the computation of the QR factorization (4.84) is also included in the former. Note that the time needed to solve (4.36) a single time *without* preconditioning is 90% of the total reconstruction time *with* preconditioning! Note furthermore that we use the BICGSTAB routine from the PIM library [4], which is an optimized fortran library, while we implemented the

SPLSQR ourselves in C, thus the speedup might even be more significant with an optimized implementation.

k	method	♯ iterations	time (s)	relative error in (4.36)
0	SPLSQR	30	630	$8.3 \cdot 10^{-6}$
	BICGSTAB	285	2631	$5.8 \cdot 10^{-6}$
12	SPLSQR	317	2991	$9.0 \cdot 10^{-6}$
	BICGSTAB	6472	59705	$8.5 \cdot 10^{-6}$

Table 5.1: A comparison between the SPLSQR algorithm and the BICGSTAB iterative method for the solution of (4.36) in case of the numerical breast phantom. The number of iterations, the solution time and the resulting accuracy are given for the first ($k = 0$) and the last ($k = 12$) step in the reconstruction algorithm.

5.1.3 The linear sampling method for breast imaging

Although quantitative microwave imaging is probably most suited for biomedical imaging, as far as reconstruction quality and information content of the images is concerned, it is very time consuming, as is apparent from the previous examples. Although the computational burden will without doubt be reduced in the future, for example by parallelization of the algorithms and by increasing computer resources, it is profitable to explore alternative imaging methods for biomedical imaging.

The recently developed linear sampling method [5, 6] can be used to detect scattering objects in a much cheaper way. It combines the advantages of solving a linear problem without introducing simplifications in the derivations of its equations and a very simple implementation. However, with the linear sampling method, it is only possible to infer information about the shape of the object and the image is only qualitative. It can however be useful when one is only interested in detecting anomalies against a known background. This could be the case when detecting breast cancer, where the tumor is the anomaly. The 3D vectorial linear sampling method for homogeneous backgrounds was proposed in [6, 7] and in [5, 8] a scalar linear sampling implementation for 2D inhomogeneous backgrounds is discussed. In this work, the 3D vectorial linear sampling method has been implemented and adapted to look for anomalies in general, 3D inhomogeneous backgrounds. A formal demonstration of the applicability of the linear sampling method to such problem is not yet available in literature at present and also not in this dissertation. We have restricted ourselves to an application of the basic principles of the linear sampling method.

Linear sampling principle

The terminology when using the linear sampling method differs from the terminology used so far for the quantitative inverse scattering problem. The “scatterer” now

refers to the unknown anomaly and the "background" can be a general, inhomogeneous dielectric environment and encompasses everything in the configuration which is known in advance. The incident field caused by the elementary dipole current $\boldsymbol{J}_{\delta,i}$ is now defined with respect to this inhomogeneous background. To avoid confusion, we will denote this field as $\boldsymbol{E}_i^{\mathrm{inc},I}$. In the terminology of Chapter 2, $\boldsymbol{E}_i^{\mathrm{inc},I}$ is the total electric field, in the presence of the known inhomogeneous background, but in absence of the anomaly. This field cannot be measured, but it can be simulated using the techniques of Chapter 3. The scattered field is now the difference of the total field $\boldsymbol{E}_i$ (the field due to $\boldsymbol{J}_{\delta,i}$ in the inhomogeneous background *with* tumor) and the incident field $\boldsymbol{E}_i^{\mathrm{inc},I}$ and it is denoted as $\boldsymbol{E}_i^{\mathrm{scat},I}$. The collection of data for the linear sampling method is the same as for quantitative inverse scattering, except that it is required in our implementation that the same receiving dipoles are used for every transmitting dipole. The position-orientation pairs $(\boldsymbol{r}_{l,i}, \hat{\boldsymbol{u}}_{l,i})$ for the receiving dipoles thus are simply denoted as $(\boldsymbol{r}_l, \hat{\boldsymbol{u}}_l)$ in the linear sampling method and their number as N^R. It is finally assumed that $N^R \geq N^I$.

In order to detect an anomaly in the breast, the discretized linear sampling method scans the investigation domain $\mathcal{D}$, i.e. for each point $\boldsymbol{r}_0$ on a testgrid that covers $\mathcal{D}$ the following system of linear equations is solved for the unknowns $g_{i,k}(\boldsymbol{r}_0)$:

$$\sum_{i=1}^{N^I} \left(\hat{\boldsymbol{u}}_l \cdot \boldsymbol{E}_i^{\mathrm{scat},I}(\boldsymbol{r}_l) \right) g_{i,k}(\boldsymbol{r}_0) = -j\omega\mu_0 \hat{\boldsymbol{u}}_l \cdot \boldsymbol{G}_{\mathrm{inh}}(\boldsymbol{r}_l, \boldsymbol{r}_0) \cdot \hat{\boldsymbol{v}}_k, \quad \forall l, k, \tag{5.1}$$

where $\hat{\boldsymbol{v}}_k$ is the direction of a test dipole which is placed in $\boldsymbol{r}_0$ and $\boldsymbol{G}_{\mathrm{inh}}(\boldsymbol{r}_l, \boldsymbol{r}_0)$ is the Green dyadic of the inhomogeneous background (the breast) for a source in $\boldsymbol{r}_0$ and a receiver in $\boldsymbol{r}_l$. The index k labels 3 orthogonal directions on the test grid. According to linear sampling theory, the indicator function $F(\boldsymbol{r}_0)$, defined as

$$F(\boldsymbol{r}_0) = \sum_{k=1}^{3} \sum_{i=1}^{N^I} \|g_{i,k}(\boldsymbol{r}_0)\|^2, \tag{5.2}$$

should become very large when $\boldsymbol{r}_0$ approaches the boundary of the anomaly from the inside or lies outside the anomaly. Again, this has not been formally demonstrated in the configuration under study.

A simulation of the incident dipole fields $\boldsymbol{E}_i^{\mathrm{inc},I}(\boldsymbol{r}_l) = -j\omega\mu_0 \boldsymbol{G}_{\mathrm{inh}}(\boldsymbol{r}_l, \boldsymbol{r}_i) \cdot \hat{\boldsymbol{u}}_i$ in presence of the breast with the VIE solver of Chapter 3 also yields the incident fields on the grid $\boldsymbol{E}_l^{\mathrm{inc},I}(\boldsymbol{r}_0) = -j\omega\mu_0 \boldsymbol{G}_{\mathrm{inh}}(\boldsymbol{r}_0, \boldsymbol{r}_l) \cdot \hat{\boldsymbol{u}}_l$, which can be used in the right hand side of (5.1) after an application of the reciprocity property

$$\hat{\boldsymbol{v}}_k \cdot \boldsymbol{G}_{\mathrm{inh}}(\boldsymbol{r}_0, \boldsymbol{r}_l) \cdot \hat{\boldsymbol{u}}_l = \hat{\boldsymbol{u}}_l \cdot \boldsymbol{G}_{\mathrm{inh}}(\boldsymbol{r}_l, \boldsymbol{r}_0) \cdot \hat{\boldsymbol{v}}_k. \tag{5.3}$$

A simulation of the incident field thus also yields the numerical values of the inhomo-

geneous Green dyadic that are needed by the Linear Sampling method.

Implementation

In order to compute the solution of the system (5.1), we will express it in a matrix notation:

$$\boldsymbol{A}^{\mathrm{scat}}\boldsymbol{g} = \boldsymbol{B}, \tag{5.4}$$

where the $(N^R \times N^I)$ - matrix $\boldsymbol{A}^{\mathrm{scat}}$ contains the scattered field for every transmitter-receiver combination, the colums of the matrix $\boldsymbol{g}$ $(N^I \times 3N^G)$ contain the unknown coefficients $g_{i,k}(\boldsymbol{r}_0)$ for every one of the N^G test points $\boldsymbol{r}_0$ on the grid and for every test direction $\hat{\boldsymbol{v}}_k$. The matrix $\boldsymbol{B}$ $(N^R \times 3N^G)$ contains the fields due to the test dipoles at the receiver locations. The system (5.4) is an ill-posed system. Consider the singular value decomposition (SVD) of the matrix $\boldsymbol{A}^{\mathrm{scat}} = \boldsymbol{U}\mathbf{S}\boldsymbol{V}^H$, where $\boldsymbol{V}^H\boldsymbol{V} = \boldsymbol{I}_{N^I}$ and $\boldsymbol{U}^H\boldsymbol{U} = \boldsymbol{I}_{N^I}$, with $\boldsymbol{I}_{N^I}$ being the $N^I \times N^I$ identity matrix, and $\mathbf{S}$ a diagonal matrix containing the singular values of $\boldsymbol{A}^{\mathrm{scat}}$ in decreasing order. The spectrum of $\boldsymbol{A}^{\mathrm{scat}}$ rapidly decreases and therefore the smallest singular values and the corresponding singular vectors are corrupted by noise on the measurements. As in [6], a Tichonov regularization is used to calculate a regularized solution $\boldsymbol{g}^\alpha$:

$$\left[\left(\boldsymbol{A}^{\mathrm{scat}}\right)^H \boldsymbol{A}^{\mathrm{scat}} + \alpha \boldsymbol{I}_{N^I}\right] \boldsymbol{g}^\alpha = \left(\boldsymbol{A}^{\mathrm{scat}}\right)^H \boldsymbol{B} \tag{5.5}$$

and using the SVD of $\boldsymbol{A}^{\mathrm{scat}}$, we obtain

$$\|\boldsymbol{g}^\alpha\|_m^2 = \sum_{i=1}^{N^I} \frac{\sigma_i^2}{\left(\sigma_i^2 + \alpha\right)^2} \|\mathbf{u}_i^H \boldsymbol{B}\|^2, \tag{5.6}$$

where σ_i is the i-th singular value of $\boldsymbol{A}^{\mathrm{scat}}$ and $\mathbf{u}_i$ the i-th right singular vector, where $\|\cdot\|$ represents the two-norm for a vector and where $\|\mathbf{g}\|_m^2 = \sum_k \|\boldsymbol{g}_k\|^2$, with $\boldsymbol{g}_k$ the k-th column of $\boldsymbol{g}$. In order to calculate the regularization parameter α, the discrepancy principle is again employed (the error on the system (5.4) is equal to the error introduced by the noise):

$$\left\|\boldsymbol{A}^{\mathrm{scat}}\boldsymbol{g}^\alpha - \boldsymbol{B}\right\|_m^2 = \epsilon^2 \left\|\boldsymbol{g}^\alpha\right\|_m^2 \tag{5.7}$$

with ϵ the largest singular value of the noise matrix $\boldsymbol{A}^{\mathrm{scat}} - \boldsymbol{A}^{\mathrm{scat}}_{clean}$, where $\boldsymbol{A}^{\mathrm{scat}}_{clean}$ is the ideal, noise free data matrix. (5.7) can be reformulated using (5.6) and the SVD factorization, resulting in

$$f(\alpha) = \sum_{i=1}^{N^I} \frac{\alpha^2 - \epsilon^2\sigma_i^2}{\left(\sigma_i^2 + \alpha\right)^2} \|\mathbf{u}_i^H \boldsymbol{B}\|^2 = 0. \tag{5.8}$$

The chosen regularization parameter thus is the root of $f(\alpha)$ and $f(\alpha)$ has a unique root in the interval $]0, \epsilon\sigma_1]$ since $f(0) < 0$, $f(\epsilon\sigma_1) \geq 0$, $f(\alpha)$ is continuous for $\alpha \geq 0$ and $df/d\alpha > 0$ for $\alpha \geq 0$.

Application

As an example, consider the same breast phantom as in Section 5.1.2. The goal is to locate the tumor when the permittivity distribution in the rest of the breast phantom is known or approximately known. The operating frequency is again 2 GHz, but the dipole configuration is slightly different. The same dipole positions are used, but there is only one polarization per dipole position. However, all dipoles are used to illuminate the phantom (Figure 5.8). This yields $N^I = N^R = 84$. Apart from the 2.5 mm phantom of Figure 5.5, we derived a second, coarser grid approximation to the full-resolution phantom of Figure 5.4 with cell size 5 mm.

Two linear sampling solutions were calculated. For the first one, the measurement data (i.e. $\hat{\boldsymbol{u}}_l \cdot \boldsymbol{E}_i(\boldsymbol{r}_l)$) were generated with the 5 mm model with tumor, and the incident dipole fields (i.e. $\hat{\boldsymbol{u}}_l \cdot \boldsymbol{E}_i^{\mathrm{inc},I}(\boldsymbol{r}_l)$) as well as the Green dyadic were calculated for the 5 mm model without a tumor. To make this example somewhat more realistic, additive Gaussian noise corresponding to SNR = 30 dB is added to the data, before the scattered field ($\hat{\boldsymbol{u}}_l \cdot \boldsymbol{E}_i^{\mathrm{scat},I}(\boldsymbol{r}_l) = \hat{\boldsymbol{u}}_l \cdot \boldsymbol{E}_i(\boldsymbol{r}_l) - \hat{\boldsymbol{u}}_l \cdot \boldsymbol{E}_i^{\mathrm{inc},I}(\boldsymbol{r}_l)$) is calculated. The indicator function F in a slice through the tumor center is depicted in Figure 5.9(a). The tumor is clearly visible as the region with minimal indicator values. For the second example, the data were generated using the 2.5 mm model with tumor, while the incident fields and the Green dyadic are calculated with the 5 mm model without tumor, thus creating a mismatch between the actual and estimated background. Although the linear sampling image is not as clear as the previous one, the tumor can still be detected, as appears from Figure 5.9(b).

The linear sampling method thus might provide a computationally cheap means to detect breast cancer. However, it requires an estimate of the breast permittivity without a tumor. From the presented example it can be concluded that the background does not need to be rigorously known. An estimate is sufficient, but it remains yet to be investigated how much this estimate can deviate from the actual background for the tumor to be detectable. Maybe the linear sampling method can be used for monitoring purposes, where one is interested in following the evolution of a tumor. In such case it might be possible to perform a detailed, quantitative scan of the breast in an initial stage and use the information obtained from that to estimate the background, which can then be used in subsequent rapid scans with the linear sampling method.

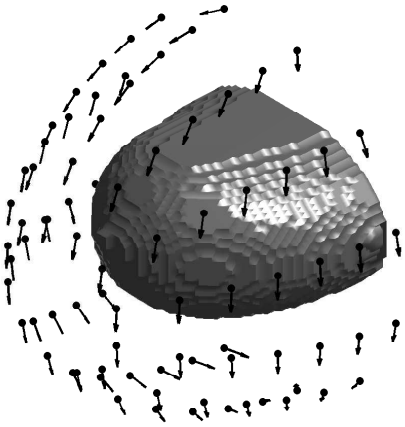

Figure 5.8: The dipole configuration for the Linear Sampling application.

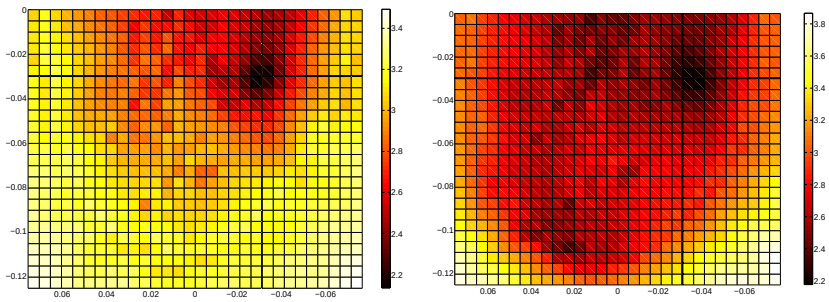

(a) (b)

Figure 5.9: A slice through the indicator function F for the two linear sampling reconstructions: (a) for data obtained with the coarse model and using the coarse model for the background, (b) for data obtained with the fine model and using the coarse model for the background. Values are in a logarithmic scale.

5.2 Inversion of experimental data

The data used in this section were gathered in the bi-static polarimetric free-space measurement facility of Institut Fresnel, Marseille, France. The data for the first target, an inhomogeneous cube, was made available to us exclusively and the data for the homogeneous targets which follow is part of a 3D database. We were invited by the SEMO group at Institut Fresnel to process these data and publish the results in a special section in Inverse Problems, together with a number of other researchers.

In an anechoic chamber, the target is illuminated by a plane wave, generated by a parabolic antenna (Figure 5.10). To obtain a good agreement between the incident dipole fields in our simulations and the actual incident field from the parabolic antenna in the measurement setup, the source dipoles are positioned far from the target, such that they approximate a plane wave in the center of the measurement setup. To allow for a comparison between simulation and measurements, the measured scattered field has been normalized by the people of the Fresnel Institute such that it corresponds to an incident field with amplitude 1 and zero phase at the origin. The 162 transmitting dipoles are depicted in Figure 5.11(a). The dipole directions are evenly distributed over the θ and ϕ directions to match the orientation of the plane waves in the measurement setup. The scattered field is collected in 36 points on a circle with radius 1.796 m in the horizontal plane and along the negative z-direction, as depicted in Figure 5.11(b). Note that, due to technical limitations, only receivers that are further away than 50° from the source meridian are used. The dimension N^D of the data vector will not be the same in all reconstructions to follow, because some measurements are excluded due to saturation of the equipment. More details about the measurement setup and methodology can be found in [9–11]. Throughout the rest of the section all targets are embedded in free space (i.e. $\epsilon_{\mathrm{b}} = \epsilon_0$).

Figure 5.10: The experimental setup of Institut Fresnel. Two parabolic transmitting antennas move on a vertical arc, while a receiving horn antenna moves on a horizontal arc. The target is positioned on top of the white cone in the center of the setup, which can be rotated around its axis to illuminate the target from different azimuthal angles.

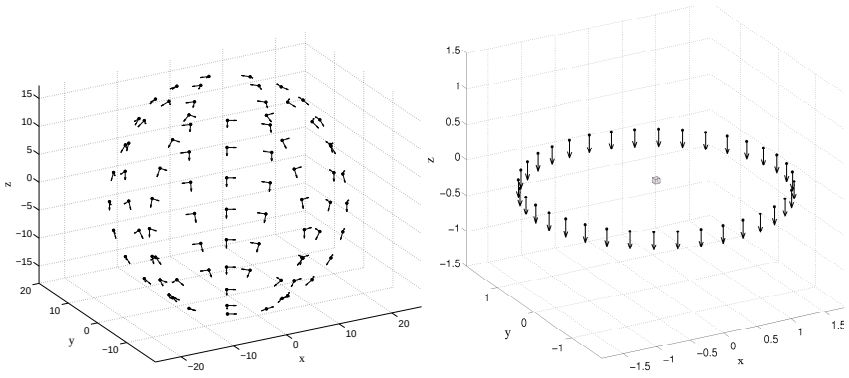

(a) (b)

Figure 5.11: The dipole configuration used for the reconstructions from the Fresnel data. 162 transmitting dipoles are placed on a sphere with radius 20 m and are oriented along the θ and ϕ directions (a) and 36 receiving dipoles are placed on a circle with radius 1.796 m in the horizontal plane and are oriented along the negative z axis (b). A typical investigation domain $\mathcal{D}$ is also depicted in (b).

5.2.1 Reconstruction of an inhomogeneous cube

We consider the reconstruction of a first real world target at an operational frequency of 8 GHz, which yields a background wavelength $\lambda_\mathrm{b} = 0.0375$ m. The target consists of a cube with side $0.67\lambda_b$ and permittivity $2.35\epsilon_0$, which is embedded in a larger cube with side $1.33\lambda_b$ and permittivity $1.45\epsilon_0$ (Figure 5.12). Within the uncertainty introduced by positioning errors, the smaller cube is centered at the point $(-0.33\lambda_b, 0.33\lambda_b, 0.33\lambda_b)$ and the larger cube at the point $(-0.27\lambda_b, 0.27\lambda_b, 0.40\lambda_b)$. The dimension of the data vector for this reconstruction is $N^D = 4365$.

The investigation domain $\mathcal{D}$ in this example is a cube with side $2.00\lambda_b$, centered at $(-0.27\lambda_b, 0.27\lambda_b, 0.40\lambda_b)$ and with edges parallel to the coordinate axes. The permittivity grid has a cell size of $0.08\lambda_b$ ($= 3$ mm), which results in 25 cells in each direction and a total of $N^\epsilon = 15625$ permittivity unknowns. Considering the limited number of data, this inverse problem thus is heavily under-determined, hence without regularization, problems can arise with the uniqueness of the solution. Moreover, the update system (4.59) would be singular when $\lambda = 0$, a problem which has been encountered before. Thanks to the VP regularization, however, a good result can still be obtained. As far as noise is concerned, there are the unavoidable measurement noise and also the discretization errors of the forward model, especially since no attempt has been made to align the permittivity grid with the actual permittivity profile of the target, i.e. the faces in the permittivity grid do not coincide with the interfaces in the scatterer. From a number of reconstructions with the multiplicative smoothing regularization with different regularization parameters, the noise level is estimated as

$T^N \approx 10^{-2}$.

The reconstruction shown in Figure 5.13 is obtained with $\gamma = 5.0$, a rather large regularization parameter because of the high amount of noise on the data. To compensate for the high noise level and the fact that the system is under-determined, some additional a priori information of the scatterer is employed: the VP values are kept real, satisfying the physical constraint $c_p \geq 1.0$. A new VP value is added each time the criterion $\|\boldsymbol{g}^Q\| \leq \sqrt{2} \cdot 10^{-4}$ (see (4.52)) is met or when the least squares data fit increases again. Starting from the background permittivity in $\mathcal{D}$, this yields 6 iterations with $P = 1$, 3 iterations with $P = 2$ and 8 iterations with $P = 3$. The position and dimensions of both cubes are quite accurately reconstructed within the resolution offered by the permittivity grid, although the inner cube is slightly too large. The reduced accuracy in the vertical direction is due to the antenna configuration, where the receiving antenna positions all are in the horizontal plane and where the transmitting dipoles are spaced further apart and span a smaller arc than the receiving dipoles. From the final VP values $\{1.42, 2.01, 1\}$ it can be concluded that the permittivity of the outer cube is accurately reconstructed and that the permittivity of the inner cube is a bit too low. However, the profile is almost piecewise constant and yields a data fit on the noise level, as can be seen from the swarm plot in Figure 5.14 (a) and the data fit curves in Figure 5.15.

The present example can be used to illustrate that the VP regularization allows for the introduction of a priori knowledge on the scatterer in an easy manner. Suppose we know that one of the permittivities in the profile is likely to be larger than 2. The lower bound on the last added VP value then can be set to 2. The result of this assumption is depicted in Figure 5.16. Again the data fit is on the noise level (Figure 5.15) and the profile is close to piecewise homogeneous (Figure 5.14 (b)) with VP values $\{1.46, 2.26, 1\}$. The additional bound thus is not restrictive in the final reconstruction, since the corresponding VP value has moved away from it. Considering only the data fit and the amount of clustering in the permittivity values, the reconstructions of Figure 5.13 and Figure 5.16 are hardly distinguishable. In the second reconstruction, however, the permittivities are much better estimated, although the inner cube is somewhat smaller.

Finally, again for comparison, a reconstruction with multiplicative smoothing regularization is shown in Figure 5.17. The noise level is reached in only 4 iterations as can be seen in Figure 5.15, but the result is not as good as with VP regularization. The overall structure of the target is present, but due to the smoothness of the reconstruction, the dimensions of the cubes as well as their permittivity cannot be easily estimated. This becomes very apparent in a swarm plot (Figure 5.14 (c)), where no clusters of permittivity values can be detected. Moreover, the imaginary parts are spread out too far from the real axis.

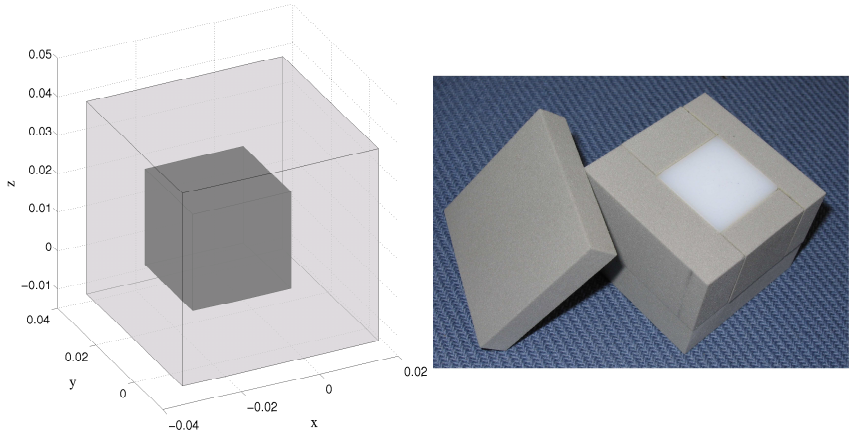

(a) (b)

Figure 5.12: The inhomogeneous cube target. A small cube with side 25 mm and permittivity $1.45\epsilon_0$ is embedded in a larger cube with side 50 mm and permittivity $2.35\epsilon_0$. Sketch (a) and a photograph of the actual target (b).

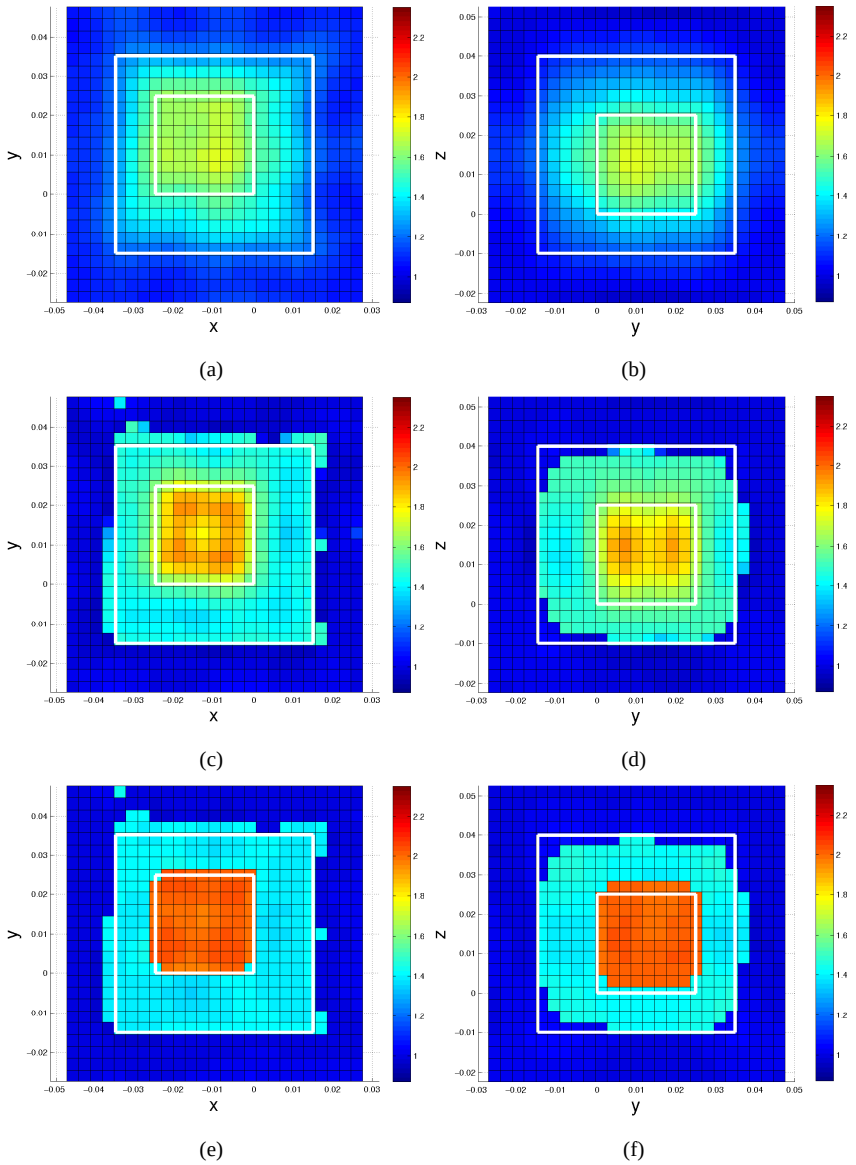

Figure 5.13: Reconstruction at 8 GHz with SRVP regularization ($\gamma = 5.0$ and real VP values) of the target of Figure 5.12. The initial guess is $\epsilon = \epsilon_0$ everywhere. Real part of the permittivity in two orthogonal cuts (left: xy-plane, right: yz-plane) through the center of the investigation domain for $P = 1$ after 6 iterations (a),(b), $P = 2$ after 3 iterations (c),(d) and $P = 3$ after 8 iterations (e),(f). The solid white lines indicate the contours in the actual target.

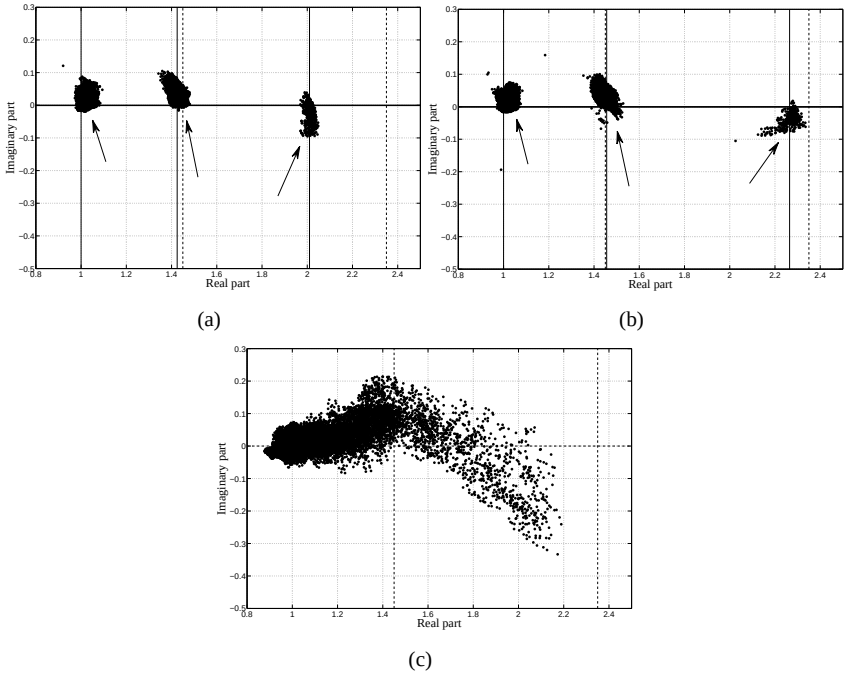

Figure 5.14: Swarm plot of the N^{ϵ} complex permittivity values on the grid, represented with dots in the complex plane, for the reconstructions of the target of Figure 5.12 from measured data. Reconstructions: (a) of Figure 5.13 (e),(f) using SRVP regularization with real VP values; (b) of Figure 5.16 using SRVP regularization with real VP values and an extra lower bound of 2 on the highest permittivity value; (c) of Figure 5.17 with multiplicative smoothing. The VP values are indicated as the intersections of the solid horizontal line and the solid vertical lines and the exact permittivity values are indicated with dashed lines.

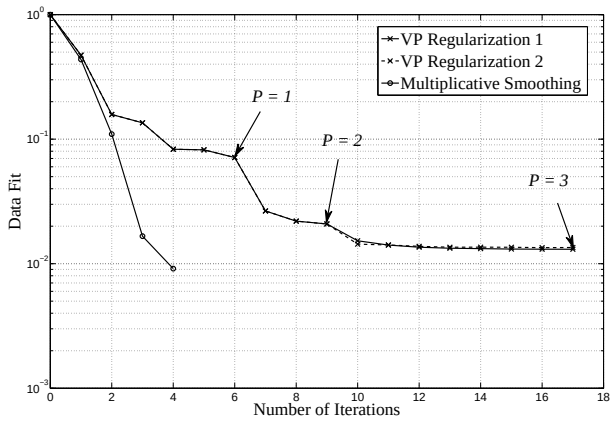

Figure 5.15: The data fit cost function $\mathcal{F}^{LS}$ versus the number of iterations for the reconstructions from measured data using VP regularization with real VP values (VP regularization 1), using SRVP regularization with real VP values and a lower bound of 2 on the largest VP value (VP regularization 2) and using multiplicative smoothing regularization. The end of each step in the stepwise relaxed VP regularization scheme is indicated with an arrow. An extra VP value is added when $\|\boldsymbol{g}^Q\| \leq \sqrt{2} \cdot 10^{-4}$ or when the data fit cost function $\mathcal{F}^{LS}$ increases again.

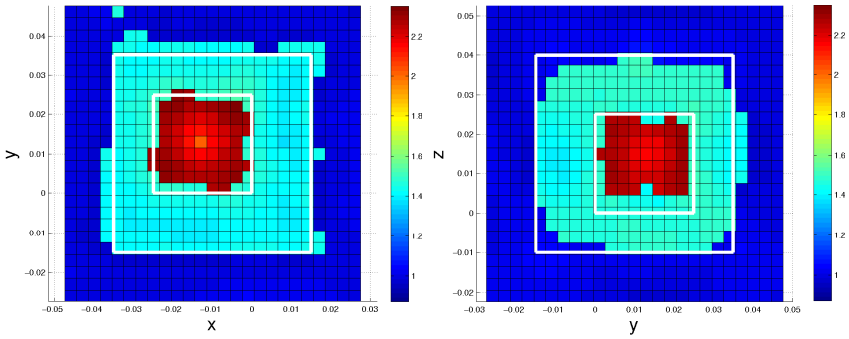

(a) (b)

Figure 5.16: The same as Figure 5.13 (e),(f) but with an additional lower bound of 2 for the highest permittivity value.

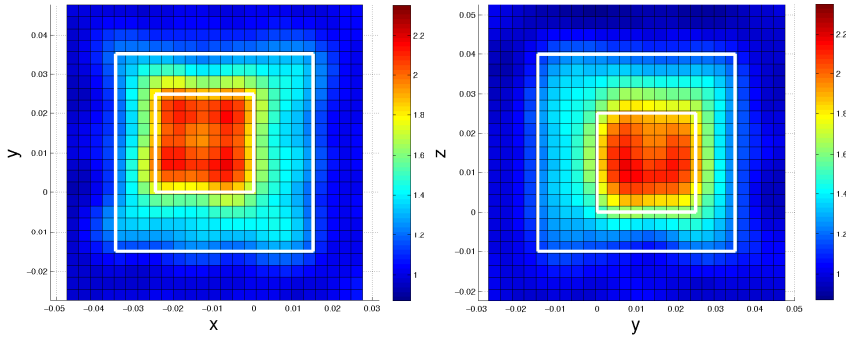

(a) (b)

Figure 5.17: Reconstruction at 8 GHz with multiplicative smoothing regularization of the target of Figure 5.12 from measured data. The initial guess is $\epsilon = \epsilon_0$ everywhere. Real part of the permittivity in two orthogonal cuts through the center of the investigation domain.

5.2.2 Reconstructions of homogeneous objects

The rest of the reconstructions in this chapter involve homogeneous objects, i.e. only two permittivity values are present in the permittivity profiles, the background permittivity and the permittivity of the target. To compensate for the high noise levels of the Fresnel data, this information will be explicitly used from now on. This means the the SRVP regularization scheme will be terminated after the step with $P = 2$. The study of every target starts with a first reconstruction using MS regularization to get an idea of the noise level. Remember that in Section 4.2.1 it is explained that the optimization with multiplicative smoothing usually stagnates when $\mathcal{F}^{LS}$ reaches the noise level, at which point an appropriate level of regularization is automatically selected. In the second step, the stepwise relaxed VP regularization (SRVP) (see Section 4.3.3) is employed. In all the following reconstructions, the permittivity variables are constrained as

$$\Re(\epsilon_\nu) > 0.5 \tag{5.9}$$

$$\Im(\epsilon_\nu) < 0.3 \tag{5.10}$$

which are only used to prevent ill-conditioning of the forward problems. The VP values are kept real and we impose an additional physical constraint:

$$c_p > 1.0. \tag{5.11}$$

Although the VP regularization yields excellent results on synthetic data with moderate noise levels (an SNR of about 30 dB, $T^N \approx 10^{-3}$) (see Section 4.3.4), we noticed in Section 5.2.1 that there are some difficulties when using it on the mea-

sured data of the Fresnel Institute, which turn out to have noise levels about ten times higher ($T^N > 10^{-2}$; estimated using the multiplicative smoothing reconstruction). For such noise levels a strong regularization (i.e. a large regularization parameter γ) is needed to obtain profiles that are close to piecewise homogeneous with only two permittivity values. In the following examples, it will be observed, however, that this can result in reconstructions in which the dimensions of the objects are overestimated, while their permittivity is underestimated, although the data fit is on the noise level and the reconstruction is close to piecewise homogeneous. This can be explained as follows: in the first step of the SRVP scheme with $P = 1$, the regularization keeps the permittivities close to the background permittivity. In the second step, a VP value is initialized at random and immediately updated (as outlined in Section 4.3.3), based on the permittivity profile after step 1. Its initial value will therefore be rather low. Apparently, due to the high noise level, the data does not contain enough information to force this second VP value sufficiently up the real axis before the data fit reaches the noise level. Extra information could be added by using multi-frequency data, e.g. by including the measured scattered field for different frequencies in the data vector $\boldsymbol{e}^{\mathrm{meas}}$ in (4.1) and by accordingly extending $\boldsymbol{e}^{\mathrm{scat}}$ through forward simulations at these different frequencies (in case of the non-dispersive Fresnel targets, no adjustments would have to be made to the regularization functions). Since we only consider single-frequency inversion, however, we have to add other a priori information.

Fortunately, the VP regularization scheme allows for the flexible introduction of such extra problem specific a priori information. In Section 5.2.1, a lower bound on the last added VP value is used. The obvious difficulty with this is where to put it without a priori information on the target. Here, a different approach is taken: an extra term is added to the cost function in the step with $P = 2$, which only depends on c_1 (the only VP value that is optimized for, since c_2 is kept fixed), i.e. we minimize

$$\mathcal{F}^{VP} + \gamma\eta\|c_1 - d_1\|^2, \tag{5.12}$$

where d_1 is some relative permittivity value which is expected to be somewhat larger then the largest permittivity in the actual profile. This will encourage the VP value c_1 to take on higher values when it is too far away from d_1. Note that the extra (quadratic) term in (5.12) does not interfere with the updating scheme for the permittivity vector, it only matters in the updating of the VP value c_1, where it is simply incorporated in the iterated quadratic minimization outlined in Section 4.3.2. The determination of the parameters γ, η and d_1 in the following is done by numerical experimentation, but is based on a set of criteria that does not use a priori information on the target. The strategy will become clear in the following paragraphs.

Two Spheres

The Two Spheres target consists of two spheres with a diameter of 50 mm and a permittivity $2.6\epsilon_0$. We employ 4 GHz data to reconstruct this target. The investigation domain $\mathcal{D}$ is a cuboid with dimensions $15.0\text{cm} \times 7.5\text{cm} \times 7.5\text{cm}$ (or, in background wavelengths λ_0: $2\lambda_0 \times \lambda_0 \times \lambda_0$) which is centered at the origin. A $40 \times 20 \times 20$ permittivity grid is used to discretize this domain with a cell size of 3.7 mm or $0.05\lambda_0$. This yields 16000 permittivity unknowns for a total of 4322 data points. The problem thus is heavily under-determined. For all reconstructions presented in the rest of this chapter, the uniform discretization grid for the fields in the forward scattering simulation coincides with the permittivity grid.

For the initial reconstruction with multiplicative smoothing, the smoothing parameter α is set to $\alpha = 10^{-3}$. After 9 iterations, the result of Figures 5.19 (a) and (b) is obtained. The data fit cost function throughout the minimization is given in Figure 5.18. We conclude that the noise level is somewhere around 0.04. The reconstruction clearly shows the spheres, but there is a very smooth transition from the background to the object. In the swarm plot of Figure 5.20 (a) the permittivity values are very much spread out, whereas in the swarm plots of the SRVP reconstructions in Figures 5.20 (b)-(e) they are clustered around the VP values. For these SRVP reconstructions, the regularization parameter is chosen to be $\gamma = 1.0$, a value which is obtained by experimentation: it should be small enough to allow reaching a comparable data fit as with multiplicative smoothing and yet it has to be high enough to get nice clustering. This experimentation can be done with $\eta = 0$ in (5.12), because the size of the clusters with other values of η is comparable, as can be seen in Figure 5.20, where $d_1 = 3$. With $\eta = 0$, the reconstructed spheres are too large while their permittivity is too low ($c_1 = 2.22$) (Figures 5.19 (c) and (d)), as anticipated.

The question remaining is: how can one choose η to prevent this without knowing the target? Typically, incorrect choices made by the VP regularization are compensated to keep the data fit cost function small. If, for a certain permittivity cell ν the largest VP value is chosen (i.e. $\epsilon_\nu \approx c_1$), while it should be a background cell (i.e. $\epsilon_\nu \approx c_2 = 1$), often the surrounding background cells have too low a permittivity, such that the local spatial permittivity average around the erroneous cell (on a subwavelength scale) is approximately the same as in the ideal configuration, yielding approximately the same data fit. From Figure 5.18 it can indeed be seen that all reconstructions yield an almost identical data fit. This compensating behavior can be detected in the swarm plots of Figure 5.20, for example in (b) and (c), since a number of permittivity values from the cluster around the background permittivity spread reasonably far to the left. This indicates that the value of η should be increased. However when η is increased too much, the permittivity values inside the target tend to be too high and this is again compensated by introducing cells with a permittivity value that is lower than the background permittivity, as can be seen in Figure 5.20 (e) where a few permittivity values are pressed against the lower bound on the real part

of the permittivity, and in Figure 5.19 (g) and (h) where the corresponding cells can be located inside the spheres. Looking only at the swarm plots, the reconstruction with $\eta = 0.025$ exhibits least of this compensating behavior and therefore is the best reconstruction among the presented ones according to our criteria. It turns out that it is also the best reconstruction when considering the actual target: the shape is accurately reconstructed within the resolution offered by the permittivity grid (bearing in mind possible positioning errors in the measurements; the reconstructions suggest a small offset, mainly in the vertical direction) and the permittivity of the reconstructed spheres is fairly close to the permittivity of the actual spheres.

Finally, the clustering of the permittivity values when using VP regularization allows for the definition of "the surface of the reconstructed target"; it is the surface that separates low permittivity values from high ones. The surface of the reconstruction with $\eta = 0.025$ is presented in Figure 5.21.

The computation time to solve the inverse scattering problem with multiplicative smoothing for this example is about 4 hours and 20 minutes on a machine with 2 quadcore AMD Opteron 2350 processors (2GHz) with 32 GByte of memory. For the reconstructions of the homogeneous Fresnel targets, the algorithms use the multithreading functions of the FFTW library [12] to distribute the computation of the FFT's needed by the forward solver over the 8 processors of the machine. 63% of this time goes to the iterative solution of the MoM-systems of the forward problem and about 13% goes to the solution of the complex update systems (4.36). The rest of the time largely goes to the computation of the scattered field on the receivers from the internal field distributions and to the calculation of the Jacobian matrix $\boldsymbol{J}$ in each iteration. The total solution time for the SRVP reconstruction of Figures 5.19 (e) and (f) is about 6 hours and 30 minutes, 63% of which is spent on the forward problems and 9% on the solution of the update systems (4.59). Note that, actually, 12 iterations were performed for the reconstruction of Figures 5.19 (e) and (f), although only 11 iterations are depicted in Figure 5.18. That is because after iteration 6, the least squares data fit in the SRVP step with $P = 1$ increased and the algorithm restarted from iteration 6 with $P = 2$. The reconstruction with SRVP regularization seems to need a bit more forward problem solutions per iteration (in the line search) than the reconstruction with multiplicative smoothing, which explains why the computation time has increased more than the number of iterations. The average time for every update system is 3 minutes and 36 seconds for the reconstruction with multiplicative smoothing and about 3 minutes for the reconstruction with SRVP regularization. The SPLSQR algorithm thus seems to perform slightly better with the VP regularization.

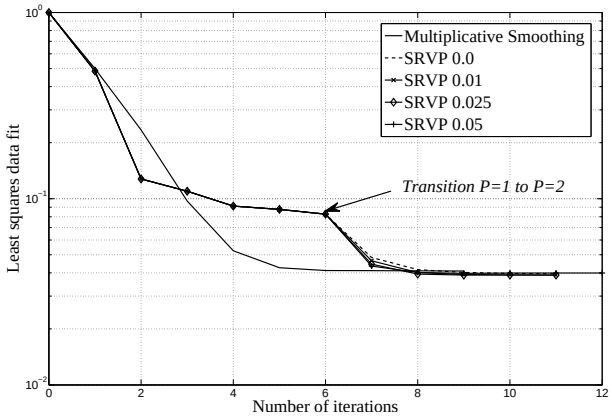

Figure 5.18: The evolution of the least squares data fit cost function $\mathcal{F}^{LS}$ over the iterations for the reconstructions of the Two Spheres target using multiplicative smoothing and SRVP regularization with $\gamma = 1$, $d_1 = 3$ and values of the weight η: $\eta = 0$ (SRVP 0.0), $\eta = 0.01$ (SRVP 0.01), $\eta = 0.025$ (SRVP 0.025) and $\eta = 0.05$ (SRVP 0.05).

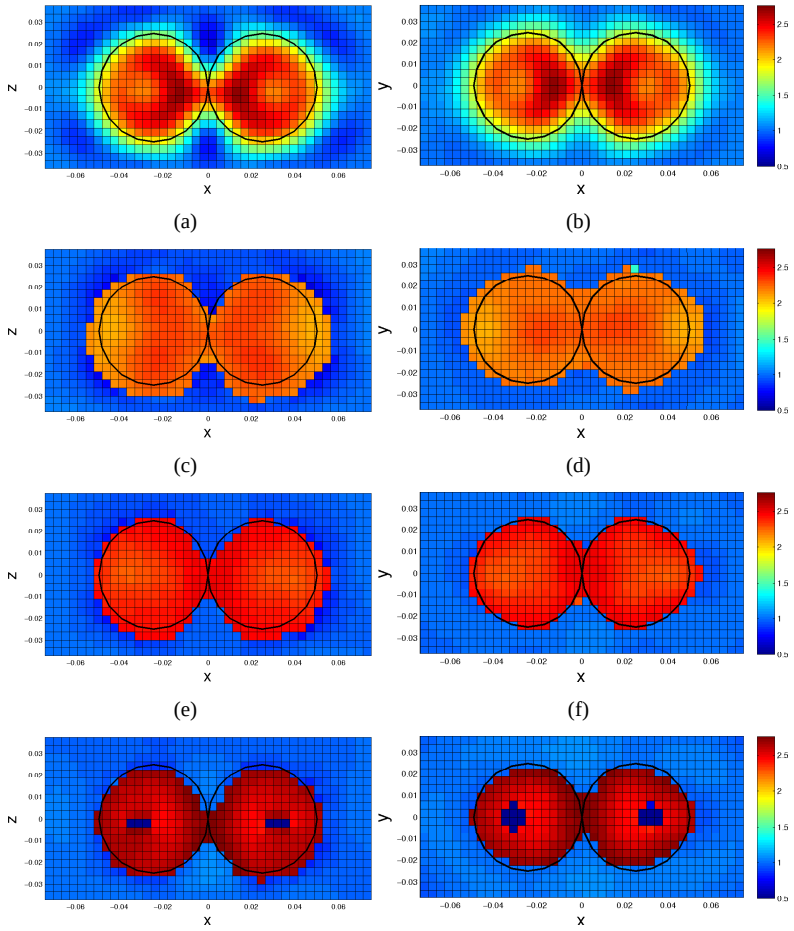

Figure 5.19: Reconstructions of the Two Spheres target at 4 GHz. The real part of the relative permittivity is depicted in the xz-plane on the left and in the xy-plane on the right. From top to bottom: reconstruction with multiplicative smoothing ($\alpha = 10^{-3}$) (a) and (b); reconstruction with SRVP ($\gamma = 1$) regularization with $\eta = 0$ (c) and (d); reconstruction with SRVP regularization with $\eta = 0.025$ and $d_1 = 3$ (e) and (f); reconstruction with SRVP regularization with $\eta = 0.05$ and $d_1 = 3$ (g) and (h). The black circles indicate the outline of the actual spheres in the considered slices through the permittivity profile.

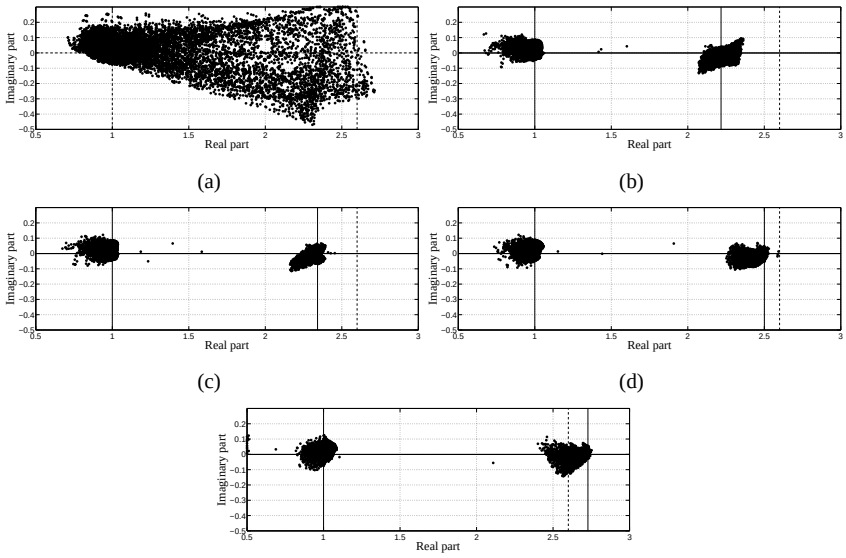

Figure 5.20: A plot of the N^{ϵ} complex permittivity values on the grid, represented in the complex plane for the reconstructions of the Two Spheres target. Reconstructions: (a) using multiplicative smoothing regularization with $\alpha = 10^{-3}$; (b) using SRVP ($\gamma = 1$) regularization with $\eta = 0$; (c) using SRVP regularization with $\eta = 0.01$ and $d_1 = 3$; (d) using SRVP regularization with $\eta = 0.025$ and $d_1 = 3$; (e) using SRVP regularization with $\eta = 0.05$ and $d_1 = 3$. The VP values are indicated as the intersections of the solid horizontal line and the solid vertical lines and the exact permittivity values are indicated with dashed lines.

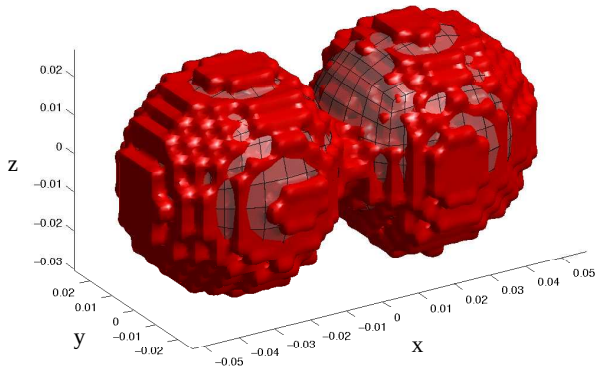

Figure 5.21: A 3D view of the surface of the reconstructed Two Spheres target, corresponding to Figure 5.19 (e) and (f). The semi-transparent spherical meshes represent the actual boundaries of the spheres.

Two Cubes

The Two Cubes target consists of two cubes with permittivity $2.3\epsilon_0$ and with side 25 mm. Because this target is approximately half as big as the Two Spheres target, the operating frequency is doubled, i.e. we use $f = 8$ GHz. The investigation domain now is a cube with side 7 cm ($1.87\lambda_0$), centered at the point $(0, 0, 0.05\,\mathrm{m})$. The cell size of the permittivity grid is 2.8 mm ($0.0747\lambda_0$), which results in 25 cells in each direction and thus $N^\epsilon = 15625$. The number of data points is 4365.

The initial reconstruction with multiplicative smoothing regularization again uses $\alpha = 10^{-3}$ and yields the result of Figures 5.22 (a) and (b) after 8 iterations and 3 hours and 20 minutes. The data fit then is reduced to 0.05 (Figure 5.23). The cubes are located at the correct position and have more or less the correct size. However, the permittivity values are a bit too low and their spreading in the complex plane (Figure 5.24 (a)) renders the determination of one permittivity value for the cubes rather difficult.

Figures 5.22 (c) and (d) show the SRVP reconstruction, obtained after 4 hours, with $\gamma = 5$, $d_1 = 3$ and $\eta = 0.01$. These parameter values are obtained in the same way as before, using the criteria of (a) a data fit close to the one with multiplicative smoothing (Figure 5.23) and (b) a good clustering (Figure 5.24(b)) to determine γ and (c) the absence of compensating behavior (Figure 5.24(b) and Figures 5.22 (c) and (d)) to determine η. The cubes are nicely reconstructed, with approximately the correct permittivity ($c_1 = 2.27$) and the reconstructed target is almost homogeneous. The surface of the reconstruction is depicted in Figure 5.25.

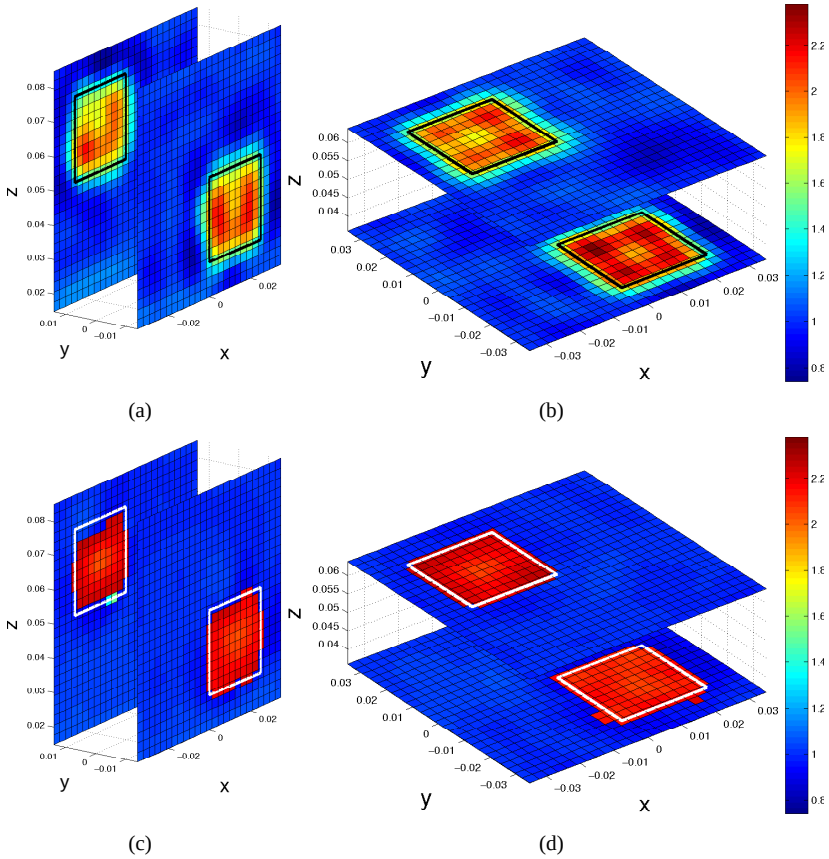

Figure 5.22: Reconstructions of the Two Cubes target at 8 GHz. The real part of the relative permittivity is depicted in two slices parallel to the xz-plane on the left and parallel to the xy-plane on the right. From top to bottom: reconstruction with multiplicative smoothing ($\alpha = 10^{-3}$) (a) and (b); reconstruction with SRVP ($\gamma = 5$) regularization with $\eta = 0.01$ and $d_1 = 3$ (c) and (d). The black squares in (a) and (b) and the white squares in (c) and (d) indicate the outline of the actual cubes in the considered slices.

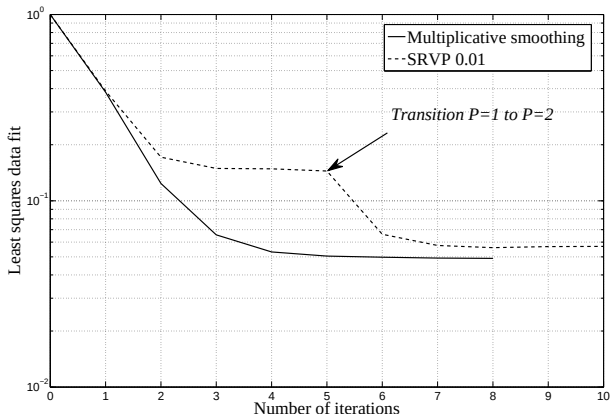

Figure 5.23: The evolution of the least squares data fit cost function $\mathcal{F}^{LS}$ over the iterations for the reconstructions of the Two Cubes target using multiplicative smoothing and SRVP regularization with $\gamma = 5$, $d_1 = 3$ and $\eta = 0.01$.

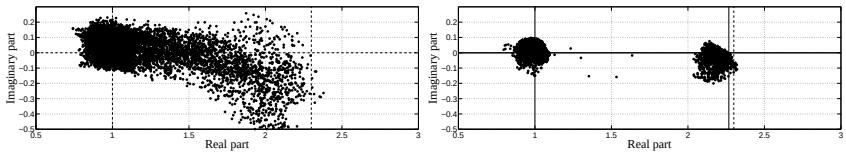

(a) (b)

Figure 5.24: A plot of the N^{ϵ} complex permittivity values on the grid, represented in the complex plane for the reconstructions of the Two Cubes target. Reconstructions: (a) using multiplicative smoothing regularization with $\alpha = 10^{-3}$; (b) using SRVP regularization with $\gamma = 5$, $d_1 = 3$ and $\eta = 0.01$. The VP values are indicated as the intersections of the solid horizontal line and the solid vertical lines and the exact permittivity values are indicated with dashed lines.

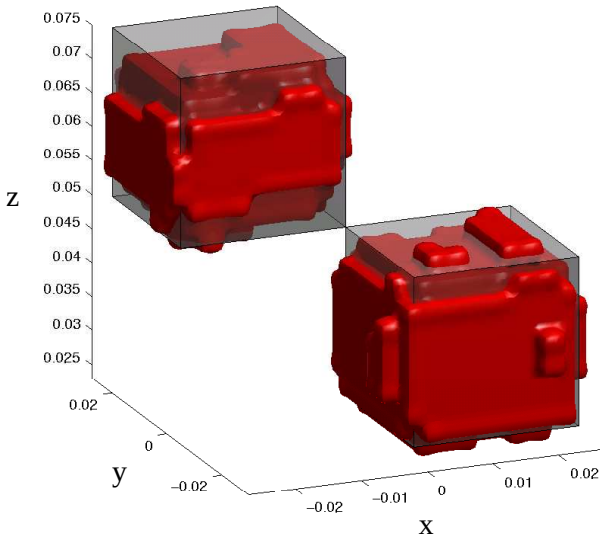

Figure 5.25: A 3D view of the surface of the reconstructed Two Cubes target, corresponding to Figure 5.22 (c) and (d). The semi-transparent cubes represent the actual boundaries of the cubes.

Cube of Spheres

The Cube of Spheres target consists of 27 spheres with radius 15.9 mm and permittivity $2.6\epsilon_0$, stacked in a cubic $3\times3\times3$ grid. The frequency used to reconstruct this target is again 8 GHz. The investigation domain is covered with a $20 \times 20 \times 23$ permittivity grid with cell size 3 mm ($0.0801\lambda_0$) which is centered at the point $(0, 0, 0.0145\,\mathrm{m})$. The number of permittivity unknowns thus is 9200, while the dimension of the data vector is $N^D = 4365$.

The reconstruction with multiplicative smoothing ($\alpha = 10^{-3}$), obtained in 2 hours and 55 minutes, is shown in Figures 5.26 (a), (c) and (e) in three orthogonal slices through the center of the investigation domain. This result is obtained in 9 iterations, yielding a final data fit of 0.012 (Figure 5.27), which is remarkably low in comparison to the data fits obtained with the previous examples. However, looking at Figures 5.26 (c) and (e), the reconstruction is not very good in the vertical z-direction. The individual spheres cannot be resolved in this direction, in contrast to slices parallel to the xy-plane, where the 3 by 3 stacking is clearly visible (Figure 5.26 (a)). This is probably due to the specific antenna configuration of the database, where only receiving antennas in the horizontal plane are used.

The reconstruction with SRVP regularization, obtained after 4 hours and 17 minutes, is depicted in Figures 5.26 (b), (d) and (f). The SRVP parameters were chosen

as $\gamma = 0.5$ and $\eta = 0.0$. This means that, from all the parameter combinations we tried, a reconstruction without the extra term (5.12) in the cost function exhibited least compensating behavior. In the horizontal cross-section of Figure 5.26(b), the spheres can be resolved and are more clearly outlined than in the reconstruction with multiplicative smoothing (Figure 5.26(a)). The resolution in the vertical direction, however, is again worse. Looking at the swarm plot of Figure 5.28(b), one can observe that the clustering in the reconstruction is less than in the reconstructions of the Two Spheres target and the Two Cubes target, although still much better than with multiplicative smoothing (Figure 5.28(a)). When we tried a higher regularization parameter, the clustering did not improve, because a strong compensating behavior occurred for all the values of η we tried. The data fit also became worse. This is probably due to the coarse grid spacing in comparison to the sphere size, which prevents an accurate modelling of the sphere boundaries such that, to obtain a good data fit, one cannot be too strict in imposing homogeneity. The permittivity of the target is also less well predicted than before ($c_1 = 2.10$). We think this mainly results from the lower resolution in the vertical direction. The surface of the reconstruction is depicted in the 3D plot of Figure 5.29.

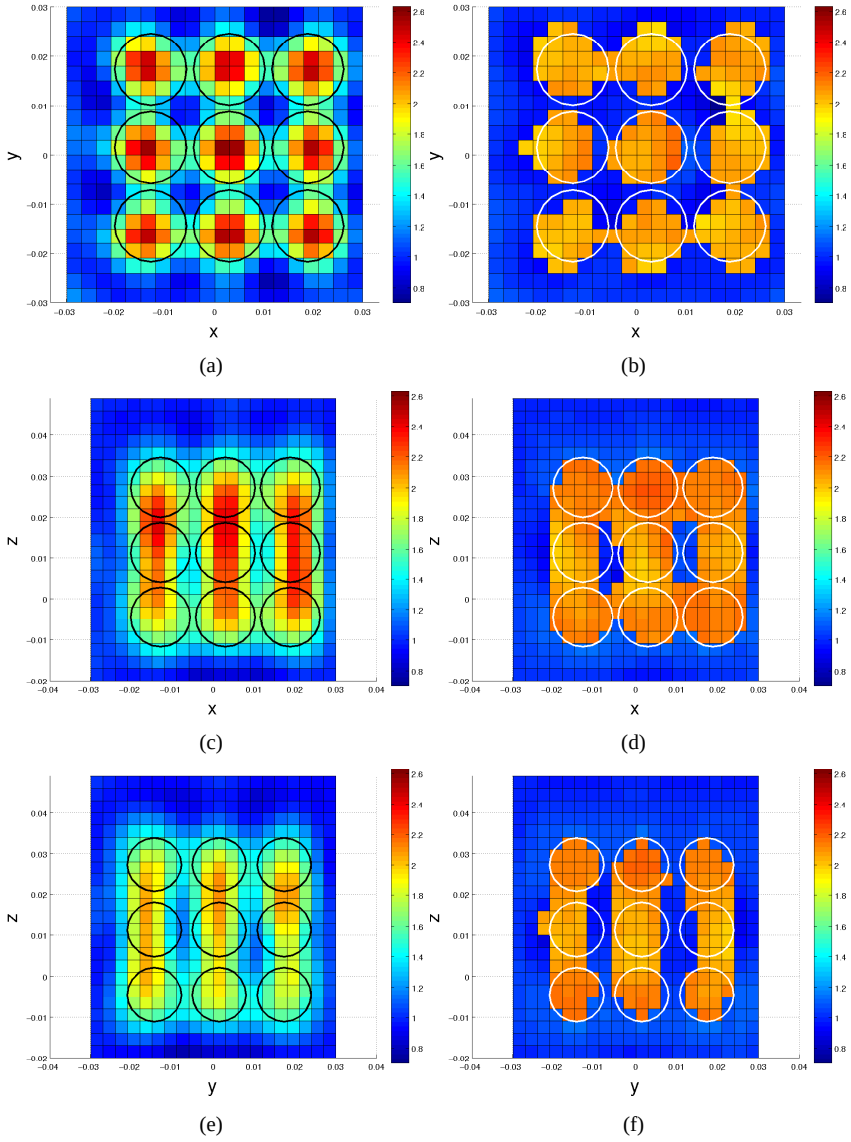

Figure 5.26: Reconstructions of the Cube of Spheres target at 8 GHz. The real part of the relative permittivity is depicted in three orthogonal slices through the center of the investigation domain: parallel to the xy-plane (a) and (b); parallel to the xz-plane (c) and (d); parallel to yz-plane (e) and (f). The reconstruction with multiplicative smoothing ($\alpha = 10^{-3}$) is on the left side and the reconstruction with SRVP ($\gamma = 0.5$) regularization with $\eta = 0.0$ is on the right side. The black circles in (a), (c) and (e) and the white circles in (b), (d) and (f) indicate the outline of the actual spheres in the considered slices. Since the exact position of the Cube of Spheres target is not given in the Fresnel database, an offset of the reference target was derived from the reconstruction.

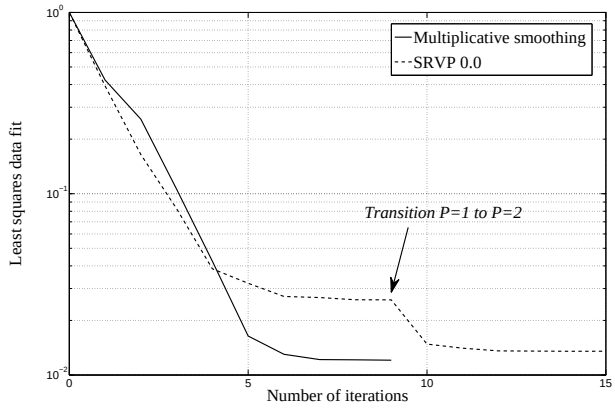

Figure 5.27: The evolution of the least squares data fit cost function $\mathcal{F}^{LS}$ over the iterations for the reconstructions of the Cube of Spheres target using multiplicative smoothing and SRVP regularization with $\gamma = 0.5$, $d_1 = 3$ and $\eta = 0.0$.

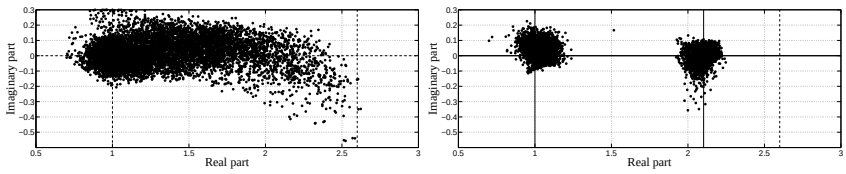

(a) (b)

Figure 5.28: A plot of the N^{ϵ} complex permittivity values on the grid, represented in the complex plane for the reconstructions of the Cube of Spheres target. Reconstructions: (a) using multiplicative smoothing regularization with $\alpha = 10^{-3}$; (b) using SRVP regularization with $\gamma = 0.5$, $d_1 = 3$ and $\eta = 0.0$. The VP values are indicated as the intersections of the solid horizontal line and the solid vertical lines and the exact permittivity values are indicated with dashed lines.

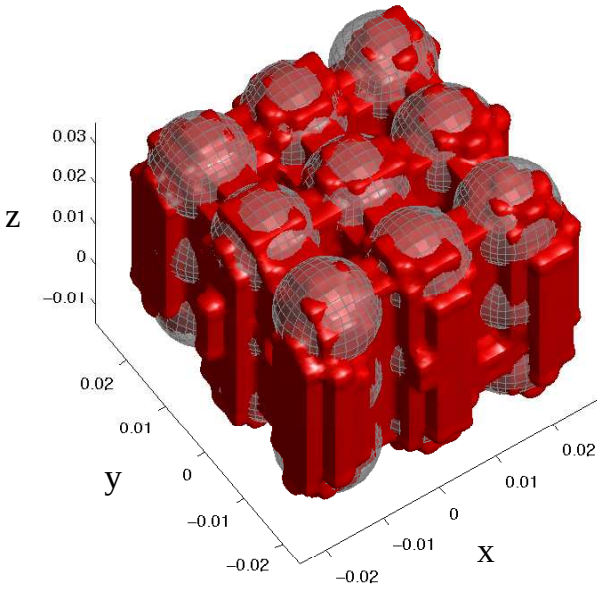

Figure 5.29: A 3D view of the surface of the reconstructed Cube of Spheres target, corresponding to Figure 5.26 (b), (d) and (f). The semi-transparent spheres represent the boundaries of the actual spheres with the same comment on the position of the target as for Figure 5.26.

Mystery target

This target is again reconstructed from the 8 GHz data, but it is not known what the actual target is. The investigation domain is a cube with side 100 mm ($2.67\lambda_0$), centered at the point $(0, 0, 20\,\mathrm{mm})$. The permittivity grid has cell size 4 mm ($0.11\lambda_0$), which yields $25 \times 25 \times 25 = 15625$ permittivity cells. The dimension of the data vector is again $N^D = 4365$.

The reconstruction with multiplicative smoothing ($\alpha = 10^{-3}$) is depicted in Figures 5.30 (a), (c), (e) and (g) in four horizontal slices through the investigation domain. The data fit after 13 iterations and 7 hours and 5 minutes is again lower than with the Two Spheres and Two Cubes targets (Figure 5.31).

The reconstruction with SRVP regularization, obtained after about 11 hours, this time with $\gamma = 2.0$, $d_1 = 3$ and $\eta = 0.015$, is given in Figures 5.30 (b), (d), (f) and (h) and the corresponding data fit curve in Figure 5.31. Before we discuss the target itself, note that in the swarm plot of Figure 5.32 (b) several permittivity values are on the lower bound on the real part, thus the compensating behavior has not been eliminated, and the cluster size is rather large. Other choices of the regularization parameters did not improve the result. Again we suspect that this is due to the

rather large cell size with respect to the detail in the target, which again appears to be composed out of small spheres. There is always a trade-off between homogeneity of the targets and data fit (Section 4.3.2) and in this case, due to the large cell size, better homogeneity in this permittivity grid apparently means a more drastic increase of the data fit cost function than in the previous examples, as can be seen in Figure 5.31. From all combinations we tried, the aforementioned regularization parameters represent a quasi-optimal trade-off between data fit and homogeneity.

Judging from the results, we believe that the target itself is an aggregation of 12 identical spheres with radius of about 13 mm and a permittivity around 2.4 ($c_1 = 2.40$). The midpoints of the spheres form the vertices of a regular icosahedron such that all the spheres touch the neighboring spheres. To verify this hypothesis, we plotted the cross sections of such an object on the permittivity plots of Figure 5.30. The radius of the spheres is determined as follows. Since in the SRVP reconstructions the surface of the reconstruction can be defined (see Figure 5.33), its volume is also known. This volume is calculated and divided by 12 to obtain the volume of one sphere, from which the radius is then obtained. This yields $R = 13.1$ mm. The position of the reference target is obtained by matching its barycenter to that of the reconstruction and its orientation is determined by visual inspection. From Figure 5.30 and Figure 5.33 we can conclude that the reconstructions match the hypothesis very well.

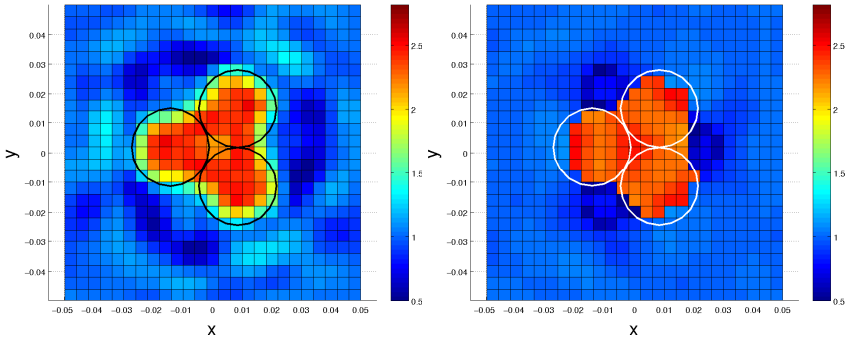

(a) (b)

Figure 5.30: First part. For caption, see second part.

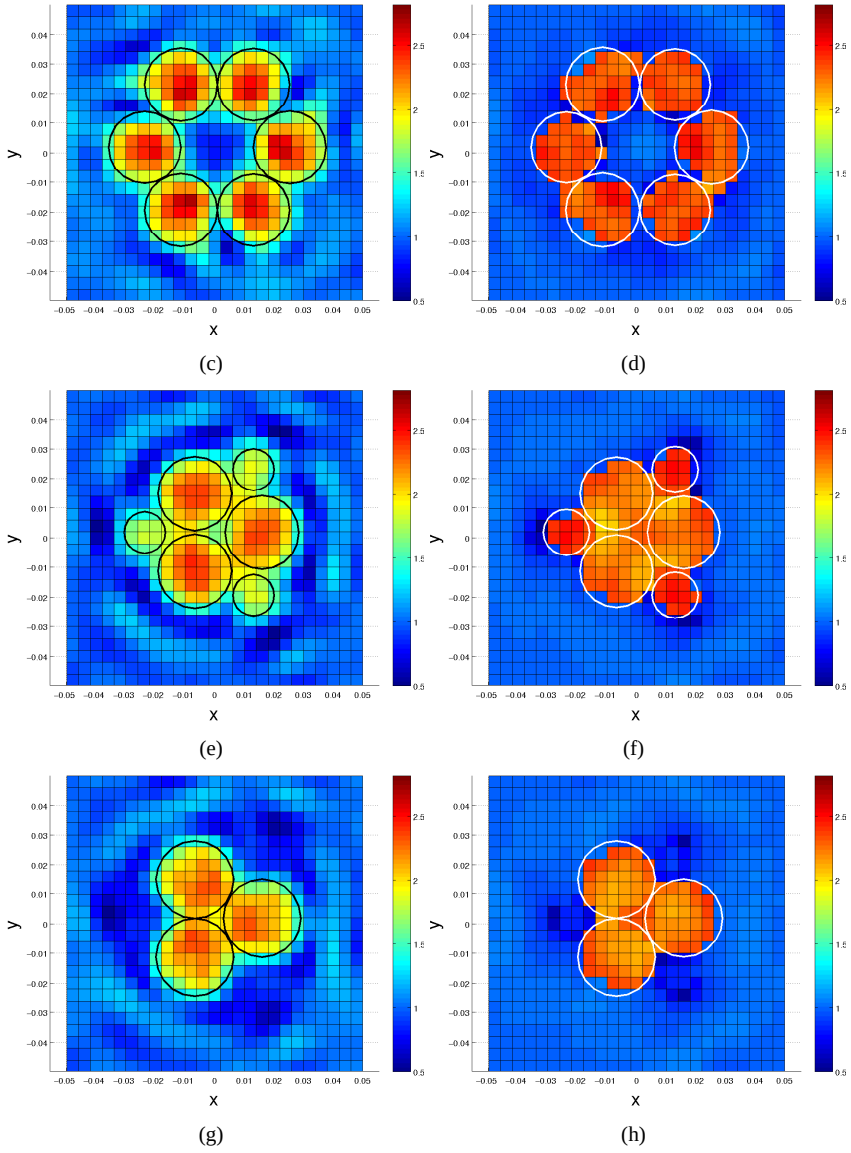

Figure 5.30: Second part. Reconstructions of the Mystery target at 8 GHz. The real part of the relative permittivity is depicted in four horizontal slices through the investigation domain: at $z = 0.0359$ m (a) and (b); at $z = 0.0159$ m (c) and (d); at $z = 0$ m (e) and (f); at $z = -0.0041$ m (g) and (h). The reconstruction with multiplicative smoothing ($\alpha = 10^{-3}$) is on the left side and the reconstruction with SRVP ($\gamma = 2.0$) regularization with $\eta = 0.015$ and $d_1 = 3$ is on the right side. The black circles in (a), (c), (e) and (g) and the white circles in (b), (d), (f) and (h) indicate the outline of a stacking of spheres with radius 13.1 mm where these spheres are placed on the vertices of a regular icosahedron.

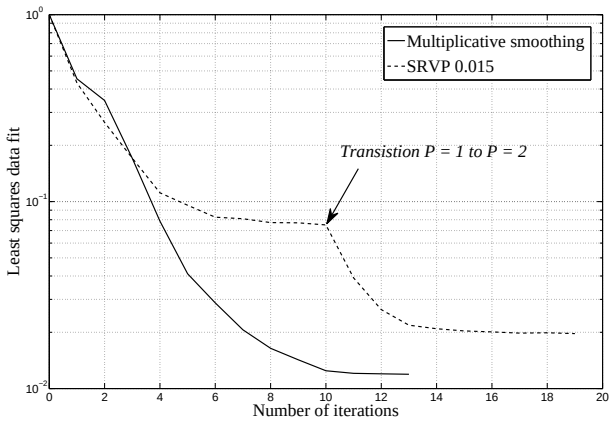

Figure 5.31: The evolution of the least squares data fit cost function $\mathcal{F}^{LS}$ over the iterations for the reconstructions of the Mystery target using multiplicative smoothing and SRVP regularization with $\gamma = 2.0$, $d_1 = 3$ and $\eta = 0.015$.

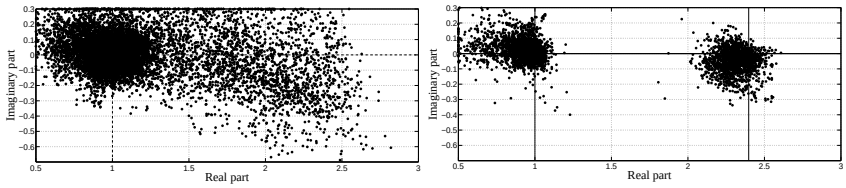

(a) (b)

Figure 5.32: A plot of the N^{ϵ} complex permittivity values on the grid, represented in the complex plane for the reconstructions of the Mystery target. Reconstructions: (a) using multiplicative smoothing regularization with $\alpha = 10^{-3}$; (b) using SRVP regularization with $\gamma = 2.0$, $d_1 = 3$ and $\eta = 0.015$. The VP values are indicated as the intersections of the solid horizontal line and the solid vertical lines and in (a) the known background permittivity is indicated with dashed lines.

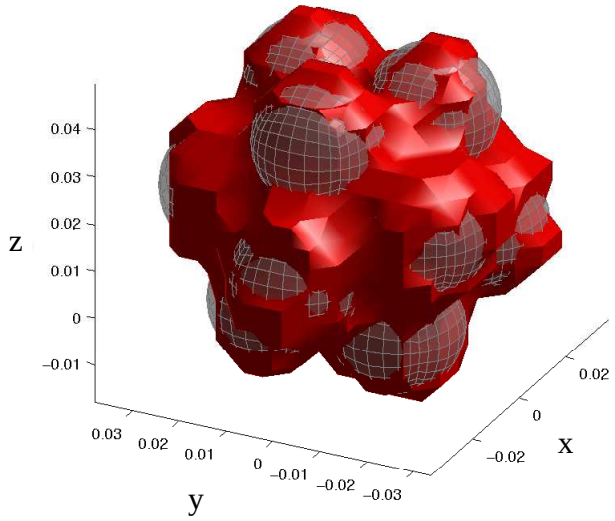

Figure 5.33: A 3D view of the surface of the reconstructed Mystery target, corresponding to Figure 5.30 (b), (d), (f) and (h). The semi-transparent spheres represent the boundaries of a stacking of spheres with radius 13.1 mm where these spheres are placed on the vertices of a regular icosahedron.

5.3 Conclusion

In this Chapter, the algorithms of Chapter 4 were employed to reconstruct biomedical phantoms from simulated data and real-world targets from experimental data. The biomedical reconstructions are challenging, because of the large contrast and the large absolute values of the permittivity. Moreover, the amount of data is often limited, because of limited accessibility of the biological targets, while the desired resolution is high. This leads to strongly under-determined inverse problems and ill-conditioned Gauss-Newton update systems. The use of MS regularization, the incorporation of constraints on the permittivity, the marching-on-scheme in the forward problem and the use of the SPLSQR algorithm are highly beneficial for these applications. The reconstructions from experimental data are very interesting, because they validate all the algorithms which have been developed in this dissertation for the 3D electromagnetic scattering problem, both forward and inverse. The VP regularization yields very accurate reconstructions of the Fresnel targets, even when using only single-frequency data. It was shown that some extra a priori information is easily incorporated in the SRVP scheme to further improve the reconstruction quality. The completely blind reconstruction of an unknown target can be called successful, since it provides a very clear image of the scatterer and detailed quantitative information about its properties.

Bibliography

[1] A. Abubakar, P.M. van den Berg, and J.J. Mallorqui. Imaging of Biomedical Data Using a Multiplicative Regularized Contrast Source Inversion Method. *IEEE Trans. Microw. Theory Tech.*, 50(7):1761–1770, 2002.

[2] M. Lazebnik, L. McCartney, D. Popovic, C.B. Watkins, M.J. Lindstrom, J. Harter, S. Sewall, A. Magliocco, J.H. Booske, M. Okoniewski, and S.C. Hagness. A large-scale study of the ultrawideband microwave dielectric properties of normal breast tissue obtained from reduction surgeries. *Physics in Medicine and Biology*, 52(10):2637–2656, May 2007.

[3] M. Lazebnik, D. Popovic, L. McCartney, C.B. Watkins, M.J. Lindstrom, J. Harter, S. Sewall, T. Ogilvie, A. Magliocco, T.M. Breslin, W. Temple, D. Mew, J.H. Booske, M. Okoniewski, and S.C. Hagness. A large-scale study of the ultrawideband microwave dielectric properties of normal, benign and malignant breast tissues obtained from cancer surgeries. *Physics in Medicine and Biology*, 52(20):6093–6115, October 2007.

[4] R.D. da Cunha and T. Hopkins. The Parallel Iterative Methods (PIM) Package for the Solution of Systems of Linear Equations on Parallel Computers. *Appl. Num. Math.*, 19(1-2):33–50, 1995.

[5] D. Colton and P. Monk. A linear sampling method for the detection of leukemia using microwaves. *SIAM J. Appl. Math.*, 58(3):926–941, 1998.

[6] D. Colton, H. Haddar, and M. Piana. The linear sampling method in inverse electromagnetic scattering theory. *Inverse problems*, 19:S105–S137, 2003.

[7] D. Colton, H. Haddar, and P. Monk. The linear sampling method for solving the electromagnetic inverse scattering problem. *SIAM J. Sci. Comput.*, 24(3):719–731, 2002.

[8] D. Colton and P. Monk. A linear sampling method for the detection of leukemia using microwaves II. *SIAM J. Appl. Math.*, 60(1):241–255, 1999.

[9] J.M. Geffrin, P. Sabouroux, and C. Eyraud. Free Space Experimental Scattering Database Continuation: Experimental Set-Up and Measurement Precision. *Inverse problems*, 21:117–130, 2005.

[10] C. Eyraud, J.M. Geffrin, P. Sabouroux, P. Chaumet, H. Tortel, H. Giovannini, and A. Litman. Validation of a 3D Bistatic Microwave Scattering Measurement Setup. *Radio Science*, doi:10.1029/2008RS003836, in press.

[11] J.M. Geffrin, P. Chaumet, C. Eyraud, K. Belkebir, and P. Sabouroux. Electromagnetic Three-Dimensional Reconstruction of Targets From Free Space Experimental Data. *Appl. Phys. Lett.*, 92:194102, 2008.

[12] M. Frigo and S.G. Johnson. The Design and Implementation of FFTW3. *Proceedings of the IEEE 93*, (2):216–231, 2005.

CHAPTER 6

Contrast source based inversion

In the previous chapters, the inverse scattering problem was solved using the conventional approach in which the optimization operates on the permittivity only and in which a forward scattering simulation has to be performed in every step of the iterative solution. Although this kind of methods can be made to converge in a few iterations, as can be observed from the presented results, the forward problem solutions in each iteration can lead to long computation times, even when using the accelerating techniques discussed in Chapter 3. The contrast source inversion (CSI) approach of van den Berg et al. [1] (see Section 2.3.3) avoids the solution of forward problems in each step of the minimization and therefore is an interesting alternative.

In this chapter two contributions are presented. First, a consistency inversion (CI) method is introduced. This method employs the same ideas as the CSI method, but the cost function is modified in order to eliminate the permittivity unknowns from the problem. The contrast currents then are the only remaining optimization variables. In the CSI method of van den Berg et al. [1–3], the two sets of physically different optimization variables, i.e. the contrast currents and the permittivity unknowns, are updated alternatingly. Since it is known that alternating variable optimization methods can exhibit slow convergence [4], we think this should be avoided as much as possible. A preliminary numerical study in noise-free inverse crime conditions supports this hypothesis and forms a motivation for the CI method. In this study, the inverse scattering problem is solved in two steps. First, the visible currents, i.e. currents that generate a non-zero field at the detector positions, are reconstructed through a pseudo-inverse of the scattering matrix and, secondly, the invisible currents are recovered with a conjugate gradient (CG) optimization of a cost function. In one case this latter cost function is the domain cost function from the CSI method, which is minimized by alternatingly updating the contrast currents and the permittivity contrast and in the other

case, it is the new consistency cost function of the CI method, which is minimized by only updating the contrast currents. This two-step approach eliminates all normalization and trade-off parameters and therefore avoids the question of how to choose these optimally. This is especially useful since those optimal parameters are likely to be different for the CI and CSI methods, which hampers an objective comparison of the two approaches. Note that CSI-like or modified-gradient-like methods exist which do not use alternating updates for field unknowns and material unknowns, see e.g. [5]. We do not make any statements in this chapter regarding such methods.

The second contribution of this chapter is the application of the stepwise relaxed value picking (VP) regularization scheme, presented in Section 4.3 for the conventional approach, to the CI method, yielding the VPCI method. In the CI method, the permittivity is absent in the optimization problem and any regularization that operates on the spatial distribution of the permittivity is therefore not applicable to the CI method. VP regularization, due to its completely different nature, can be applied here. The incorporation of VP regularization in a contrast source based method such as the CI method is somewhat more complicated than its use in a conventional method, but the quality of the reconstructions is again greatly improved.

The implementation of the CI method has so far only been done for 2D inverse scattering problems with transverse magnetic (TM) polarization. Therefore, this chapter starts with a reformulation of the inverse scattering problem for this configuration. The CI method and the incorporation of the VP regularization in this method are discussed subsequently.

6.1 Problem formulation and discretization

A 2D inhomogeneous scatterer with complex permittivity $\epsilon(\boldsymbol{\rho})$ and magnetic permeability μ_0 (the permeability of vacuum) is embedded in an infinite homogeneous background with permittivity ϵ_b and permeability μ_0 and lies completely within a bounding box $\mathcal{D}$. The position vector in the plane spanned by the orthogonal unit vectors $\hat{\boldsymbol{x}}$ and $\hat{\boldsymbol{y}}$ is denoted $\boldsymbol{\rho} = x\hat{\boldsymbol{x}} + y\hat{\boldsymbol{y}}$. There are I equidistant source-detector positions $\boldsymbol{\rho}_i$, $i = 1, \ldots, I$, on a circle with radius R around the center of $\mathcal{D}$. The source is a line current parallel to the z-axis, which illuminates the object from successive positions $\boldsymbol{\rho}_i$ and which is time-harmonic with angular frequency ω. In the following, the time dependency $e^{j\omega t}$ has been omitted (in all the examples of this chapter the frequency is fixed to 1 GHz). In the TM situation considered here, the electric field only has a z-component, i.e. $\boldsymbol{E}(\boldsymbol{\rho}) = E(\boldsymbol{\rho})\hat{\boldsymbol{z}}$, hence a scalar problem remains [6].

The incident field $E_i^\mathrm{inc}(\boldsymbol{\rho})$ due to a unit line current in $\boldsymbol{\rho}_i$ is

$$E_i^\mathrm{inc}(\boldsymbol{\rho}) = j\omega\mu_0 G_\mathrm{b}(\boldsymbol{\rho} - \boldsymbol{\rho}_i). \tag{6.1}$$

The Green function G_b is given by $G_\mathrm{b}(\boldsymbol{\rho} - \boldsymbol{\rho}_i) = \frac{j}{4} H_0^{(2)}(k_\mathrm{b}\|\boldsymbol{\rho} - \boldsymbol{\rho}_i\|)$, in which $H_0^{(2)}$

is the zeroth order Hankel function of the second kind and $k_\mathrm{b} = \omega\sqrt{\mu_0\epsilon_\mathrm{b}}$ is the wave number of the background medium. The corresponding total field $E_i(\boldsymbol{\rho})$ is governed by the contrast source volume integral equation

$$E_i(\boldsymbol{\rho}) = E_i^\mathrm{inc}(\boldsymbol{\rho}) + j\omega\mu_0 \int_\mathcal{D} G_\mathrm{b}(\boldsymbol{\rho}-\boldsymbol{\rho}')j\omega\chi(\boldsymbol{\rho}')E_i(\boldsymbol{\rho}')\mathrm{d}\boldsymbol{\rho}', \quad \forall\boldsymbol{\rho} \tag{6.2}$$

in which $\chi = \epsilon - \epsilon_\mathrm{b}$ is the contrast function, which is zero outside $\mathcal{D}$. Once (6.2) is solved for $E_i(\boldsymbol{\rho})$ inside $\mathcal{D}$, the scattered field $E_i^\mathrm{s}(\boldsymbol{\rho}_l) = E_i(\boldsymbol{\rho}_l) - E_i^\mathrm{inc}(\boldsymbol{\rho}_l)$ at the detector positions $\boldsymbol{\rho}_l$ can be calculated as

$$E_i^\mathrm{s}(\boldsymbol{\rho}_l) = j\omega\mu_0 \int_\mathcal{D} G_\mathrm{b}(\boldsymbol{\rho}_l-\boldsymbol{\rho}')j\omega\chi(\boldsymbol{\rho}')E_i(\boldsymbol{\rho}')\mathrm{d}\boldsymbol{\rho}'. \tag{6.3}$$

The 2D inverse scattering problem consists of solving the data equation (6.3) for the unknown function χ, starting from known values of $E_i^\mathrm{s}(\boldsymbol{\rho}_l)$, $i,l = 1\ldots I$, and subject to the domain equation (6.2). Since the total field depends on $\chi(\boldsymbol{\rho})$ through (6.2), this is a nonlinear problem.

For the discretization of (6.2)-(6.3), the investigation domain $\mathcal{D}$ is divided in N square cells and a Garlerkin Method of Moments is applied in which the total field and the contrast function are expanded in pulse basis functions, i.e. in cell n, the field $E_i(\boldsymbol{\rho})$ and the contrast $\chi(\boldsymbol{\rho})$ assume the constant values $E_{i,n}$ and χ_n respectively. This yields the following matrix equation:

$$\boldsymbol{e}_i = \boldsymbol{e}_i^\mathrm{inc} + j\omega\boldsymbol{Z}\boldsymbol{X}\boldsymbol{e}_i, \tag{6.4}$$

where the elements of the N-dimensional vectors $\boldsymbol{e}_i$ and $\boldsymbol{e}_i^\mathrm{inc}$ and of the $N\times N$ matrices $\boldsymbol{Z}$ and $\boldsymbol{X}$ are given by

$$\begin{aligned}
\left[\boldsymbol{e}_i\right]_n &= E_{i,n}, &(6.5)\\
\left[\boldsymbol{e}_i^\mathrm{inc}\right]_n &= \int_n E_i^\mathrm{inc}(\boldsymbol{\rho})\mathrm{d}\boldsymbol{\rho}, &(6.6)\\
\boldsymbol{Z}_{n,n'} &= j\omega\mu_b \int_n\int_{n'} G_\mathrm{b}(\boldsymbol{\rho}-\boldsymbol{\rho}')\mathrm{d}\boldsymbol{\rho}\mathrm{d}\boldsymbol{\rho}', &(6.7)\\
\boldsymbol{X}_{n,n'} &= \delta_{n,n'}\chi_n, &(6.8)
\end{aligned}$$

in which $\delta_{n,n'}$ is the Kronecker delta. The integral signs in (6.6) and (6.7) denote integration over single cells and the interaction integrals in (6.7) are calculated as in [7], where the two 2D numerical integrations are replaced with a single 1D quadrature and some analytical integrations, also taking into account the singularity in G_b very elegantly. Within the same discrete framework, the data equation (6.3) can be replaced by a matrix equation

$$\boldsymbol{e}_i^\mathrm{s} = j\omega\boldsymbol{A}\boldsymbol{X}\boldsymbol{e}_i. \tag{6.9}$$

The entries of the I-dimensional vectors $\boldsymbol{e}_i^{\mathrm{s}}$ and of the $I \times N$ matrix $\boldsymbol{A}$ are

$$[\boldsymbol{e}_i^{\mathrm{s}}]_l = E_i^{\mathrm{s}}(\boldsymbol{\rho}_l), \tag{6.10}$$

$$\boldsymbol{A}_{l,n} = j\omega\mu_b \int_n G_{\mathrm{b}}(\boldsymbol{\rho}_l - \boldsymbol{\rho})\mathrm{d}\boldsymbol{\rho}. \tag{6.11}$$

$$\tag{6.12}$$

Note that, thanks to the convolutional symmetry of (6.7), the multiplication of $\boldsymbol{Z}$ with the vector $\boldsymbol{X}\boldsymbol{e}_i$ in (6.4) can be done very efficiently with the use of Fast Fourier Transforms (FFT's) [8,9], which is also the case for the multiplication of $\boldsymbol{Z}^H$ (the conjugate transpose of $\boldsymbol{Z}$) with a vector (this is needed to calculate gradient vectors in the following).

6.2 Consistency inversion

6.2.1 Consistency cost function

In the discrete formulation, the inverse problem consists of determining the diagonal contrast matrix $\boldsymbol{X}$ from known scattered field vectors $\boldsymbol{e}_i^{\mathrm{s}}$, such that (6.9) and (6.4) are satisfied, for all illuminations $i = 1, \ldots, I$. In the conventional approach, where $\boldsymbol{X}$ is updated iteratively until (6.9) is (approximately) satisfied, the total field vectors $\boldsymbol{e}_i$ in each iteration are calculated by solving the discrete domain equation (6.4). The drawback of this approach is the necessity to solve several forward problems, which is computationally expensive, even with fast methods as the FFT-method. The CSI method does not solve any forward problem, but uses a conjugate gradient optimization method that alternately calculates updates for the contrast matrix $\boldsymbol{X}$ and the set of contrast current vectors $\boldsymbol{j}_i$ until following two equations are (approximately) satisfied: a data equation

$$\boldsymbol{e}_i^{\mathrm{s}} = \boldsymbol{A}\boldsymbol{j}_i \tag{6.13}$$

and a modified domain equation

$$\boldsymbol{j}_i = j\omega\boldsymbol{X}\boldsymbol{e}_i, \tag{6.14}$$

where the field vectors $\boldsymbol{e}_i$ are a function of the contrast current vectors:

$$\boldsymbol{e}_i = \boldsymbol{e}_i^{\mathrm{inc}} + \boldsymbol{Z}\boldsymbol{j}_i. \tag{6.15}$$

It is well known that the contrast current vectors are not entirely determined by (6.13), because in a realistic setup the matrix $\boldsymbol{A}$ has less rows (I) than it has columns (N) and hence has a null space [10]. The components of $\boldsymbol{j}_i$ in this null-space have to be determined by (6.14) and (6.15). In the conventional approach, (6.14) and (6.15)

are simultaneously satisfied at any time, while in the CSI method this is gradually achieved throughout the optimization. Typically, in a CSI implementation, a cost function of the following form is minimized:

$$\mathcal{F}(\boldsymbol{j}_1,\ldots,\boldsymbol{j}_I,\boldsymbol{X}) = \gamma\mathcal{F}^D(\boldsymbol{j}_1,\ldots,\boldsymbol{j}_I) + \lambda\mathcal{F}^{CSI}(\boldsymbol{j}_1,\ldots,\boldsymbol{j}_I,\boldsymbol{X}), \tag{6.16}$$

where the data fit cost function $\mathcal{F}^D$ and the domain cost function $\mathcal{F}^{CSI}$ are given by

$$\mathcal{F}^D(\boldsymbol{j}_1,\ldots,\boldsymbol{j}_I) = \frac{\sum_{i=1}^I \|\boldsymbol{e}_i^s - \boldsymbol{A}\boldsymbol{j}_i\|^2}{\sum_{i=1}^I \|\boldsymbol{e}_i^s\|^2} \tag{6.17}$$

$$\mathcal{F}^{CSI}(\boldsymbol{j}_1,\ldots,\boldsymbol{j}_I,\boldsymbol{X}) = \sum_{i=1}^I \|\boldsymbol{j}_i - j\omega\boldsymbol{X}\boldsymbol{e}_i\|^2. \tag{6.18}$$

The positive constant γ is a trade-off parameter and λ is a normalization constant, which possibly varies over the iterations of the minimization algorithm as in [1, 3], where it is chosen in the m-th iteration as

$$\lambda^m = \frac{1}{\sum_{i=1}^I \|\omega\boldsymbol{X}^{m-1}\boldsymbol{e}_i^{\text{inc}}\|^2}. \tag{6.19}$$

The meaning of (6.14) is that the ratio of the contrast current in a certain cell of the discretization grid and the total field in the same cell is independent of the illumination. We call this "consistency". This consistency can be imposed in yet another way. Indeed, the following statement can easily be proven:

If, for the general N-dimensional vectors $\boldsymbol{j}_i$ and $\boldsymbol{e}_i$, $i = 1,\ldots,I$, the condition

$$\forall i : \nexists\, n \text{ for which } [\boldsymbol{e}_i]_n = 0 \text{ and } [\boldsymbol{j}_i]_n \neq 0, \tag{6.20}$$

is satisfied, the following statements are equivalent:
i) a bounded diagonal matrix $\boldsymbol{X}$ exists such that

$$\boldsymbol{j}_i = j\omega\boldsymbol{X}\boldsymbol{e}_i, \quad \forall i. \tag{6.21}$$

ii)

$$\boldsymbol{j}_i \circ \boldsymbol{e}_l = \boldsymbol{e}_i \circ \boldsymbol{j}_l, \quad \forall i,l. \tag{6.22}$$

In (6.22), "$\circ$" stands for element-wise multiplication of two N-dimensional vectors. If (6.21) holds, then (6.22) immediately follows. In the other direction, condition

(6.20) ensures that bounded diagonal matrices $\boldsymbol{X}_i$ exist such that

$$\boldsymbol{j}_i = j\omega \boldsymbol{X}_i \boldsymbol{e}_i, \tag{6.23}$$

and then (6.22) implies that these diagonal matrices can be chosen equal to each other: $\boldsymbol{X}_i = \boldsymbol{X}, \forall i$.

Because of the above property, we propose to replace the domain cost function $\mathcal{F}^{CSI}$ in (6.16) by the consistency cost function

$$\mathcal{F}^{CI}(\boldsymbol{j}_1, \ldots, \boldsymbol{j}_I) = \sum_{k \in K} \sum_{i=1}^{I} \|\boldsymbol{j}_i \circ \boldsymbol{e}_{i-k} - \boldsymbol{j}_{i-k} \circ \boldsymbol{e}_i\|^2, \tag{6.24}$$

where K is a (random) set of numbers between 1 and I and periodic boundary conditions for the indices are used, i.e. $\boldsymbol{j}_i = \boldsymbol{j}_{i+I}$ and $\boldsymbol{e}_i = \boldsymbol{e}_{i+I}$, and where $\boldsymbol{e}_i$ is computed with (6.15). The contrast matrix $\boldsymbol{X}$ is then no longer an optimization unknown. We furthermore choose to modify the data fit term:

$$\mathcal{F}(\boldsymbol{j}_1, \ldots, \boldsymbol{j}_I) = \gamma \left[\mathcal{F}^D(\boldsymbol{j}_1, \ldots, \boldsymbol{j}_I) - h\right]^2 + \lambda \mathcal{F}^{CI}(\boldsymbol{j}_1, \ldots, \boldsymbol{j}_I). \tag{6.25}$$

The constant h is an estimate of the noise level, i.e. the data fit $\mathcal{F}^D(\boldsymbol{j}_1^0, \ldots, \boldsymbol{j}_I^0)$ obtained for the contrast currents $\boldsymbol{j}_i^0$ that correspond to the discrete contrast profile $\boldsymbol{X}^0$ which best approximates the actual contrast profile. With this modification, the first term in (6.25) can be minimized to zero (or close to zero) even if the data are noisy, thus avoiding a trade-off between data fit and consistency at the end of the minimization.

Both cost functions (6.16) and (6.25) are conveniently minimized using a conjugate gradient approach. In both the CSI and the CI methods, the contrast currents are updated by performing a line search along a Polak-Ribière search direction in each iteration. Appendix C discusses this in more detail. In the CSI method, the contrast matrix $\boldsymbol{X}$ also has to be updated in every iteration and this can be done as in [1,3] (for the unregularized CSI method without upper and lower bounds on the permittivity) by taking

$$\boldsymbol{X}_{n,n}^m = \frac{1}{j\omega} \frac{\sum_{i=1}^{I} \left([\boldsymbol{e}_i^m]_n\right)^* [\boldsymbol{j}_i^m]_n}{\sum_{i=1}^{I} |[\boldsymbol{e}^m{}_i]_n|^2} \tag{6.26}$$

in iteration m, a choice which minimizes (6.18) for fixed $\boldsymbol{e}_i^m$ and $\boldsymbol{j}_i^m$. The CSI method thus alternatingly updates the contrast currents and the contrast. By using the cost function (6.25), the CI method avoids these alternating updates. This may reduce the number of iterations in the optimization. Indeed, in the beginning of the optimization, when the contrast currents are still far from the solution, the CSI update of the contrast (6.26) is based on incorrect contrast currents and is not likely to be much closer to the actual contrast. The subsequent update of the contrast currents, is again based on this

incorrect contrast, such that it is possible that not much progress is made.

The CI method only retrieves the contrast at the end of the minimization of (6.25) by using (6.26), where m in this case denotes the final iteration of the CI method. If, at this point, condition (6.20) is not satisfied, the CI method, strictly speaking, has not found a solution $\boldsymbol{X}$ to the inverse scattering problem, because then (6.21) does not follow from (6.22). However, this situation has not been encountered in our experiments with the method and even if it occurs, it is still possible to obtain an estimate of the contrast using (6.26), as long as for every cell n there is a non-zero $[\boldsymbol{e}_i^m]_n$ for some illumination i.

6.2.2 Motivation for the CI method

In this section we test wether the CI method can indeed yield faster convergence than the CSI method. Because we cannot use the choice (6.19) for the parameter λ in the CI method, since the contrast has been eliminated, it is not clear which choice of the normalization parameter allows for an objective comparison of the two approaches. Also, in our implementation of the CI method, we use the modified data term as in (6.25) with an adjustable γ, while the CSI method in [1, 3] uses (6.16) with $\gamma = 1$. In this dissertation a preliminary test under ideal circumstances is conducted using a two-step procedure which avoids difficulties with the choice of the normalization and trade-off parameters as well as the form of the data term. These ideal circumstances assume that a contrast matrix $\boldsymbol{X}$ and contrast currents $\boldsymbol{j}_i$ exist for which (6.13), (6.14) and (6.15) are exactly satisfied, i.e. when there is no noise on the data and when the vectors $\boldsymbol{e}_i^s$ have been generated with the same discretization as is used in the inverse problem.

Under such assumption, the first step of the two-step procedure retrieves the visible currents $\boldsymbol{j}_i^V$, i.e. the components of the contrast currents $\boldsymbol{j}_i$ that do not lie in the null space of $\boldsymbol{A}$, by solving (6.13) for its minimum norm solution:

$$\boldsymbol{j}_i^V = \boldsymbol{V}\boldsymbol{S}^{-1}\boldsymbol{U}^H\boldsymbol{e}_i^{\mathrm{s}}, \tag{6.27}$$

where the matrices $\boldsymbol{U}$, $\boldsymbol{S}$ and $\boldsymbol{V}$ form the thin Singular Value Decomposition (SVD) of $\boldsymbol{A}$, i.e.

$$\boldsymbol{A} = \boldsymbol{U}\boldsymbol{S}\boldsymbol{V}^H. \tag{6.28}$$

The dimensions of the matrices $\boldsymbol{U}$, $\boldsymbol{V}$ and $\boldsymbol{S}$ are $(I \times I)$, $(N \times I)$ and $(I \times I)$ respectively. Both $\boldsymbol{U}$ and $\boldsymbol{V}$ have orthonormal columns that span the range of $\boldsymbol{A}$ and the range of $\boldsymbol{A}^H$ respectively. $\boldsymbol{S}$ is a diagonal $(I \times I)$-matrix that contains the non-zero singular values of $\boldsymbol{A}$. Note that, even for large inverse scattering problems, where N becomes very large, I generally remains relatively small and the thin SVD of $\boldsymbol{A}$ can be computed quite efficiently. The projections of the contrast currents $\boldsymbol{j}_i$ on the null space of $\boldsymbol{A}$, i.e. $\boldsymbol{j}_i^{\mathrm{NV}} = \boldsymbol{j}_i - \boldsymbol{j}_i^V = \boldsymbol{j}_i - \boldsymbol{V}\boldsymbol{V}^H\boldsymbol{j}_i$, are denoted the invisible current vectors

and have to be determined by minimizing (6.18) or (6.24). Note that, historically, a number of attempts have been made to only use the pseudo-inverse solution (6.27) to reconstruct the contrast currents $\boldsymbol{j}_i$ and from those the permittivity in the investigation domain [11, 12]. In [10] it is shown that this is not a viable approach and that the invisible currents have to be taken into account.

Since the visible currents have been determined exactly, the data fit cost function (6.17) is zero irrespective of the invisible current vectors and if we further only optimize for the invisible currents in the second step of the two-step procedure, it remains zero. The minimization of (6.18) and (6.24) with respect to the invisible currents is achieved by performing line searches along conjugate gradient update directions for the invisible current vectors $\boldsymbol{j}_i^{\mathrm{NV}}$ only. In Appendix C it is shown how these steps can be taken in the null space of $\boldsymbol{A}$ without constructing a basis for this null space. The line search in both methods simply consists of finding the roots of a polynomial which is linear in the CSI formulation and cubic in the CI formulation. The gradient vectors needed by the conjugate gradient method are given in Appendix D. After every update of the contrast sources in the CSI formulation, the contrast matrix $\boldsymbol{X}$ has to be updated and this is achieved in our implementation with (6.26).

Figure 6.1 shows two discretized real permittivity profiles which are used as test cases for the comparison. Test case 1 (Figure 6.1 (a)) consists of a larger cylinder with a diameter $2\lambda_b$ (0.60 m) ($\lambda_{\mathrm{b}} = 0.30$ m is the wavelength in the background medium) and permittivity $1.5\epsilon_0$ with inside it a smaller cylinder with diameter $0.8\lambda_b$ (0.24 m) and permittivity $2\epsilon_0$. Test case 2 (Figure 6.1 (b)) consists of two non overlapping cylinders with diameter $0.8\lambda_b$ (0.24 m), one with permittivity $1.7\epsilon_0$ and one with permittity $2\epsilon_0$. In both cases the permittivity grid is a 25×25 grid with cell size $0.1\lambda_b$ (0.03 m) and the background medium is air ($\epsilon_{\mathrm{b}} = \epsilon_0$). To simulate the scattering data, 40 line sources are placed on a circle with radius $R = 3\lambda_b$ (0.9 m) (Figure 6.2) and for each such illumination (6.4) is solved and (6.9) evaluated for detectors in all source positions. For these test cases, we plot (6.18) after every iteration in the CSI approach and after every iteration in the CI method, we calculate $\boldsymbol{X}$ with (6.26) and then also plot (6.18) (note that the calculation of $\boldsymbol{X}$ is only performed here for visualization purposes and is not included in a normal iteration of the CI method). We are therefore comparing two ways of minimizing the CSI cost function (6.18).

Figure 6.3 shows the result over 200 iterations. Different, randomly chosen sets K in the definition of $\mathcal{F}^{CI}$ are considered and apparently, for all the sets except the smallest one (1 k-value), the CI formulation yields faster convergence and a better overall consistency than the CSI formulation in both test cases. Increasing the set K yields a longer computation time per iteration, although this increase is limited, since no extra multiplications with $\boldsymbol{Z}$ (to calculate the field vectors in (6.15)) or $\boldsymbol{Z}^H$ (to calculate the gradient vectors, see Appendix D) are introduced. However, a larger set K apparently also reduces the number of iterations needed to reach a certain consistency, although there is not much difference between the cases with 3 and 5 k-values. The real part of

the permittivity after 200 iterations of the CSI formulation and of the CI formulation with $K = \{34, 19, 16\}$ is shown in Figure 6.4 for test case 1 and in Figure 6.5 for test case 2. Apparently both methods yield similar reconstructions. The CI reconstructions are slightly better than the CSI reconstructions, but not significantly. Indeed, let the reconstruction error be defined as

$$\mathrm{err}_\epsilon = \sqrt{\frac{\sum_{n=1}^{N} |\epsilon_n^r - \epsilon_n^{r,0}|^2}{\sum_{n=1}^{N} |\epsilon_n^{r,0}|^2}}, \tag{6.29}$$

where $\epsilon_n^{r,0}$ is the ideal relative permittivity in cell n, corresponding to $\boldsymbol{X}^0$. This reconstruction error for test case 1 is $\mathrm{err}_\epsilon = 0.052$ for the CI reconstruction and $\mathrm{err}_\epsilon = 0.071$ for the CSI reconstruction, while for the test case 2, these values are 0.077 and 0.080 respectively.

In these idealized circumstances, the CI approach thus indeed yields faster convergence, i.e. needs less iterations to obtain the same level of consistency, and when lower values for $\mathcal{F}^{CSI}$ are required, this difference seems to grow. However, the computation time per iteration is longer in the CI method. For the examples above, one iteration of the CSI method takes 0.12 s in our MATLAB implementation. The CI method requires 0.15 s, 0.20 s, 0.24 s and 0.33 s, respectively for a set K with 1, 2, 3 and 5 values, respectively. However, it can be seen from Figure 6.3 that, depending on the desired level of consistency, the CI method can still be faster than the CSI approach in the considered circumstances. For example, to reach a normalized consistency of 10^{-4} for test case 1, the CSI method needs 200 iterations, while the CI method with $K = \{34, 19, 16\}$ only needs 30, which yields a total speedup factor of 3.33. In test case 2, the CSI method achieves a normalized consistency of $5 \cdot 10^{-5}$ in 200 iterations, while the same consistency is reached in 80 iterations in the CI method with the same set K. The CI method then is still 1.25 times faster. To determine which one of the methods is preferred in general circumstances with noisy data, or in cases where regularization is applied to the cost functions, more research is needed.

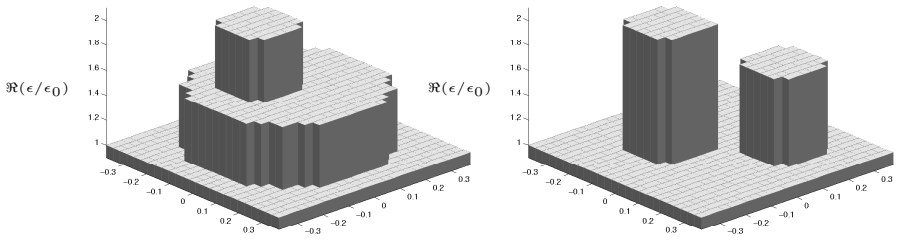

(a) (b)

Figure 6.1: The (real) permittivity profiles of test case 1 (a) and test case 2 (b).

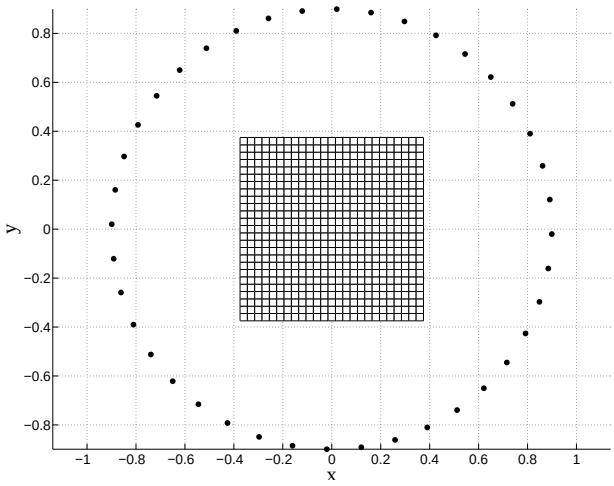

Figure 6.2: The permittivity grid and line source configuration for the reconstructions of test case 1 (Figure 6.1 (a)) and test case 2 (Figure 6.1 (b)). The grid is square with side $2.5\lambda_b$ (0.75 m) and has cell size $0.1\lambda_b$ (0.03 m) and 40 line sources are distributed over a circle with radius $3\lambda_b$ (0.9 m), which is centered at the center of the permittivity grid.

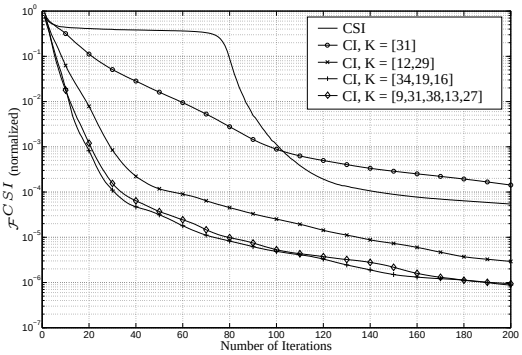

(a)

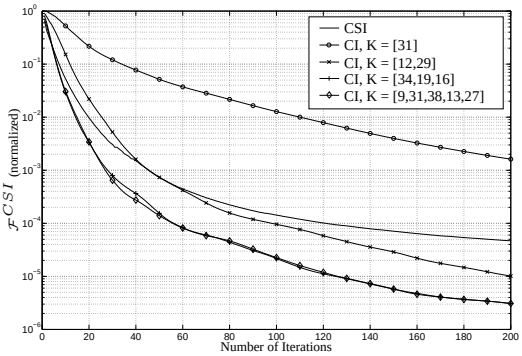

(b)

Figure 6.3: The domain cost function $\mathcal{F}^{CSI}$ for the reconstructions of test case 1 (a) and test case 2 (b) from noiseless data using the CSI method and the CI method with different sets K in the definition (6.24). The curves have been normalized with a single normalization factor, common to all curves.

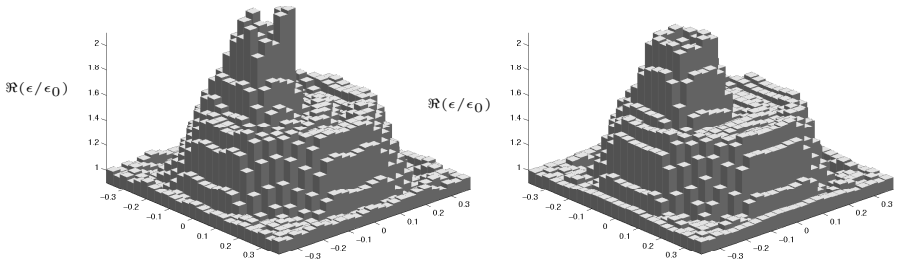

(a) (b)

Figure 6.4: Reconstructions after 200 iterations of test case 1 from noiseless data. Results obtained with the CSI method (a) and with the CI method (b).

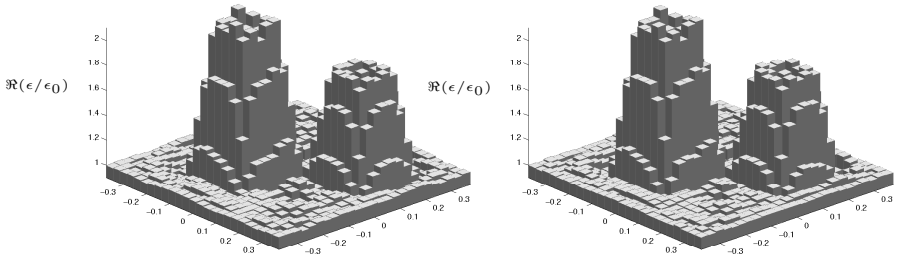

(a) (b)

Figure 6.5: Reconstructions after 200 iterations of test case 2 from noiseless data. Results obtained with the CSI method (a) and with the CI method (b).

6.3 Value picking regularization

It is clear from Figures 6.4 and 6.5 that both unregularized CSI and CI formulations do not succeed in obtaining perfect reconstructions even under noise free conditions. This conclusion stands even after continued minimization: after 1000 iterations the permittivity profiles still look much like Figure 6.4 and Figure 6.5 and the reconstruction errors are 0.05 and 0.071, respectively, for the CI and CSI reconstructions of test case 1 and 0.076 and 0.080, respectively, for the CI and CSI reconstructions of test case 2. The reconstructions thus have hardly improved or have even slightly deteriorated. Therefore regularization needs to be added, not only to mitigate the effect of noise on the data, but even to make the inverse crime problem better posed.

For the CSI method, several regularization approaches have been applied. Since they all act directly on the contrast, they cannot be applied to the CI method, in which the contrast is absent during the optimization. Value Picking (VP) Regularization, however, can be modified and applied to the CI method, without re-introducing N

contrast unknowns. This yields the VP regularized consistency inversion or VPCI method. We show that this method is especially suited to reconstruct piecewise constant permittivity profiles, for example the ones of Figure 6.1.

6.3.1 The VPCI cost function

The idea is to enforce the property that the contrast matrix $\boldsymbol{X}$ only contains a small number P of different values c_p with $p \in \{1, \ldots, P\}$, which act as auxiliary variables and are denoted the VP values. This is done by minimizing the cost function

$$\mathcal{F}(\boldsymbol{j}_1, \ldots, \boldsymbol{j}_I, \boldsymbol{c}) = \gamma \left[\mathcal{F}^D(\boldsymbol{j}_1, \ldots, \boldsymbol{j}_I) - h\right]^2 + \lambda_1 \mathcal{F}^P(\boldsymbol{j}_1, \ldots, \boldsymbol{j}_I, \boldsymbol{c}), \tag{6.30}$$

where the VPCI function $\mathcal{F}^P$ is given by

$$\mathcal{F}^P(\boldsymbol{j}_1, \ldots, \boldsymbol{j}_I, \boldsymbol{c}) = \sum_{n=1}^{N} f^P(U_n + \lambda_2 V_{n,1}, \ldots, U_n + \lambda_2 V_{n,P}), \tag{6.31}$$

with

$$U_n(\boldsymbol{j}_1, \ldots, \boldsymbol{j}_I) = \sum_{i=1}^{I} \sum_{k \in K} \left| [\boldsymbol{j}_i]_n [\boldsymbol{e}_{i-k}]_n - [\boldsymbol{j}_{i-k}]_n [\boldsymbol{e}_i]_n \right|^2, \tag{6.32}$$

$$V_{n,p}(\boldsymbol{j}_1, \ldots, \boldsymbol{j}_I, \boldsymbol{c}) = \sum_{i=1}^{I} H_{i,n} \left| [\boldsymbol{j}_i]_n - j\omega c_p [\boldsymbol{e}_i]_n \right|^2, \tag{6.33}$$

$$H_{i,n} = \sum_{k \in K} \left| [\boldsymbol{e}_{i-k}^{\text{init}}]_n \right|^2, \tag{6.34}$$

$$\lambda_1 = \frac{1}{\mathcal{F}^P(\boldsymbol{j}_1^{\text{init}}, \ldots, \boldsymbol{j}_I^{\text{init}}, \boldsymbol{c}^{\text{init}})}. \tag{6.35}$$

In (6.31), $\boldsymbol{c}$ is the vector of VP values and f^P is the P-dimensional choice function, defined in (4.41). The function U_n expresses consistency for cell n of the permittivity grid and the function $V_{n,p}$ expresses the error in (6.14) for cell n when $\boldsymbol{X}_{n,n} = c_p$. The positive parameter γ determines the trade-off between data fit and regularized consistency and the parameter λ_2 is a regularization parameter. The normalization constants λ_1 and $H_{i,n}$ are computed for initial estimates $\boldsymbol{j}_i^{\text{init}}$ for the contrast current vectors, $\boldsymbol{e}_i^{\text{init}}$ for the field vectors and $\boldsymbol{c}^{\text{init}}$ for the VP values. Note that the last VP value c_P is fixed to zero (the contrast of the background medium), because we are certain that this value will occur in $\boldsymbol{X}$.
The three most important properties of the choice function are (see Appendix B for an extensive list of properties and their proofs):

i) the positive choice function f^P is zero (and thus minimal) if and only if at least one of its arguments is zero (see Theorem B.4),

ii) when P_l arguments of f^P are much larger then the other $P_s = P - P_l$ arguments, f^P reduces to f^{P_s} evaluated in the smaller arguments (see (B.25)),

iii) when all its arguments are equal and change in an identical way, f^P is a scaled version of f^1, i.e. $f^P(u, \ldots, u) \propto f^1(u) = u$ (see Theorem B.5).

In (6.30), the consistency requirement and the regularization are both incorporated in the function $\mathcal{F}^P$. According to property i), this function is zero if and only if consistency is reached for every cell n (i.e. $U_n = 0$, $\forall n$) and if this consistency is realized with $\boldsymbol{X}_{n,n} = c_p$, for some $p \in \{1, \ldots, P\}$ (i.e. $V_{n,p} = 0$). In other words, minimization of $\mathcal{F}^P$ imposes consistency as well as the choice of one VP value for each cell to represent the contrast in that cell. From properties ii) and iii), it is furthermore observed that when (6.30) is minimized

- initially only consistency is enforced since with properly chosen λ_2 the optimization starts with $U_n \gg \lambda_2 V_{n,p}$. All the arguments thus are of comparable size and therefore they are simultaneously minimized, because of property iii).
- after a while, when some consistency is already present, the differences between the arguments of the choice functions introduced by the functions $V_{n,p}$ become important. Gradually, the larger arguments will be disregarded and the smaller arguments will be further minimized, because of property ii).
- finally, the VP regularization picks one VP value c_p for each cell n to enforce (6.14) through the minimization of the corresponding functions $V_{n,p}$ and U_n.

Note that it is possible that VP values merge in the course of the minimization.

6.3.2 The minimization

The algorithm for the minimization of the cost function (6.30) consists of alternately updating the contrast currents and the VP values. The updates of the contrast currents are still obtained with a line search along a conjugate gradient search direction (see Appendix D for the expressions of the gradient vectors). Since the cost function (6.30) is no longer polynomial in the line parameter (because the choice function is not linear for $P > 1$) the line search can no longer be performed by polynomial root finding and it might seem at first glance that more general line search algorithms have to be used, which would probably increase the computation time considerably. However, this can be avoided by using Theorem B.11 and Conjecture B.1 of Appendix B. Indeed, consider the fourth order function

$$\mathcal{Q}^P(\boldsymbol{j}_1, \ldots, \boldsymbol{j}_I, \boldsymbol{c}) = \sum_{n=1}^{N} \sum_{p=1}^{P} W_{n,p} \left(U_n + \lambda_2 V_{n,p}\right), \tag{6.36}$$

where the $W_{n,p}$ represent constant weight factors with $0 \leq W_{n,p} \leq 1$. In iteration m of the iterative minimization, which starts from the estimates $(\boldsymbol{j}_1^m, \ldots, \boldsymbol{j}_I^m)$ for the current vectors and $\boldsymbol{c}^m$ for the VP vector, these weights are calculated initially as

$$W_{n,p} = B_p^P(U_n^m + \lambda_2 V_{n,1}^m, \ldots, U_n^m + \lambda_2 V_{n,P}^m), \tag{6.37}$$

where the functions B_p^P are defined in Appendix B and where the superscript m indicates quantities evaluated for $(\boldsymbol{j}_1^m, \ldots, \boldsymbol{j}_I^m, \boldsymbol{c}^m)$. Because of Theorem B.11 and Conjecture B.1, the modified cost function

$$\mathcal{F}^Q(\boldsymbol{j}_1, \ldots, \boldsymbol{j}_I, \boldsymbol{c}) = \gamma \left[\mathcal{F}^D(\boldsymbol{j}_1, \ldots, \boldsymbol{j}_I) - h\right]^2 + \lambda_1 \mathcal{Q}^P(\boldsymbol{j}_1, \ldots, \boldsymbol{j}_I, \boldsymbol{c}) \tag{6.38}$$

touches with $\mathcal{F}$ in $(\boldsymbol{j}_1^m, \ldots, \boldsymbol{j}_I^m, \boldsymbol{c}^m)$ and lies above $\mathcal{F}$ in all other points. Therefore, minimizing $\mathcal{F}^Q$ along a descent direction starting from $(\boldsymbol{j}_1^m, \ldots, \boldsymbol{j}_I^m, \boldsymbol{c}^m)$ will also reduce $\mathcal{F}$. After this initial line search on $\mathcal{F}^Q$ yielding $(\boldsymbol{j}_1^{m,1}, \ldots, \boldsymbol{j}_I^{m,1}, \boldsymbol{c}^m)$, the weights $W_{n,p}$ are updated using (6.37) evaluated in $(\boldsymbol{j}_1^{m,1}, \ldots, \boldsymbol{j}_I^{m,1}, \boldsymbol{c}^m)$, such that $\mathcal{F}$ and $\mathcal{F}^Q$ touch again in this point. Then the procedure is repeated to obtain $(\boldsymbol{j}_1^{m,2}, \ldots, \boldsymbol{j}_I^{m,2}, \boldsymbol{c}^m)$ etc. When, after q cycles no improvements are made in this rapid sequence of polynomial line searches, the currents are updated from $(\boldsymbol{j}_1^m, \ldots, \boldsymbol{j}_I^m)$ to $(\boldsymbol{j}_1^{m+1}, \ldots, \boldsymbol{j}_I^{m+1}) = (\boldsymbol{j}_1^{m,q}, \ldots, \boldsymbol{j}_I^{m,q})$.

To subsequently update the VP values, the same fourth-order approximation (6.36) of the choice function is employed. It can be observed from (6.36) and (6.33) that $\mathcal{F}^Q$ is quadratic in the VP values. This means that, to minimize $\mathcal{F}^Q$ for fixed weights $W_{n,p}$ and for fixed contrast current vectors $(\boldsymbol{j}_1^{m+1}, \ldots, \boldsymbol{j}_I^{m+1})$, a simple quadratic programming method can be used [4]. Moreover, it is very simple to introduce constraints on the VP values in such a method, yielding a quadratic active set method (see Section 4.3.2 or [4]). Again this quadratic minimization can be repeated in a sequence where the weights $W_{n,p}$ are updated until no further progress is made. At this point we have completed iteration m and have obtained $(\boldsymbol{j}_1^{m+1}, \ldots, \boldsymbol{j}_I^{m+1}, \boldsymbol{c}^{m+1})$.

6.3.3 Stepwise relaxed VP regularization

An issue unmentioned until now is the choice of the number of VP values P. It might be that the ideal value of P is known in advance, but certainly this is not always the case. In theory the value of P can be larger than the actual number of different permittivity values in the profile, since the VP regularization algorithm allows for the merging of two or more VP values. In practice however, it is best to let P be as small as possible, since a larger number of VP values introduces a larger freedom in the optimization space, which is not always beneficial, especially not in the beginning of the minimization. Indeed, when still far from the solution, the VP regularization might make incorrect choices, i.e. choices that prevent simultaneous satisfaction of the requirements of data fit and consistency. Although such choices may be corrected

by further minimization of the cost function, they may also lead to local minima in the cost function in which the local optimization algorithm can get trapped. Therefore we choose to adopt a stepwise relaxed VP regularization, which in Chapter 4 has proven to be a good strategy to avoid the problem of incorrect choices and which can also be seen as an extra updating scheme for the auxiliary discrete variable P.

In the stepwise relaxed VP regularization strategy, the minimization is started from an initial estimate (see Section 6.3.4) with $P = 1$ and a sufficiently large regularization parameter λ_2. When the convergence rate has decreased below a predefined threshold, an extra VP value is introduced. This relaxes the VP regularization, as can be seen from Theorem B.10 in Appendix B. With $P = 2$ the minimization is continued until again stagnation occurs. Each time a VP value is added this way until this introduces no further progress. The addition of a VP value is done by initializing it at random (making sure it does not coincide with an already present VP value) and applying the repeated quadratic minimization algorithm which is mentioned at the end of Section 6.3.2.

6.3.4 Initial estimate

Before the iterations with VP regularization are started, a first estimate of the contrast currents is obtained using unregularized consistency inversion, i.e. by minimizing (6.25). These first iterations are stopped quite early, because high accuracy is not needed. To initialize this initial consistency inversion itself, an estimate of the visible currents is first obtained from (6.13). However, whereas in Section 6.2.2 the visible parts of the current vectors were obtained exactly using the pseudo-inverse of $\boldsymbol{A}$, this is no longer possible due to noise on the data: the minimum norm solution to (6.13) fits the data perfectly, including the noise, which is not the case for the actual visible current vectors. Moreover, $\boldsymbol{A}$ is typically ill-posed and the minimum norm solutions can be very different from the actual visible current vectors due to noise amplification. Therefore we consider a Tikhonov regularized solution to (6.13) (see Section 2.2):

$$\boldsymbol{j}_{i,\alpha}^{R} = \boldsymbol{V}\left(\boldsymbol{S}^2 + \alpha \boldsymbol{I}\right)^{-1} \boldsymbol{S}\boldsymbol{U}^H \boldsymbol{e}_i^{\mathrm{s}}. \tag{6.39}$$

The regularization parameter α is obtained using the discrepancy principle [13], i.e. α is such that

$$\frac{\sum_{i=1}^{I} \|\boldsymbol{e}_i^s - \boldsymbol{A}\boldsymbol{j}_{i,\alpha}^{R}\|^2}{\sum_{i=1}^{I} \|\boldsymbol{e}_i^s\|^2} = h. \tag{6.40}$$

As a consequence the initial contrast currents already yield a data fit on the noise level. The first term in (6.25) and (6.30) thus simply keeps the data fit around the noise level during the optimization and is squared to keep the cost function positive. This is a generalization of the strategy we employ in the noiseless case, where the data fit is satisfied exactly after the visible currents have been determined by (6.27) and

where the further optimization only looks for the invisible currents and leaves the data fit unaltered. The normalization parameter λ in the initial minimization of (6.25) is chosen as

$$\lambda = \frac{1}{\mathcal{F}^{CI}(\boldsymbol{j}^R_{1,\alpha}, \ldots, \boldsymbol{j}^R_{I,\alpha})}. \tag{6.41}$$

6.4 Numerical examples

To illustrate the effect of the VP regularization on the CI inversion method, the same test cases as in Section 6.2.2 are first considered. For both test cases, we start with an inversion from noiseless data. As mentioned above, the unregularized CI and CSI methods do not succeed in obtaining a quasi-perfect reconstruction even under such inverse crime conditions. If the VP regularization is used, the result is improved drastically. For all the following reconstructions with VP regularization, the regularization parameter is $\lambda_2 = 0.001$ and we impose physical constraints on the VP values:

$$\Re(c_p) \geq 0.0, \quad \forall p \tag{6.42}$$

$$\Im(c_p) \leq 0.0, \quad \forall p. \tag{6.43}$$

The following stopping criteria are used for the different steps in the stepwise relaxed VPCI scheme (an iteration in the following refers to a complete update of the optimization variables, i.e. a line search along a CG direction and possibly an update of the VP values):

- The initial CI iterations (minimizing (6.25)) are stopped when $\mathcal{F} < 0.01$, when the relative difference $|\Delta\mathcal{F}|/\mathcal{F}$ between two subsequent iterates is smaller then 0.001 or after 500 iterations
- Every step in the stepwise relaxed VPCI scheme (minimizing (6.30) for fixed P) is stopped when $\mathcal{F} < 10^{-6}$, when $|\Delta\mathcal{F}|/\mathcal{F} < 0.001$ or after 500 iterations
- When adding a new VP value leads to only one additional iteration before the minimization is stopped by the above stopping criterion, this last step in the stepwise relaxed VP regularization scheme is disregarded and the complete algorithm is stopped.

Using these criteria, the result in Figure 6.6 is obtained. The number of iterations which the algorithm performed during the initial CI inversion and the subsequent VPCI inversions with increasing number of VP values is given in Table 6.1. For both test cases the correct number of VP values is obtained and the reconstruction error is only $4.6 \cdot 10^{-4}$ for test case 1 and $2.9 \cdot 10^{-4}$ for test case 2, two virtually perfect reconstructions.

	Test case 1				
	CI	$P = 1$	$P = 2$	$P = 3$	$P = 4$
noiseless	12	28	140	418	/
30 dB	72	43	61	500	15
20 dB	57	46	81	474	/
	Test case 2				
noiseless	14	44	258	350	/
30 dB	60	47	262	439	/
20 dB	56	38	300	353	/

Table 6.1: The number of iterations in every step (initial CIinversion and the subsequent steps with increasing number of VP values P) of the stepwise relaxed VPCI reconstructions of the targets of Figure 6.1 for different values of the SNR.

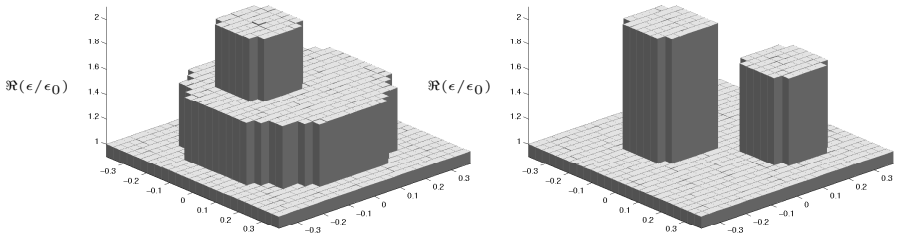

(a) (b)

Figure 6.6: Reconstructions of test case 1 (a) and test case (2) from noiseless data using the stepwise relaxed VPCI method with $\lambda_2 = 0.001$.

Next the data is corrupted with noise. We add Gaussian noise to the data of both test cases, once with an SNR of 30 dB and once with an SNR of 20 dB. As mentioned before the data fit term in (6.30) must keep the data fit on or close to the noise level h, while the second term is minimized to yield consistency. If the noise level h is exactly known, the proposed cost function (6.30) can in principle be minimized to zero, since it is zero for the actual permittivity profile. Therefore, with this cost function there is no real trade-off between data fit and consistency in the minimum of the cost function as is the case, for example, for CSI inversion with the cost function (6.16). If h is only an approximation of the actual noise level, however, there is a trade-off, which is regulated by the parameter γ. To make sure that the degree of consistency is high enough when convergence is reached in such a situation, it seems logical to give more weight to the consistency term when there is more noise on the data, since more noise also implies a larger uncertainty on the noise level. It is, however, not clear that the regularization parameter λ_2 should be modified in case of noisy data, since it merely determines the level of consistency where the VP regularization starts picking VP

values. Therefore, we try keeping it fixed to the value $\lambda_2 = 0.001$ which is also used for the noiseless data. The parameters γ and h are chosen as $\gamma = 10^5$ and $h = 0.001$ in case of the 30 dB data and as $\gamma = 10^4$ and $h = 0.01$ in case of the 20 dB data.

The reconstructions with 30 dB noise are shown in Figure 6.7. From Table 6.1 it follows that the algorithm overestimates the number of VP values in test case 1, probably because the iterations with $P = 3$ are terminated when the maximum number of iterations is reached and not when convergence has occurred. However, two VP values are close to each other ($0.474{\cdot}10^{-11}$ and $0.443{\cdot}10^{-11}$, corresponding to relative permittivities 1.535 and 1.500) and the reconstruction error is 0.015. With respect to the exact profile, some incorrect choices were made by the VP regularization along the contour of the largest object (close to the leftmost corner of the smaller inclusion as seen in Figure 6.7 (a)). For test case 2 the correct number of VP values is obtained and the reconstruction error is 0.022. An incorrect choice has been made for the pixel on the lefmost corner of the object with permittivity $2\epsilon_0$. The reconstructions with 20 dB noise are shown in Figure 6.8. This time the correct number of VP values is obtained for both test cases, as can be seen in Table 6.1, and the reconstruction errors are 0.02 and 0.044, respectively, for test case 1 and test case 2. Again the main causes of error are some incorrect VP choices along the outline of the object with lowest permittivity in test case 1 and the object with the highest permittivity in test case 2. However, it is clear that, even with noise on the data the VPCI results are much better than the CI and CSI reconstructions of the noiseless data.

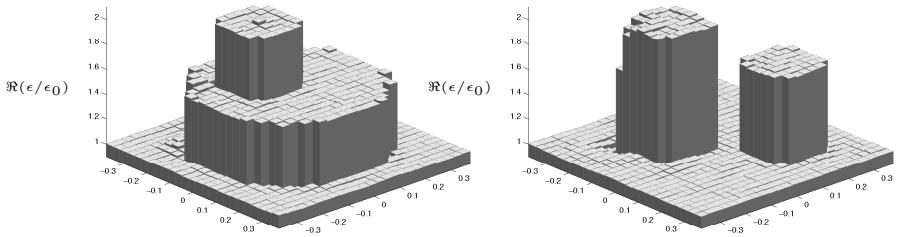

(a) (b)

Figure 6.7: Reconstructions of test case 1 (a) and test case (2) from noisy data with SNR $= 30$ dB using the stepwise relaxed VPCI method with $\lambda_2 = 0.001$, $h = 0.001$ and $\gamma = 10^5$.

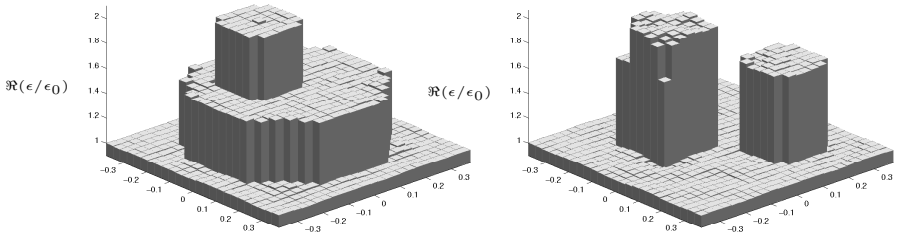

(a) (b)

Figure 6.8: Reconstructions of test case 1 (a) and test case (2) from noisy data with SNR $= 20$ dB using the stepwise relaxed VPCI method with $\lambda_2 = 0.001$, $h = 0.01$ and $\gamma = 10^4$.

The last example is adopted from literature, more specifically from [2], where a CSI method with both smoothing and total variation regularization is used. The target is a square cylinder with side λ_b (0.3 m) and permittivity $(1.6 - 0.2j)\epsilon_0$ which is enclosed in a larger square with side $2\lambda_b$ (0.6 m) and permittivity $(1.3 - 0.4j)\epsilon_0$ (Figure 6.9). The discretization grid is a 29×29 grid with side $3\lambda_b$ (0.9 m). Both squares and the grid are centered at the origin. The illuminating line sources are evenly distributed over a circle with radius $R = 3\lambda_b$ (0.9 m) and $I = 29$. For this third example, denoted test case 3, the inversion parameters are the same as before, i.e. $\lambda_2 = 0.001$ and depending on the SNR, 30 dB or 20 dB respectively, the parameters γ and h are chosen as $\gamma = 10^5$ and $h = 0.001$ or as $\gamma = 10^4$ and $h = 0.01$, respectively. The set K, however, is different, because the number of line sources is different. This set is now $K = \{7, 17, 27\}$. Figure 6.10 shows the result for a reconstruction of noiseless data. The reconstruction is again almost perfect ($err_\epsilon = 6.2 \cdot 10^{-4}$) and from Table 6.2 we conclude that the correct number of permittivity values is estimated. When noise is added to the data, we obtain the results from Figure 6.11 for SNR $= 30$ dB and Figure 6.12 for SNR $= 20$ dB. In both cases the number of VP values is overestimated. However, for SNR $= 30$ dB two VP values are very close to each other (relative permittivities $(1.307 - 0.399j)$ and $(1.307 - 0.400j)$) and the reconstruction error is only $7.3 \cdot 10^{-3}$, which is less than 1% and thus also almost perfect. Only in the reconstruction with SNR $= 20$ dB does the noise have a noticeable influence on the reconstruction. Here, some incorrect choices are made along the outline of both squares and the algorithm only terminates for $P = 5$, but the reconstruction error is still only 0.041 and the VP values fall apart in two pairs of close values (permittivities $(1.297 - 0.393j)$ and $(1.299 - 0.390j)$ on the one hand and $(1.520 - 0.267j)$ and $(1.550 - 0.228j)$ on the other hand). To appreciate this result more, Figure 6.13 shows the reconstruction for SNR $= 20$ dB obtained by the CI method without regularization after 192 iterations (to reach the stopping criterion $\mathcal{F} < 10^{-6}$), which is clearly worse than the reconstruction with the VPCI method. Not only is the reconstruction error larger ($err_\epsilon = 0.093$), the boundaries of the squares cannot easily be distinguished and two permittivity values for the squares are not readily identified, in contrast to

the result of Figure 6.12. The reconstructions of test case 3, obtained with the VPCI method are of comparable quality as those obtained in [2, 3] with the CSI method with TV regularization. To conclude, Figure 6.14 shows the convergence of both unregularized CI and CSI methods in the inverse crime conditions of Section 6.2.2. Under these circumstances, the CI approach again yields faster convergence.

	Test case 3					
	CI	$P = 1$	$P = 2$	$P = 3$	$P = 4$	$P = 5$
noiseless	12	56	148	293	/	/
30 dB	70	72	279	500	104	/
20 dB	39	63	393	500	33	2

Table 6.2: The number of iterations in every step (initial CI inversion and the subsequent steps with increasing number of VP values P) of the stepwise relaxed VPCI reconstructions of the target of Figure 6.9 for different values of the SNR.

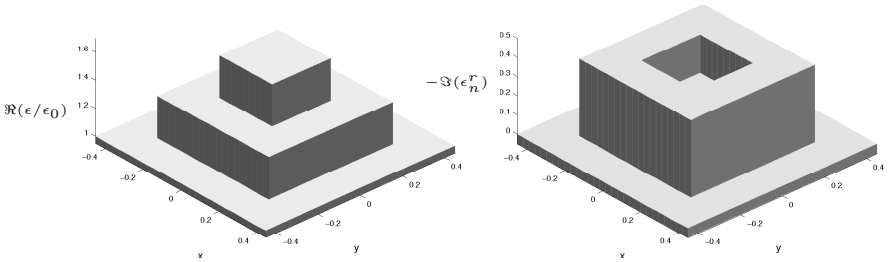

(a) (b)

Figure 6.9: The (complex) permittivity profile of test case 3. Real part (a) and inverse of the imaginary part (b).

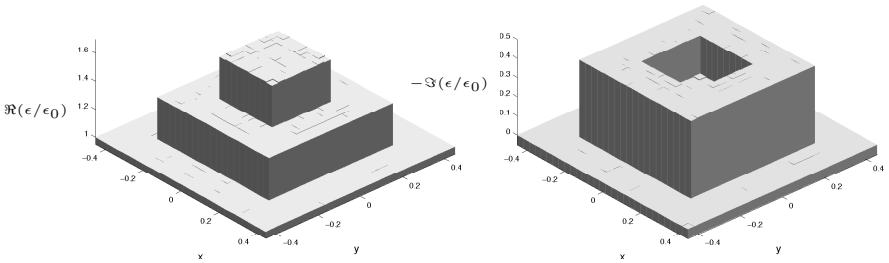

(a) (b)

Figure 6.10: Reconstruction of test case 3 from noiseless data using the stepwise relaxed VPCI method with $\lambda_2 = 0.001$. Real part (a) and inverse of the imaginary part (b).

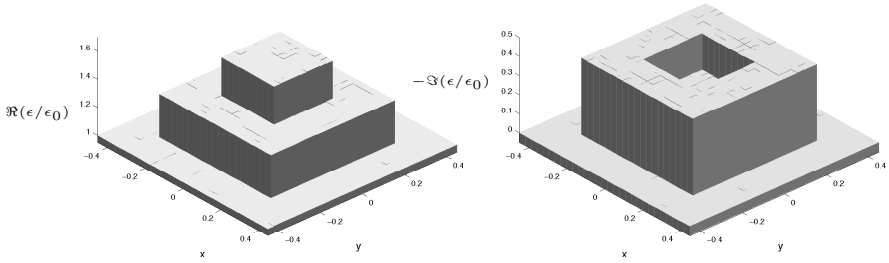

(a) (b)

Figure 6.11: Reconstruction of test case 3 from noisy data with SNR $= 30$ dB data using the stepwise relaxed VPCI method with $\lambda_2 = 0.001$, $h = 0.001$ and $\gamma = 10^5$. Real part (a) and inverse of the imaginary part (b).

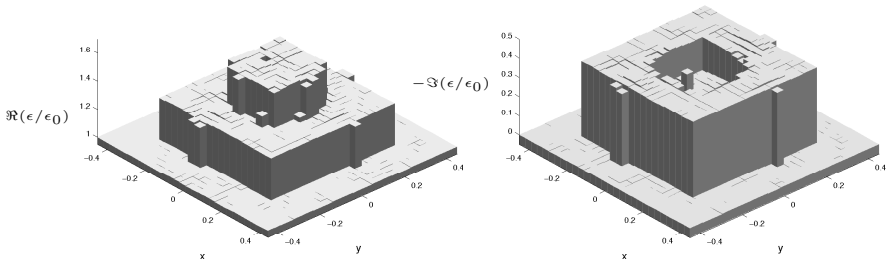

(a) (b)

Figure 6.12: Reconstruction of test case 3 from noisy data with SNR $= 20$ dB data using the stepwise relaxed VPCI method with $\lambda_2 = 0.01$, $h = 0.001$ and $\gamma = 10^4$. Real part (a) and inverse of the imaginary part (b).

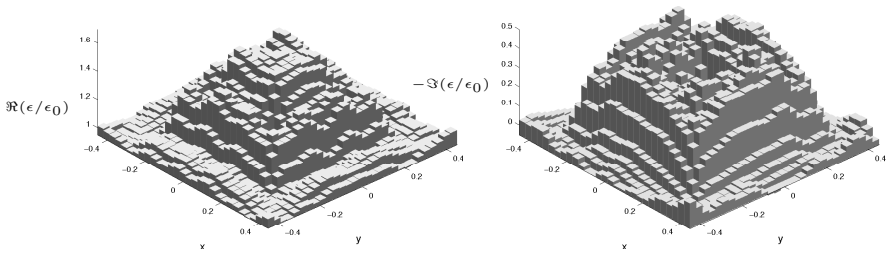

(a) (b)

Figure 6.13: Reconstruction of test case 3 from noisy data with SNR $= 20$ dB data using the unregularized CI method with $h = 0.001$ and $\gamma = 10^4$. Real part (a) and inverse of the imaginary part (b).

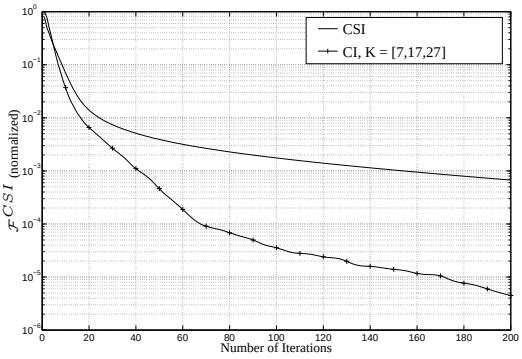

Figure 6.14: The domain cost function $\mathcal{F}^{CSI}$ for the reconstructions of test case 3 from noiseless data using the CSI method and the CI method with $K = [7, 17, 27]$ in the definition (6.24). The curves have been normalized with a single normalization factor, common to both curves.

6.5 Conclusion

Two major conclusions can be drawn from this chapter. First, it is possible to reformulate the contrast source inversion method such that the permittivity unknowns are eliminated from the optimization problem. This consistency inversion method produces results, comparable to those of the CSI method, but, avoiding the alternating updates of contrast currents and permittivity, it is expected to convergence faster. A preliminary study under idealized circumstances confirms this, but more research is required to validate this statement in general. Second, the value picking regularization, which was recently proposed for use in the conventional approach to inverse scattering, can be incorporated in the CI method, whereas other regularization methods that operate directly on the permittivity cannot. The resulting VPCI method is capable of accurately reconstructing piecewise homogeneous permittivity profiles, conserving edges and constant regions in the reconstruction with minimal a priori information. At this point it is not clear whether or not the VPCI method outperforms other contrast source based inversion schemes, such as the CSI method with TV regularization, either in reconstruction quality or in computation time, but it certainly is a viable alternative. Finally note that the VP regularization can also be incorporated in the CSI method, either as this is done for the CI method, or operating directly on the permittivity as is done in Chapter 4.

Bibliography

[1] P.M. van den Berg and R.E. Kleinman. A Contrast Source Inversion Method. *Inverse Problems*, 13(6):1607–1620, 1997.

[2] P.M. van den Berg, A.L. van Broekhoven, and A. Abubakar. Extended Contrast Source Inversion. *Inverse Problems*, 15(5):1325–1344, 1999.

[3] P.M. van den Berg and A. Abubakar. Contrast source inversion method: state of the art. *PIER*, 34:189–218, 2001.

[4] R. Fletcher. *Practical Methods of Optimization*. John Wiley, New York, 1990.

[5] T. Isernia, V. Pascazio, and R. Pierri. A Nonlinear Estimation Method in Tomographic Imaging. *IEEE Trans. Geosci. Remote Sens.*, 35(4):910–923, 1997.

[6] J. Van Bladel. *Electromagnetic Fields, second edition*. John Wiley & Sons, Inc., New Jersey, 2007.

[7] I. Bogaert, L. Knockaert, and F. Olyslager. Efficient calculation of moment integrals for tensor product basis functions. *Proceedings of the IEEE Symposium on Antennas and Propagation, Honolulu, USA*, pages 5636–5639, 2007.

[8] T.K. Sarkar, E. Sarvas, and S.M. Rao. Application of FFT and the Conjugate Gradient Method for the Solution of Electromagnetic Radiation from Electrically Large and Small Conducting Bodies. *IEEE Trans. Antennas Propagat.*, 34(5):635–640, 1986.

[9] C. C. Su. Calculation of electromagnetic scattering from a dielectric cylinder using the conjugate gradient method and FFT. *IEEE Trans. Antennas Propagat.*, 35:1418–1425, 1987.

[10] W.C. Chew, Y.M. Wang, G. Otto, D. Lesselier, and J.C. Bolomey. On The Inverse Source Method For Solving Inverse Scattering Problems. *Inverse Problems*, 10(3):547–553, 1994.

[11] M.M. Ney, A.M. Smith, and S.S. Stuchly. A Solution of Electromagnetic Imaging Using Pseudoinverse Transformation. *IEEE Trans. Med. Imag.*, 3(4):155–162, 1984.

[12] S. Caorsi, G.L. Gragnani, and M. Pastorino. Reconstruction of dielectric permittivity distributions in arbitrary 2-D inhomogeneous biological bodies by a multiview microwave numerical method. *IEEE Trans. Med. Imag.*, 12(2):232–239, 1993.

[13] V.A. Morozov. On the solution of functional equations by the method of regularization. *Soviet Math. Dokl.*, 7:414–417, 1966.

CHAPTER 7

Conclusions and Perspectives

In this doctoral research, algorithms for quantitative microwave imaging, or electromagnetic inverse scattering, have been developed. The emphasis was on 3D imaging, a field of research which has only recently been given the full attention of the inverse scattering community. Our numerical experiments with the CI method have been conducted in 2D, but with the discretization techniques of Chapter 3, it is readily extendable to three dimensions. This dissertation presented several improvements to the forward and inverse scattering algorithms, aiming at both a better efficiency and an improved reconstruction quality.

A first couple of improvements concerned the numerical solution of the forward problem, which constitutes an important part of conventional inverse scattering algorithms. In Chapter 3, a full-wave vectorial volume integral equation approach was adopted to simulate the forward scattering from a given 3D complex permittivity profile. The large linear systems that arise from the MoM discretization of the VIE are solved iteratively and two improvements were proposed to do this more efficiently. A first improvement is the hybrid MLFMA-FFT method, which combines the strengths of the Multilevel Fast Multipole Algorithm and the FFT-method to speed up the individual matrix-vector multiplications in the iterative solution. A second improvement is the use of an extrapolation technique, based on the marching-on-in-source-position scheme and the Born approximation, to reduce the number of iterations by choosing a better initial estimate. Although the full potential of the MLFMA-FFT method has not been further exploited in our inversion experiments, the method can be useful in future applications with sparser scattering configurations as illustrated in Chapter 3. In contrast source based inversion methods, such as the CSI method or the CI method presented in Chapter 6, the solution of a multi-view forward scattering is not necessary, but even here the MLFMA-FFT method is applicable, since it can be used to

evaluate the fields in the investigation domain generated by the contrast currents.

We explored two approaches to solve the inverse scattering problem in this work. The conventional approach eliminates the electric fields (or equivalently the contrast currents) from the optimization problem and retains only the permittivity as unknown quantity, whereas the CI method eliminates the permittivity and only optimizes for the contrast currents. The major part of this dissertation is devoted to 3D microwave reconstruction algorithms which employ a Gauss-Newton optimization strategy to solve the inverse scattering problem in the conventional approach (Chapters 4 and 5). The Gauss-Newton optimization algorithm is well known and widely used for minimizing sums of squares cost functions, such as the least squares data fit cost function. In this work, the Gauss-Newton framework has been modified to minimize regularized cost functions. Two different regularization strategies were proposed: multiplicative smoothing and Value Picking regularization.

Multiplicative smoothing regularization is a flexible, adaptive tool which allows for reconstructions of objects on which not much a priori information is available. It reduces the ill-posedness of the inverse scattering problem by limiting the optimization space to profiles that are sufficiently smooth and therefore do not suffer from high frequency perturbations. Although this regularization smooths away the sharp interfaces in objects with piecewise constant permittivity profiles, it provides useful reconstructions in any case and is very suitable for reconstructing permittivity profiles without very sharp edges and a wide range of permittivity values, such as some biological phantoms. Moreover, the multiplicative nature of this regularization renders the choice of a regularization parameter less critical.

VP regularization is a new regularization method, more suited for imaging piecewise homogeneous objects and also easily incorporated in the Gauss-Newton framework via a half-quadratic optimization scheme. It is based on the knowledge that only a few different permittivity values occur in such profiles, the values of which need not be known in advance. The VP regularization is introduced in the solution of the inverse problem by adding a choice function to the data fit cost function for every permittivity unknown. When minimized, the VP regularizing function clusters the complex permittivity values in the complex plane around a number of VP values, which are treated as auxiliary optimization variables. The stepwise relaxation of VP regularization, resulting in the SRVP regularization strategy, introduces an updating scheme for the number of VP values. The Gauss-Newton method with SRVP regularization provides very good reconstruction quality even when it is applied to experimental data.

Both regularization methods allow for the use of the SPLSQR method to solve the Gauss-Newton update systems iteratively, which results in less iterations and hence a lower computational cost and a wider application range of the inverse scattering algorithm. This algorithm extracts from the original Gauss-Newton update system a smaller system, which inherits the ill-conditioning, but can be rapidly solved in a direct manner. The remainder of the system is better conditioned and can be solved

iteratively with much less iterations than the original system. Finally, the use of upper and lower bounds on the real and imaginary parts of the permittivity has been made possible through the use of a constrained line search path. This approach requires little adaptations of the unconstrained Gauss-Newton algorithm while offering more control over the optimization process.

The developed reconstruction algorithms were tested on both synthetic and experimental data. Biomedical objects are challenging test cases for inverse scattering methods, because of the high permittivities and large contrasts involved. Some numerical biological phantoms were considered in this dissertation and illustrate the applicability of our general inverse scattering algorithms to biomedical microwave imaging. In particular, the reconstruction of a numerical breast phantom supports the international efforts made to develop practical microwave imaging methods for breast cancer screening and monitoring. The successful inversion of the experimental Fresnel data with our algorithms demonstrates the validity of the algorithms for both the forward and inverse problems. Moreover, we showed that, even with single frequency data and despite the high noise levels, very accurate reconstructions can be obtained by using suitable regularization, in our case SRVP regularization.

The other approach to inverse scattering, which is based on the introduction of contrast currents as auxiliary optimization variables, has also been investigated in this work. It has been shown that it is possible to eliminate the permittivity unknowns from the optimization problem in the CSI method, resulting in a method which we named consistency inversion. This method optimizes for one type of physical quantities only, the contrast currents, and is expected to yield faster convergence than the CSI method, where both contrast currents and the permittivity are updated alternatingly. This behavior indeed has been observed in a number of test cases and it should be investigated whether it occurs systematically. The SRVP regularization scheme has been incorporated in the CI method as well. Like in the conventional approach, the reconstruction quality in case of piecewise constant permittivity profiles is greatly improved because of this.

Despite the advances made in solving the 3D inverse scattering problem, several improvements are still possible and should probably be incorporated in a practical microwave imaging algorithm. As far as the forward scattering problem is concerned, following suggestions can be made.

a) The forward scattering algorithms can be parallelized for optimal efficiency, i.e. the workload can be distributed over different computing cores simultaneously. This is possible in two ways. First of all, several forward simulations, corresponding to different illuminations, can run in parallel. Because of this, it is often said that the conventional approach to inverse scattering is *embarrassingly* parallel. Second of all, the routines to calculate FFT's and the MLFMA are parallelizable on themselves. Recently, a lot of effort has been put in the development of parallel MLFMA codes that can run on ordinary computer net-

works [1, 2]. A large speed-up can be expected from a combination of parallelization of the forward problem with the extrapolation approach presented in Chapter 3.

b) It has been observed that the VIE of Chapter 3 is not always as well-conditioned as one would like, for example when inverting biomedical examples with large contrast and especially when the background permittivity is much higher than the average permittivity in the biomedical phantom. Therefore, it might be profitable to look for better conditioned formulations of the VIE or for suitable preconditioning techniques for the forward problem.

c) In measurement configurations where the antennas are close to the investigation domain and where the complete setup is electromagnetically shielded from its surroundings, for example in medical imaging, the VIE might not be the best choice to solve the forward problem. Indeed, in such situations, it loses its largest assets, which are not having to discretize large areas of empty space in the measurement setup and not having to truncate the mesh artificially. In those circumstances, a finite element (FE) approach might be the better choice [3].

d) Finally, for real world applications, it may be necessary to include more realistic antenna models in the reconstruction algorithm. It should also be investigated to which extent mutual coupling between the antennas of a fixed antenna array, as will be used in microwave biomedical imaging, and the coupling of the antennas with the object under study influence the imaging performance. Possibly, this should be taken into account. Also, the forward problem code could be extended to include inhomogeneous backgrounds. This could be achieved by using embedding techniques [4], possibly employing a coupling of a finite element system in the investigation domain with a boundary integral approach to account for the radiation condition or the interaction with the surrounding known environment [5, 6].

Concerning the Gauss-Newton approach to microwave imaging, future work might include:

a) a comparison between SRVP regularization and other edge-preserving techniques.

b) the generalization of the VP regularization scheme to a Region Picking regularization strategy, as suggested in Section 4.5.

c) the development of procedures to determine the regularization parameter for SRVP regularization in an a priori or adaptive way.

d) the extension of the SPLSQR algorithm to situations where not every cell in the permittivity grid is included in the optimization problem or where several

cells are clustered in cell groups. In such a situation the truncated 3D discrete cosine base can no longer be used and should be replaced by a different coarse subspace.

e) the search for more rigorous yet efficient ways to incorporate constraints on the permittivity.

f) the reduction of storage requirements of Gauss-Newton based inversion. Mainly the storage of the jacobian matrix $\boldsymbol{J}$ (or $\boldsymbol{K}$ when using the SPLSQR algorithm) is limiting for the application to larger inverse scattering problems.

Finally there is some work to do to further validate the CI method. Its convergence rate should be compared more extensively with that of the CSI method and it should be tested on experimental data. The choice of the parameters of the method also requires some further investigation and, obviously, the CI method should be extended to the 3D case and compared to the conventional approach.

Bibliography

[1] J. Fostier, F. Olyslager, and . An asynchronous parallel MLFMA for scattering at multiple dielectric objects. *IEEE Trans. Antennas Propagat.*, 56(8):2346–2355, 2008.

[2] J. Fostier and F. Olyslager. A provably scalable parallel multilevel fast multipole algorithm. *Electronics Letters*, 44(19):111–1113, 2008.

[3] R. Lencrerot, A. Litman, H. Tortel, and J.M. Geffrin. A microwave imaging circular setup for soil moisture information. *Geoscience and Remote Sensing Symposium, 2007. IGARSS 2007. IEEE International*, (4394–4397).

[4] A. Franchois and A.G. Tijhuis. A Quasi-Newton Reconstruction Algorithm for a Complex Microwave Imaging Scanner Environment. *Radio Science*, 38(2), 2003.

[5] H. Rogier, F. Olyslager, and D. De Zutter. A hybrid finite element integral equation approach for the eigenmode analysis of complex anisotropic dielectric waveguides. *Radio Science*, 31(4):999–1010, 1996.

[6] H. Rogier and D. De Zutter. A new finite element-FDTD-boundary integral equation technique with biconjugate gradient solver for modeling electromagnetic problems in the frequency domain. *Radion Science*, 38(6), 2003.

APPENDICES

APPENDIX A

Recursive calculation of the truncated translation operator

As mentioned in Section 3.4 of Chapter 3, the integration in (3.23) is based on a Fourier-representation of the radiation patterns $\boldsymbol{U}_a$ and $\boldsymbol{V}_{\beta,b}$. Since the Fourier-spectra of $\boldsymbol{U}_a(\theta,\phi)$ and $\boldsymbol{V}_{\beta,b}(\theta,\phi)$ are exponentially decaying, as mentioned in Section 3.4.2, they can be represented by a finite amount of samples in θ and ϕ with any desired accuracy. The product of the translation operator $T_{ba}(\theta,\phi)$ (3.19) and $|\sin\theta|$ is not bandlimited and can therefore not be represented accurately by a finite number of samples. However, since it is integrated in (3.23) with a quasi-bandlimited function, it can be smoothed (i.e. its Fourier spectrum can be truncated) to the total bandwidth of the remainder of the integrand. This truncated version of $T_{ba}(\theta,\phi)|\sin\theta|$ *can* be represented by a finite number of samples. The following derivation was done by Dr. Ignace Bogaert.

To obtain the smoothed translation operator, we need to compute the Fourier spectrum of $T_{ba}(\theta,\phi)\,|\sin\theta|$:

$$b_{mn} = \frac{1}{4\pi^2}\int_0^{2\pi}\int_0^{2\pi} T_{ba}(\theta,\phi)\,|\sin\theta|\,e^{-j(m\theta+n\phi)}\mathrm{d}\theta\mathrm{d}\phi. \tag{A.1}$$

Upon substituting (3.19) in this expression, we get

$$\begin{aligned} b_{mn} &= \sum_{l=0}^{L}(2l+1)j^{-l}h_l^{(2)}(k_{\mathrm{b}}r_{ba})\frac{1}{4\pi^2} \\ &\quad \times \int_0^{2\pi}\int_0^{2\pi} P_l(\hat{\boldsymbol{k}}(\theta,\phi)\cdot\hat{\boldsymbol{r}}_{ba})\,|\sin\theta|\,e^{-j(m\theta+n\phi)}\mathrm{d}\theta\mathrm{d}\phi \qquad \text{(A.2)} \\ &= \sum_{l=0}^{L}(2l+1)j^{-l}h_l^{(2)}(k_{\mathrm{b}}r_{ba})\frac{1}{4\pi^2}f_{mn}^{l} \qquad \text{(A.3)} \end{aligned}$$

with

$$f_{mn}^{l} = \int_0^{2\pi}\int_0^{2\pi} P_l(\hat{\boldsymbol{k}}(\theta,\phi)\cdot\hat{\boldsymbol{r}}_{ba})\,|\sin\theta|\,e^{-j(m\theta+n\phi)}\mathrm{d}\theta\mathrm{d}\phi. \qquad \text{(A.4)}$$

To calculate these coefficients numerically, we derive a recursion. To this end we make use of a recursion formula for the Legendre function

$$(l+1)P_{l+1}(x) = (2l+1)xP_l(x) - lP_{l-1}(x) \qquad \text{(A.5)}$$

which, together with the identity

$$\hat{\boldsymbol{k}}(\theta,\phi)\cdot\hat{\boldsymbol{r}}_{ba} = \cos\theta\cos\theta_{ba} + \sin\theta\sin\theta_{ba}\cos(\phi-\phi_{ba}) \qquad \text{(A.6)}$$

leads to

$$f_{mn}^{l+1} = \frac{2l+1}{l+1}(\cos\theta_{ba}a_{mn}^{l} + \sin\theta_{ba}\cos\phi_{ba}b_{mn}^{l} + \sin\theta_{ba}\sin\phi_{ba}c_{mn}^{l}) - \frac{l}{l+1}f_{mn}^{l-1} \qquad \text{(A.7)}$$

with, by definition

$$\begin{aligned} a_{mn}^{l} &= \int_0^{2\pi}\int_0^{2\pi} \cos\theta P_l(\hat{\boldsymbol{k}}(\theta,\phi)\cdot\hat{\boldsymbol{r}}_{ba})\,|\sin\theta|\,e^{-j(m\theta+n\phi)}\mathrm{d}\theta\mathrm{d}\phi, \qquad \text{(A.8)} \\ b_{mn}^{l} &= \int_0^{2\pi}\int_0^{2\pi} \sin\theta\cos\phi P_l(\hat{\boldsymbol{k}}(\theta,\phi)\cdot\hat{\boldsymbol{r}}_{ba})\,|\sin\theta|\,e^{-j(m\theta+n\phi)}\mathrm{d}\theta\mathrm{d}\phi, \qquad \text{(A.9)} \\ c_{mn}^{l} &= \int_0^{2\pi}\int_0^{2\pi} \sin\theta\sin\phi P_l(\hat{\boldsymbol{k}}(\theta,\phi)\cdot\hat{\boldsymbol{r}}_{ba})\,|\sin\theta|\,e^{-j(m\theta+n\phi)}\mathrm{d}\theta\mathrm{d}\phi \qquad \text{(A.10)} \end{aligned}$$

These coefficients in turn satisfy the recursion formulas

$$\begin{aligned} a_{mn}^{l} &= \frac{1}{2}\left[f_{m-1,n}^{l} + f_{m+1,n}^{l}\right] \qquad \text{(A.11)} \\ b_{mn}^{l} &= \frac{1}{4j}\left[f_{m-1,n-1}^{l} + f_{m-1,n+1}^{l} - f_{m+1,n-1}^{l} - f_{m+1,n+1}^{l}\right] \qquad \text{(A.12)} \\ c_{mn}^{l} &= \frac{-1}{4}\left[f_{m-1,n-1}^{l} + f_{m+1,n+1}^{l} - f_{m+1,n-1}^{l} - f_{m-1,n+1}^{l}\right] \qquad \text{(A.13)} \end{aligned}$$

as can easily be verified. To start the recursion, some initial values are needed. These are given by

$$f_{mn}^{0} = \int_{0}^{2\pi}\int_{0}^{2\pi} |\sin\theta|\, e^{-j(m\theta+n\phi)}\mathrm{d}\theta\mathrm{d}\phi \tag{A.14}$$

$$= -4\pi\frac{1+(-1)^m}{m^2-1}\delta_{n0}. \tag{A.15}$$

APPENDIX B

Definition and properties of the Choice Function for VP Regularization

In this appendix, the choice function used in Value Picking regularization is defined and its relevant properties are proven.

B.1 Definitions

Definition B.1 *The choice function of dimension P, $f^P : \mathbb{R}_+^P \to \mathbb{R}_+$ ($\mathbb{R}_+$ is the set of non-negative real numbers), is defined as*

$$f^P(u_1,\ldots,u_P) = \frac{\prod_{k=1}^{K^P}\left(\prod_{I\subset\mathcal{C}_{2k-1}^{\{P\}}}\mathcal{S}_I(u_1,\ldots,u_P)\right)}{\prod_{l=1}^{L^P}\left(\prod_{J\subset\mathcal{C}_{2l}^{\{P\}}}\mathcal{S}_J(u_1,\ldots,u_P)\right)} \tag{B.1}$$

$$= \frac{\prod_{k=1}^{K^P}\mathcal{P}_{2k-1}^P(u_1,\ldots,u_P)}{\prod_{l=1}^{L^P}\mathcal{P}_{2l}^P(u_1,\ldots,u_P)} \tag{B.2}$$

$$= \frac{\mathcal{T}^P(u_1,\ldots,u_P)}{\mathcal{N}^P(u_1,\ldots,u_P)}, \tag{B.3}$$

where $\{P\}$ is short for $\{1,\ldots,P\}$, where $K^P = \lceil P/2\rceil$ and $L^P = \lfloor P/2\rfloor$, and where $\mathcal{C}_k^{\{P\}}$ is the set of all combinations of k different indices, chosen from $\{P\}$. $\mathcal{S}_I(u_1,\ldots,u_P)$ is given by

$$\mathcal{S}_I(u_1,\ldots,u_P) = \sum_{i\in I} u_i. \tag{B.4}$$

To see more clearly what this definition means, consider the choice function in 1, 2, 3 and 4 dimensions:

$$f^1(u_1) = u_1 \tag{B.5}$$

$$f^2(u_1,u_2) = \frac{u_1u_2}{u_1+u_2} \tag{B.6}$$

$$f^3(u_1,u_2,u_3) = \frac{u_1u_2u_3(u_1+u_2+u_3)}{(u_1+u_2)(u_1+u_3)(u_2+u_3)} \tag{B.7}$$

$$\begin{aligned} f^4(u_1,u_2,u_3,u_4) &= \frac{u_1u_2u_3u_4(u_1+u_2+u_3)}{(u_1+u_2)(u_1+u_3)(u_1+u_4)(u_2+u_3)(u_2+u_4)(u_3+u_4)} \\ &\quad \times \frac{(u_1+u_2+u_4)(u_1+u_3+u_4)(u_2+u_3+u_4)}{(u_1+u_2+u_3+u_4)} \end{aligned} \tag{B.8}$$

In the numerator, sums over all combinations of odd numbers of arguments can be found. De denominator contains sums over all the combinations of even numbers of arguments. From this observation, it is easily realized that the Choice Function is invariable under arbitrary permutations of its arguments and hence

Theorem B.1 *f^P is a fully symmetric function.*

To gain in generality, we define the auxiliary function F^P

Definition B.2 *$F^P : \mathbb{R}_+^{P+1} \to \mathbb{R}_+$ is defined as*

$$F^P(u_1,\ldots,u_P;x) = \frac{\prod_{k=1}^{K^P}\left[\prod_{I\subset\mathcal{C}_{2k-1}^{\{P\}}}(\mathcal{S}_I(u_1,\ldots,u_P)+x)\right]}{\prod_{l=1}^{L^P}\left[\prod_{J\subset\mathcal{C}_{2l}^{\{P\}}}(\mathcal{S}_J(u_1,\ldots,u_P)+x)\right]}. \tag{B.9}$$

It follows that

$$f^P(u_1,\ldots,u_P) = F^P(u_1,\ldots,u_P;0) \tag{B.10}$$

and it can be observed that F^P satisfies the recursion formula

$$F^P(u_1,\ldots,u_P;x) = (u_P+x)\frac{F^{P-1}(u_1,\ldots,u_{P-1};x)}{F^{P-1}(u_1,\ldots,u_{P-1};u_P+x)}. \tag{B.11}$$

This formula allows for an elegant recursive calculation of the choice function of arbitrary dimension P. Finally, we introduce the function G^P

Definition B.3 *$G^P : \mathbb{R}_+^{P+1} \to \mathbb{R}$ is defined as*

$$G^P(u_1,\ldots,u_P;x) = \left(\frac{\partial}{\partial x}\ln F^P\right)(u_1,\ldots,u_P;x). \tag{B.12}$$

Using (B.11), and this definition, the recursion

$$\begin{aligned} G^P(u_1,\ldots,u_P;x) &= \frac{1}{u_P+x} + G^{P-1}(u_1,\ldots,u_{P-1};x) \\ &\quad -G^{P-1}(u_1,\ldots,u_{P-1};x+u_P), \end{aligned} \tag{B.13}$$

is obtained with

$$G^1(u_1;x) = \frac{1}{u_1+x}. \tag{B.14}$$

This function is not defined for $x=0$ whenever one of the arguments u_p is zero, but is always finite when $x \neq 0$ or when $x=0$ and $u_p > 0, \forall p \in \{P\}$. Since F^P is fully symmetric in the arguments $(u_1,\ldots,u_P)$, G^P is too and we can use the shorthand notation $u_{\{P\}} = \{u_p : p \in \{P\}\}$ to write

$$F^P(u_{\{P\}};x) = F^P(u_1,\ldots,u_P;x), \tag{B.15}$$

$$G^P(u_{\{P\}};x) = G^P(u_1,\ldots,u_P;x). \tag{B.16}$$

B.2 Properties of the choice function

B.2.1 Limits of f^P and F^P

It might seem at first glance that the domain of the choice function in Definition B.1 has been chosen too large. Indeed, if more than one argument of the function f^P is zero, zero factors appear in the denominator of (B.3). However, the limit for one or more arguments going to zero is always defined and is equal to zero, as will be shown in the following lemmas and theorems.

Lemma B.1 *For $u_p > 0, \forall p \in \{P\}$,*

$$\lim_{x\to+\infty} \frac{F^P(u_{\{P\}};x)}{x} = 1. \tag{B.17}$$

Proof The proof uses a recursive argument. The Lemma clearly holds for $F^1(u_1;x) = u_1 + x$. If it holds for $P-1$, we can deduce

$$\lim_{x\to+\infty} \frac{F^P(u_{\{P\}};x)}{x} = \frac{\lim_{x\to+\infty} \frac{F^{P-1}(u_{\{P-1\}};x)}{x}}{\lim_{x\to+\infty} \frac{F^{P-1}(u_{\{P-1\}};x+u_P)}{x+u_P}} \tag{B.18}$$

$$= 1 \quad \square \tag{B.19}$$

As a direct result of this and the recursion formula (B.11) we have

Corollary B.1 *For* $u_p > 0, \forall p \in \{P\}$,

$$\lim_{u_P \to +\infty} F^P(u_{\{P\}}; x) = F^{P-1}(u_{\{P-1\}}; x). \tag{B.20}$$

Due to the symmetry in the arguments $u_{\{P\}}$, the previous statement can be generalized to

Corollary B.2 *For* $u_p > 0, \forall p \in \{P\}$,

$$\lim_{u_p \to +\infty} F^P(u_{\{P\}}; x) = F^{P-1}(u_{\{P\}\setminus p}; x). \tag{B.21}$$

In other words, whenever one of its arguments grows much larger then the other arguments, the choice function reduces to the choice function of one dimension less, evaluated in the remaining arguments. Suppose we let all arguments approach infinity, except the arguments u_i that belong to a set $I \subset \{P\}$. Suppose the number of elements in I is $N(I) = k$. We can let the arguments go to infinity one by one and every time the dimension of the choice function will reduce by one. Eventually, only the k- dimensional choice function will remain, evaluated in the arguments u_i, $i \in I$. This can be summarized in the following important theorem

Theorem B.2 *For* $u_p > 0$, $\forall p \in \{P\}$, *for* $I \subset \{P\}$ *with* $N(I) = k$ *and with* $\alpha u_{\{P\}\setminus I} = \{\alpha u_p : p \in \{P\} \setminus I\}$

$$\lim_{\alpha \to +\infty} F^P(u_I, \alpha u_{\{P\}\setminus I}; x) = F^k(u_I; x). \tag{B.22}$$

Using also the following lemma

Lemma B.2 *For* $u_p > 0, \forall p \in \{P\}$, *and for* $\alpha > 0$

$$F^P(\alpha u_1, \ldots, \alpha u_P; \alpha x) = \alpha F^P(u_{\{P\}}; x), \tag{B.23}$$

$$G^P(\alpha u_1, \ldots, \alpha u_P; \alpha x) = \frac{1}{\alpha} G^P(u_{\{P\}}; x), \tag{B.24}$$

(The proof is trivial using (B.11), (B.13) and a recursive argument)
one can conversely conclude that if k of its arguments are much smaller than the rest, the P-dimensional choice function reduces to the choice function of dimension k, evaluated in the smaller arguments, i.e.

$$f^P(u_{\{P\}}) \approx f^k(u_I), \quad \text{when} \quad u_i \ll u_p, \quad \forall i \in I, \quad \forall p \in \{P\} \setminus I. \tag{B.25}$$

Finally, when k arguments u_i with $i \in I$ go to zero, the choice function reduces to zero, as stated by the following theorem

Theorem B.3 *For $u_p > 0, \forall p \in \{P\}$, for $\alpha > 0$ and with $\alpha u_I = \{\alpha u_i : i \in I\}$*

$$\lim_{\alpha \to 0} f^P(\alpha u_I, u_{\{P\}\setminus I}) = 0. \tag{B.26}$$

Proof Using Lemma B.2 and Theorem B.2, we obtain

$$\begin{aligned} \lim_{\alpha \to 0} f^P(\alpha u_I, u_{\{P\}\setminus I}) &= \lim_{\alpha \to 0} F^P(\alpha u_I, u_{\{P\}\setminus I}; 0) \\ &= \lim_{\alpha \to 0} \alpha F^P(u_I, \frac{1}{\alpha} u_{\{P\}\setminus I}; 0) \\ &= \lim_{\alpha \to 0} \alpha F^k(u_I; 0) \\ &= 0 \quad \square \end{aligned} \tag{B.27}$$

Finally, from the properties above and from its definition, we can conclude

Theorem B.4 *$f^P(u_{\{P\}}) = 0$ if and only if at least one of the arguments u_p is zero.*

B.2.2 The choice function for identical arguments

Theorem B.5 *For any positive constant c*

$$F^P(u, \ldots, u; cu) \propto u \tag{B.28}$$

Proof The theorem clearly holds for $P = 1$ since $F^1(u; cu) = (c+1)u$. If it hold for $P - 1$, then we have

$$F^P(u, \ldots, u; cu) = (u + cu) \frac{F^{P-1}(u, \ldots, u; cu)}{F^{P-1}(u, \ldots, u; (c+1)u)} \tag{B.29}$$

$$\propto u. \tag{B.30}$$

A recursive argument concludes the proof. $\square$

As a special case we have

$$f^P(u, \ldots, u) \propto u, \tag{B.31}$$

thus when all its arguments are identical, the P-dimensional choice function is a scaled version of f^1.

B.2.3 Limits of G^P

Lemma B.3 *For $u_p > 0, \forall p \in \{P\}$,*

$$\lim_{x \to +\infty} G^P(u_{\{P\}}; x) = 0. \tag{B.32}$$

Proof The proof is recursive. For $G^1(u_1, x) = 1/(u_1 + x)$, the lemma holds. If it holds for $P - 1$, then we obtain, using (B.13)

$$\begin{aligned} \lim_{x\to+\infty} G^P(u_{\{P\}}; x) &= \lim_{x\to+\infty} \left[\frac{1}{u_P + x} + G^{P-1}(u_{\{P-1\}}; x) \right. \\ &\quad \left. -G^{P-1}(u_{\{P-1\}}; x + u_P) \right] \\ &= 0 \quad \square \end{aligned} \tag{B.33}$$

As a result of this and the recursion formula (B.13) we obtain

Corollary B.3 *For $u_p > 0, \forall p \in \{P\}$,*

$$\lim_{u_P\to+\infty} G^P(u_{\{P\}}; x) = G^{P-1}(u_{\{P-1\}}; x), \tag{B.34}$$

which can again be generalized to

Corollary B.4 *For $u_p > 0, \forall p \in \{P\}$,*

$$\lim_{u_p\to+\infty} G^P(u_{\{P\}}; x) = G^{P-1}(u_{\{P\}\setminus p}; x) \tag{B.35}$$

and

Theorem B.6 *For $u_p > 0$, $\forall p \in \{P\}$, for $I \subset \{P\}$ with $N(I) = k$ and with $\alpha u_{\{P\}\setminus I} = \{\alpha u_p : p \in \{P\} \setminus I\}$*

$$\lim_{\alpha\to+\infty} G^P(u_I, \alpha u_{\{P\}\setminus I}; x) = G^k(u_I; x). \tag{B.36}$$

B.2.4 Derivatives of the choice function and their properties

From Definition B.3 and from the recursion formula (B.11), an expression for the derivative of F^P with respect to u_P can be derived:

$$\begin{aligned} \left(\frac{\partial F^P}{\partial u_P}\right)(u_1, \ldots, u_P; x) &= F^P(u_{\{P\}}; x) \left(\frac{\partial \ln F^P}{\partial u_P}\right)(u_1, \ldots, u_P; x) \\ &= F^P(u_{\{P\}}; x) \left[\frac{1}{u_P + x} \right. \\ &\quad \left. -G^{P-1}(u_{\{P-1\}}; x + u_P) \right]. \end{aligned} \tag{B.37}$$

Because of the symmetry in F^P, this can be generalized to

$$\left(\frac{\partial F^P}{\partial u_p}\right)(u_1,\ldots,u_P;x) = F^P(u_{\{P\}};x)\left[\frac{1}{u_p+x} - G^{P-1}(u_{\{P\}\setminus p};x+u_p)\right]. \quad \text{(B.38)}$$

For $x=0$, we obtain de derivatives of the choice function f^P

$$\begin{aligned}\left(\frac{\partial f^P}{\partial u_p}\right)(u_1,\ldots,u_P) &= f^P(u_{\{P\}})\left[\frac{1}{u_p} - G^{P-1}(u_{\{P\}\setminus p};u_p)\right] \\ &= B_p^P(u_1,\ldots,u_P), \quad \text{(B.39)}\end{aligned}$$

where (B.39) defines the *weight functions* B_p^P. The choice for this name will become clear later on. We will now prove that the range of the weight functions is the interval $[0,1]$.

Lemma B.4 *For $u_p>0, \forall p\in\{P\}$ and for $x\geq 0$*

$$\left(\frac{\partial^k G^P}{\partial x^k}\right)(u_{\{P\}};x) = \begin{cases} >0 & \textit{for even } k \\ <0 & \textit{for odd } k \end{cases} \quad \text{(B.40)}$$

Proof For $P=1$, the lemma holds, since

$$\left(\frac{\partial^k G^1}{\partial x^k}\right)(u_1;x) = (-1)^k k!(u_1+x)^{-(k+1)}. \quad \text{(B.41)}$$

For general P we have

$$\begin{aligned}\left(\frac{\partial^k G^P}{\partial x^k}\right)(u_{\{P\}};x) &= (-1)^k k!(u_P+x)^{-(k+1)} + \left(\frac{\partial^k G^{P-1}}{\partial x^k}\right)(u_{\{P-1\}};x) \\ &\quad - \left(\frac{\partial^k G^{P-1}}{\partial x^k}\right)(u_{\{P-1\}};x+u_P). \quad \text{(B.42)}\end{aligned}$$

If the theorem holds for $P-1$ and when k is even, (B.42) is positive, because its first term is positive and the difference between the second and third term is positive too. Indeed, since k is even, $k+1$ is odd and $\left(\frac{\partial^k G^{P-1}}{\partial x^k}\right)(u_{\{P-1\}};x)$ is a monotonously decreasing function of x. When k is odd, (B.42) is negative, because its first term is negative and $\left(\frac{\partial^k G^{P-1}}{\partial x^k}\right)(u_{\{P-1\}};x)$ is a monotonously increasing function of x. A recursive argument then concludes the proof. □

As a special case, we have

Corollary B.5 *For $u_p > 0, \forall p \in \{P\}$ and for $x \geq 0$*

$$G^P(u_{\{P\}}; x) > 0. \tag{B.43}$$

Lemma B.5 *For $u_p > 0, \forall p \in \{P\}$ and for $x \geq 0$*

$$\left(\frac{\partial^k}{\partial x^k}\left[\frac{1}{x} - G^P\right]\right)(u_{\{P\}}; x) = \begin{cases} > 0 & \textit{for even } k \\ < 0 & \textit{for odd } k \end{cases} \tag{B.44}$$

Proof For $P = 1$, the lemma holds, since

$$\left(\frac{\partial^k}{\partial x^k}\left[\frac{1}{x} - G^1\right]\right)(u_1; x) = (-1)^k k!\left[x^{-(k+1)} - (u_1 + x)^{-(k+1)}\right]. \tag{B.45}$$

For general P we have

$$\left(\frac{\partial^k}{\partial x^k}\left[\frac{1}{x} - G^P\right]\right)(u_{\{P\}}; x) =$$

$$\left(\frac{\partial^k}{\partial x^k}\left[\frac{1}{x} - G^{P-1}\right]\right)(u_{\{P-1\}}; x) \tag{B.46}$$

$$-\left(\frac{\partial^k}{\partial x^k}\left[\frac{1}{x + u_P} - G^{P-1}\right]\right)(u_{\{P-1\}}; x + u_P). \tag{B.47}$$

The proof is concluded with a similar argument as is used in the proof of Lemma (B.4). □

As a result of Lemma B.5 and the definition (B.39) of the weight functions B_p^P, the following theorem is obtained

Theorem B.7 *For $u_p > 0, \forall p \in \{P\}$*

$$B_p^P(u_1, \ldots, u_P) > 0. \tag{B.48}$$

In other words, away from the boundaries of their domain, the functions B_p^P are always strictly positive. We will now show that they are also bounded above by 1.

Lemma B.6 *For $u_p > 0, \forall p \in \{P\}$,*

$$f^P(u_{\{P\}}) < u_p, \quad \forall p \in \{P\}. \tag{B.49}$$

Proof Consider first

$$\begin{aligned}\left(\frac{\partial F^{P-1}}{\partial x}\right)(u_{\{P\}\backslash p};x) &= F^{P-1}(u_{\{P\}\backslash p};x)\left(\frac{\partial \ln F^{P-1}}{\partial x}\right)(u_{\{P\}\backslash p};x)\\ &= F^{P-1}(u_{\{P\}\backslash p};x)G^{P-1}(u_{\{P\}\backslash p};x)\\ &> 0, \end{aligned} \tag{B.50}$$

where we have used the definition for G^{P-1} and Corollary B.5. Expression (B.50) says that F^{P-1} is monotonously increasing as a function of x, which implies

$$F^{P-1}(u_{\{P\}\backslash p};x) < F^{P-1}(u_{\{P\}\backslash p};x+u_p), \tag{B.51}$$

which in turn, using a straightforward generalization of (B.11), results in

$$\begin{aligned}F^{P}(u_{\{P\}};0) &= u_p\frac{F^{P-1}(u_{\{P\}\backslash p};0)}{F^{P-1}(u_{\{P\}\backslash p};u_p)}\\ &< u_p. \end{aligned} \tag{B.52}$$

This concludes the proof. □

Theorem B.8 *For $u_p > 0, \forall p \in \{P\}$,*

$$B_p^P(u_1,\ldots,u_P) < 1. \tag{B.53}$$

Proof This follows immediately from the definition (B.39), the positivity of G^{P-1} and Lemma B.6:

$$\begin{aligned}B_p^P(u_1,\ldots,u_P) &= f^P(u_{\{P\}})\left[\frac{1}{u_p} - G^{P-1}(u_{\{P\}\backslash p};u_p)\right]\\ &< \frac{f^P(u_{\{P\}})}{u_p}\\ &< 1. \quad \square \end{aligned} \tag{B.54}$$

It remains to be investigated what happens on the boundaries of the domain.

Lemma B.7 *For $u_p > 0, \forall p \in \{P\}$, for $\alpha > 0$, for $\alpha u_I = \{\alpha u_i : i \in I\}$ and for $p \notin I$,*

$$\lim_{\alpha\to 0} F^P(\alpha u_I, u_{\{P\}\backslash I};0)\left[\frac{1}{u_p} - G^{P-1}(\alpha u_I, u_{\{P\}\backslash(I\cup\{p\})};u_p)\right] = 0 \tag{B.55}$$

Proof Since $u_p > 0$, the expression between square brackets in (B.55) is finite ($G^P(u_{\{P\}};x)$ is always finite for $x > 0$). The first factor (B.55) approaches zero because of Theorem B.3. □

Lemma B.8 *For $u_p > 0, \forall p \in \{P\}$, for $\alpha > 0$, for $I \subset \{P\}$ with $N(I) = k$, for $\alpha u_I = \{\alpha u_i : i \in I\}$ and for $j \in I$,*

$$\lim_{\alpha \to 0} F^P(\alpha u_I, u_{\{P\}\setminus I}; 0) \left[\frac{1}{\alpha u_j} - G^{P-1}(\alpha u_{I\setminus j}, u_{\{P\}\setminus I}; \alpha u_j) \right]$$

$$= F^k(u_I; 0) \left[\frac{1}{u_j} - G^{k-1}(u_{I\setminus j}; u_j) \right] \tag{B.56}$$

Proof We use Lemma B.2, Theorem B.2 and Theorem B.6 to derive

$$\lim_{\alpha \to 0} F^P(\alpha u_I, u_{\{P\}\setminus I}; 0) \left[\frac{1}{\alpha u_j} - G^{P-1}(\alpha u_{I\setminus j}, u_{\{P\}\setminus I}; \alpha u_j) \right]$$

$$= \lim_{\alpha \to 0} \alpha F^P(u_I, \frac{1}{\alpha} u_{\{P\}\setminus I}; 0) \frac{1}{\alpha} \left[\frac{1}{u_j} - G^{P-1}(u_{I\setminus j}, \frac{1}{\alpha} u_{\{P\}\setminus I}; u_j) \right]$$

$$= F^k(u_I; 0) \left[\frac{1}{u_j} - G^{k-1}(u_{I\setminus j}; u_j) \right]. \quad \square \tag{B.57}$$

We can now formulate the following theorem which describes the range of B_p^P everywhere in the domain $\mathbb{R}_+^P$:

Theorem B.9 *The weight functions B_p^P have range $[0, 1]$, with*

$$B_p^P(u_1, \ldots, u_P) = 0 \quad \Leftrightarrow \quad \exists p' \neq p : u_{p'} = 0 \text{ and } u_p \neq 0, \tag{B.58}$$

$$B_p^P(u_1, \ldots, u_P) = 1 \quad \Leftrightarrow \quad u_p = 0 \text{ and } u_{p'} \neq 0, \ \forall p' \neq p. \tag{B.59}$$

In the intersections of the hyperplane $u_p = 0$ with other hyperplanes $u_{p'} = 0$ ($p' \neq p$), B_p^P is not uniquely defined. However, when approaching these intersections, a finite limit value in the interval $]0, 1[$ always exists which depends on the approach path.

Proof To proof the theorem, we consider four possibilities for the arguments u_p, which encompass all argument configurations:

i) $u_{p'} > 0, \forall p' \in \{P\}$:
In this case, Theorems B.7 and B.8 show that the values of $B_p^P(u_1, \ldots, u_P)$ lie in the interval $]0, 1[$.

ii) $u_p \neq 0$ and $\exists p' \neq p : u_{p'} = 0$:
When $u_p \neq 0$ and at least one $u_{p'}$ with $p' \neq p$ approaches zero, B_p^P approaches zero, as a result of Lemma B.7. Therefore

$$B_p^P(u_1, \ldots, u_P) = 0 \quad \Leftarrow \quad \exists p' \neq p : u_{p'} = 0 \text{ and } u_p \neq 0. \tag{B.60}$$

iii) $u_p = 0$ and $u_{p'} \neq 0, \forall p' \neq p$:
To investigate the case $u_p \to 0$ and $u_{p'} \neq 0, \forall p' \neq p$, we can put $I = \{p\}$ in Lemma B.8 and obtain

$$\lim_{\alpha \to 0} F^P(\alpha u_p, u_{\{P\}\setminus p}; 0) \left[\frac{1}{\alpha u_p} - G^{P-1}(u_{\{P\}\setminus p}; \alpha u_p) \right]$$
$$= u_p \left[\frac{1}{u_p} \right] = 1, \tag{B.61}$$

where we have put G^0 equal to zero, as is consistent with the recursion formula (B.13) and with $G^1(u_1; x) = 1/(u_1 + x)$. Therefore

$$B_p^P(u_1, \ldots, u_P) = 1 \quad \Leftarrow \quad u_p = 0 \text{ and } u_{p'} \neq 0, \ \forall p' \neq p. \tag{B.62}$$

iv) $u_p = 0$ and $\exists p' \neq p : u_{p'} = 0$:
consider Lemma B.8 when I includes p, but also some other indices, and when $j = p$. The set u_I then defines the approach direction to the intersection of the hyperplanes $u_i = 0$ with $i \in I$. The left hand side of (B.56) then is the limit of $B_p^P(u_1, \ldots, u_P)$ along the approach path to the intersection and the right hand side of (B.56) then equals $B_1^k(P_p(u_I))$, where $P_p(u_I)$ is a permutation of the arguments u_i, with $i \in I$, which puts u_p in the first position. This quantity lies in $]0, 1[$ because of Lemmas B.7 and B.8.

The value of B_p^P thus always lies in $]0, 1[$ except in the cases ii) and iii). This proves the last statement in Theorem B.9. Only in case ii), B_p^P equals zero. This, together with (B.60) proves (B.58). Only in case iii), B_p^P equals one. This, together with (B.62) proves (B.59). All cases together prove the first statement in Theorem B.9. □

B.2.5 Relaxation of the choice function

Lemma B.9 *For $u_p > 0, \forall p \in \{P\}$ and for $x > 0$*

$$\frac{F^P(u_{\{P\}}; x)}{x} > 1. \tag{B.63}$$

Proof First, note that F^P/x is a monotonously decreasing function of x. Indeed,

$$\begin{aligned} \frac{\partial}{\partial x} \frac{F^P}{x} &= \frac{1}{x} F^P \frac{\partial}{\partial x} \ln F^P - \frac{1}{x^2} F^P \\ &= \frac{1}{x} F^P G^P - \frac{1}{x^2} F^P \\ &= -\frac{F^P}{x} \left[\frac{1}{x} - G^P \right] \\ &< 0 \end{aligned} \tag{B.64}$$

where we used Lemma B.5 in the final step. Using this property and the recursion formula (B.11), we derive

$$\begin{aligned} \frac{F^P(u_{\{P\}};x)}{x} &= \frac{(u_P+x)}{F^{P-1}(u_{\{P-1\}};u_P+x)}\frac{F^{P-1}(u_{\{P-1\}};x)}{x} \\ &> 1. \end{aligned} \tag{B.65}$$

As a result of this lemma, the following theorem is obtained:

Theorem B.10

$$f^P(u_{\{P\}}) \leq f^{P-1}(u_{\{P\}\setminus p}). \tag{B.66}$$

Proof When $u_p > 0, \forall p \in \{P\}$, we obtain, by combining recursion formula (B.11) with Lemma B.9,

$$F^P(u_1,\ldots,u_P;x) < F^{P-1}(u_1,\ldots,u_{P-1};x), \tag{B.67}$$

which is valid for any $x \geq 0$ and which, due to the symmetry in the arguments u_p, leads to

$$f^P(u_{\{P\}}) < f^{P-1}(u_{\{P\}\setminus p}). \tag{B.68}$$

Whenever one or more arguments u_p are zero, the left hand side of (B.66) is zero, while the right hand side is non-negative, hence (B.68) can be generalized to (B.66). □

The above property is important in the Stepwise Relaxed VP regularization scheme, since it means a relaxation of the regularization when more VP values are added.

B.2.6 Touching hyperplane

Lemma B.10 *For* $u_p > 0, \forall p \in \{P\}$,

$$\sum_{p=1}^{P}\left[\frac{1}{u_p+x} - G^{P-1}(u_{\{P\}\setminus p};x+u_p)\right]u_p + G^P(u_{\{P\}};x)x = 1. \tag{B.69}$$

Proof Using the recursion formula (B.13) and some recombinations, the left hand

side of (B.69) can be rewritten as

$$\begin{aligned}
&\sum_{p=1}^{P}\frac{u_p}{u_p+x}-\sum_{p=1}^{P}G^{P-1}(u_{\{P\}\setminus p};x+u_p)u_p+\frac{x}{u_P+x}\\
&+G^{P-1}(u_{\{P\}\setminus P};x)x-G^{P-1}(u_{\{P\}\setminus P};x+u_P)x\\
=\;&\frac{u_P+x}{u_P+x}+\sum_{p=1}^{P-1}\frac{u_p}{u_p+x}-\sum_{p=1}^{P-1}G^{P-1}(u_{\{P\}\setminus p};x+u_p)u_p\\
&+G^{P-1}(u_{\{P\}\setminus P};x)x-G^{P-1}(u_{\{P\}\setminus P};x+u_P)(x+u_P)\\
=\;&1+\sum_{p=1}^{P-1}\frac{u_p}{u_p+x}-\sum_{p=1}^{P-1}G^{P-2}(u_{\{P\}\setminus\{p,P\}};x+u_p)u_p\\
&+\sum_{p=1}^{P-1}G^{P-2}(u_{\{P\}\setminus\{p,P\}};x+u_p+u_P)u_p-\sum_{p=1}^{P-1}\frac{u_p}{u_p+u_P+x}\\
&+G^{P-1}(u_{\{P\}\setminus P};x)x-G^{P-1}(u_{\{P\}\setminus P};x+u_P)(x+u_P).
\end{aligned}$$

By regrouping the terms in this expression and by assuming that the Lemma holds for $P-1$, we obtain

$$\begin{aligned}
&1+\left\{\sum_{p=1}^{P-1}\left[\frac{1}{u_p+x}-G^{P-2}(u_{\{P\}\setminus\{p,P\}};x+u_p)\right]u_p+G^{P-1}(u_{\{P-1\}})x\right\}\\
&-\left\{\sum_{p=1}^{P-1}\left[\frac{1}{u_p+u_P+x}-G^{P-2}(u_{\{P\}\setminus\{p,P\}};x+u_p+u_P)\right]u_p\right.\\
&\left.+G^{P-1}(u_{\{P-1\}};x+u_P)(x+u_P)\right\}\\
=\;&1+1-1=1.
\end{aligned}$$

By noting that the lemma holds for $P=1$, the lemma is proven. □

As a result of the previous lemma, we obtain the important theorem

Theorem B.11 *The hyperplane*

$$Q^P(u_1,\ldots,u_P;v_1,\ldots,v_P)=\sum_{p=1}^{P}B_p^P(v_1,\ldots,v_P)u_p \tag{B.70}$$

for fixed $(v_1,\ldots,v_P)\in\mathbb{R}_+^P$ *touches (i.e. coincides with and has the same gradient vector as)* f^P *in the point* $(v_1,\ldots,v_P)$.

Proof Consider first the case where $v_p > 0, \forall p \in \{P\}$. Lemma B.10 then results in

$$\begin{aligned} & Q^P(v_1, \ldots, v_P; v_1, \ldots, v_P) \\ & \quad = \sum_{p=1}^{P} B_p^P(v_1, \ldots, v_P) v_p & \text{(B.71)} \\ & \quad = F^P(v_{\{P\}}; 0) \sum_{p=1}^{P} \left[\frac{1}{v_p} - G^{P-1}(v_{\{P\}\setminus p}; v_p) \right] v_p & \text{(B.72)} \\ & \quad = f^P(v_{\{P\}}; 0). & \text{(B.73)} \end{aligned}$$

The functions Q^P and f^P thus coincide in $(v_1, \ldots, v_P)$. Also, by definition (B.39), the derivatives of Q^P and those of F^P with respect to u_p are identical and equal to $B_p^P(v_1, \ldots, v_P)$ in $(v_1, \ldots, v_P)$. Consider next the case where k arguments v_i with $i \in I$ are zero. The weights in (B.70) corresponding to these arguments will take on a value in the interval $[0, 1]$ and the weights corresponding to the other arguments will be zero, as follows from Theorem B.9. Evaluated in the point $(v_1, \ldots, v_P)$, Q^P will thus be zero and since f^P also is zero in this point, both functions coincide. In an arbitrary point $(v_1, \ldots, v_P)$ on the boundaries of the domain $\mathbb{R}_+^P$, the weights $B_p^P(v_1, \ldots, v_P)$ are not always uniquely defined as mentioned before, but along any approach path, they coincide with the derivatives of f^P in $B_p^P(v_1, \ldots, v_P)$. Therefore, in every point where the derivatives of f^P are defined, the hyperplane Q^P defined in this point, will touch with f^P in the same point. □

Finally, there is a statement which has been extensively tested on numerical test grids, but which we were unable to prove so far. Nevertheless, it plays an important role in the development of VP regularization. We formulate it as a conjecture:

Conjecture B.1 *The hyperplane*

$$Q^P(u_1, \ldots, u_P; v_1, \ldots, v_P) = \sum_{p=1}^{P} B_p^P(v_1, \ldots, v_P) u_p \qquad \text{(B.74)}$$

for fixed $(v_1, \ldots, v_P) \in \mathbb{R}_+^P$ *satisfies*

$$Q^P(u_1, \ldots, u_P; v_1, \ldots, v_P) \geq f^P(u_{\{P\}}) \qquad \text{(B.75)}$$

for all $u_{\{P\}}$ *in* $\mathbb{R}_+^P$.

If one were to proof that $f^P(u_{\{P\}})$ is concave, but not necessarily strictly concave (we suspect that this is true), this fact, together with Theorem B.11 would prove the conjecture. For the specific cases $P = 1$ and $P = 2$, the conjecture has been shown to hold.

We can now motivate the choice of the name *weight functions* for B_p^P. According to Theorem B.11, $f^P(u_{\{P\}})$ can be written as

$$f^P(u_{\{P\}}) = \sum_{p=1}^{P} B_p^P(u_1, \ldots, u_P) u_p, \tag{B.76}$$

which has the form of a weighted sum of the arguments u_p with weights $B_p^P(u_1, \ldots, u_P)$ which lie between 0 and 1. Suppose that the weights B_p^P in the right hand side of this expression are fixed at their values in $(u_1, \ldots, u_P)$. We then write

$$f^P(u_{\{P\}}) = \sum_{p=1}^{P} w_p u_p, \tag{B.77}$$

where $w_p = B_p^P(u_1, \ldots, u_P)$. Suppose furthermore that the arguments are updated from $(u_1, \ldots, u_P)$ to $(u'_1, \ldots, u'_P)$ and that this update entails a reduction of the right hand side in this expression. Due to Conjecture B.1 we then have

$$f^P(u'_{\{P\}}) \leq \sum_{p=1}^{P} w_p u'_p < \sum_{p=1}^{P} w_p u_p, \tag{B.78}$$

which means that the update also implies a reduction of the choice function. This observation plays an important role in VP regularization, because it allows for a fixed point iteration where the choice function in each step is temporarily replaced by a weighted sum of the form (B.77) and where the update of the arguments is based on this weighted sum.

B.3 Proof of (4.71)

Let us use the notations of Section 4.3 and state (4.71) as a theorem:

Theorem B.12

$$\mathcal{F}^P(\boldsymbol{\varepsilon}, \boldsymbol{c}) = 0 \Leftrightarrow \begin{cases} \frac{\partial \mathcal{F}^P}{\partial \epsilon_\nu} = 0, & \forall \nu \\ \frac{\partial \mathcal{F}^P}{\partial c_p} = 0, & c \in \{P-1\} \end{cases} \tag{B.79}$$

Proof Consider first a point $(\boldsymbol{\varepsilon}', \boldsymbol{c}')$ where $\mathcal{F}^P(\boldsymbol{\varepsilon}', \boldsymbol{c}') = 0$. This means, due to Theorem B.4 and the fact that $f^P \geq 0$, that for every optimization variable ϵ'_ν there is at least one VP value c'_q such that $(\epsilon'_\nu - c'_q) = 0$. Since the weights $b_{p,\nu}^P(\boldsymbol{\varepsilon}', \boldsymbol{c}')$, defined in (4.48), always lie in $[0, 1]$ due to Theorem B.9 and since $b_{p,\nu}^P(\boldsymbol{\varepsilon}', \boldsymbol{c}') = 0$ if $|\epsilon'_\nu - c'_p| \neq 0$ and if there is a $q \neq p$ for which $|\epsilon'_\nu - c'_q| = 0$ due to the same theorem,

we have

$$\frac{\partial \mathcal{F}^P}{\partial \epsilon_\nu}(\boldsymbol{\varepsilon}', \boldsymbol{c}') = \frac{1}{N^\epsilon} \sum_{p'=1}^{P} b^P_{p',\nu}(\boldsymbol{\varepsilon}, \boldsymbol{c}) \left(\epsilon'_\nu - c'_{p'}\right)^* = 0, \tag{B.80}$$

$$\frac{\partial \mathcal{F}^P}{\partial c_p}(\boldsymbol{\varepsilon}', \boldsymbol{c}') = -\frac{1}{N^\epsilon} \sum_{\nu'=1}^{N^\epsilon} b^P_{p,\nu'}(\boldsymbol{\varepsilon}', \boldsymbol{c}') \left(\epsilon'_{\nu'} - c'_p\right)^* = 0, \tag{B.81}$$

for every ν and for every p.

Consider next a point $(\boldsymbol{\varepsilon}', \boldsymbol{c}')$ where $\mathcal{F}^P(\boldsymbol{\varepsilon}', \boldsymbol{c}') \neq 0$. This means that at least for one optimization variable ϵ'_υ we have $|\epsilon'_\upsilon - c'_p| \neq 0$, for all p. Therefore, due to Theorem B.9, $b^P_{p,\upsilon}(\boldsymbol{\varepsilon}', \boldsymbol{c}')$ lies in $]0, 1[$, for all p. Now consider the quadratic function of the arguments $(\boldsymbol{\varepsilon}, \boldsymbol{c})$ and depending on the parameters $(\boldsymbol{\varepsilon}', \boldsymbol{c}')$,

$$\mathcal{Q}^P(\boldsymbol{\varepsilon}, \boldsymbol{c}; \boldsymbol{\varepsilon}', \boldsymbol{c}') = \frac{1}{N^\epsilon} \sum_{\nu=1}^{N^\epsilon} \sum_{p=1}^{P} b^P_{p,\nu}(\boldsymbol{\varepsilon}', \boldsymbol{c}') \mid \epsilon_\nu - c_p \mid^2, \tag{B.82}$$

which touches with $\mathcal{F}^P$ in $(\boldsymbol{\varepsilon}', \boldsymbol{c}')$ because of Theorem B.11. We therefore have $\mathcal{Q}^P(\boldsymbol{\varepsilon}', \boldsymbol{c}'; \boldsymbol{\varepsilon}', \boldsymbol{c}') = \mathcal{F}^P(\boldsymbol{\varepsilon}', \boldsymbol{c}') \neq 0$. The choice $\epsilon''_\nu = c''_p$ for all ν and p minimizes $\mathcal{Q}^P$, i.e. $\mathcal{Q}^P(\boldsymbol{\varepsilon}'', \boldsymbol{c}''; \boldsymbol{\varepsilon}', \boldsymbol{c}') = 0$. Since c''_P is fixed to $\epsilon_\mathrm{b}/\epsilon_0$ (Section 4.3.1), this can only be the case when $\epsilon''_\nu = c''_p = \epsilon_\mathrm{b}/\epsilon_0$, for all ν and p. It is now possible to prove that $(\boldsymbol{\varepsilon}'', \boldsymbol{c}'')$ is the unique minimizer of $\mathcal{Q}^P$. Indeed, we certainly have

$$\mathcal{Q}^P(\boldsymbol{\varepsilon}'', \boldsymbol{c}''; \boldsymbol{\varepsilon}', \boldsymbol{c}') \geq \frac{1}{N^\epsilon} \sum_{p=1}^{P} b^P_{p,\upsilon}(\boldsymbol{\varepsilon}', \boldsymbol{c}') \mid \epsilon''_\upsilon - c''_p \mid^2, \tag{B.83}$$

and therefore $\mathcal{Q}^P = 0$ requires

$$\frac{1}{N^\epsilon} \sum_{p=1}^{P} b^P_{p,\upsilon}(\boldsymbol{\varepsilon}', \boldsymbol{c}') \mid \epsilon''_\upsilon - c''_p \mid^2 = 0, \tag{B.84}$$

which, because $b^P_{p,\upsilon}(\boldsymbol{\varepsilon}', \boldsymbol{c}') > 0$, $\forall p$, requires $\epsilon''_\upsilon = c''_p = \epsilon_\mathrm{b}/\epsilon_0$, for all p, thus all VP values c''_p are identical. Since it can easily be deduced from Theorem B.9 that never all weights $b^P_{\nu,p}(\boldsymbol{\varepsilon}', \boldsymbol{c}')$ for a certain ν can be zero simultaneously, $\mathcal{Q}^P(\boldsymbol{\varepsilon}'', \boldsymbol{c}''; \boldsymbol{\varepsilon}', \boldsymbol{c}') = 0$ furthermore requires that there is at least one VP value c''_q for every optimization variable ϵ''_ν such that $\epsilon''_\nu = c''_q$. As a result, the condition $\epsilon''_\nu = \epsilon_\mathrm{b}/\epsilon_0$, has to be satisfied for all ν. The point $(\boldsymbol{\varepsilon}'', \boldsymbol{c}'')$ with $\epsilon''_\nu = c''_p = \epsilon_\mathrm{b}/\epsilon_0$ for all ν and p thus is the unique minimizer of $\mathcal{Q}^P(\boldsymbol{\varepsilon}, \boldsymbol{c}; \boldsymbol{\varepsilon}', \boldsymbol{c}')$. It can now be seen that $\mathcal{Q}^P(\boldsymbol{\varepsilon}, \boldsymbol{c}; \boldsymbol{\varepsilon}', \boldsymbol{c}')$ has non-zero derivatives with respect to both ϵ_ν and c_p, for all ν and p, in $(\boldsymbol{\varepsilon}', \boldsymbol{c}')$, since it has just been proven that $\mathcal{Q}^P$ has a unique minimum $(\boldsymbol{\varepsilon}'', \boldsymbol{c}'')$ where $\mathcal{Q}^P = 0$ and this unique minimum has to be the only stationary point of $\mathcal{Q}^P$, because $\mathcal{Q}^P$ is a quadratic

function.

Summarizing, we have

$$\mathcal{F}^P(\boldsymbol{\varepsilon}, \boldsymbol{c}) = 0 \Rightarrow \begin{cases} \frac{\partial \mathcal{F}^P}{\partial \epsilon_\nu} = 0, & \forall \nu \\ \frac{\partial \mathcal{F}^P}{\partial c_p} = 0, & c \in \{P-1\} \end{cases} \tag{B.85}$$

and

$$\mathcal{F}^P(\boldsymbol{\varepsilon}, \boldsymbol{c}) \neq 0 \Rightarrow \begin{cases} \frac{\partial \mathcal{F}^P}{\partial \epsilon_\nu} \neq 0, & \forall \nu \\ \frac{\partial \mathcal{F}^P}{\partial c_p} \neq 0, & c \in \{P-1\} \end{cases} \tag{B.86}$$

which proves the Theorem. □

APPENDIX C

Conjugate gradient optimization

Consider a real-valued function $\mathcal{F}(\boldsymbol{j}_1, \ldots, \boldsymbol{j}_I)$ of the complex contrast current vectors $\boldsymbol{j}_i$ and the gradient vectors $\boldsymbol{g}_i$

$$[\boldsymbol{g}_i]_n = \frac{\partial \mathcal{F}}{\partial [\boldsymbol{j}_i^*]_n}. \tag{C.1}$$

We first consider the minimization of $\mathcal{F}$ with respect to $\boldsymbol{j}_i$. Starting from an iterate $\boldsymbol{j}_i^m$, the next estimation of the contrast current vectors is calculated as

$$\boldsymbol{j}_i^{m+1} = \boldsymbol{j}_i^m + \alpha^m \boldsymbol{p}_{1,i}^m, \tag{C.2}$$

where $\boldsymbol{p}_{1,i}^m$ are the Polak-Ribière update vectors

$$\boldsymbol{p}_{1,i}^m = -\boldsymbol{g}_i^m + \beta_1^m \boldsymbol{p}_{1,i}^{m-1}, \tag{C.3}$$

$$\beta_1^m = \frac{\Re\left[\sum_{i=1}^I \left(\boldsymbol{g}_i^m - \boldsymbol{g}_i^{m-1}\right)^H \boldsymbol{g}_i^m\right]}{\sum_{i=1}^I \left(\boldsymbol{g}_i^{m-1}\right)^H \boldsymbol{g}_i^{m-1}}, \tag{C.4}$$

where $\beta_1^1 = 0$ in the first iteration. The real-valued line parameter α^m is determined with a line search. Since all the cost functions in Chapter 6 are fourth or second order polynomials in the contrast currents $\boldsymbol{j}_i$ and their complex conjugates $\boldsymbol{j}_i^*$, they are fourth or second order polynomials as a function of the line parameter α^m. The line search is then simply performed by determining the roots of the differentiated polynomials, which can be done analytically or numerically by solving for the eigenvalues of the companion matrix [1].

In case we want to optimize $\mathcal{F}$ for the non-radiating current vectors only, we seek for $(N - I)$-dimensional coefficient vectors $\boldsymbol{c}_i$ that contain the projections of $\boldsymbol{j}_i$ on

the null space of $\boldsymbol{A}$:

$$\begin{aligned} \boldsymbol{c}_i &= \boldsymbol{W}^H \boldsymbol{j}_i, && \text{(C.5)} \\ \boldsymbol{j}_i^{\mathrm{NR}} &= \boldsymbol{W}\boldsymbol{c}_i, && \text{(C.6)} \end{aligned}$$

where $\boldsymbol{W}$ is a $(N \times (N-I))$-matrix with orthonormal columns that span the null space of $\boldsymbol{A}$ and that are orthonormal to the columns of the matrix $\boldsymbol{V}$ of the truncated SVD decomposition (6.28) of $\boldsymbol{A}$, i.e. $\boldsymbol{W}^H\boldsymbol{V} = 0$. The gradient vectors $\boldsymbol{f}_i$ with respect to these coefficient vectors, defined by

$$[\boldsymbol{f}_i]_m = \frac{\partial \mathcal{F}}{\partial \left[\boldsymbol{c}_i^*\right]_m}. \tag{C.7}$$

are obtained by an application of the chain rule:

$$\boldsymbol{f}_i = \boldsymbol{W}^H \boldsymbol{g}_i. \tag{C.8}$$

Therefore, the corresponding Polak-Ribière updates are

$$\begin{aligned} \boldsymbol{c}_i^{m+1} &= \boldsymbol{c}_i^m + \alpha^m \boldsymbol{q}_i^m, && \text{(C.9)} \\ \boldsymbol{q}_i^m &= -\boldsymbol{f}_i^m + \beta_2^m \boldsymbol{q}_i^{m-1} = -\boldsymbol{W}^H \boldsymbol{g}_i^m + \beta_2^m \boldsymbol{q}_i^{m-1}, && \text{(C.10)} \\ \beta_2^m &= \frac{\Re\left[\sum_{i=1}^I \left(\boldsymbol{f}_i^m - \boldsymbol{f}_i^{m-1}\right)^H \boldsymbol{f}_i^m\right]}{\sum_{i=1}^I \left(\boldsymbol{f}_i^{m-1}\right)^H \boldsymbol{f}_i^{m-1}} \\ &= \frac{\Re\left[\sum_{i=1}^I \left(\boldsymbol{g}_i^m - \boldsymbol{g}_i^{m-1}\right)^H \boldsymbol{W}\boldsymbol{W}^H \boldsymbol{g}_i^m\right]}{\sum_{i=1}^I \left(\boldsymbol{g}_i^{m-1}\right)^H \boldsymbol{W}\boldsymbol{W}^H \boldsymbol{g}_i^{m-1}}. && \text{(C.11)} \end{aligned}$$

Defining $\boldsymbol{p}_{2,i}^m = \boldsymbol{W}\boldsymbol{q}_i^m$ and using $\boldsymbol{W}\boldsymbol{W}^H\boldsymbol{x} = \boldsymbol{x} - \boldsymbol{V}\boldsymbol{V}^H\boldsymbol{x}$, for every N-dimensional vector $\boldsymbol{x}$, we obtain following updates for the contrast current vectors $\boldsymbol{j}_i$ directly:

$$\begin{aligned} \boldsymbol{j}_i^{m+1} &= \boldsymbol{j}_i^m + \alpha^m \boldsymbol{p}_{2,i}^m, && \text{(C.12)} \\ \boldsymbol{p}_{2,i}^m &= -\left(\boldsymbol{g}_i^m - \boldsymbol{V}\boldsymbol{V}^H \boldsymbol{g}_i^m\right) + \beta_2^m \boldsymbol{p}_{2,i}^{m-1}, && \text{(C.13)} \\ \beta_2^m &= \frac{\Re\left[\sum_{i=1}^I \left(\boldsymbol{g}_i^m - \boldsymbol{g}_i^{m-1}\right)^H \left(\boldsymbol{g}_i^m - \boldsymbol{V}\boldsymbol{V}^H \boldsymbol{g}_i^m\right)\right]}{\sum_{i=1}^I \left(\boldsymbol{g}_i^{\mathrm{C},m-1}\right)^H \left(\boldsymbol{g}_i^{m-1} - \boldsymbol{V}\boldsymbol{V}^H \boldsymbol{g}_i^{m-1}\right)}. && \text{(C.14)} \end{aligned}$$

Note that multiplications of the form $\boldsymbol{V}\boldsymbol{V}^H\boldsymbol{x}$ can be evaluated relatively cheaply as $\boldsymbol{V}(\boldsymbol{V}^H\boldsymbol{x})$ since $\boldsymbol{V}$ only has a small number of columns.

Bibliography

[1] A. Edelman and H. Murakami. Polynomial roots from companion matrix eigenvalues. *Math. Comp.*, 64:763–776, 1995.

APPENDIX D

Expressions for the gradient vectors in the CI method

In this appendix, the explicit expressions for the gradient vectors in the Consistency Inversion method of Chapter 6 are given. We only consider the expressions of the gradient vectors $\boldsymbol{g}_i^D$, $\boldsymbol{g}_i^{CSI}$, $\boldsymbol{g}_i^{CI}$ and $\boldsymbol{g}_i^P$ of $\mathcal{F}^D$, $\mathcal{F}^{CSI}$, $\mathcal{F}^{CI}$ and $\mathcal{F}^P$ respectively, since all other gradient vectors are simple combinations of those.

- The gradient vectors of $\mathcal{F}^D$:

$$\boldsymbol{g}_i^D = \frac{1}{\sum_{i=1}^{I} \|\boldsymbol{e}_i^s\|^2} \boldsymbol{A}^H \left(\boldsymbol{A}\boldsymbol{j}_i - \boldsymbol{e}_i^s\right) \tag{D.1}$$

- The gradient vectors of $\mathcal{F}^{CSI}$:

$$\boldsymbol{g}_i^{CSI} = \boldsymbol{j}_i - j\omega\boldsymbol{X}\boldsymbol{e}_i + j\omega\boldsymbol{Z}^H\boldsymbol{X}^* \left(\boldsymbol{j}_i - j\omega\boldsymbol{X}\boldsymbol{e}_i\right) \tag{D.2}$$

- The gradient vectors of $\mathcal{F}^{CI}$:

$$\boldsymbol{g}_i^{CI} = \sum_{k\in K} \left[\boldsymbol{u}_{i,k} \circ \boldsymbol{e}_{i-k}^* - \boldsymbol{u}_{i+k,k} \circ \boldsymbol{e}_{i+k}^* + \boldsymbol{Z}^H \left(\boldsymbol{u}_{i+k,k} \circ \boldsymbol{j}_{i+k}^* - \boldsymbol{u}_{i,k} \circ \boldsymbol{j}_{i-k}^*\right)\right], \tag{D.3}$$

  with

$$\boldsymbol{u}_{i,k} = \boldsymbol{j}_i \circ \boldsymbol{e}_{i-k} - \boldsymbol{j}_{i-k} \circ \boldsymbol{e}_i \tag{D.4}$$

- The gradient vectors of $\mathcal{F}^P$:

$$\begin{aligned}
\boldsymbol{g}_i^P &= \left(\sum_{p=1}^{P} \boldsymbol{w}_p\right) \circ \sum_{k\in K} \left(\boldsymbol{u}_{i,k} \circ \boldsymbol{e}_{i-k}^* - \boldsymbol{u}_{i+k,k} \circ \boldsymbol{e}_{i+k}^*\right) \\
&\quad + \lambda_2 \boldsymbol{h}_i \circ \sum_{p=1}^{P} \boldsymbol{w}_p \circ (\boldsymbol{j}_i - j\omega c_p \boldsymbol{e}_i) \qquad \text{(D.5)} \\
&\quad + \boldsymbol{Z}^H \Bigg[\left(\sum_{p=1}^{P} \boldsymbol{w}_p\right) \circ \sum_{k\in K} \left(\boldsymbol{u}_{i+k,k} \circ \boldsymbol{j}_{i+k}^* - \boldsymbol{u}_{i,k} \circ \boldsymbol{j}_{i-k}^*\right) \\
&\quad + \lambda_2 j\omega \boldsymbol{h}_i \circ \sum_{p=1}^{P} c_p^* \boldsymbol{w}_p \circ (\boldsymbol{j}_i - j\omega c_p \boldsymbol{e}_i) \Bigg], \qquad \text{(D.6)}
\end{aligned}$$

  where $\boldsymbol{h}_i$ is an N-dimensional vector containing the normalization constants $H_{i,n}$ for a certain excitation i and where the N-dimensional vector $\boldsymbol{w}_p$ contains the weights $W_{n,p}$, defined as

$$W_{n,p} = B_p^P(U_n + \lambda_2 V_{n,1}, \ldots, U_n + \lambda_2 V_{n,P}), \qquad \text{(D.7)}$$

  where the functions B_p^P are defined in (B.39).

Note that, in the linear combinations of the above gradient vectors which give the gradient vectors of the total cost function, the matrix $\boldsymbol{Z}^H$ can be brought up front and hence only one multiplication with this matrix has to be performed for every excitation i.

Research funded by a Ph.D grant of the Fund for Scientific Research in Flanders (FWO-Vlaanderen).